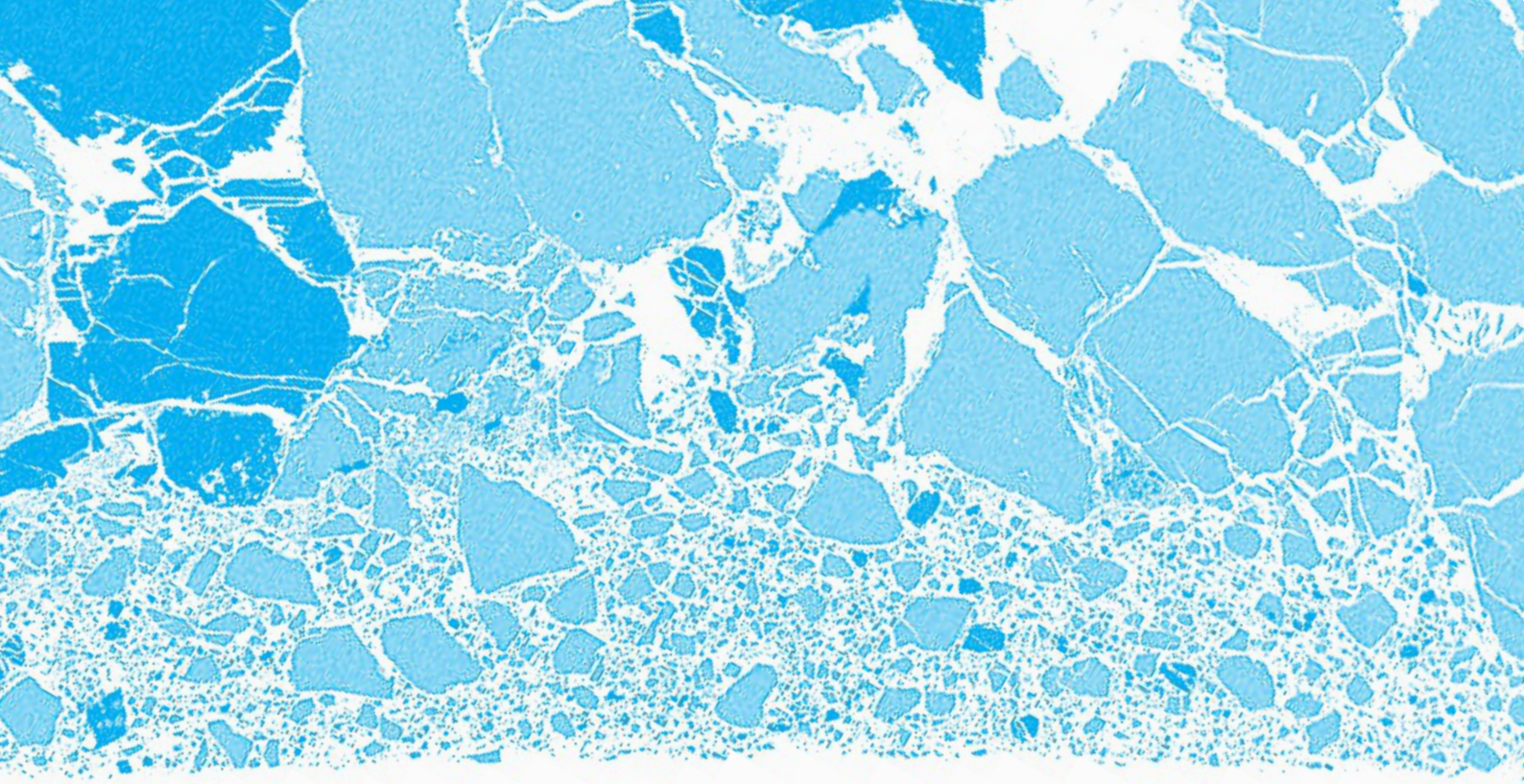

Geomechanical Characterization of the Buntsandstein including a Fracture Model

Thomas Hinkofer

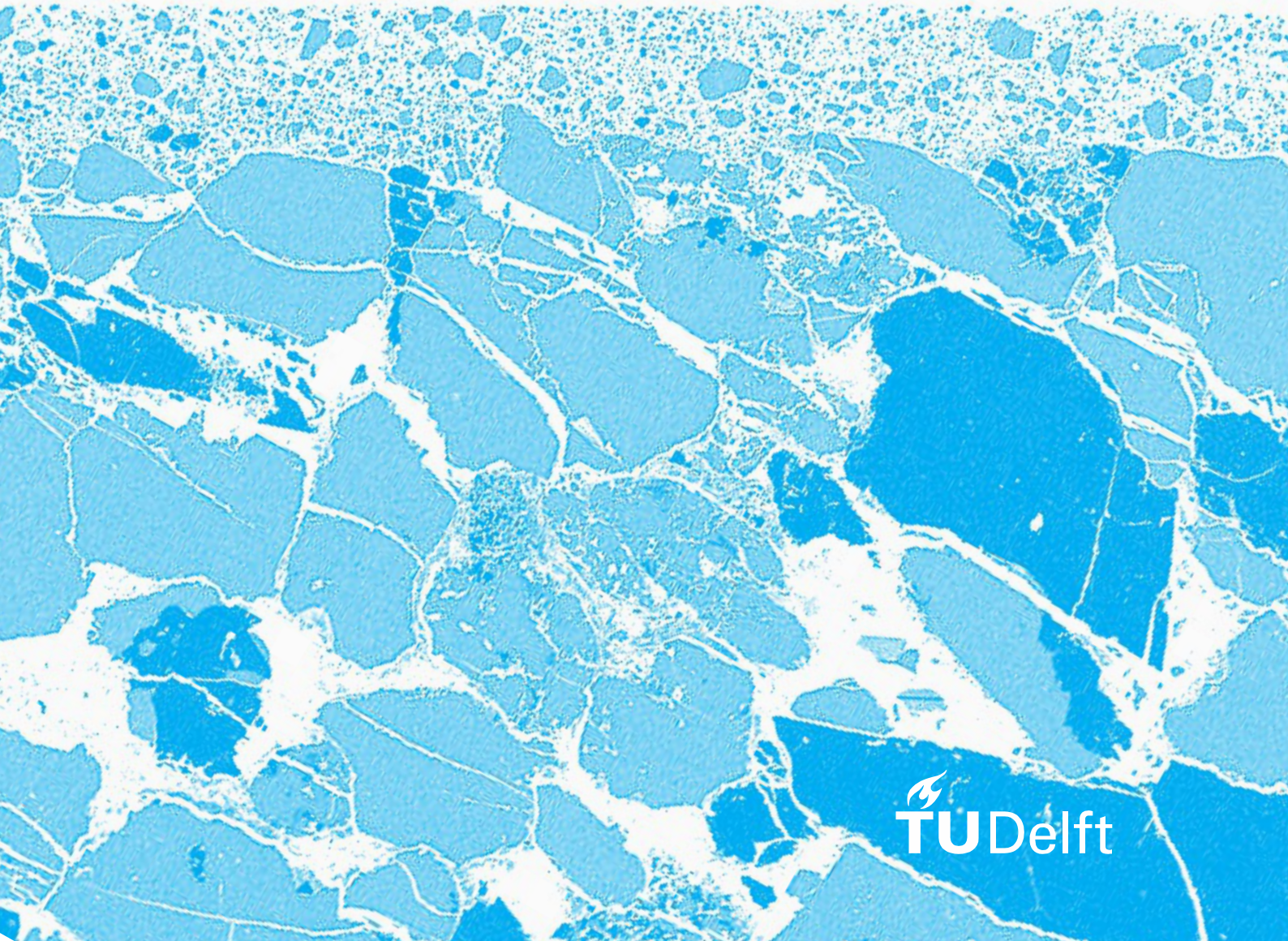

Thomas Hinkofer

Department of Geoscience & Engineering

Delft University of Technology

This dissertation is submitted for the degree of

Master of Science

August 2017

Geomechanical Characterization of the Buntsandstein including a Fracture Model

by

Thomas Hinkofer

in partial fulfilment of the requirements for the degree of

Master of Science

in Petroleum Engineering and Geosciences

at the Delft University of Technology,

to be defended publicly on Monday August 7, 2017 at 13:00 PM.

Supervisors:	Prof Dr D.F. Bruhn	TU Delft / GFZ Potsdam
	Dr R.R. Bakker	TU Delft
Thesis committee:	Dr A. Barnhoorn	TU Delft
	Dr N. Gholizadeh Doonechaly	TU Delft
	Dr F. Deon	TU Delft / GFZ Potsdam

This thesis is confidential and cannot be made public until December 31, 2019.

TU Delft

Abstract

With an increased demand for renewable energy sources, geothermal developments have moved into the spotlight, including sedimentary structures. In the western part of the Netherlands, cretaceous sandstone bodies are already in use for the geothermal energy production. However, these reservoirs are generally producing water at temperatures less than 100°C from depths of 1500 to 3000 m. To reach higher temperatures, deeper reservoirs need to be targeted.

Being more than 130 m thick in some parts and up to 4000 m deep, the Lower Triassic Buntsandstein would provide an ideal target reservoir for geothermal exploration in the West Netherlands Basin, given the high temperatures of over 140°C at this depth. However, the Buntsandstein is relatively heterogeneous in terms of porosity, as seen in numerous rock samples, and the overall permeability that was found in the Buntsandstein in various wells was generally low. Therefore a conventional development of a Buntsandstein reservoir, with a geothermal doublet in a natural hydrothermal reservoir, might not be applicable. To enhance the permeability and achieve economic flow rates, hydraulic stimulation can be performed. This technique has proven to be effective in many other reservoirs. To assess such effects on the Buntsandstein, this thesis focusses on the effect of fractures on the fluid flow in the Buntsandstein. Geomechanical characteristics and physical properties of the Buntsandstein at relevant pressure and temperature (PT) conditions are investigated in core experiments in uniaxial compression tests and triaxial tests. The laboratory experiments on cores provide reliable intrinsic information of permeability at relevant PT conditions and give a realistic estimation of fluid flow parameters. Triaxial deformation tests were conducted on different sandstones varying in porosity, clay content, degree of oxidization and initial permeability. Changes in permeability before and after deformation are compared. Moreover, the effect of increasing confining pressure on the permeability is measured on intact sandstones. Two principal modes of brittle fracture (extension fracture and shear fracture) were tested on samples under confining pressure. Experiments revealed that the permeability decreases by a factor of 17 in porous sandstones, from 85 mD to 5 mD, when inducing shear fractures at 30 MPa effective pressure. Buntsandstein samples with a low initial permeability (~1 mD) show a slight increase to 2 mD. For tensile fractures the permeability increased exponentially with the increase in apparent fracture aperture. Up to apertures of around 1000 µm, the permeability increased by factor of 2 for increments of 100 µm.

Ultimately, effects of fractures and resulting changes in flow properties are analyzed for the impact on the production life of a geothermal injector-producer pair. Results from lab experiments are implemented in a field scale thermo-hydro-mechanical model, making it possible to predict the PT distribution in the reservoir in regard to a change in permeability. The laboratory experiments and the numerical modeling procedure indicate that the in-situ permeability is too low for a geothermal reservoir production and would require some sort of stimulation to enhance the permeability.

Acknowledgment

Since I have started my thesis research I have collaborated with many different people from a variety of backgrounds. All of them have added a lot of additional value to this project, and therefore I would like to express my gratitude.

Foremost I would like to thank my supervisor Professor David Bruhn for giving me the opportunity of doing this research and for being very eager to help me choose the best possible project in geothermal engineering. Moreover I would like to thank him for always taking his time when I needed it and for bringing up a lot of new ideas, especially when it comes to collaborations with other people.

My special thanks go to Dr Richard Bakker as my daily supervisor. He gave me immense support and was always available when I needed help. Through his constant guidance and profound geomechanical knowledge I have learnt a lot. He always gave useful input and tried to really make me understand what I am doing and why I am doing it.

Besides, I am very grateful to Dr Nima Gholizadeh Doonechaly for constantly helping me about my questions in numerical modeling and hydraulic fracturing. I would also like to thank Dr Fiorenza Deon for always taking her time and for working with me at the GFZ Potsdam. I really appreciated her constant good mood and that she was very dedicated towards my progress in the project.

Furthermore I would like to thank Dr Auke Barnhoorn, Reuben Zotz-wilson and Lisanne Douma for being there when I had questions and needed help. I would like to thank Marc Friebel and Karel Heller for helping me setting up my experiments and for guaranteeing that the lab is still intact after I have used it. Furthermore I have to thank Jens van den Berg for showing me how to make perfect core samples and for teaching me how to do my own (less perfect) thin sections.

I also have to thank Wim Verwaal, Jolanda van Haagen-Donker and Ellen Meijvogel-de Koning for generating great CT-scan images. I thank Dr. Karl-Heinz Wolf for the use of the facilities of the Geoscience and Engineering laboratory at the TU Delft. Additionally my gratitude goes to Dr Franziska Wilke and Oona Appelt from the Electron microprobe laboratory of the GFZ for their help with the EPMA. Ruud Hendrikx at the Department of Materials Science and Engineering of the Delft University of Technology is acknowledged for the X-ray analysis.

At last I owe my deep appreciation to my parents, my brother and my grandparents, who have constantly supported and encouraged me throughout the years.

Abbreviations

BHP	bottomhole pressure
BHT	bottomhole temperature
CB	compaction bands
DSSM	Delft Sandstone Member
EDS	energy dispersive X-ray spectroscopy
EGS	enhanced geothermal systems
EPMA	electron probe microanalyzer
HDR	hot dry rock
HF	hydrofluoric acid
LVDT	linear variable differential transformers
MD	measured depth
PT	pressure and temperature conditions
RFT	repeat formation tester
RJD	radial jet drilling
SD	standard deviation
SIF	stress intensity factor
THM	thermo-hydro-mechanical
TVD	true vertical depth
UCS	uniaxial compressive strength
WNB	West Netherlands Basin
XRD	X-ray powder diffraction
XRF	X-Ray fluorescence analysis

Table of Contents

1. Introduction

1.1 General

In recent years the energy politics in Europe changed considerably. Close to 90% of the newly added power of Europe's electricity grid in 2016 came from renewable sources such as wind, solar, biomass, hydropower and geothermal (Vaughan, 2017). In the Netherlands, however, only 5.8% of the total energy production were accountable for renewable energy in 2016. Since the Renewable Energy Directive 2009/28/EC, a binding goal was set for the Netherlands to reach at least 14% share in renewables by 2020 (Daumas, 2017). With this goal being set, there is an increased demand for renewable energy sources and geothermal developments have moved into the spotlight. A large number of future potential geothermal projects has come up in the Netherlands over the last years, with an increasing number being developed in the near future. In 2008, the first geothermal well was realized in the Netherlands. Since then, the amount of geothermal doublets increased continuously (see Figure 1.1; www.geothermie.nl, 2017).

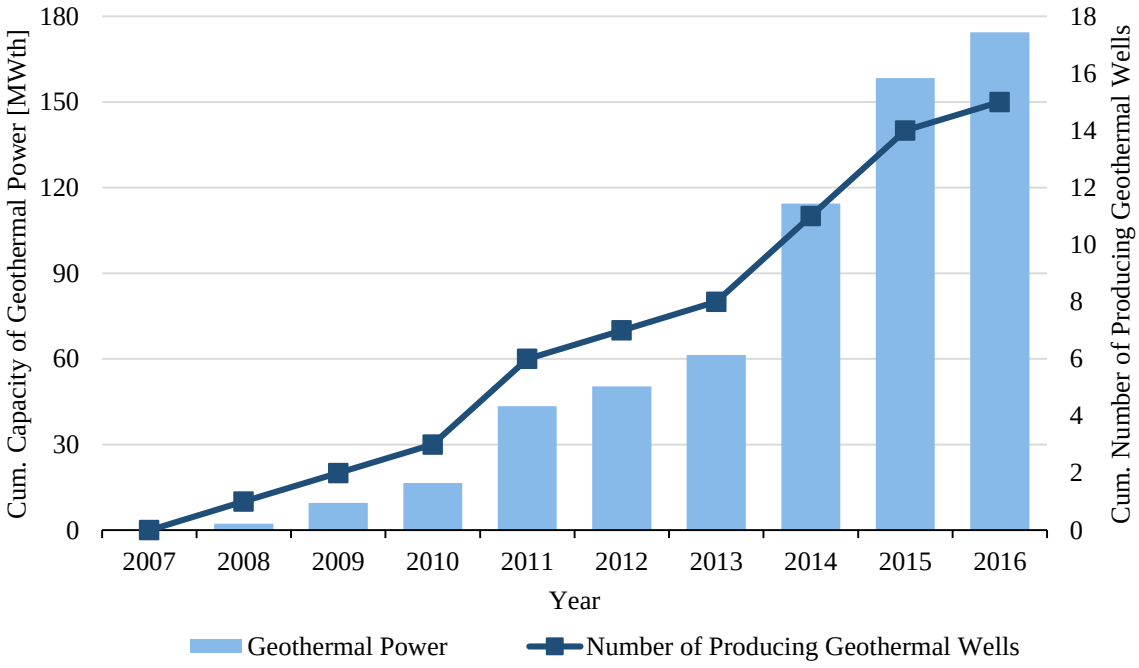

Figure 1.1: Cumulative annual number of producing geothermal wells and capacity of geothermal power. Data retrieved from www.geothermie.nl (2017).

With Zuid-Holland having a relatively high urban density compared to other areas in Central Europe, the demand for sustainable energy is especially high. Recent deep geothermal projects in the area, such as the geothermal doublet in Vierpolders, have been very successful. Here, warm water is

produced from the subsurface (production well), and then reinjected again in a second well (injection well) after the energy is extracted. The energy is primarily used for heating greenhouses, but can also be used for district heating of houses (Appendix A). Water temperatures are often below 85°C (www.geothermie.nl, 2017). However, for generating electricity, temperatures above 100°C and high flow rates (> 100 L/s) are generally needed to economically power a binary cycle power plant (Frick et al., 2010; Pavicic, 2015; Appendix A). Therefore, deeper exploration targets have to be set to achieve these temperatures.

1.2 Geothermal Energy in the West Netherlands Basin

For the future generation of energy in the Netherlands, geothermal projects within the area of Zuid-Holland are of major importance. In terms of geology, the region lies above the West Netherlands Basin (WNB; Figure 1.2). The basin has been an exploration target for the oil and gas industry over the last 30 years and is well studied. Especially the Lower Triassic Buntsandstein formation (approx. 245 Ma) showed excellent reservoir quality in some fields in the North Sea (Fig. 1.3; Van Hulten, 2009). For local geothermal exploitation, the Delft Sandstone Member (DSSM) has proven to be a good reservoir in terms of productivity. The DSSM is part of the Lower Cretaceous fluvial sandstones from the Nieuwekerk Formation (Schieland Group; Fig. 1.3; Donselaar, 2015). So far, several geothermal wells were drilled in the DSSM. As an example, the Green Well Westland project has reached a depth of around 2800 m, producing 85°C hot water at 50 L/s (Green Well Westland, 2016). In order to increase the production even more, higher temperatures are required. This should be achieved by drilling deeper wells where increased temperatures prevail. As a potential target, the deeper Buntsandstein (Fig. 1.3) could provide significantly higher temperatures. At a depth of around 2900 m (well VAL-01, www.nlog.nl, 2017; Figure 1.2) in the central part of the West Netherlands Basin and deeper (~3850 m depth in well GAG-03, www.nlog.nl, 2017; Figure 1.2), the considerably thick (around 125 m in well GAG-03) Buntsandstein could be an ideal target reservoir for geothermal exploration. However, due to the low permeability found in the Buntsandstein offshore and onshore in the Netherlands (Van Hulten, 2006), the potential for a use of geothermal energy remains questionable.

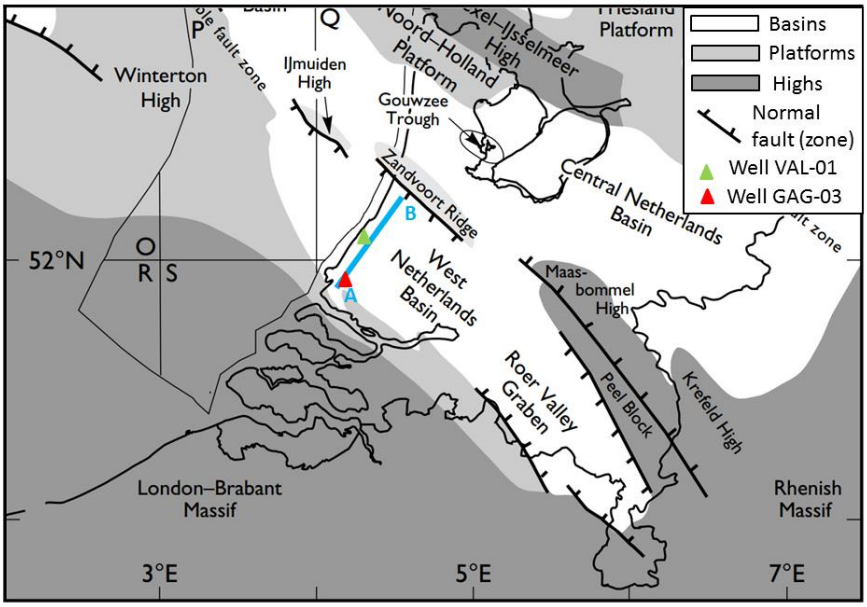

Figure 1.2: Map showing major basin elements, platforms and structural highs (subaerial landmass) as well as the basin boundary faults (modified after Van Adrichem Boogaert & Kouwe, 1997). A cross section through the West Netherlands Basin is shown as a blue line from A to B and depicted in Figure 1.3. The location of two wells (VAL-01 and GAG-3) are indicated as triangles in the map. The Green Well Westland lies 10 km North-West of well GAG-3.

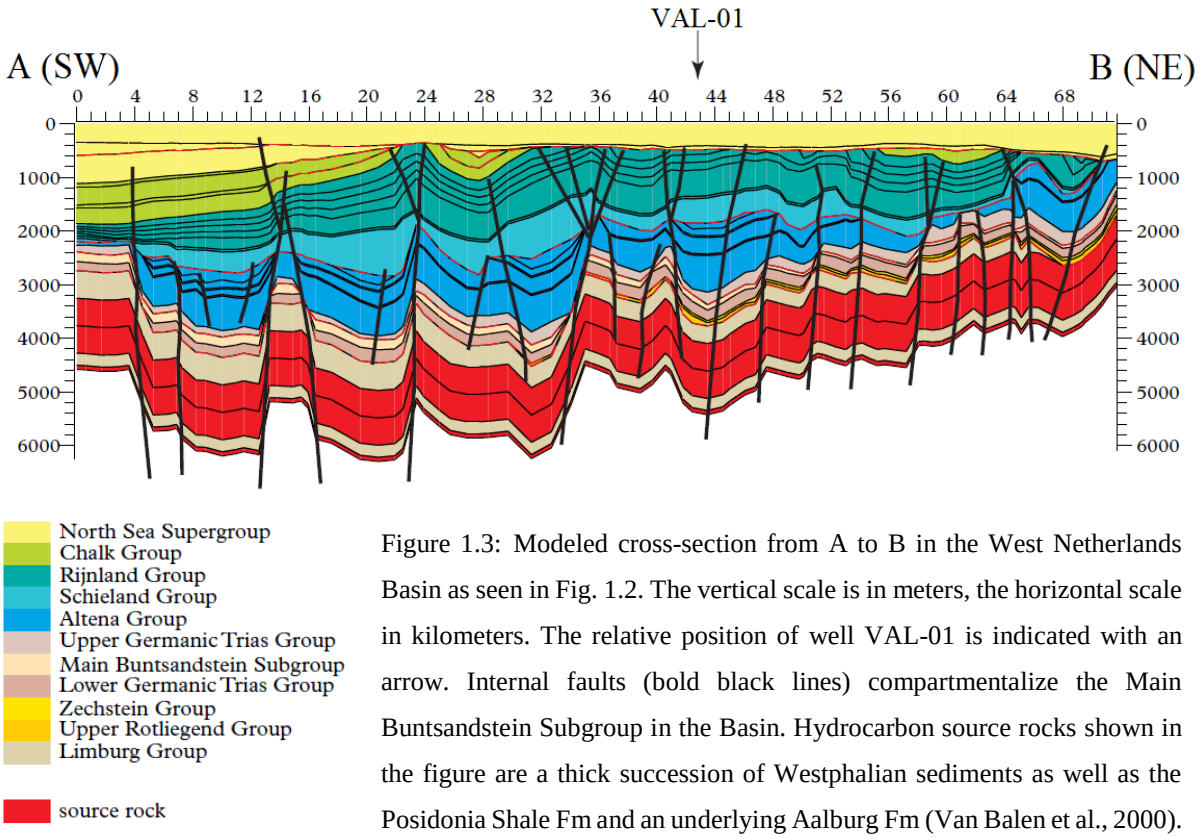

Figure 1.3: Modeled cross-section from A to B in the West Netherlands Basin as seen in Fig. 1.2. The vertical scale is in meters, the horizontal scale in kilometers. The relative position of well VAL-01 is indicated with an arrow. Internal faults (bold black lines) compartmentalize the Main Buntsandstein Subgroup in the Basin. Hydrocarbon source rocks shown in the figure are a thick succession of Westphalian sediments as well as the Posidonia Shale Fm and an underlying Aalburg Fm (Van Balen et al., 2000).

Natural Aquifers in the Netherlands do often not allow an economically viable production for certain reservoirs due to the low permeability found (Van Hulten, 2006). However, reservoirs that cannot be developed in the conventional way, with a geothermal doublet in a natural hydrothermal reservoir (Appendix A), can be enhanced by stimulation techniques such as acidizing, radial jet drilling or hydraulic fracturing. These enhanced reservoirs, so called Enhanced Geothermal Systems (EGS), might unlock the potential of geothermal energy in the Netherlands, as they offer the application of a different exploration strategy of reservoirs. In case of matrix acidizing of sandstones, certain acids, such as, for example, hydrofluoric acid (HF acid), are injected into the bedrock, penetrating the rock pores. However, acids are often highly toxic and the risk of contamination is regarded as very high (Kakar, 2013). Since the acid can only be injected if there is a fluid pathway, acidizing can only be used in reservoirs with a moderate permeability or a naturally fractured reservoir (Shafiq & Mahmud, 2017). As another possibility to improve field-scale permeability, radial jet drilling (RJD) can be used. There, numerous horizontal laterals (boreholes; up to 5 cm in diameter) are jetted into the target formation in various directions, penetrating up to 100 m (Peters, 2015). This technique is especially useful in tight sandstone reservoirs and for revitalizing old oilfields (e.g., Kalol VIII reservoir, India; see Kohar & Gogoi, 2014; Donelson West field, USA; see Kamel, 2014), but the technique can also be used in geothermal reservoirs. However, the impact of RJD on the rock around the laterals is not fully understood. Furthermore, the long-term stability of the laterals still remains to be investigated and is part of ongoing research. Hydraulic stimulation ("hydraulic fracturing"), in contrast, has been studied for a considerably longer time and is widely applied in the oil industry. For the hydraulic stimulation of a reservoir, a mixture of usually water, sand and chemicals is injected into the reservoir at pressures high enough to fracture the targeting rock. The created fractures can have lengths up to around 600 m and widths to about 2.5 cm (King, 2009). Ultimately, these fractures in the reservoir might lead to an enhancement of the permeability and economic flow rates (Tester et al., 2006; Tiab & Donaldson, 2015). Applying hydraulic stimulation in two boreholes (or more) can essentially create a large connected fracture network, which can be used for developing an EGS system. Therefore, the effect of fractures on the fluid flow in the rock is of major importance for the successful development of an EGS project and needs to be researched accordingly.

1.3 Fracture Types

In general, fractures form due to stress occurring externally or internally in a volume. They form discontinuities in displacement and can facilitate the movement or storage of fluids, but may also act as fluid flow barriers. The most common types of fractures are extensional fractures (tensile opening; Mode I) and shear fractures, which can be subdivided into in-plane shearing (Mode II) and anti-plane shearing (Mode III; Figure 1.4). Moreover, contraction or closing fractures (anticracks, Mode IV) can technically occur (Fossen, 2010).

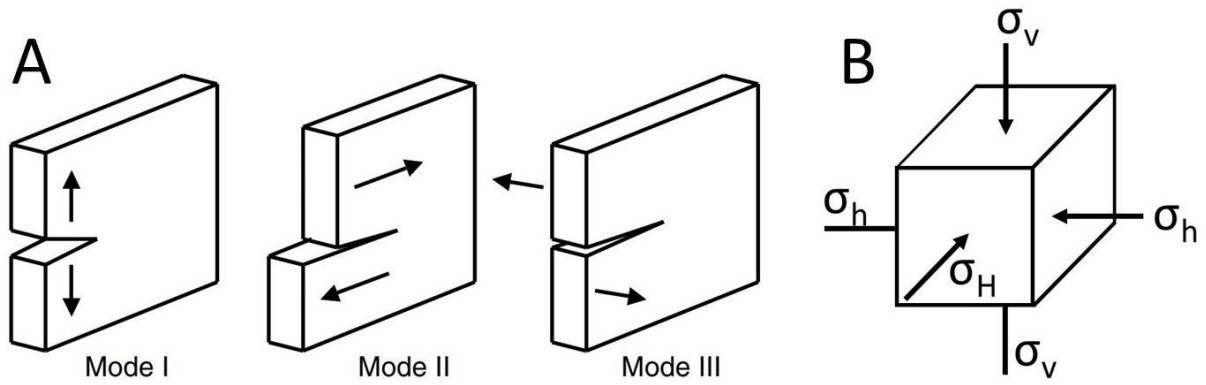

Figure 1.4: A: Illustration of three principle loading modes (after Tomac, 2014). Mode I: extensional; Mode II: in-plane shearing (sliding); Mode III: anti-plane shearing (tearing). B: Principle state of stress in the subsurface (after Council, 2013). By convention σv > σH > σh.

For shear fractures, the relative movement is parallel to the fault plane. They mostly develop oblique to the direction of the principal stress σ_1 ($\sigma_1 > \sigma_2 > \sigma_3$; Figure 1.4) and typically form at angles between 20° and 30°. Extensional fractures usually open perpendicular towards σ_3 (see Appendix A.2) and fractures extend parallel to the axis where compression acts (Fossen, 2010). In hydraulic fracturing, fractures generally tend to propagate in Mode I, since extension requires only a minimum amount of energy in quasi-brittle materials. To quantify the propagation of fractures, the stress intensity factor (SIF) can be used. A fracture propagates when the stress intensity factor reaches a critical point, which is expressed as the fracture toughness value K_{IC} (Tomac, 2014).

1.4 Hydraulic Fracturing

To extract the thermal energy stored in the Earth's crust, circulating water can be extracted, which has been heated up underground by staying in contact with the hot rock. For water to circulate in a tight reservoir with low permeability, fractures need to make up a connected fracture network, so a closed loop with an injector/producer pair is possible. Essential for hydraulic fracturing treatments in a geothermal reservoir are the productivity index of a producing well and the injectivity index of an

injection well, defining the volume of water that can be produced at a specific pressure differential between the wellbore and the reservoir.

So far, conventional hydraulic fracturing is initiated by injecting a fluid under high pressure into the reservoir to overcome native stress, leading to failure of the rock material (Tiab & Donaldson, 2015), and thus creating extensional fractures (Figure 1.4). These fractures thereby develop by the connection of micro-fractures, resulting in macro-fractures (Figure 1.5). In this process, both extensional fractures and shear fractures can form. The macro-fracture propagates by the linkage of newly formed microfractures ahead of the crack tip ("process zone"), where a concentration of the stress occurs (Fossen, 2010).

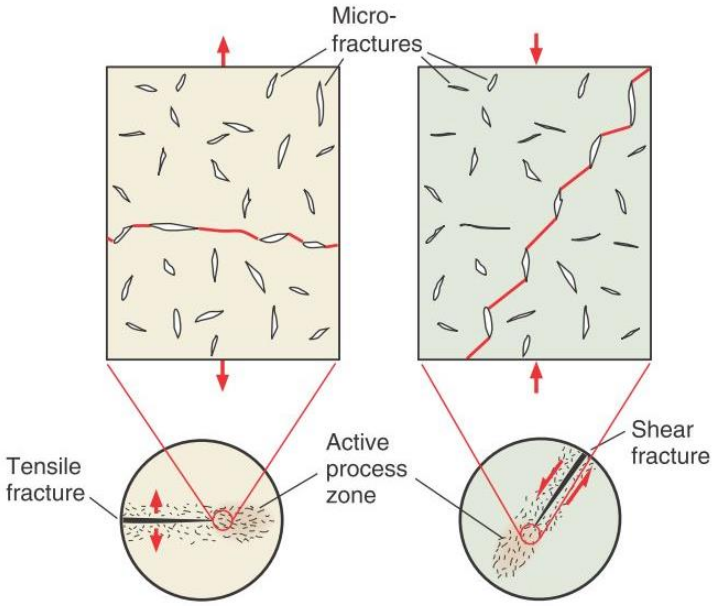

Figure 1.5: Illustration of the processes responsible for the development of extensional (left) and shear fractures (right; Fossen, 2010). A linkage of micro-fractures (rectangular view) leads to a growth of macro-fractures (circles; centimeter scale) and the fractures propagate in the fracture tip ("process zone").

To keep fractures open after hydraulic stimulation, proppant material (e.g., sand) is injected into the fractures with the help of highly viscous gels (Tester et al., 2006). However, these extensional fractures will not remain open indefinitely, since stresses in the underground change. Especially in areas with high deviatoric stresses, such as in the Cooper Basin, proppant treatment fails (Hossain et al., 2002), as the stresses result in grain boundary sliding and grain boundary cracks (Tomac, 2014). Moreover, high temperatures and plastic deformation of the rocks can lead to a closure of fractures. As an alternative, so called "shear dilation" treatment provides a proppant free technology for reservoirs containing natural faults, fractures and/or planes of weakness (Figure 1.6). Here, injection is conducted at a slow rate that leads to a juxtaposition of the original fracture walls and subsequently slippage and dilation if the injection pressure is kept above a threshold pressure. Instead of extensional

fractures (Mode I) caused in conventional fracturing, the fractures fail by shear sliding (Mode II). After injection, the rough asperities of the fracture surfaces keep the fracture from closing due to the shear slippage (Hossain et al., 2002). Concerning both opening and shear fractures, mineral precipitation from hydrothermal fluids circulating in the fractures can lead to a clogging of the fluid pathway. Thereby, microseismic events, elevated pore pressures, and, to a certain extent, acidizing can contribute to keep fractures open.

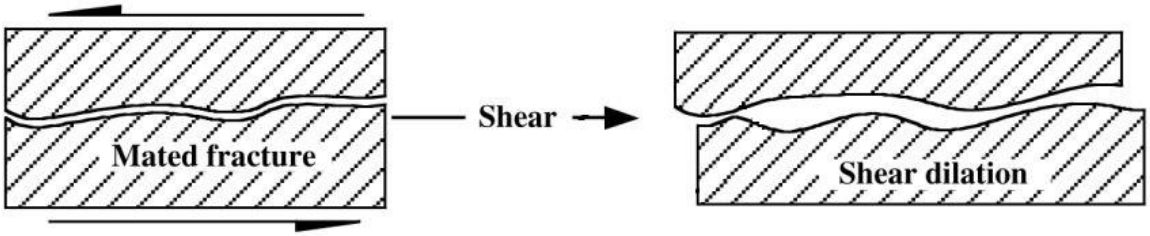

Figure 1.6: Schematic principle of shear dilation. After shear slippage the fracture remains open due to the asperities of the fracture surfaces (after Hossain et al., 2002).

1.5 Research Objective

In regard to conventional hydraulic fracturing and shear dilation, both principles need to be investigated in detail to understand the impact of creating fractures in a reservoir with specific in-situ properties. Therefore, this thesis focuses on the effect of fracking of the Buntsandstein Formation in the West Netherlands Basin, as the Buntsandstein is of main interest for the geothermal industry in the Netherlands (see Chapter 1). To link the effect of fractures to a resulting change in permeability, physical properties are studied in a variety of experiments on different Buntsandstein samples. Fractures are thereby artificially induced, either in unconfined (uniaxial compression test) or confined conditions (triaxial deformation test). With two principal modes of fracturing (Mode 1 and Mode 2) created in lab experiments, permeability measurements can show whether fractures increase or decrease permeability (Al Enezi et al., 2007; Teufel, 1987) after fracturing the Buntsandstein. Additionally, triaxial deformation tests can indicate the effect of increasing confining pressure on the permeability in comparison with the initial permeability measured on intact sandstones as well as after fractures have been created. Investigations on the microstructure thereby helps to understand the processes occurring at the microscale, which can be linked to the overall behavior of the Buntsandstein samples. The microstructure has been analyzed with the help of micro-CT scans, EPMA and thin section analysis, as well as XRF/XRD measurements. Moreover, acoustic velocity anisotropies during uniaxial compression give an indication of micro-/macro- cracking occurring in the samples with an increase in axial load. This is useful to understand, for example, the processes occurring around faults. Brazilian disc tests done on Buntsandstein samples are useful for determining

the rock tensile strength and the fracture toughness, which are important for solving problems concerning the fracture propagation.

Overall, geomechanical parameters found in the tests should give a valuable insight into the physical rock behavior and contribute to a mechanical characterization of the rocks. Knowing the physical properties of the Buntsandstein is essential for a successful development of hydraulic stimulation of the target rock formation. Results contribute to an understanding on how geothermal exploration techniques have to be applied for developing a project in the Buntsandstein Formation. To scale the found observations to field examples, a numerical simulation of a geothermal field is used. As input, measurement data from the experiments are taken. This allows to gain an insight on the effects of fractures and a resulting change in flow properties in the subsurface on the production life of a geothermal injector-producer pair.

2. Regional Geology and Reservoir Properties

2.1 Geologic History of the West Netherlands Basin

The West Netherlands Basin (WNB) is an inverted rift basin and existed from the Late Permian on till the Late Cretaceous. Large-scale half graben structures formed during the Middle to Late Triassic, in the early Kimmerian tectonic phase, leading to significant faulting. In the Late Jurassic to Early Cretaceous rifting phase, uplift, combined with erosion and divergent oblique-slip faulting, took place. This faulting caused a block faulted depression between the Zandvoort Ridge and the London-Brabant Massif trending SE-NW. Normal faults were then reactivated in the basin inversion phase in the Late Cretaceous to Early Tertiary, when compression lead to further uplift and erosion, as well as convergent oblique-slip faulting. These events led to the formation of symmetrical anticlines, which are commonly bound by upward divergent reverse faults and form the essential traps of the oil fields in the WNB (Racero-Baena & Drake, 1996). Oil bearing reservoirs have been found in various formations between the Triassic Buntsandstein Group and the Tertiary. However, Cretaceous oil fields in the basin are found to be the only ones which can be exploited economically (Racero-Baena & Drake, 1996; Geluk, 2007).

2.2 Present West Netherlands Basin

Situated both onshore and offshore in the west of the Netherlands, the WNB nowadays comprises a large part of the country's subsurface geology. It extends from southeast to northwest and lies between the London-Brabant Massif and the Central Netherlands Basin (see Chapter 1, Figure 1.2). The basin is bounded by several faults, mainly the Zandvoort Ridge in the northeast and the Ijmuiden High as an extension of the Zandvoort Ridge. As part of the Mid Netherlands Fault zone, these faults separate the basin from the Central Netherlands Basin (Van Adrichem Boogaert & Kouwe, 1997). Towards the southeast, the basin merges with the Roer Valley Graben.

2.3 Lower Triassic Buntsandstein

The Lower Germanic Trias Group is comprised of the Lower Buntsandstein and the Main Buntsandstein Subgroup, which is divided into Hardegsen, Dethfurth and Volpriehausen formations (from youngest to oldest sediment; Figure 2.1). The sediments of the Lower Buntsandstein Formation consist of fine-grained lacustrine sandstone alternating with clay siltstones (Geluk, 2007). In the central part of the WNB, these sediments can be 20 to 70 m thick and thin out on the edges of the basin. Appendix B.2 shows the thicknesses of each formation. Deposits of the Main Buntsandstein Subgroup consist of a cyclic alternation of clayey siltstones and (sub)-arkosic sandstones. The lowest

member of the Main Buntsandstein, the Volpriehausen Sandstone Member, can be up to 70 m thick in the central WNB (Appendix B.2) and shows thicknesses of more than 200 m in the Dutch Central Graben (Geluk, 2007). According to Geluk (2007), the arcosic sandstone can be highly cemented by calcite and dolomite, especially in the lowermost part. In comparison, the Volpriehausen Clay-Siltstone consists of lacustrine siltstones and marls with more fine-grained sandstone sections that are cemented with calcite, dolomite and ankerite (Geluk, 2007). The member can be equally thick as the Volpriehausen sandstone, being around 30 m thick on average in the central WNB (Appendix B.2). The Detfurth Sandstone Member in the WNB is entirely made up of sandstones and cuts into the Volpriehausen Formation at its base (Detfurth unconformity). According to Geluk (2007) the sandstone is loosely quartz-cemented and between 20 to 40 m thick in the WNB. In the Central WNB, the cross section of Appendix B.4 shows that the thickness is found to be only between 4 and 20 m. In turn, the Dethfurth Claystone varies between 8 and 29 m (Appendix B.2) and is composed of claystones with siltstone intercalations. The uppermost Hardegsen Formation varies significantly in thickness due to erosion on the top ("pre-Solling erosion"), followed by the sedimentation of the Solling Formation (Geluk, 2007). However, the average thickness in the central WNB is 40 m (Appendix B.2). Siltstone is the main component of the formation, but thin sandstone beds are present.

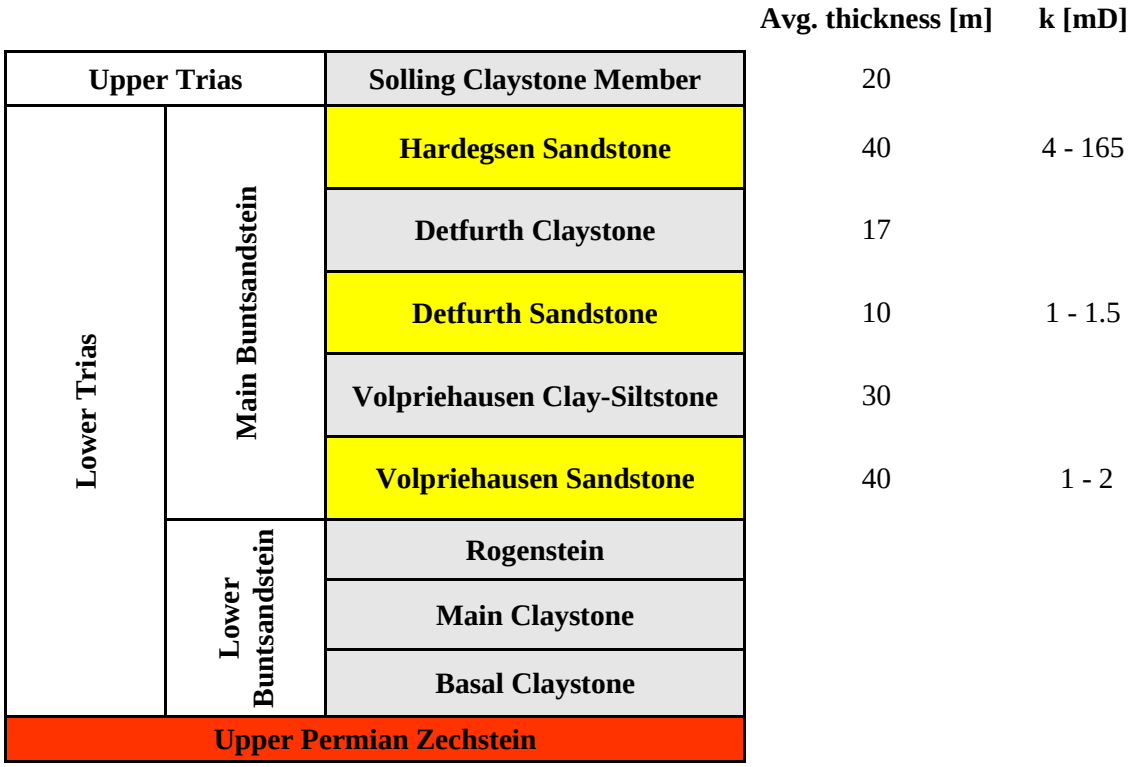

Figure 2.1: Stratigraphic section in the West Netherlands Basin, including the Lower Triassic Buntsandstein formations. The approximate average thicknesses for the most important formations are indicated. The main reservoir sections of the Main Buntsandstein are indicated in yellow. Non reservoir sections are shown in grey.

2.4 Reservoir Properties

To quantify the properties and the in-situ conditions of the Buntsandstein reservoir formations in the subsurface of the WNB, a well data analysis were conducted as part of this thesis, taking into account the majority of the wells drilled into the Buntsandstein in the onshore WNB. In this thesis borehole data have been extracted from the public website NLog.nl. In total, data from 64 wells has been taken into account for the analysis of depth, pressure, temperature, porosity and permeability. A list of all wells used can be found in Appendix B.3. The well names and their locations are shown in Appendix B.4 and Appendix B.5, respectively.

2.5 Buntsandstein Depth

To get an overview of the depth of the Buntsandstein formations, measured depth data were converted to true vertical depth and the thickness of each formation was calculated. A cross section from well RZB-01 at the outer boundary of the WNB (close to Rozenburg) to well URS-01 (East of Alkmaar) was made and is displayed in Appendix B.4. This cross section crosses the Zandvoort Ridge (roughly at the location of SPL-01), therefore indicating shallower depths of the Buntsandstein towards the northeast. The maximum depth of the Buntsandstein was observed in well GAG-06-S1. Here the Lower Volpriehausen Sandstone Member goes down to almost 4000 m TVD. The Main Buntsandstein Group in this well reaches a considerable vertical thickness of 200 m.

Knowing the depth of the Buntsandstein formations, the thickness of each formation and member was evaluated and is shown in Appendix B.2. The table indicates that both the Hardegsen Sandstone Member and the Volpriehausen Sandstone Member are relatively thick (40 m on average) and would make up a good reservoir unit if the layers are laterally extensive. Based on the well log interpretations of Chapter 2.3, the layers are relatively continuous in the WNB. Nevertheless the thickness can vary locally, adding a great uncertainty towards the formations as an exploration target. Interlayering non-reservoir units are on average 20 m thick, acting as possible seals between the reservoir units, which is important for the overall sweep.

2.6 Porosity and Permeability

Around half of the researched well data contained valuable information on porosity and permeability. Core plugs provide air-permeability data that are generally regarded as very optimistic in comparison to the absolute brine permeability, which is measured on cores at in-situ stress conditions (triaxial lab experiments) and appropriately saturated with brine. This overestimation is especially noticeable in the low permeability range (Juhasz, 1986). Therefore, a conversion of the air-permeability to in-situ brine permeability was done by making use of the Juhasz correction method described in Juhasz

(1986). Furthermore, large porosity datasets from neutron-porosity-logs were used to estimate the permeability using porosity bins and by applying Swanson Mean regression on the porosity (Table 2.1). This method, however, may give underestimated permeability values, as reported by Delfiner (2007), mainly due to the repeated transformation between arithmetic and logarithmic scale and the permeability upscaling. The porosity from core measurements was corrected for Triassic rocks with a core compaction-correction factor of 0.9 at in-situ pressures, as proposed by Nieto et al. (1994).

Observable in the permeability data are the great variability occurring within a single member. As an example, well SPKO-01-S1 shows a permeability of 310 mD in the Hardegsen Formation (2510 m TVD), whereas 5 km east the permeability in well RTD-01 is only 17 mD at a depth of 2820 m TVD. Thereby the Hardegsen shows on average the highest permeability of all formations with an average of around 126 mD (Table 2.1). A trend for higher or lower permeability in specific areas of the WNB is generally not recognizable in the available data, except in the area in the west of Rotterdam, which makes up the boundary of the WNB. Here, wells such as SPKO-01-S1, PRW-01 and BTL-01 show excellent reservoir properties in the Buntsandstein formations with a permeability between 157 and 310 mD. Additional to the Hardegsen Formation, the Lower Dethfurth shows the highest permeability, with a maximum of 157 mD in well BTL-01, but almost zero permeability in wells GAG-03 or BRAK-01. The higher permeability in the Hardegsen Formation compared to the deeper Dethfurth and Volrpiehausen Formations has also been observed in an analysis done by TNO in 2015 (Veldkamp & Boxem, 2015).

Economic flowrates for geothermal wells in the Buntsandstein, such as in the project in Vierpolders, are expected to be at least around 30 mD (A. Sandén & F. Veeger, Veegeo Energy, personal communication). However, this permeability value strongly depends on the purpose and the desired flow rates in a geothermal project. Based on this information, the Hardegsen Formation is the most promising exploration target. Other formations in of the Main Buntsandstein do on average not provide a sufficient permeability and would require stimulation.

Table 2.1: Calculated permeability, k, and porosities, ϕ, for different members of the Buntsandstein with data retrieved from NLog.nl. The standard deviation can be higher than the mean due to high outliers. SD = standard deviation.

Formation	avg. k ± SD [mD]	avg. ϕ ± SD [%]
Hardegsen Formation	125.8 ± 143.6	12.5 ± 3.4
Upper Detfurth Sandstone Member	1.3 ± 1.3	10.9 ± 3.5
Lower Detfurth Sandstone Member	15.3 ± 36.2	10.6 ± 2.7
Upper Volpriehausen Sandstone Member	4.3 ± 6.6	9.9 ± 3.9
Lower Volpriehausen Sandstone Member	5.1 ± 2.3	8.2 ± 2.8

2.7 Temperature

Temperature values were extracted from NLog.nl from 24 wells (see Appendix B.3) in the WNB and plotted against true vertical depth in Figure 2.2. In the figure, temperature data has been weighted to rectify the difference in data points per well. Furthermore the temperature gradient does not cut through zero in Figure 2.2 but rather 12°C, as underground temperatures in the "neutral zone" at 25 m are already about 12°C (Berlin.de). Well GAG-03 indicates higher geothermal gradients than the average. This might lead to the assumption that the present heat exchange at this location is rather weak and there is a lack of circulation. Another possibility could be the presence of a local convection cell, which leads to this thermal anomaly. Convective fluid flow in fractures, as possibly present in the Luttelgeest carbonate platform in the north of the Netherlands, have a high potential for geothermal exploitation (Lipsey et al., 2016). However, another possibility is that this might be the result of inaccurate measurements, as the data are rather irregular and show large steps in high and low temperature.

Overall, the general geothermal gradient for the WNB can be expressed as follows:

$$\textbf{Temperature [°C] = 0.0347 x Depth [m] + 12} \quad \textbf{(1)}$$

Actual production data of 10 producing geothermal plants (see Appendix B.6) in the WNB were implemented in Figure 2.2. This shows that the actual production data lie more or less in the range of the calculated geothermal gradient.

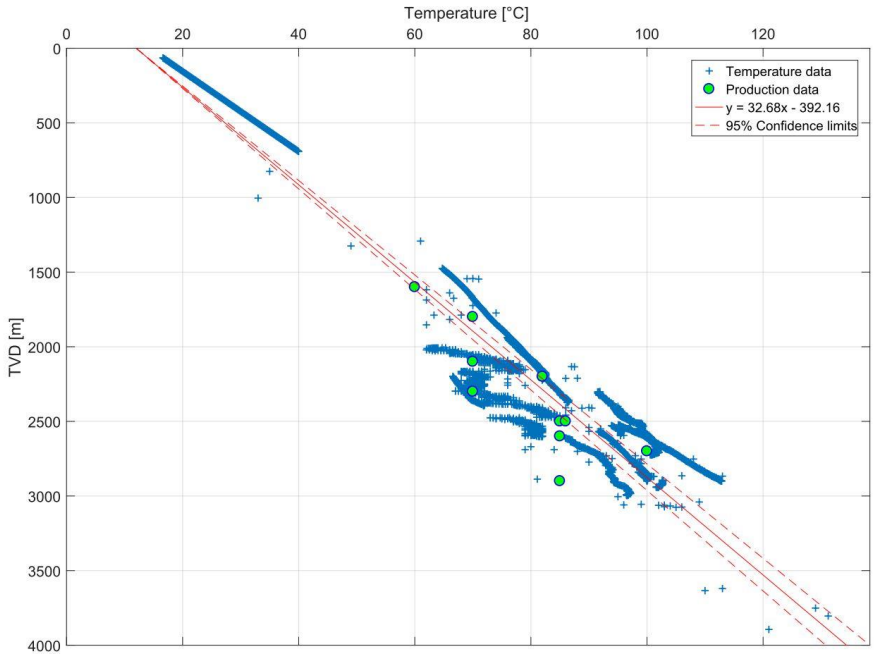

Figure 2.2: Temperature profile in the West Netherlands Basin. Note: Temperature values from well data are not corrected for the drilling mud temperature.

As the bottomhole temperature (BHT) is usually measured with logging tools in the drilling mud, the temperature needs to be corrected accordingly. The mud generally has a lower temperature as the surrounding formation, resulting in an underestimation of the actual temperature (Deming, 1989). This is essentially important for choosing the right cementation procedure. For geothermal projects on the other hand, the true temperatures are an important factor for feasibility studies.

To correct for the temperature, a number of studies propose different empirical methods or a correction procedures such as with the Horner plot. In general the average correction lies between 10 and 15°C (Deming, 1989; Goutorbe et al., 2007). However, this strongly depends on the depth and the specific area. In regard, a study done by Matev (2011) in the West Netherlands Basin results in a correction factor of 11.6% for temperatures measured between 2200 m TVD and 3800 m TVD. An applied correction of this factor for the temperatures taken in this study would result in a high geothermal gradient of 46.7°C/km. The initially calculated geothermal gradient is 42.6°C/km, which is in comparison to other areas, such as the Molasse basin in Bavaria (geothermal gradient of around 30°C/km; STMWIVT, 2012), still considered as high. Moreover, the calculated gradient of 42.6°C is equal to the gradient proposed by Matev (2011) for well data that only includes measurements of production tests from the Main Buntsandstein or for temperature measurement where the drilling mud circulation was stopped for at least 18 hours.

Since data from currently producing geothermal plants align with the uncorrected geothermal gradient, a temperature correction might be negligible, as it would cause a strong overestimation (see Appendix B.7).

2.8 Pressure

Pressure data from repeat formation tester (RFT) tool measurements from wells in the WNB were gathered and plotted against true vertical depth in Figure 2.3. Pressure data are weighted for each well, as there have been differences in the amount of pressure measurement points per well.

The hydrostatic pressure gradient in the WNB can be written as:

$$\textbf{Hydrostatic pressure [MPa]} = 0.0109 \times \textbf{Depth [m]} \qquad \textbf{(2)}$$

Figure 2.3 indicates two areas with higher pressures and off the trendline. These pressures were measured in wells BRTZ-01 (data around 2500 m) and SPG-01-S2 (2700 m to 3000 m). The higher pressures occur in both wells in the Lower Jurassic Aalburg Formation, which are shales that are a potential type II source rock (Jager et al., 1996). Overpressures possibly originate as generated oil was trapped by claystones of the overlying Werkendam Formation in structural traps. Both wells intersected normal faults before overpressures occurred.

Two out of the 64 studied wells have data of a minifrac test and a leak off test performed in the WNB. Minifrac tests have a great potential when determining the in-situ stress and deformation properties. Another way to get this information is by lab experiments conducted with the triaxial apparatus, which can also give reliable results if done with precision, even though it might not exactly represent the present in-situ conditions.

A minifrac test (or injection-falloff diagnostic test) was done in well GAG-05. The test was performed due to the low deliverability of gas from the Buntsandstein and Limburg sands, where the permeability ranges between 1 and 10 mD. A hydraulic propped fracture treatment of the upper reservoir part (Hardegsen to Upper Volpriehausen Formation) between roughly 3530 and 3640 m TVD resulted in a breakdown of the formation at 36.9 MPa surface pressure. At this point, the surface pressure no longer increases linearly for each increment in the volume of mud that is pumped into the wellbore. If the minifrac were conducted until the formation fractures completely, a sudden drop of the surface pressure would seen. The fracture closure pressure was 51.5 MPa (bottomhole). As the closure pressure is equal to the minimum principle stress, this is also the pressure required to open an existing fracture, counteracting the stress in the rock perpendicular to the fracture.

In well MON-03, a leak off test was performed at 2676 m TVD in the Muschelkalk Evaporite Member. The formation breakdown pressure was at 15.5 MPa surface pressure.

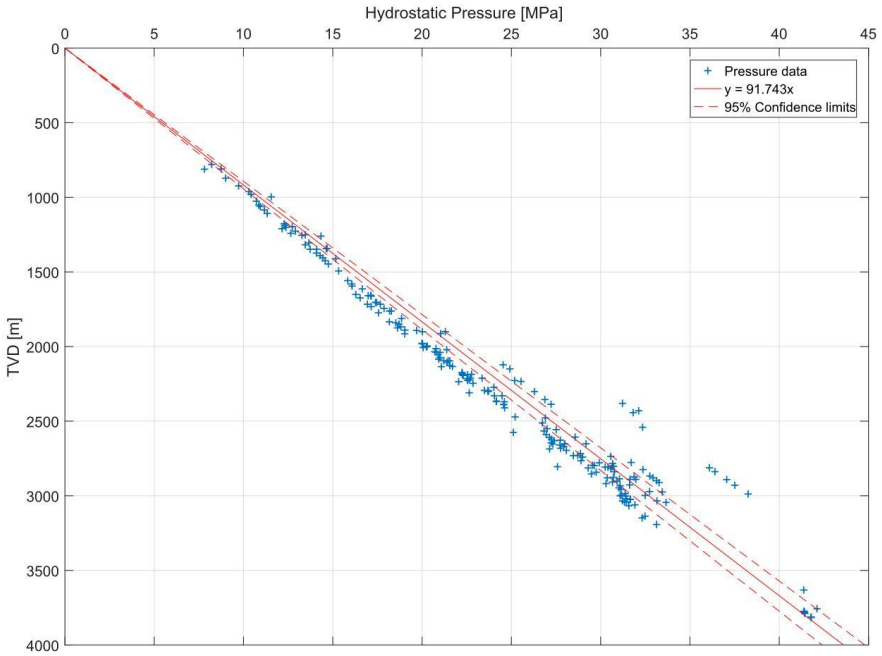

Figure 2.3: Hydrostatic pressure profile in the West Netherlands Basin with data from RFT measurements.

3. Methodology

The properties of the Buntsandstein are investigated in core experiments in uniaxial compression tests and triaxial tests, where geomechanical characteristics and physical properties at relevant pressure and temperature conditions (PT) are measured. Additionally, tensile strength tests for rock fracture-toughness determinations were conducted with the Brazilian disc test method. In order to give a realistic estimation of fluid flow parameters, lab experiments on cores provide reliable intrinsic information of permeability at relevant PT conditions and give a realistic estimation of fluid flow parameters.

3.1 Mechanical Characterization

3.1.1 Material and Material Properties

Rock samples of the Buntsandstein were taken from quarries in Germany in Bad Dürkheim and Miltenberg. For comparing the rock properties of the Buntsandstein with different types of sandstones, additional samples of the Bentheim sandstone and the Rüthener Grünsandstein were used. A summary of the sampling locations of the rocks used is found in Appendix C.1. From these rock samples, numerous cores in different orientations with respect to bedding were drilled, to evaluate anisotropy. Samples cored normal to the bedding (hereafter referred to as Z-direction) and parallel to bedding (X- or Y-direction; Figure 3.1) are labeled accordingly. As an example, sample BD-51-Y1 is from the Buntsandstein sample block BD-51 and is drilled in Y-direction.

After cutting the long specimens with a diamond-blade to the right length (around 75 mm), the surfaces were ground plan parallel, enabling a good contact between the machine and the rock interface, helping to avoid point-load effects during experiments. The final core samples consist of right-cylinders (i.e., with plan-parallel end faces), which is crucial for conducting measurements of porosity or permeability on the cores (www.coretest.com/, 2016), as the interface of the core can have an impact on the relation between effective and absolute porosity/permeability and can influence any petrophysical measurements (Byrne & Patey, 2004). All processes of the sample preparation such as coring and grinding were done in the laboratories of the Delft University of Technology. It was made sure that all samples were dried at around 50°C for several days in order to assure that all samples were completely dry before the start of an experiment. Cores used in uniaxial compression tests and in triaxial deformation tests had an approximate diameter of 30 mm and a length between 70 and 75 mm, keeping the sample length to diameter ratio (L/D) close to 2.5:1. This will help reducing end effects problems (Paterson & Wong, 2005). Appendix C.2 lists all properties for each core sample used.

The dry porosity for the used core samples is deduced from the measurements of matrix volume using a helium-pycnometer (Ultrapycnometer 1000 Version 2.12). Before each day of measuring, the pycnometer was calibrated using calibration samples according to the pycnometer lab-manual. The pycnometer was set to 6 (or 10) runs with helium gas, with an averaging over 3 runs. For each run, a series of pulses was set. A run was complete after achieving a deviation of 0.005% or less.

An identification of the individual chemical compounds and elements in the Buntsandstein was done with an X-ray Powder Diffraction (XRD) analysis and an X-Ray Fluorescence analysis (XRF). Both XRD and XRF measurements were done at the facilities of the department of Materials Science and Engineering (MSE) in the faculty of 3mE of the Delft University of Technology. The results for each sample analysis are shown in Appendix C.5. For the analysis, rock samples were crushed to obtain a powder in µm fraction.

In view of the variability of rock properties, and when enough samples are available, repeated testing was done to determine average values. Different Buntsandstein samples cored in Z-, X- and Y-direction (Figure 3.1) allow to gain additional information on the permeability-anisotropy of the rock (i.e., k_v/k_h). In all samples showing an internal bedding, no clear distinction between X- or Y-direction was made, as the exact orientation of each sample block within the formation is unknown. Moreover the differences in X- and Y-direction might not be systematic in a geological sense, considering e.g., trough cross-bedding in a meandering river system, which can have a wide range of orientations in a meander belt. Furthermore, the significance in regard of the permeability anisotropy is only little for porous sandstones such as the Bentheim sandstone (max. 7% anisotropy) or the Diemelstadt sandstone. For a cross-bedded sandstone, such as the Crab Orchard sandstone with 4.5% porosity, the permeability for both X- and Y-direction is considered equal, and no differentiation is made (Benson et al., 2005; Baud et al., 2012).

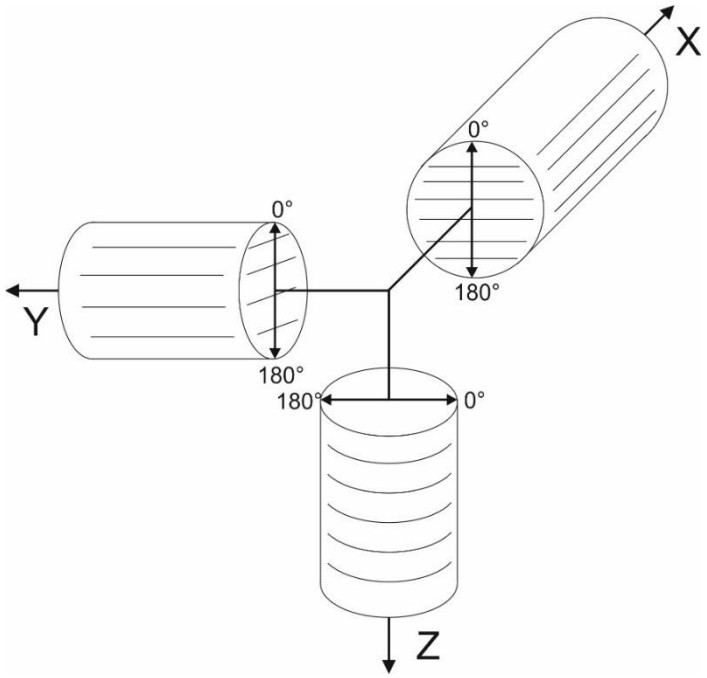

Figure 3.1: Schematic of the drilled core samples, showing the reference axes and the general orientations.

Compaction localization might be enhanced in some orientations, resulting in different flow properties (Baud et al., 2012). Furthermore, a high permeability contrast (up to two orders of magnitude) can occur between the porous sandstones (host rock) and the compaction bands (CB). Due to this permeability contrast, with a permeability reduction in the CBs, the compaction bands can form barriers to flow (Baud et al., 2012).

However, the Buntsandstein samples taken in the quarries do not show any CBs or pre-existing structural anisotropies from deformation, such as high-angle shear bands, also because, for example, CBs occur generally in relatively porous sandstones, such as Bentheim sandstone or Diemelstadt sandstone used by Vajdova et al. (2004) and Baud et al. (2012) with porosities of around 23%.

3.1.2 Micro-structure Analysis

Thin sections were used to examine the micro-textural and mineralogical features of the samples, the pore fill and deformation and recrystallization. For the analysis of the thin sections a Leica DMLP petrographic microscope was used.

Further analyses of the micro-structure were conducted with the help of a JXA-8230 SuperProbe Electron Probe Microanalyzer (EPMA). The EPMA is stationed in the Electron Microprobe Laboratory, Department of Inorganic and Isotope Geochemistry at the Helmholtz Centre Potsdam—German Research Centre for Geosciences (GFZ) in Potsdam, Germany. Prepared thin sections with a thickness of 30 μm are coated with a thin film of carbon prior to the measurements to ensure a dissipation of electrical charges. The EPMA chemical analysis of the minerals present in the thin

sections was done with either a “spot” or an “area” analysis. The analytical conditions of the EPMA include an accelerating voltage of 15 kV, a beam current of 10 nA and a focused beam. Grains of plagioclase, olivine and pyroxene, which are well-characterized, were used as standards.

3.1.3 Uniaxial Compression Tests

Uniaxial compression tests allowed to measure the maximum load that can be applied to each rock specimen until failure and enabled the determination of the elastic properties, which are represented by the Young’s modulus and the Poisson’s ratio.

For the mechanical tests, a servo-controlled uniaxial compressive machine with 500 kN capacity has been used, which is located in the Laboratory of Geoscience and Engineering, Faculty of Civil Engineering and Geosciences. The setup consists of a stiff load frame, a load cell, an axial pump and multiple measurements tools (Fig. 3.2).

Axial load is applied on the sample with an upwards moving, hydraulic bottom plate. The top plate is fixed to the load frame. Due to the high stiffness of the load frame, elastic energy stored in the load frame results in negligible displacement. To fix and remove the sample, the servo-hydraulic cylinder was operated in load control. In all measurements in this thesis, compression will be denoted as a positive number, whereas extension is negative.

The displacement during the experiment was measured with two highly accurate, axial displacement transducers (or Linear Variable Differential Transformers; LVDTs) and a radial displacement chain measurement device mounted around the core sample at mid-height (Figure 3.3). The LVDTs used were Solartron Metrology AX/S/1 with an accuracy of 1 µm (in terms of measurement performance), the extensometer measuring the circumference deformation is an electronic clip-on extensometer from MTS Systems Corporation (Model 632.11C-20

The axial displacement recorded by the LVDTs is used to calculate the axial strain, the radial strain is calculated with the radial displacement measured from the extensometer. In this work, the term strain refers to engineering strain, which is defined as the deformation in relation to a reference length, expressed as follows:

$$\varepsilon = \frac{\Delta L}{L_0} \qquad \textbf{(3)}$$

with ΔL as the amount of deformation (positive for elongation) and L_0 as the initial length.

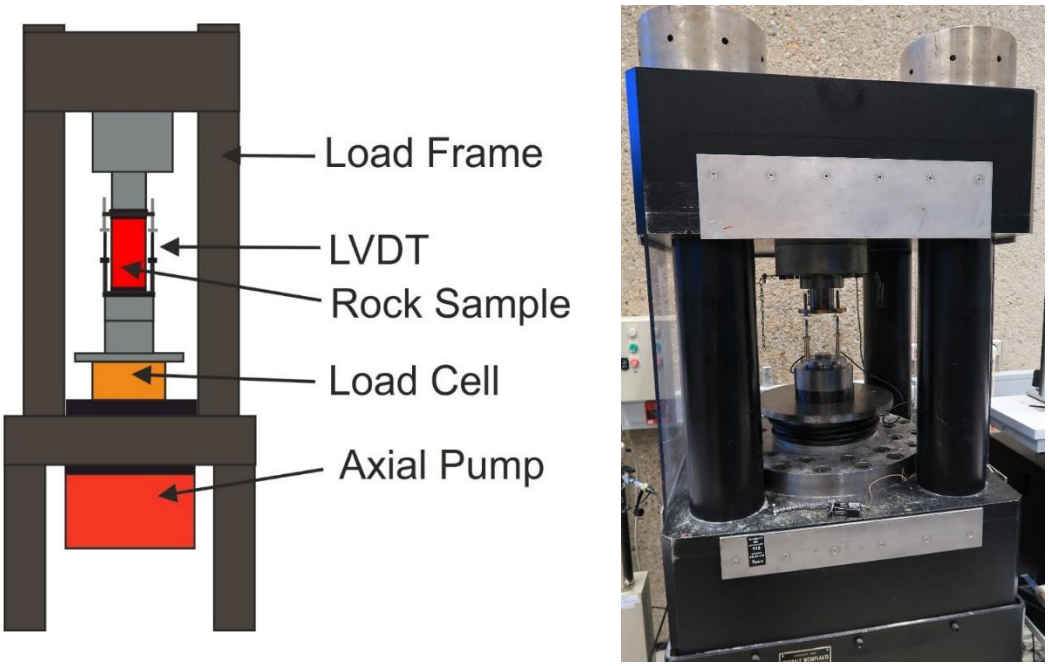

Figure 3.2: Left: Schematic setup of the uniaxial compression test. Right: Uniaxial compressive machine with a capacity of 500 kN. The LVDTs for measuring the axial displacement are mounted in golden holders.

3.1.4 Acoustic Property Measurements

To gain more information of the Buntsandstein in particular, the acoustic properties of the samples were measured during the uniaxial compression tests. A change in the velocity of wave propagation was then used as an indicator for microcracking (Angus et al., 2012; Pellet & Keshavarz, 2010) occurring in the tested samples. Moreover, dynamic elastic moduli (Young's modulus, Poisson's ratio) can then be compared indirectly to the static elastic moduli. The difference between the dynamic and the static method is, that the dynamic method is based on the measurements of sonic body wave velocities, and the static method implies measuring the deformation induced in a material (e.g., rock samples) by applying a certain force.

All acoustic measurements performed have been conducted using P- and S-wave transducers from Olympus Panametrics-NDT (direct contact series V153-RM and V103-RM). The operating frequency of the P– and S–wave transducers was 1.0 MHz. The transducers were placed inside a custom made stainless steel cups, preventing deformation of the transducers during axial loading (Figure 3.3). The steel cups were placed on top and on the bottom of the rock sample between the steel pistons. As tests with the steel cups solely showed that there is a non-negligible axial strain on the cups, the axial strain was subtracted from the strain measured for the various rock specimens. Therefore, the elastic properties of the sensor cups were measured beforehand, giving the displacement at each load. The displacement is then subtracted from the measured displacement with the rock sample in order to arrive to the sample displacement only.

Figure 3.3: Sample BD-53-Z2B after failure from the unconfined compression test of. The sample is placed between two steel cups, in which the acoustic transducers sit in. The chain around the sample is from the extensometer, to the right and left are the LVDT's.

To guarantee an optimum contact between the specimen and the steel mounts, shear gel (ultrasonic couplant from Sonotech) was placed on the interface of the steel cups and the rock specimen.
Over all, P– and S–wave velocities were measured before applying axial load. This was primarily done to facilitate the picking of the first arrivals when applying axial load, as the first arrivals change with an increasing compression. During the uniaxial compressive strength (UCS) tests it was not possible to mount both P- and S-wave transducers between the sample and the steel piston. Since the arrival of P-waves can also be seen with S-wave transducers, only S-wave transducers have been used during the experiments. As the first arrival of the S-wave was sometimes difficult to interpret, the first arrivals measured beforehand were used as a reference point in the seismic wavelet. Figure 3.4 illustrates an example where the P- and S-waves recorded prior to the experiment (black and red line) are plotted in the normalized wavelet (blue line) recorded with S-wave transducers at a certain applied load. Here, the S-wave arrival occurs at more or less $4.2 \cdot 10^{-5}$ seconds. The P-wave arrives at around $3 \cdot 10^{-5}$ seconds.

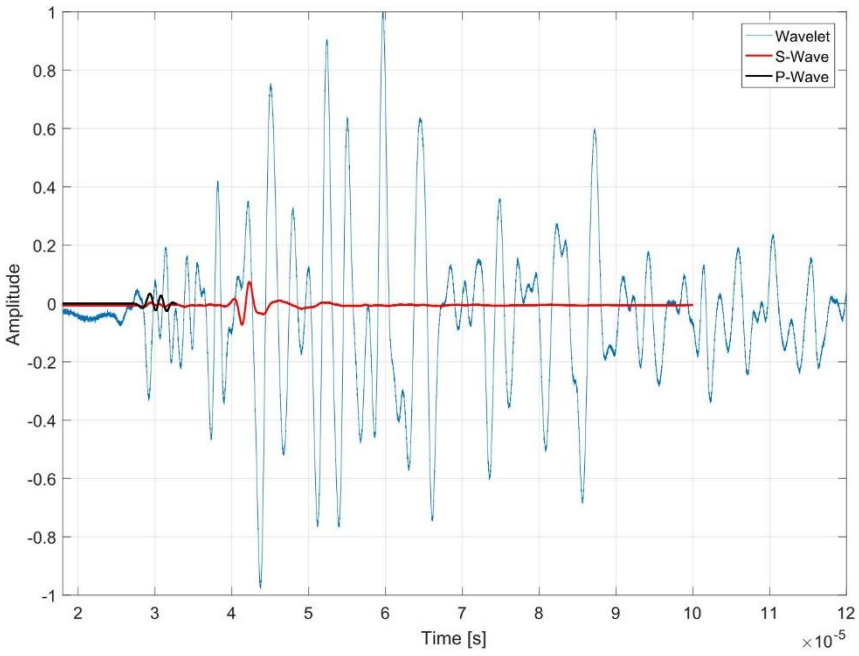

Figure 3.4: Exemplary seismic wavelet (S-wave) of sample BD-53-X2B (blue) recorded during a uniaxial compression test. S-wave and P-wave arrivals were determined before the experiment and are used to pick the arrivals in the wavelet after the experiment.

3.1.5 Brazilian Indirect Tensile Strength Tests

Brazilian indirect tensile strength tests (or Brazilian disc tests; BDM) were conducted in the uniaxial compressive machine in order to determine the tensile strength of the intact Buntsandstein and the fracture toughness. To conduct the test in compliance with to newest ISRM standards, smaller specimens were cut from the large sample cores. The cylindrical discs had a diameter of around 30 mm and the height was approximately 15 mm. Brazilian disc tests on samples that showed clear layering were carried out multiple times with different sample orientations. By this tensile fractures were created along as well as angular and perpendicular to the bedding plane (Figure 3.5).

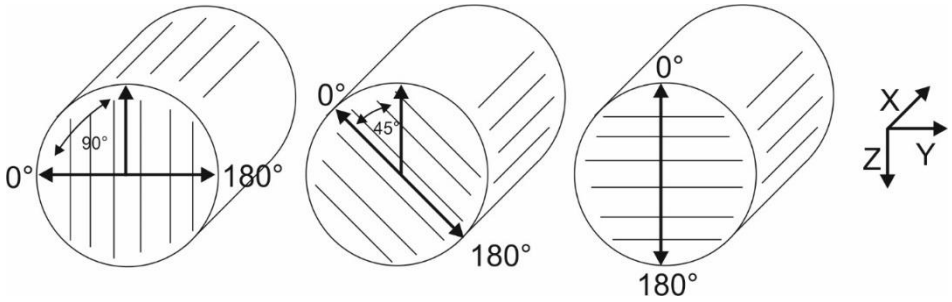

Figure 3.5: Schematic of the rock specimens used in the Brazilian disc test, showing the reference axes and the different orientations of the samples during the tests.

The loading direction for each test disc was marked beforehand and the sample dimensions were recorded. Additionally the porosity for each rock sample was taken. All tests were conducted at ambient conditions.

For the experiment, each rock specimen was placed inside a pair of curved bearing steel blocks. The two blocks were connected with steel pins to ensure they would stay in place during the deformation experiment (Figure 3.6).

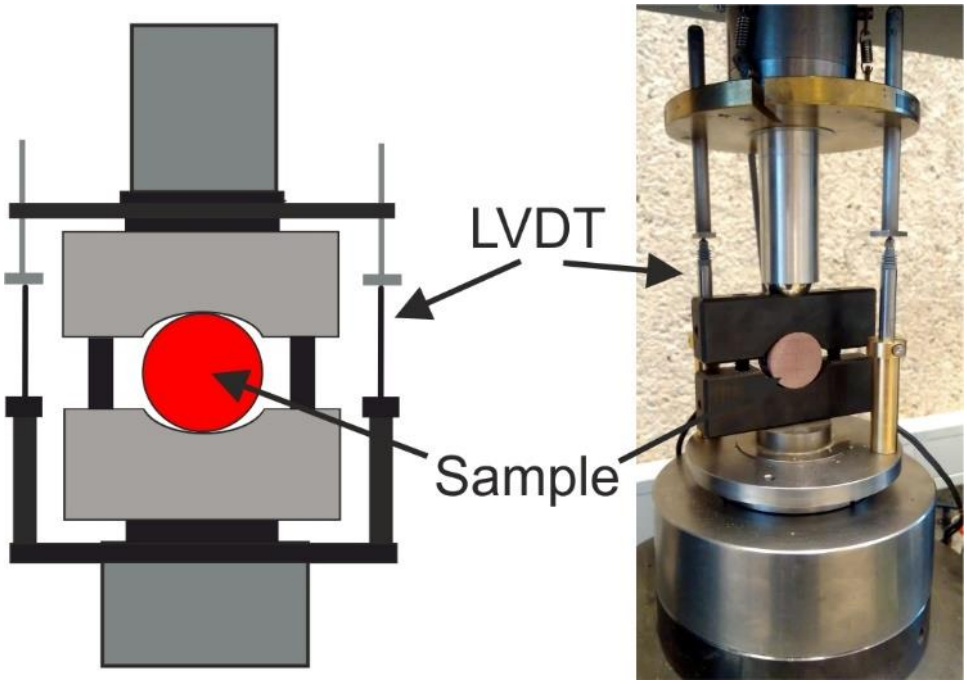

Figure 3.6: Brazilian testing setup for measuring tensile strength in the UCS machine.

The axial loading causes compression across the diameter of the rock sample, generating a bi-axial stress field resulting in highest tensile stress at the center of the cylindrical disc. The stress is caused perpendicular to the direction of the applied axial load. Upon reaching a critical load, the rock specimen started to split along its diameter in tension (Fig. 3.7).

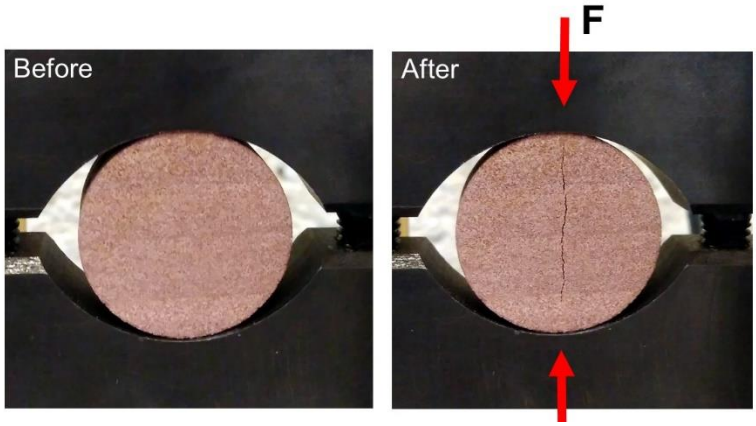

Figure 3.7: Buntsandstein rock sample before and after the mechanical test. The bedding of the rock sample is perpendicular to the direction of the applied load (F).

3.2 Permeability and Triaxial Deformation Tests

Triaxial deformation tests and permeability tests are conducted on different sandstones (mainly Buntsandstein) with both low (< 5 mD) and high initial permeability (> 600 mD).

3.2.1 Ruska Gas Permeameter

To assess the permeability prior to the triaxial experiments a number of samples has been tested with the "Ruska Gas Permeameter". In the permeameter, the discharge of air through a rock core is measured. In principle, a clean and dry rock core is placed in a rubber sleeve with the same inner diameter. The sleeve around the sample is tightened by placing it in the core holder assembly. After the core holder is closed and sealed, an air upstream pressure is applied with a regulator. The air streams through the sample (if the rock is not impermeable) and the flowrate (measured in cm) can be read from the flow tubes. With according conversion tables, the flow rate can be converted into cc/s, from which the permeability can be calculated using Darcy's law (Equation 4). However, low permeable specimens need a correction for gas-slippage.

The maximal length of the rock cores that can be used is around 3 cm. Therefore, cores tested in the permeameter are different from cores used in triaxial experiments. The cores that were used in the triaxial apparatus itself can reveal a very different permeability, depending on the heterogeneity of the samples. The permeameter only gives an approximation, as the measurements in the triaxial apparatus are considered more accurate, since the permeability does not need a correction for the Klinkenberg gas-slippage effect.

3.2.2 Triaxial Setup

Permeability measurements on cores were conducted within the triaxial apparatus in the lab at the Delft University of Technology, by using the available pore fluid system. During the permeability measurements, the Buntsandstein rock samples that were placed inside the triaxial apparatus were subjected to hydrostatic pressures ranging up to 50 MPa. In general, the cell can handle an axial load up to 300 kN and radial pressure up to 70 MPa acting on the axial piston (see Fig. 3.8).

In principal, the triaxial setup is similar to the setup of the uniaxial compression test, with the difference that the rock sample is placed inside an oil-filled cylinder, allowing to expose the sample to radial pressure. Elastic axial deformation in the frame are again assumed to be negligible, since the load frame is very stiff.

For all experiments in the triaxial apparatus the axial stress (σ_a) and the radial pressure (P_{rad}) were recorded as well as the axial strain (ε_a), the radial strain (ε_r), the flow rates of both pumps A and B (Q), the volume in the pump reservoirs (V) and the pore pressure difference (P_{diff}). All tests were carried out at room temperature.

During the experiment, the rock sample is placed between two steel pistons, fixed with a jacket around the sample and additional tie wraps to ensure alignment of the sample. O-rings on both ends guarantee a full isolation of the sample from the oil. The lower steel piston rests on a load cell, whereas the upper piston is in contact with the axial piston that enables to apply axial force on the sample. The load cell itself rests on a larger steel disk that acts as the bottom closure of the hollow cylinder (pressure cell) that is then filled with oil. Figure 3.8 shows the entire triaxial setup before the load cell including the steel pistons and the sample that will later be inserted in the hollow cylinder above. LVDTs (MHR 250 ASSY from RoHS Compliant) on both sides of the sample recorded the axial deformation with a very high sensitivity of 0.12% on the full range of ± 6.35 mm. The changes in radial direction were measured by a chain-type extensometer (MTS 632.92H-04) mounted around the sample.

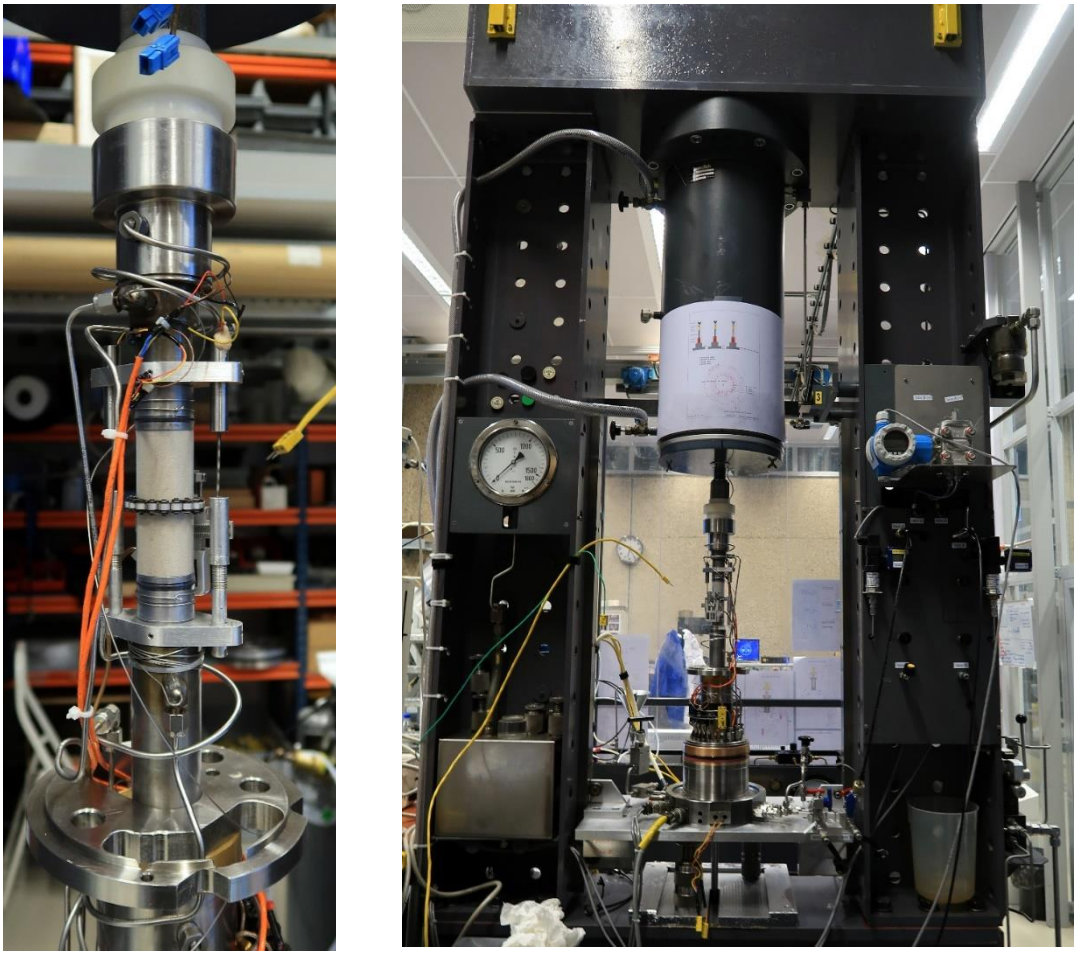

Figure 3.8: Left: Rock specimen sealed with a transparent shrink-tube type jacket between two steel pistons. Around the sample is the chain-type radial strain measurement device, on the side are the two LVDTS. Right: Triaxial setup with the pressure cell on the top and the column with the rock specimen (see left picture) below, that is later inserted into the pressure cell. At mid height on the right of the load frame the blue differential pore-pressure transducer can be seen.

After the jacketed sample and the measurement tools where ready, the sample assembly including the load cell and the bottom plate were mechanically lifted upwards into the pressure cell. Prior to the experiment it was made sure that all the equipment was properly working and that no wires, pipes and cables caused any interference with the setup when being inserted into the pressure cell. Once inside the pressure cell, the base was fixed with steel pillars to make sure that the load cell can't move downwards when applying axial load. Once inside, a connection between the axial piston and steel piston on top of the rock sample was made by forcing down the axial piston with a manual hydraulic pump. Then, oil from an external reservoir was pumped slowly from the bottom up into the pressure cell, pushing out air through an outlet above. To remove the oil again after an experiment, an air pump pushes air into the pressure cell from the top, pushing back the oil into the reservoir (Figure 3.9).

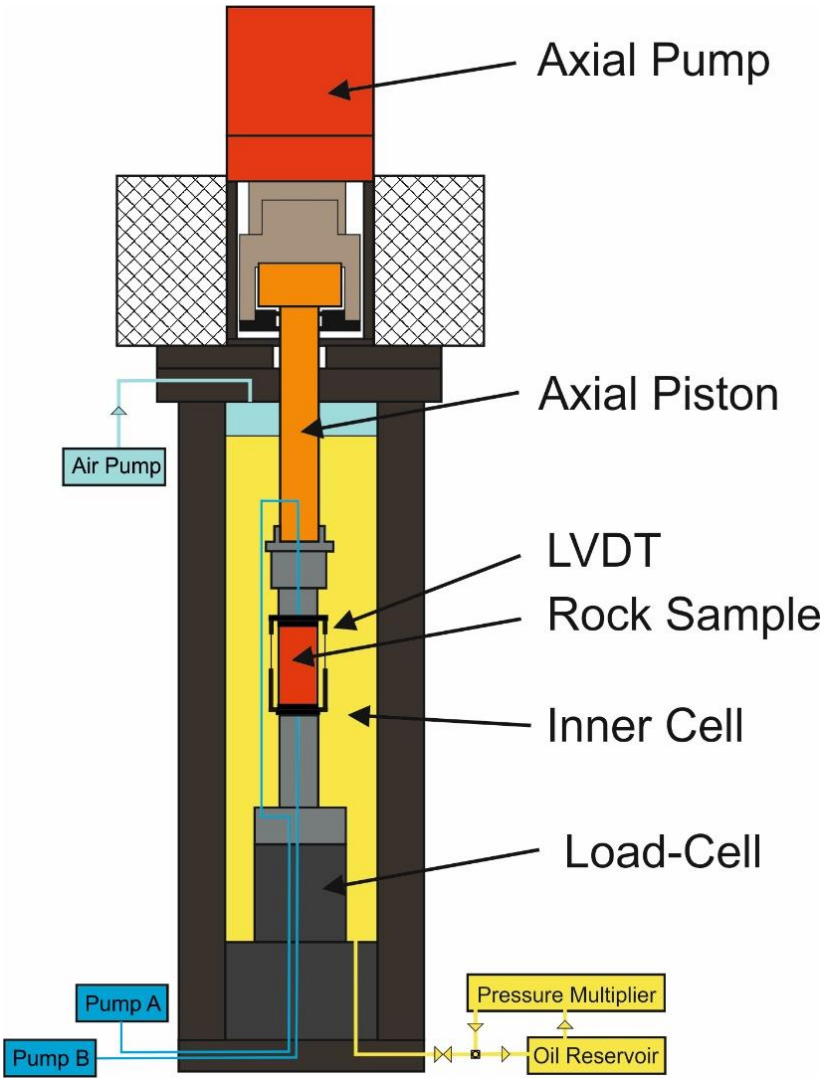

Figure 3.9: Schematic setup of the triaxial apparatus with the main components indicated.

When the pressure cell was completely filled and closed, some radial pressure was applied (e.g., 10 bars) and the pipes and the sample where prepared before initiating the experiment in the steps described in Appendix C.3. The pumps used for the water flow through the sample were two ISCO

Syringe Pump 100 DM, which have a flow rate accuracy of ± 0.3% (maximum 0.25 µl/min seal leakage; ISCO 100DM manual, 2009).

To measure the pore space compaction of each specimen, one of the ISCO pumps, e.g., pump B, was set to constant pressure-mode, adjusting the piston volume in order to maintain the pressure. When the confining or the axial pressures were changed, a volume flow was measured in pump A, when a fluid is pressed out of or into the sample. Based on the total volume flow measured by one of the pumps, the associated change in porosity was calculated. Thereby, all volume changes recorded in the pumps are assumed to be due to changes in the pore volume of the sample, since the effect of pressure on the pore fluid lines is negligible.

3.2.3 Permeability Measurements in the Triaxial Apparatus

The pore pressure during all experiments remained constant at 25 bars and did not change during the experiment. Conducting the permeability measurements under hydrostatic conditions additionally allowed to avoid time dependent (inelastic) behavior. For the experiments conducted in the triaxial apparatus, distilled water is used to run through the fully water saturated core sample. To make the water pressure act evenly on both ends of the specimen, the two steel pistons, in between the rock sample is set, had a uniform pattern carved in (Appendix C.4).

Since the water saturation will have an impact on the compressive strength of the rock (Brantut et al., 2013), it is important that all pores have been filled with water. In the experiments, distilled water with a viscosity of 0.001 Pa·s was used. The distilled water is helpful to avoid any chemical changes occurring within the sample and makes the compressibility of water negligible since the water is free of air. Before the core sample was saturated with water, the pore fluid system was vacuum dried for more than 10 minutes. Afterwards, the core was flushed with CO_2 to remove all air in the pore space and then flushed with the distilled water. At least 3 times the pore volume of each test core was flushed trough the sample to make sure that all CO_2 is properly dissolved. The flushing was done at 25 bar, since carbon dioxide dissolves better in water at high pressures.

To measure the effect of increasing confining pressure on the permeability, the pressure in the cell was increased multiple times. A maximum of 70 MPa (700 bar) confining pressure could be reached through a pressure multiplier (2.5 times 260 bar) that is connected between the oil reservoir and the pressure cell. Both axial and radial pressure were adjusted via a software, where the required pressures are entered. When changing the pressures in the cell, LVDTs indicated the stability of the sample.

Initially, the permeability was measured with the Buntsandstein sample still intact. Then the sample was deformed at constant confining pressure and an increasing axial load until failure. To guarantee that there is no leakage and that only the actual permeability of the rock sample is measured, thick rubber jackets (4 mm wall thickness) were used, that proved to be still sealing after fracturing the sample. Initially used thin shrinktube jackets around the core sample were not sturdy enough and broke upon failure of the samples.

The additional effect under pressure on the radial strain due to the rubber jacket was regarded in the calculations of the strain. In some experiments, the extensometer fell off after fracturing the rock due to either the shock caused by the fracturing or the measurement stayed at a maximum value due to the exceedance of the displacement range. Therefore the radial strain was estimated with values at similar confining pressure for strain measurements prior to failure of the rock specimen.

Permeability values during triaxial compression have been calculated from the steady state fluid flow rate and the sample dimensions by application of Darcy's law, given by Equation 4.

$$Q = \frac{k \cdot A}{\mu}\left(\frac{\partial P}{\partial X}\right) \qquad \textbf{(4)}$$

with flowrate Q [m³/s], permeability k [m²], cross-sectional area A [m²] and viscosity μ [Pa·s]. The term ($\partial P/\partial X$) represents the pressure change in Pascal over the sample with a specific length X [m]. The pressure differences during the experiment were measured accurately with a differential pressure transmitter (KEMA 03 ATEX 1561 from Endress+Hauser) with an error of max. 500 Pa. The pore pressure difference was kept below the hydrostatic pressure at all times. In most cases the pore pressure difference was kept to less than 5% of the confining pressure. The detection limit is set at approximately 20 bar pressure difference for a flow rate of 0.001 mL/min.

Moreover, the permeability measurements were done sequentially at different increments of volumetric strain, indicating any reduction or increase of rock bulk volume and sub resulting in a loss or an addition of pore space. In order to get statistically more robust results for the permeability values, various measurements at different flow rates were done at a specific constant confining pressure, before going to the next pressure step. Figure 3.10 indicates these steps of different flow rate and a resulting change in pore pressure differences.

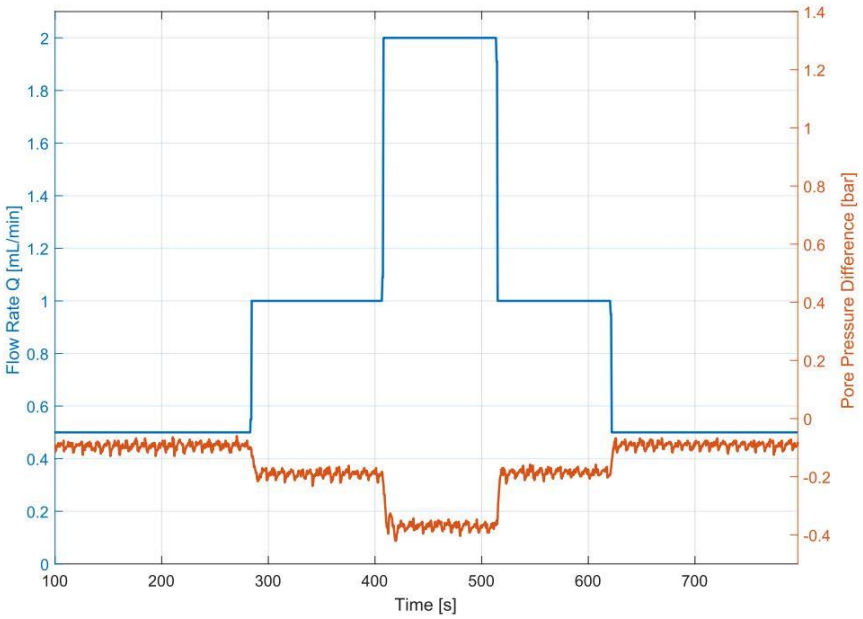

Figure 3.10: Different steps of flow rates in mL/min (blue) at constant axial and radial pressure. Due to the change in flow rates, the pore pressure difference (orange) changes accordingly.

Studies from the Buntsandstein in the Soultz-sous-Forêts site showed that the fluids were dominantly saline NaCl brines (Aquilina et al., 2000; Sanjuan et al., 2010). But, since in general the viscosity of water increases with increasing pressure at isothermal conditions (Zanotto, 2005), the difference between the use of salt water (as mostly present in the Buntsandstein layers in the subsurface) and distilled water should be marginal and has therefore no major impact on the experiments at higher confining pressures.

The dissolution of minerals from the sample was quantified by measuring the connectivity and the pH of the water before an experiment, during the experiment and after the experiment.

The distilled water reservoir was stored in a closed glass container. From this glass container, two reservoirs in two pumps (A and B) were filled. Each pump reservoir contained about 100 mL of distilled water. During the experiments, the water was pumped from one reservoir (e.g., pump A) through the sample to the second reservoir (i.e. pump B). Once one of the reservoirs was empty, the pump direction was changed and the water flowed back through the sample into the empty reservoir. Thereby the direction of the fluid flow did not have an impact on the permeability.

3.2.4 Triaxial Rock Deformation

3.2.4.1 Shear Deformation

A much greater effect of pressure on the permeability and the fluid flow within a formation is expected with the occurrence of fractures in the rock. As the Buntsandstein samples do not show any fractures, the effect of fractures can be measured by artificially inducing them. Shear deformation was achieved by applying a high axial load within the triaxial cell at a constant confining pressure. Due to the fact that the axial load piston is pushed upwards when increasing the confining pressure and vice versa, the application of the right confining pressure and the appropriate axial pressure (equal or slightly higher than the radial pressure) was achieved by adjusting the pressures stepwise until the correct values were reached. When bringing the rock specimen to failure, the increase of the load had to be entered manually in a stepwise procedure due to the limitations of the software, since the increase of the axial pressure is done in load control mode. As an example, the stress-strain curves from experimental results shown in Chapter 5 (Figure 5.10) show the stepwise increase.

In some cases sliding along the fracture plane was done by a fast increase of the axial load, followed by a fast decrease. The movement along the fracture plane can be expected, as the axial displacement showed a significant change in value.

3.2.4.2 Tensile Fracturing

Since the principal failure mode caused by an increasing load on the specimen through common steel piston is shear failure, special devices have been developed at the Delft University of Technology. With these devices it is essentially possible to create opening fractures (Mode I). The assembly consists of a wedge and two counterparts that make up a 1.5 cm long cylinder (Figure 3.11). The material used is hardened steel. Through the middle of the steel wedge is a hole with a diameter of 3 mm, where water can be pushed through onto the sample. In the triaxial setup, these “Mode I frackers” are placed between the sample and the upper and lower steel piston (see Fig. 3.8 and Figure 3.11). As in the other triaxial experiments, the sample including the frackers are placed inside a rubber tube to seal the sample from the oil in the triaxial cell. Since the maximum assembly length that can be placed between the steel pistons is 8 cm, the rock samples can have a maximum length of around 5 cm (Figure 3.11).

The principle behind these devices is, that high stresses are imposed through the wedges on a small area and a crack is initiated. Since the frackers are on both sides and the crests of the frackers are aligned parallel to each other, the crack is “forced” to propagate in a desired direction. In order to break the sample, the axial stress on the sample is applied manually with a hydraulic hand pump. The wedges cut further into the sample and the counterparts slide to the sides. To assure a smooth sliding

of the steel wedge, the surfaces are wetted with a thin film of grease. A breakage of the sample is indicated by a noticeable increase in the diameter of the sample, measured by the extensometer. The relationship between the diameter after fracturing the rock and the measured diameter during further testing can be related to an approximate apparent fracture aperture, assuming a single straight fracture plane through the sample from one fracker to the other. No topology is assumed for these apparent apertures. CT-images of samples fractured with the Mode I frackers are depicted in Appendix H.1.2.

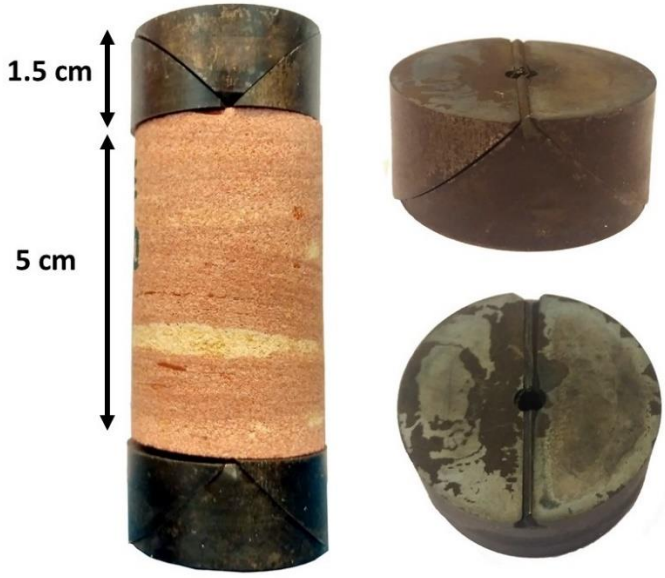

Figure 3.11: Assembly to create Mode I fractures in the triaxial apparatus including the two “Mode I frackers”.

3.2.5 Micro-structure Analysis after Deformation

After completing an experiment in the triaxial apparatus, the fractures in the rock samples were analyzed with a micro CT-scan image analysis. The CT-scanner is a phoenix nanotom s (Industrial Nanofocus CT System) with a highest resolution of smaller than 1µm on a sample of around 1 mm^3. However, in most cases a quantitative interpretation by inspection of the sample from outside was sufficient, since the main fractures that occurred were clearly visible. Fractures induced in the cores in the triaxial apparatus were preserved by injecting glue into the rubber jacket. The epoxy based adhesive resin that was used penetrated the pores, as the jacketed core sample was placed inside a pressure chamber for two days. Afterwards the jacket around the core sample was cut away and the core was prepared for making thin sections along the fracture plane. For this purpose the core was cut in half in axial direction, allowing a quantitative analysis of the fractures. Thin sections were analyzed with a petrographic microscope and an electron microprobe (EPMA).

3.3 Principles

3.3.1 Porosity and Matrix Density

Both effective porosity and matrix density are calculated by measuring the matrix volume (V_{ma} [cm³]) and the density with a gas-expansion pycnometer. With a known mass M [g], the density ρ [g/cm³] is given by

$$\rho = \frac{M}{V_{ma}} \quad \textbf{(5)}$$

With known dimensions of each sample used and the calculated total volume (V_t [cm³]), the effective porosity ϕ was calculated using the matrix volume given by the pycnometer as follows:

$$\phi = \frac{V_t - V_{ma}}{V_t} \quad \textbf{(6)}$$

Since each specimen placed in the pycnometer was cut and ground by hand, the actual sample shapes deviate from a perfect cylinder.

3.3.2 Elastic Properties

3.3.2.1 Static Method

In order to obtain the complete response in the post failure regime, the radial strain (ε_r) was recorded in addition to the axial strain (ε_a) and the axial stress (σ_a) during the uniaxial compression test as well as in multiple triaxial compression test, when loading the rock specimens till failure. For each measurement, the peak value of the axial compressive stress (σ_c) was recorded and two elastic parameters, Young's modulus and Poisson's ratio, were determined.

The primary parameter deduced from the recorded data was the axial stress σ_a, defined as

$$\sigma_a = \frac{F_a}{A} \quad \textbf{(7)}$$

with F_a [kN] as the axial force applied on the rock sample and A [m²] as the samples cross sectional area.

The uniaxial compressive strength σ_c is representing the peak value of the axial stress. Here, stresses and strains are defined as positive in compressive loading and in terms of deformation.

Two axial displacement measurement devices on each side of the sample (opposite of each other) recorded the axial displacement (δ_a). The average values of these two were used to calculate the axial strain, which is defined as

$$\varepsilon_a = \frac{\delta_a}{L_a} \quad \textbf{(8)}$$

with L_a [m] being the specimen length/height.

The radial deformation was recorded by a chain mounted at mid-height around the core sample. By measuring the change of the chain opening gap, the radial (or circumferential) strain could be calculated with the following formula:

$$\varepsilon_r = \frac{\Delta C}{C_i} \quad \textbf{(9)}$$

with the initial specimen circumference C_i and the change in the specimen circumference ΔC, which are defined as

$$C_i = 2\pi R_i \quad \textbf{(10)}$$

$$\Delta C = \frac{\pi \Delta X}{\sin\left(\frac{\theta_i}{2}\right) + \left(\pi - \frac{\theta_i}{2}\right)\cos\left(\frac{\theta_i}{2}\right)} \quad \textbf{(11)}$$

where ΔX [m] is the change from the initial chain gap to the chain gap at a given time and θ_i is the initial chord angle that is

$$\theta_i = 2\arcsin\left[\frac{L_i}{2(R_i + r)}\right] \quad \textbf{(12)}$$

with the initial chord length L_i, the initial specimen radius R_i and the roller radius r [m].

Given the radial strain, the volumetric strain can be derived with the axial strain. If the cross-terms between the ε_i are neglected, the volumetric strain can be defined as

$$\varepsilon_{vol} = \varepsilon_a + 2\varepsilon_r \quad \textbf{(13)}$$

Given the above, the elastic parameters were derived. For both the Young's modulus (E) and the Poisson's ratio (ν), stress strain curves were used to determine tangent E and tangent ν, which are defined as follows:

$$\mathrm{E} = \frac{\delta\sigma_a}{\delta\varepsilon_a} \qquad \nu = -\frac{\delta\varepsilon_r}{\delta\varepsilon_a} \quad \textbf{(14), (15)}$$

3.3.2.2 Dynamic Method

Based on the recorded first arrivals of P- and S-waves, the Young's modulus and the Poisson's ratio were obtained through density and velocity measurements according to the following equations:

$$\mathrm{E} = \rho \cdot {V_s}^2 \cdot \frac{3 \cdot V_p^2 - 4 \cdot {V_s}^2}{V_p^2 - {V_s}^2} \quad \textbf{(16)}$$

$$\nu = 0.5 \cdot \frac{V_p^2 - 2 \cdot {V_s}^2}{V_p^2 - {V_s}^2} \quad \textbf{(17)}$$

where V_s [m/s] is the S-wave velocity and V_p [m/s] is the P-wave velocity.

3.3.3 Fracture Toughness

To gain a measure of the energy required to produce a flaw, in terms of a brittle crack extension due to a specific load, the splitting tensile strength of multiple rock samples was determined in Brazilian tests. The Brazilian tests were conducted after the method of Guo et al. (1993), where the Mode I fracture toughness K_I [MN/m$^{1.5}$] is defined as follows:

$$K_I = B \cdot P \cdot \Phi(c/R) \quad \textbf{(18)}$$

with factor B [m$^{1.5}$] being:

$$B = \frac{2}{\pi^{\frac{3}{2}} \cdot R^{\frac{1}{2}} \cdot t \cdot \alpha} \quad \textbf{(19)}$$

where R [m] is the disc radius of the specimen, t [m] is the disc thickness and α is half the arc distance in which the pressure, P, is assumed to be radially distributed (Figure 3.12). For the disc specimens used with a diameter of roughly 30 mm, α is assumed to be around 5°.

The dimensionless stress intensity factor (SIF) coefficient is expressed in the term Φ(c/R) and can be defined in the following equation:

$$\Phi(c/R) = \left(\frac{c}{R}\right)^{\frac{1}{2}} \int_0^{c/R} \left[\frac{\phi\left(\frac{r}{R}\right)}{\left(\frac{c^2}{R} - \frac{r^2}{R}\right)^{\frac{1}{2}}} \right] d\left(\frac{r}{R}\right) \quad \textbf{(20)}$$

where 2c is the length of the crack occurring at maximum load P_{max} and with (r,θ) as polar coordinates based on the center of the disc (r = 0 equals to the center of the disc). As illustrated in Figure 3.12, σ_r is the stress alongside the crack in the vertical direction. According to Guo et al., (1993) it has no

influence on the propagation of the crack. The stress controlling the crack propagation is indicated as σ_θ (tensile) and distributed differently for various α. Its maximum is seen at $r = 0$.

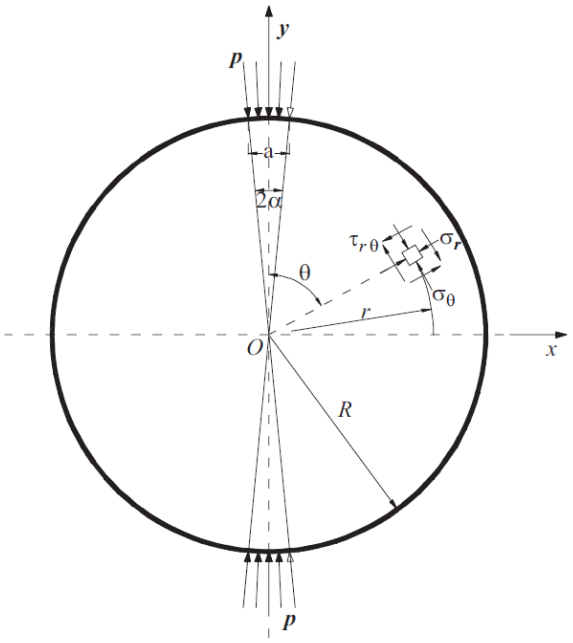

Figure 3.12: Schematic drawing of the disc specimen in the Brazilian test with the pressure P and the arc distance 2α in which the pressure is assumed to be radially distributed (Jianhong et al., 2009).

As Guo et al., (1993) proposes, the crack length can be predicted theoretically, allowing to determine the fracture toughness with a known local load minimum P_{min} (indicated in Figure 3.13) and the maximum SIF ($\Phi(c_0/R)$). Taking the dimensionless radius of the test samples used, the dimensionless SIF can be estimated from Guo et al., (1993) for $\alpha = 5°$ (Appendix C.6). Thereby, the dimensionless SIF was estimated to be 0.08 for a dimensionless radius of 0.15 for the samples used. This estimation method has a considerable estimation error. However, it enables to indicate the fracture toughness without having to measure the actual critical crack length (c_0/R).

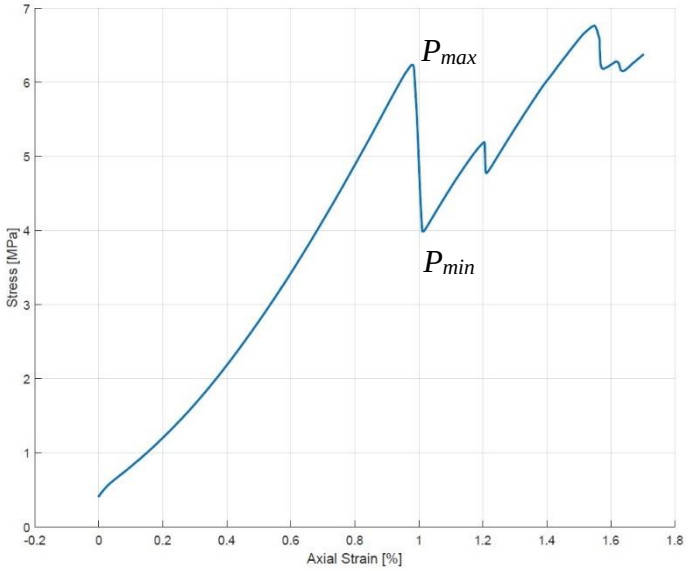

Figure 3.13: Characteristic failure curve for an altered Buntsandstein sample in the Brazilian test. The local stress maximum (critical stress) and the local stress minimum are indicated as P_{max} and P_{min}. Up to P_{max} the rock sample shows an elastic behavior, until a crack is formed and the crack propagates. When the crack stabilizes, a local minimum occurs at P_{min} and the crack finally starts to propagate further afterwards. Additionally, multiple other cracks start to occur.

4. Rock Characterization

Within the framework of this work, cores were drilled from 8 sample blocks of different sandstones. These sample blocks were analyzed with a petrographic microscope as well as with X-ray Powder Diffraction (XRD) and X-ray fluorescence (XRF) at the TU Delft. Furthermore an electron microprobe (EPMA) was used at GFZ Potsdam. Thin section images are shown in Appendix D.1. Results of the XRF are reported in Appendix C.5. All blocks have been classified after Folk (1965) and the QFL diagrams are presented in Appendix D.2.

4.1 Sample Origin

Tested Buntsandstein samples originate from 2 locations in Germany (Appendix C.1) and are either "Leistädter" sandstones (blocks SBS6-BD) or "Miltenberger" sandstones (blocks SRM6-MI). The Leistädter sandstones belong to the so called "Rehberg formations" (and "Schloßberg formations"), which, in turn, belong to the Lower to Middle Triassic Buntsandstein. The Rehbergschichten are 120 m thick at the location of the quarry. Their age is between 251 and 243 Ma (personal communication with Göbel, A.; Dachroth, 2013). The red Miltenberger sandstones belong to the "Gelnhausen formation" and are of Lower Triassic age (personal communication with Wassum, P; Menschik, 2015). Further on in this thesis the Leistädter sandstone will be referred to as "unaltered Buntsandstein", whereas the "Miltenberger sandstone" is mentioned as "altered Buntsandstein".
The Rüthener Grünsandstein (block SRG6-RU) from the Cretaceous (Albian – Cenomanian; 90 – 110 Ma) is a medium-grained clastic sedimentary rock. It often has a grey-green color due to the abundance of glauconite grains present in the rock (Kirsch, n.d.).

4.2 Sample Analysis

4.2.1 Block SBS6-BD-50

The examination of the microtextural and mineralogical features in the thin sections of sample block BD-50 with a petrographic microscope (Leica DMLP) showed that the sandstone is well sorted and the average grain size of the components ranges from 0.1 to 0.2 mm. The maximum grain size found in the thin section was 0.5 mm. The equant grains are primarily subangular to angular and appear quite weathered. The majority of the grains shows partial dissolution on the edges. Few grains are dissolved almost entirely (Figure 4.1). Partly, the thin section shows very porous sections, whereas other parts consist of grains that are welded together. The intergranular cement consists mostly of ply alkali-feldspar minerals (microcline), clay and a minor amount of quartz which were identified in the

EMP measurements as well as in the XRD analysis, supported by XRF. As an accessory mineral in the cement, rutile (TiO_2) has been identified in the EPMA measurements. Based on the on the peaks and detected elements given by the energy dispersive X-ray spectroscopy (EDS) spectra, the supposed clay type occurring in the rock is illite. However, XRD analyses performed solely on the separated clay fraction can indicate exactly the clay type.

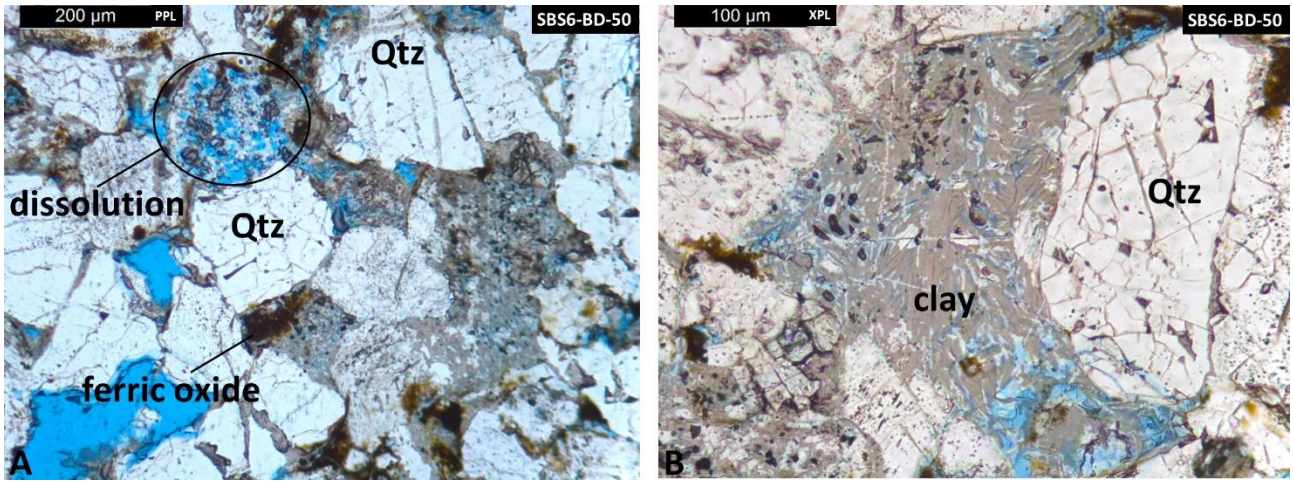

Figure 4.1: Microphotographs of block SBS6-BD-50 from optical microscopy. A: Ferric oxide aggregations and dissolution. B: Clay as pore fill.

The overall porosity is around 25%, taking into account the big voids. However, the cemented regions have a porosity of 10 - 15%, which is in the range of the porosity measured with the pycnometer. Furthermore, iron oxides occur in some parts of the cemented pore space.

Mineral grains are mostly monocrystalline quartz (90% of total thin section), followed by kalifeldspars (9%) and phyllosilicates (< 1%). The ferric oxide makes up about 1% of the thin section. This sandstone can be classified as subarkose after Folk (1965). A corresponding QFL diagram can be found in Appendix D.2. The indicated presence of dolomite in the XRD analysis could not be validated in the thin sections and the EPMA measurements because no grain could be found in the sample. However, this does not exclude the occurrence of small amounts of dolomite as cement fraction.

4.2.2 Block SBS6-BD-51

Block BD-51 is a well sorted sandstone with grains 0.25 mm wide on average, with a maximum grain size of 0.7 mm. The equant grains are usually subangular to round (Figure 4.2). Monocrystalline quartz is the dominant component (75%), followed by alkali-feldspar (10%) and phyllosiliccates (5%). Both XRD analysis and EPMA analysis suggests microcline as feldspar-type. Furthermore, rutile was identified as an accessory mineral similar to block BD-50.

The majority of the grains shows strong weathering. Around the grains, chemical zoning of feldspar is present. Dissolution is scarce. The sandstone is relatively clean, but smaller areas show oxidation of the grains (Figure 4.2). The XRF analysis showed a ferric oxide content of less than 1% wt., an amount which cannot be detected with XRD. Primary pores are mostly filled with microcrystalline quartz and phyllosiliccates, which grow often intergranular or around the grains as flakes. Phyllosilicates are up to 0.25 mm in length and intragranular phyllosilicates of 0.1 mm are common. The porosity is about 20%.

After Folk (1965), this sandstone would be classified as a subarkose, consisting 75% or more of quartz with a higher alkali-feldspar content.

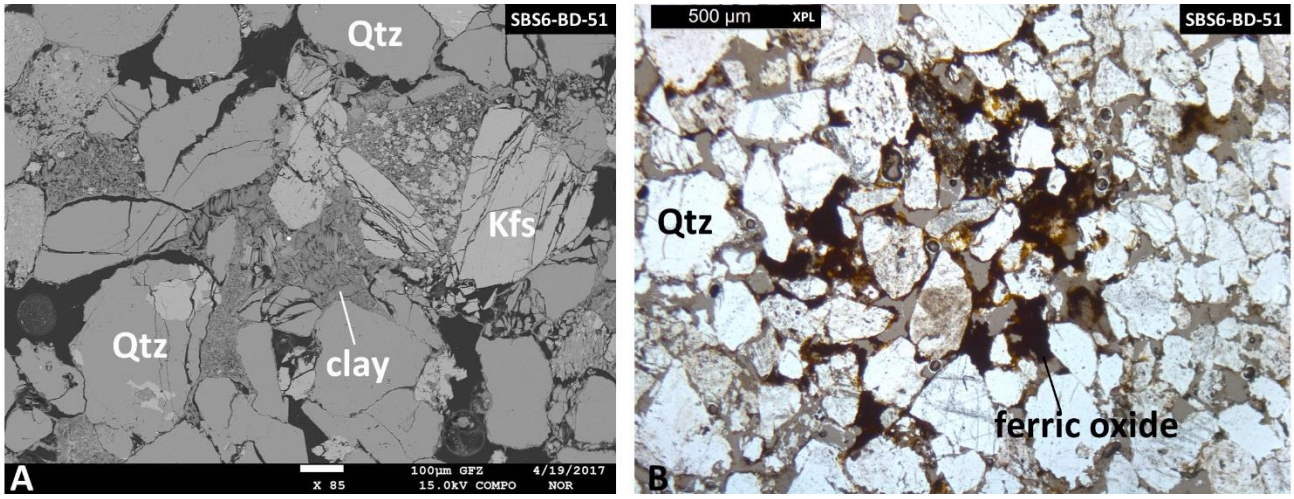

Figure 4.2: A: Secondary-electron image of block SBS6-BD-51 showing clay as pore fill between broken grains. B: Microphotograph showing ferric iron as pore fill.

4.2.3 Block SBS6-BD-52

In comparison to blocks BD-50 and BD-51, this sandstone appears much more compact. According to the thin sections, the porosity lies between 15 and 20%. The measured porosity in the pycnometer gives a similar value, with an average porosity of 19.5%. The main components are almost identical to the ones from block BD-51, with subangular to rounded quartz grains making up around 80% of the minerals. The average grain size is 0.2 - 0.3 mm in diameter, whereas the largest grains found are not larger than 0.5 mm. All grains are quite weathered. Pores are generally clear, around the grains there is often a quartzitic rim (Appendix D.1). Some sections of the sandstone show areas where oxidation occurred, which is visible as dark-brown rust in the thin sections. Moreover, spikey clay minerals are regularly seen between the pores, making up around 2% of the minerals in the whole thin section. Based on the detected elements the supposed clay type is illite (Appendix D.1). Accessory minerals in the rock are rutile and baddeleyit (a rare zircon oxide). Some of the grains show a damaged zone and compaction features as seen in Appendix D.1. This can be seen as evidence that the sandstone has experienced previous compaction, for example, due to tectonic movements.

4.2.4 Block SBS6-BD-53

Grains of block BD-53 are mostly broken, weathered and have an average size of 0.3 mm (max: 0.7 mm). The overall porosity is more or less 20%. Similar to the other sandstone blocks of the BD-series, smaller aggregations of ferric oxide are common. The most abundant components are quartz (90%), alkali-feldspar (10%) and phyllosilicates plus ferric oxide (together less than 1%). XRD/XRF analysis as well as the mineral identification with EPMA predict a comparable composition as sample block BD-53. Heavy minerals are present in trace amounts similar to all other sample rocks and include rutile and less commonly zircon.

4.2.5 Block SBS6-BD-54

Comparing sample block BD-54 to BD-52, the grains present show much less weathering and basically no ferric oxide. Furthermore, grains show only little dissolution and hardly any cementation. Overall, the sandstone is very clean, consisting of approximately 95% quartz and 5% feldspars. According to the thin section analysis micas were basically not present. The mean of the grain sizes in the sandstone is between 0.35 and 0.4 mm, and therefore slightly larger as in the blocks BD-50 to BD-53. The largest grains were found to be 0.7 mm. Grains were subangular to angular in shape. The weight percentages of the compounds identified in the XRD analysis showed similar results to the other blocks from the BD-series.

4.2.6 Block SRM6-MI-50

The altered rock sample SRM6-MI-50 is thin-bedded and has a brick-red appearance. The thin section analysis combined with the mineral identification in the EPMA show that the color is due to oxidized iron, which covers almost all grains of this rock sample (Figure 4.3). The round to subangular grains are commonly around 0.3 mm, whereas the maximum grain size is about 0.5 mm. All grains are strongly weathered and partly dissolved, generating minor amounts of secondary intraparticle macro-porosity (Figure 4.3). The overall porosity of this rock is around 15%.

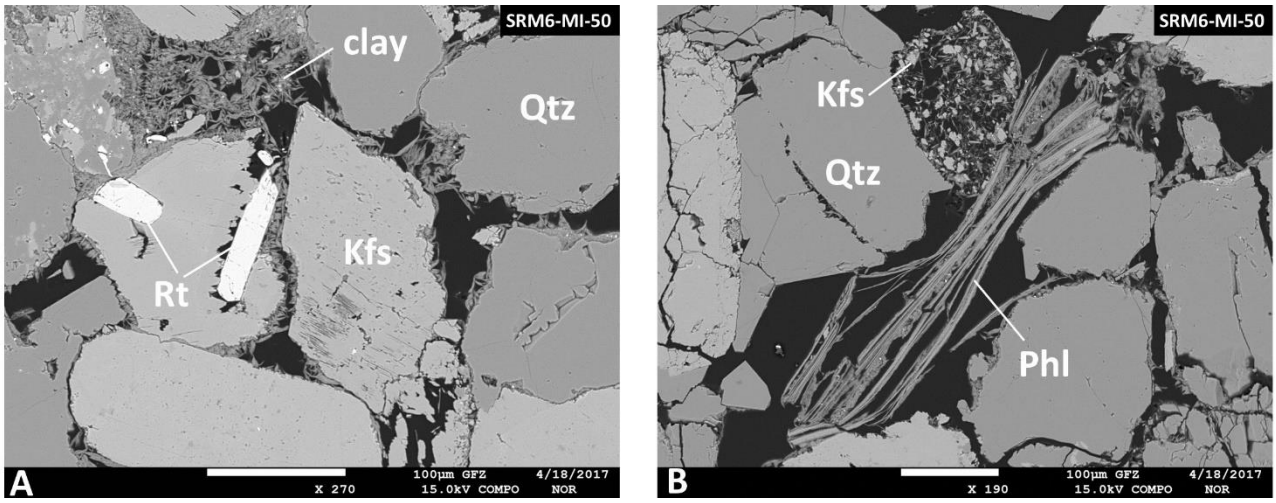

Figure 4.3: Secondary-electron images of block SRM6-MI-50 rutile, alkali-feldspar and phyllosilicates. A: Rims of ferric iron can be identified around the grains.

The sandstone consists of around 90% quartz, 8% feldspars and 1 - 2% phyllosilicates. Therefore it can be classified similar to the sandstones from the BD-series as subarkose according to Folk (1965). The alkali-feldspars present were identified to be primarily microcline. Concentrations of the main compounds of sample SRM6-MI-50 according to the XRD analysis are very similar to the compounds found in sample BD-50 (see Appendix D.1).

4.2.7 Block SRM6-MI-52

A distinctive difference to the sample block SRM6-MI-50 is the colored internal layering of the sample as well as the cross bedding. Beige layers alternate with red appearing, oxidized layers. Layers vary in thickness, but are mostly between 10 and 2 mm thick. The porosity encountered in the rock sample is mixed, depending on the different layers. Altered layers show very high porosities of up to 50% in the analyzed thin sections (Appendix D.1). In contrast, the beige, non-altered layers have a relatively tight appearance with porosities of around 10% (Appendix D.1). The average grain size in both layers is 0.2 - 0.3 mm (max. 0.4 mm) and the grains are well sorted. Grains are strongly weathered and are surrounded by a ferric oxide rim in the altered layers. The strong oxidization of the iron is reflected in the two times higher Fe2O3 content of sample SRM6-MI-52 in comparison the sample SRM6-MI-50. Apart from the ferric oxide content, both rock samples have similar weight percentages of all compounds (see Appendix D.1).

Only around 1% micas are present in the rock sample and are common both in altered and unaltered layers. Main components are quartz (95%) and feldspar (4%). Grains are generally angular to subangular and there is hardly any dissolution of the grains.

4.2.8 Block SRG6-RU

This sample block from the Rüthener Grünsandstein is a very clean and well sorted sandstone. Grains are round to subangluar in shape and are 0.1 - 0.2 mm on average. The maximum grain size is around 0.4 mm. The sample consists of 80% quartz, 15% glauconite and 5% alkali-feldspars. No micas were identified in the thin sections. Based on the EPMA measurements, barite occurs as a trace mineral (see Appendix D.1). The overall porosity is around 25%.

Glauconite grains are round and have a characteristic green color (see Appendix D.1). Grains are slightly weathered, and ferric iron accumulated in aggregates mostly close to the glauconite grains. A minor amount of quartz grains shows partial dissolution or is even completely dissolved. After Folk (1965), the sandstone can be classified as sublitharenite (Appendix 3).

4.3 Microfracture Analysis

After shear fracturing the Buntsandstein samples in the triaxial apparatus, thin sections were made from cores cut in axial direction. The cores show a localization of shear strain, the shear zones are relatively narrow with widths ranging from 200 µm to 400 µm (see Figure 4.4 and Appendix D.1). In the shear zone, the grain size was reduced down to as little as 1 µm by cataclasis. Initially, grains are around 150 µm to 200 µm in size. Fine grained matrix minerals in the shear zone have been identified as similar to larger sized grains, mainly being quartz, feldspar and phyllosilicates. Phyllosilicates are generally split along the cleavage planes in the shear and damage zone.

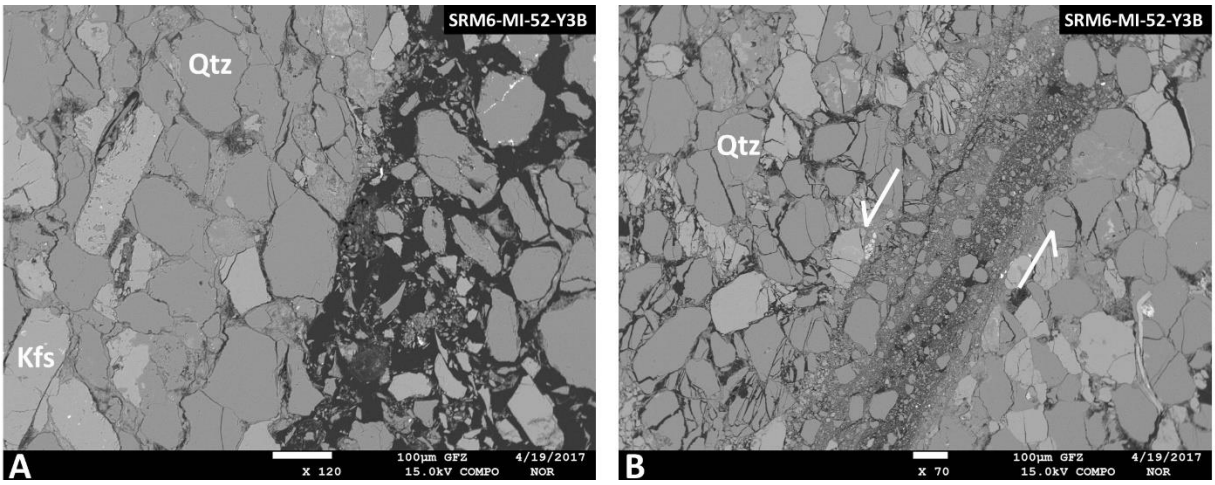

Figure 4.4: Secondary-electron image of sample SRM6-MI-52-Y3B after shear deformation in the triaxial apparatus. The relative shear direction is indicated in B.

As shown in images from the shear zone and the surrounding damage zone in Figure 4.4, quartz and feldspar clasts have serrate edges. Evidence of mechanical abrasion can be found, especially on the grains in the shear zone. Intergranular fracturing is common, mostly in the damage zone of the hanging wall. The damage zone of the footwall is very compacted, the porosity is generally 1% to

5%. The total width of the damage zone varies for each sample core. As an example, the shear zone of sample MI-52-X2 is approximately 300 µm in width, whereas the damage zone on each side is about 800 µm wide. Overall, shear fractures of the more porous Buntsandstein block SBS6-BD-51 show equal properties of the developed shear zone (i.e. equal reduction in grain size, compaction, damage zone, etc.) compared to the altered Buntsandstein blocks (SRM6-MI-50, SRM6-MI-52).

5. Results

5.1 Uniaxial Compression Tests

Uniaxial compression tests were done on the unaltered sample blocks SBS6-BD-50, SBS6-BD-51, SBS6-BD-52, SBS6-BD-53 and SBS6-BD-54, the altered Buntsandstein blocks SRM6-MI-50 and SRM6-MI-52, and the Rüthener Grünsandstein block SRG6-RU. The Young's modulus was calculated according to the lower part of the most constant sections of the stress-strain curve, corresponding predominantly to an axial load of 20 to 40% of the axial peak stress (σ_c; see Figure 6.2). Choosing this section ensures that the elastic moduli are taken during linear elastic deformation after crack closure (further details in Chapter 6.2).

The altered and unaltered Buntsandstein samples show a clear distinction between each other in terms of yield strength, UCS, Young's modulus and Poisson's ratio (Table 5.1). Appendix E.2 illustrates the stress-strain curves for each sample in different orientations (X, Y and Z).

Appendix E.2.1 shows that unaltered Buntsandstein samples from the same formation but from different blocks have a significant difference. Samples cored parallel to bedding indicate the higher ultimate strength of block SBS6-BD-50, which is around 50 MPa. In comparison, the other unaltered Buntsandstein blocks have a mean UCS of 25 MPa. The Young's modulus is much higher with around 11 GPa for the SBS6-BD-50 block compared to 6 GPa for the other blocks, implying that the sandstone has a much higher resistance to strain. Also the altered Buntsandstein blocks SRM6-MI-50 and SRM6-MI-52, which are from the same formation, show differences between different blocks. Cores in X- and Y-direction from bock SRM6-MI-52 have an almost 80% higher ultimate strength compared to cores from SRM6-MI-50. The Young's modulus is two times higher, with ~11 GPa compared to 5.5 GPa. In each case, the Poisson's ratio for blocks with a higher ultimate strength is lower than for samples with a lower ultimate strength (Table 5.1).

Compared to the Buntsandstein samples, specimens from the Rüthener Grünsandstein (block SRG6-RU) have a very low UCS and Young's modulus. The calculated Poisson's ratio is very low with a value of 0.09.

Table 5.1: Result overview of the uniaxial compression tests.

Sample block	Sample	Core direction	Yield strength [MPa] (axial strain [%])	Uniaxial compressive strength [MPa]	Young's modulus [GPa]	Poisson's ratio [-]
SBS6-BD-50	BD-50-Y2	Y	44 (0.7)	49.42	11.62	0.34
	BD-50-Y4	Y	43 (0.5)	51.00	10.65	0.29
	BD-50-Z2	Z	50 (0.5)	59.50	11.53	0.30
	BD-50-Z3	Z	54 (0.65)	60.70	11.17	0.34
SBS6-BD-51	BD-51-X1	X	21 (0.63)	22.45	5.03	0.33
	BD-51-Z2	Z	31 (0.6)	33.78	8.53	0.35
SBS6-BD-52	BD-52-X1B	X	23 (0.53)	26.96	6.38	0.32
	BD-52-Z2	Z	30 (0.47)	36.00	9.51	0.29
SBS6-BD-53	BD-53-X2B	X	20 (0.57)	22.76	4.90	0.36
	BD-53-Z2B	Z	40 (0.56)	44.47	10.69	0.32
SBS6-BD-54	BD-54-X3A	X	25 (0.45)	28.84	8.28	0.30
	BD-54-Z2A	Z	20 (0.4)	25.68	8.27	0.17
SRM6-MI-50	MI-50-Y3	Y	30 (0.7)	36.10	5.57	0.47
	MI-50-Y6	Y	34 (0.6)	37.82	5.83	0.45
	MI-50-Z1	Z	45 (0.5)	51.48	10.17	0.30
	MI-50-Z3	Z	45 (0.65)	51.10	10.77	0.32
SRM6-MI-52	MI-52-Y4A	Y	55 (0.7)	62.96	9.81	0.33
	MI-52-X1	X	60 (0.71)	66.53	11.16	0.33
	MI-52-Z7	Z	50 (0.78)	54.17	9.34	0.32
SRG6-RU-51	RU-X3	X	10 (0.27)	13.53	4.84	0.09
	RU-Z3	Z	8.5 (0.26)	15.17	5.05	0.09

In general, cores in Z-direction have a higher uniaxial compressive strength compared to samples drilled in X- and Y-direction. Tests on Z-cores confirm the overall behavior of the different blocks mentioned above, with Rüthener Grünsandstein samples having the lowest UCS, Young's modulus and Poisson's ratio (Table 5.1).

Figure 5.1 shows the stress-strain curves of specimens in Z- and Y-direction. Except for block SBS6-BD-54, Buntsandstein samples show a higher yield strength and UCS in the Z-direction than in the X- or Y-directions. The yielding occurs at similar percentages of axial strain. Calculated volumetric strains reveal the higher initial compaction of specimens in X- and Y-direction, as seen on the exemplary stress-strain curves in Figure 5.1 for samples MI-50-Y3 and MI-50-Z3. A comparison to these altered sandstones is found in Appendix E.1, where examples from the unaltered Buntsandstein block SBS6-BD-50 are shown.

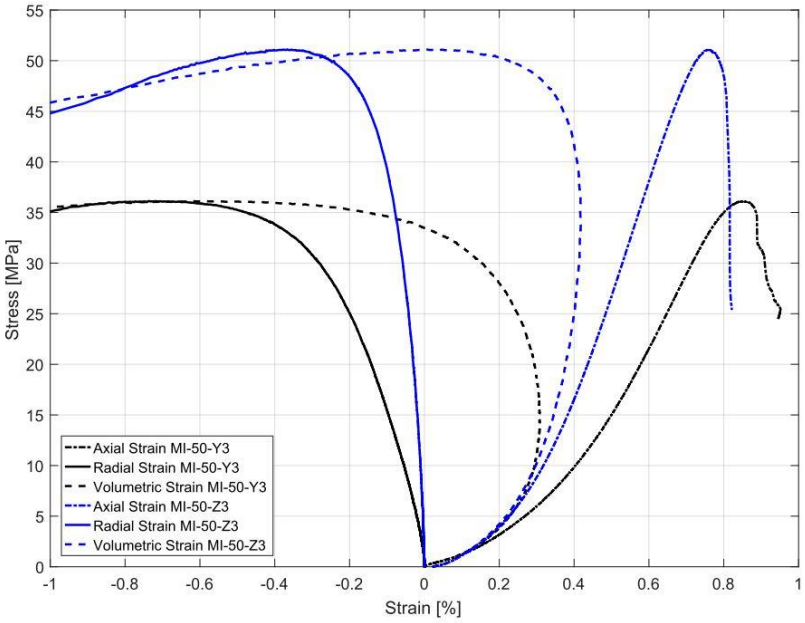

Figure 5.1: Axial strain, radial strain and volumetric strain as a function of axial stress for unaltered Buntsandstein samples MI-50-Y3 and MI-50-Z3 from unconfined compression tests.

In detail, Appendix E.2.2 and E.2.4 show that the Buntsandstein sample MI-50-Y3 (Y-direction) behaves very differently from sample MI-50-Z3, showing a significantly larger sample strain before reaching the elastic region. The Young's modulus is more than 90% smaller than for MI-50-Z3, with a value of 10.8 GPa, and the Poisson's ratio is much higher (Table 5.1). This observation could also be made for samples of the unaltered Buntsandstein samples. For the Rüthener Grünsandstein, no significant changes can be seen between X- and Z-direction (Figure 5.2).

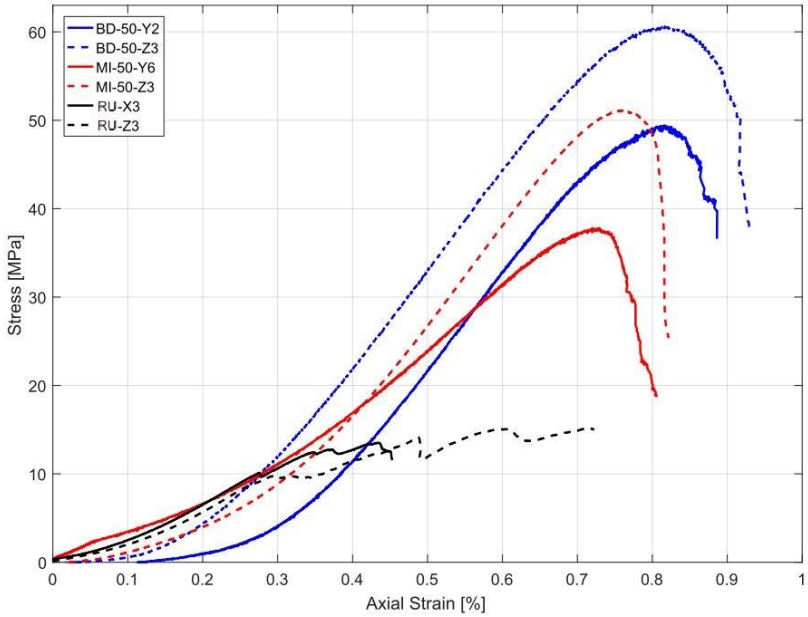

Figure 5.2: Stress versus axial strain curves for six samples drilled parallel (Y, X) and perpendicular (Z) to the bedding. Two of the samples are altered Buntsandstein (MI-50-Y6, MI-50-Z3), two were unaltered sandstones (BD-50-Y2, BD-50-Z3), and two are from the Rüthener Grünsandstein (RU-X3, RU-Z3).

The fractures of all samples show a clear trend for each orientation of the samples. Figure 5.3 and Appendix E.3 show images of post failure rock specimens. Samples in Y-direction (e.g., BD-50-Y2, BD-50-Y4 and MI-50-Y3) often show a single fracture (Figure 5.3). In MI-50-Y3 the fracture occurs parallel to bedding, whereas the fractures in BD-50-Y2 and BD-50-Y4 are angular towards the bedding and some internal layers. Buntsandstein samples cored in Z-direction (e.g., BD-50-Z2 and MI-50-Z1, MI-50-Z3) show more spalling towards the center, especially BD-50-Z2 with fractures perpendicular to bedding as well as fractures angular to the bedding (Figure 5.3). However, this phenomenon is also observed in sample MI-50-Y6 (Y-direction).

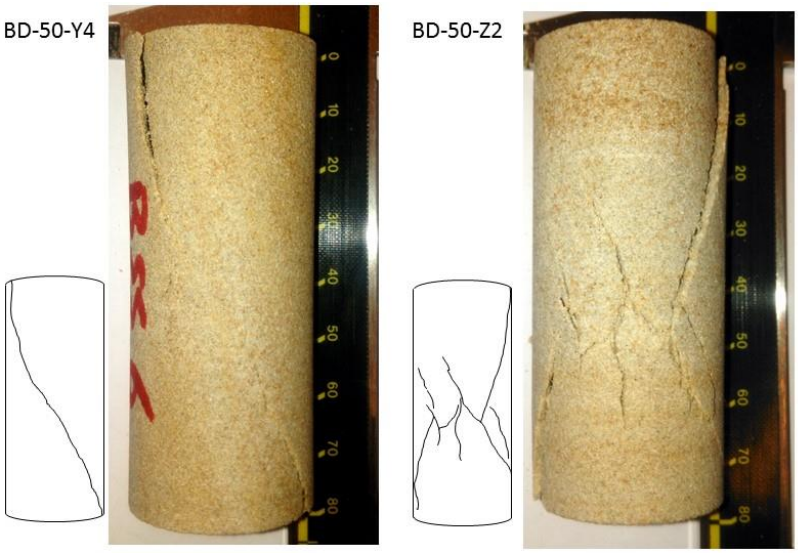

Figure 5.3: Samples BD-50-Y4 and BD-50-Z2 after the uniaxial compression test.

5.2 Acoustic Measurements

P- and S-wave velocities were measured for 14 samples during UCS testing and are displayed in Appendix E.4 and E.5. Overall, velocities increase with higher axial load. For each sample the minimal velocities were measured at the lowest state of stress. After the sample reaches the maximum yield strength, the velocities start decreasing slowly before dropping down abruptly after failure of the sample. An exemplary plot illustrating this common behavior is depicted in Appendix E.5.3 and E.5.4.

Moreover, results indicate that samples with higher porosity have lower velocities and vice versa. Specimen from block SBS6-BD-50, SBS6-BD-54 and SRM6-MI-50 reach P-wave velocities (V_p) of over 4000 m/s at stresses of 10 MPa (see Appendix E.4). Initial P-wave velocities under atmospheric conditions are represented as "Min. V_p" in Table 5.2. Here, the altered sample MI-50-Z1 shows the highest V_p with 4203 m/s, whereas the Rüthener Grünsandstein sample RU-Z3 and the Buntsandstein

core BD-53-X2B have the lowest V_p with 2706 m/s and 2613 m/s, respectively. Similar for these samples, S-wave velocities are found to be very low.

In Appendix E.5.4 it is apparent that the S-wave velocities (V_s) show the same behavior, with rising velocities over increasing stress, than P-wave velocities (see e.g., sample BD-50-Y2, BD-54-X3A and MI-50-Y6). As an example, the S-wave velocity for sample MI-50-Y6 rises from 1725 m/s at zero axial load to 2191 m/s at 30 m/s. At a peak stress of 60 MPa, the velocity increased to a maximum of 2237 m/s. The P-wave velocity increased from 4203 m/s to 4261 m/s at peak stress (Table 5.2).

Table 5.2: P- and S-wave velocities measured during the UCS tests for samples drilled in different directions towards the bedding.

Sample block	Sample	Core direction	ϕ [%]	Velocities [m/s]			
				Min. V_p	Max. V_p	Min. V_s	Max. V_s
SBS6-BD-50	BD-50-Y2	Y	14	3426	4248	1918	2256
	BD-50-Z3	Z	14	3791	4020	1897	2386
SBS6-BD-52	BD-52-X1B	X	19	2903	3688	1724	1865
	BD-52-Z2	Z	22	3193	3989	1761	1926
SBS6-BD-53	BD-53-X2B	X	21	2613	3511	1754	1922
	BD-53-Z2B	Z	20	3192	4006	1754	2002
SBS6-BD-54	BD-54-X3A	X	19	3456	4070	2009	2165
	BD-54-Z2A	Z	19	3426	4248	1918	2256
SRM6-MI-50	MI-50-Y6	Y	19	3155	4145	1910	2237
	MI-50-Z1	Z	19	4203	4261	1725	2074
SRM6-MI-52	MI-52-Y4A	Y	10	3041	4003	2038	2141
	MI-52-Z7	Z	10	3910	4081	1968	2101
SRG6-RU	RU-X3	X	25	2843	3439	1584	1698
	RU-Z3	Z	27	2706	3477	1638	1840

5.3 Cyclic Loading

To observe the effect of cyclic-loading on the Buntsandstein, samples MI-52-Y2C, BD-53-Z1A and BD-53-X2A were subjected to different levels of load in an unconfined compression test. The load maxima of each cycle are listed in Appendix F.1. Figure 5.4 illustrates the significant lower peak compressive strength of sample MI-52-Y2C compared to sample MI-52-Y4A. Sample MI-52-Y4A was equal in terms of rock type and has been tested under constant strain rate conditions with loading until failure. Where the ultimate strength of MI-52-Y4A was around 63 MPa, sample MI-52-Y2C has a 20% lower ultimate strength of about 49 MPa (Figure 5.4; Table 5.2). This observation is also seen in sample BD-53-Z1A, which has an approximately 10 MPa lower ultimate strength than sample BD-53-Z2B (Appendix F.2). Sample BD-53-X2A has an ultimate strength of 27.2 MPa, around 5 MPa lower compared to sample BD-53-X2B (tested under constant strain rate conditions).

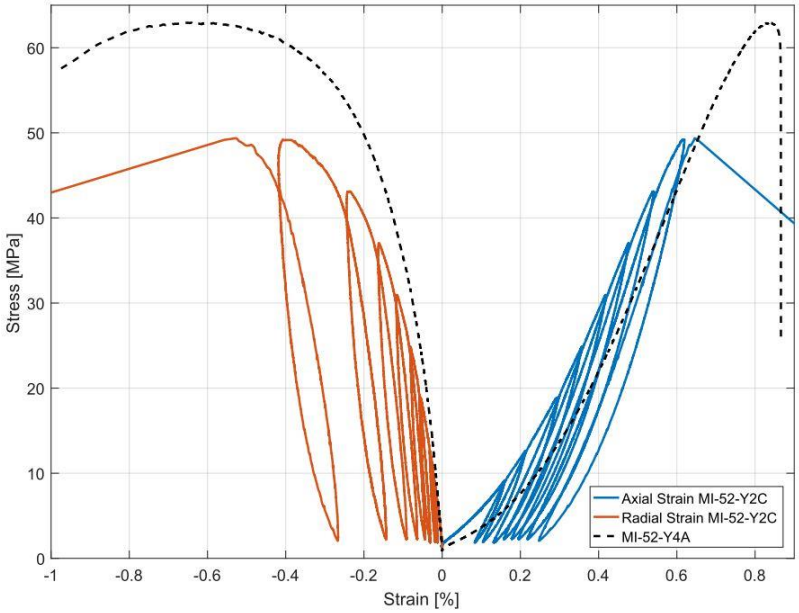

Figure 5.4: Stress-strain curves for the cyclic loading experiment on sample MI-52-Y2C. In comparison, the stress-strain curve of sample MI-52-Y4A, which has been performed with a constant strain and loading until failure, is plotted (black dotted lines). Negative strain values correspond to the radial strain, positive values belong to the axial strain.

The effect of cyclic loading is visible in the changes of the elastic moduli in each cycle in case of the tested Buntsandstein samples. Figure 5.5 and Appendix F.3 show the changes in Young's moduli and Poisson's ratios for each cycle. Overall the figures illustrate the increase of the Young's modulus, E, with a higher number of cycles. In the last cycle, E decreases slightly or stays about equal. In turn, the Poisson's ratio, *v*, increases continuously after each cycle. In Figure 5.5 and Appendix F.3 it is noticeable that the increase in *v* is more accelerated after each cycle. All tested samples broke in the last cycle shown in the figures.

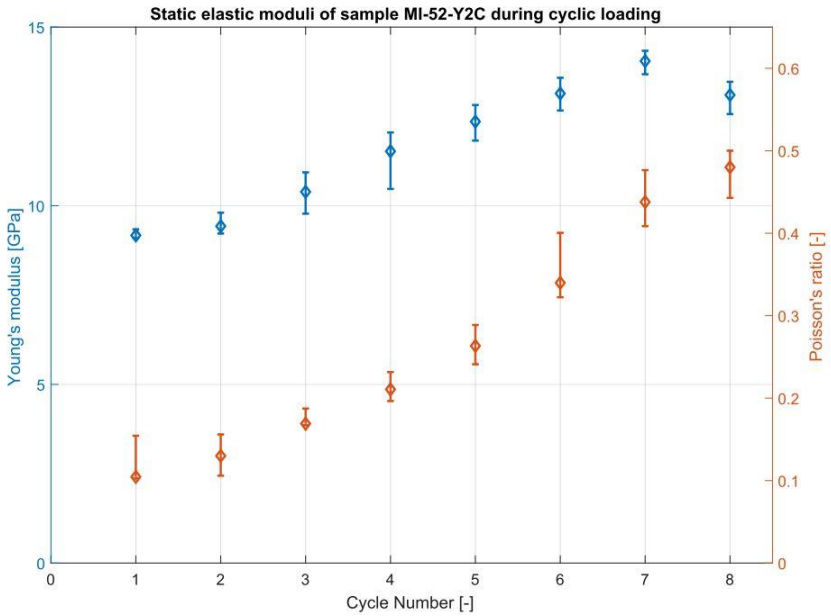

Figure 5.5: Evolution of the Young's modulus and the Poisson's ratio for sample MI-52-Y2C for each cycle of the cyclic loading test. Relative errors are indicated as bars.

5.4 Brazilian Indirect Tensile Strength-Test

The Brazilian tests were done on sample blocks SBS6-BD-52, SBS6-BD-53, SRM6-MI-52 and SRG6-RU. A total of 37 specimens was tested. Characteristics and results for each specimen are listed in Appendix G.

The only sample rock that was used in the Brazilian tests and showed internal bedding were samples from block SRM6-MI-52 cored in Y-direction. Occurring macrocracks propagated along the loading direction, independent of the bedding. This was similar to the observations made for samples without an apparent bedding. In the unaltered Buntsandstein discs as well as in the Rüthener Grünsandstein it was not possible to identify the orientation of the bedding on the sample scale.

The results for specimens of block SRM6-MI-52 show that the splitting tensile strength is on average more than twice as high if the bedding of the rock is oriented perpendicular to the load (Table 5.3). If samples are oriented with an angle of 45° towards bedding, the splitting tensile strength is around 50% higher. The tensile splitting strength for samples along bedding is around 0.27 ± 0.06 MPa. The difference in the maximum applied stress and the overall behavior of the samples during the Brazil test with respect to the bedding towards the direction of the load can be observed in Figure 5.6, with 3 exemplary test results from block SRM6-MI-52.

Overall, the sample blocks of the unaltered Buntsandstein SBS6-BD-52 and SBS6-BD-53 show very similar results amongst each other. Specimen discs cored in Z-direction have a splitting tensile

strength of about 2.7 MPa. Cores from the X-direction have lower values in general, as seen in Table 5.3.

Samples from the Rüthener Grünsandstein show a splitting tensile strength between 2.4 and 2.6 MPa. The fracture toughness of sample from block SRM6-MI-52 along bedding lies around 0.26 ± 0.06 MN/m$^{1.5}$. The average fracture toughness K_{IC} perpendicular to bedding is significantly above this value with 0.45 ± 0.04 MN/m$^{1.5}$. Compared to these results, samples placed with a 45° angle of the bedding towards the direction of the applied force showed intermediate values with an average K_{IC} of 0.38 ± 0.05 MN/m$^{1.5}$ (Table 5.3).

The unaltered Buntsandstein samples from the X-direction indicate lower values in general. As an example, specimens from block SBS6-BD-53 show an approximately 25% lower fracture toughness in X-direction compared to the Z-direction. In turn, block SBS6-BD-52 has only slightly different results for the average fracture toughness with 0.24 ± 0.03 MN/m$^{1.5}$ (X-direction) compared to 0.25 ± 0.04 MN/m$^{1.5}$ (Z-direction).

The Rüthener Grünsandstein samples from block SRG6-RU showed the lowest fracture toughness on average (Table 5.3). Results between specimens in X- and Y-direction are equal in terms of fracture toughness, both having a K_{IC} of 0.22 ± 0.01 MN/m$^{1.5}$.

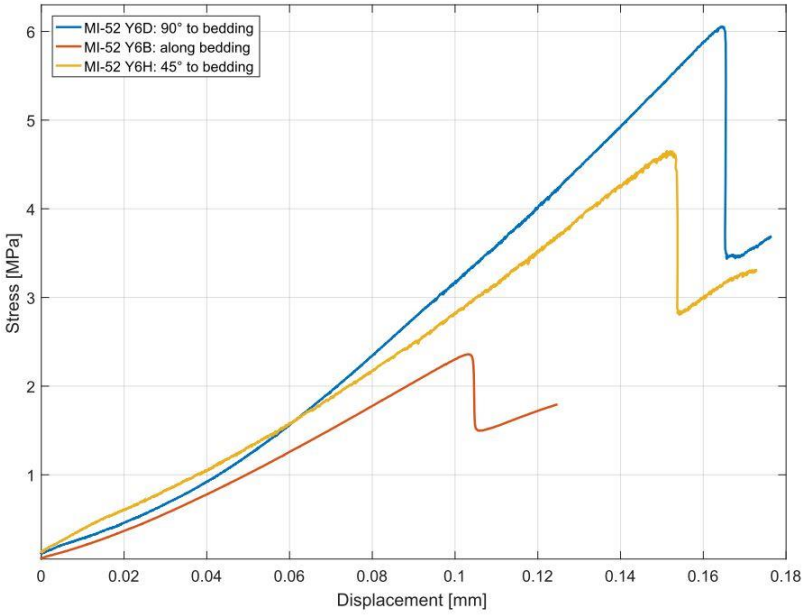

Figure 5.6: Results for 3 samples from block SRM6-MI-52 with different orientations of the bedding towards the direction of the applied load.

Table 5.3: Brazilian test results showing mean and standard deviation (SD) of the values displayed in Appendix G. σ_t = splitting tensile strength, F_{max} = maximum applied load, P_{min} = local minimum load, K_{IC} = fracture toughness.

Sample block	Core direction	Orientation of applied load towards bedding	$\sigma_t \pm$ SD [MPa]	$F_{max} \pm$ SD [kN]	$P_{min} \pm$ SD [kN]	$K_{IC} \pm$ SD [MN/m$^{1.5}$]
SBS6-BD52	Z	n.a	2.7 ± 0.4	2.0 ± 0.4	1.5 ± 0.2	0.25 ± 0.04
	X	n.a	2.5 ± 0.3	1.7 ± 0.1	1.4 ± 0.1	0.24 ± 0.03
SBS6-BD53	Z	n.a	2.7 ± 0.3	2.0 ± 0.2	1.3 ± 0.1	0.24 ± 0.01
	X	n.a	2.0 ± 0.1	1.5 ± 0.1	1.1 ± 0.05	0.19 ± 0.01
SRM6-MI-52	Y	perpendicular	6.2 ± 0.5	4.4 ± 0.3	2.5 ± 0.2	0.45 ± 0.04
	Y	along	2.7 ± 0.6	2.0 ± 0.5	1.5 ± 0.4	0.26 ± 0.06
	Y	angular	4.8 ± 0.6	3.1 ± 0.4	2.0 ± 0.3	0.38 ± 0.05
SRG6-RU	Z	n.a	2.4 ± 0.1	1.7 ± 0.05	1.3 ± 0.05	0.22 ± 0.01
	X	n.a	2.6 ± 0.03	1.9 ± 0.1	1.3 ± 0.1	0.22 ± 0.01

5.5 Triaxial Experiments

5.5.1 Pore Volume Change

Confined pressure experiments were conducted on 16 samples. Of those, 14 samples were Buntsandstein specimens and two were from the Bentheim sandstone and Rüthener Grünsandstein in order to compare the properties. The samples have been loaded in steps up to a maximum of 50 MPa effective hydrostatic pressure. With an increase in pressure, all samples show volumetric compaction. The relative error of the measurements is given by the accuracy of the pumps (flow rate accuracy ± 0.3% mL/min). The increase in radial pressure took roughly 2 min (for 5 MPa pressure increase) to 5 min (for 10 MPa pressure increase). This results in very small relative errors between $1 \cdot 10^{-4}$ and $4 \cdot 10^{-4}$% porosity.

The pressure loading and unloading of porous Rüthener Grünsandstein in Figure 5.7 shows the general porosity decrease with an increase in hydrostatic stress applied to the sample, which was also observed in other samples. Here, the initial porosity of 22.72% decreased to 22.665% at 50 MPa effective hydrostatic pressure. A slight decrease between 0.03 and 0.06% was observed in other samples. Figure 5.7 Appendix H.2 show 6 samples where a clear change in porosity has been detected. At a certain point, the radial and the axial pressure have been decreased, which resulted in an increase in pore space. In case of the Rüthener Grünsandstein the porosity does not increase in the same manner as it decreased before, indicating a permanent compaction and porosity reduction of the sample.

However, in case of the unaltered Buntsandstein sample BD-51-Y1, the compaction does not appear to be permanent. After a decrease in confining pressure, the pore volume increases again and the porosity closely matches the initial porosity at 2.5 MPa eff. hydrostatic pressure (Appendix H.2). This possibly implies a small gain in volume, as a minor volume enlargement can be expected when unloading the sample.

Overall, based on thin sections, the porosity in Buntsandstein samples from block SBS6-BD-51 decreases by approximately 2 - 4%. The initial permeability was around 23.5%. For the altered Buntsandstein SRM6-MI-50 with an initial porosity of around 14%, the porosity decreased 1 to 2% after applying up to 35 MPa effective hydrostatic pressure.

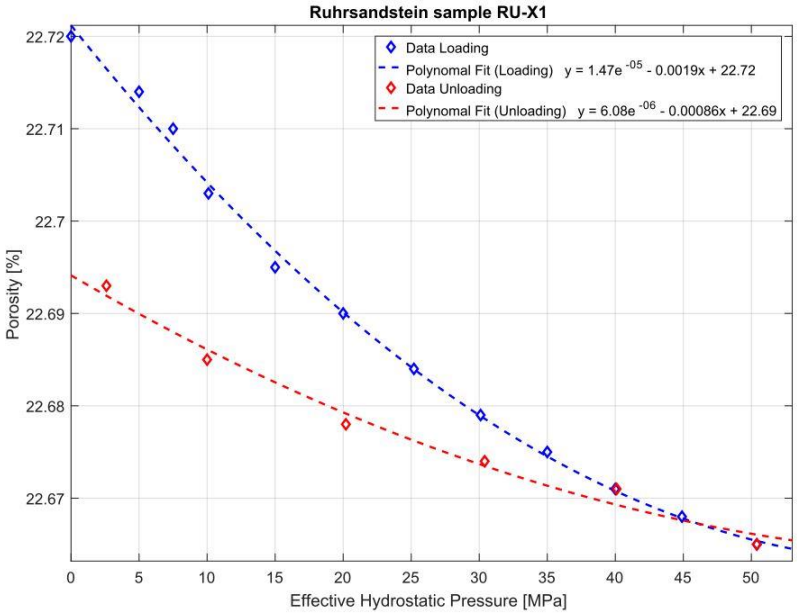

Figure 5.7: Porosity decrease and increases related to changes in effective hydrostatic pressures of the Rüthener Grünsandstein sample RU-X1. Relative errors are within the marker points.

5.5.2 Chemical Changes of Pore Fluid

As mentioned in Chapter 3.2, the samples were flushed with distilled water during triaxial testing. This allowed the quantification of the dissolution of minerals from the sample by taking water samples at different stages of the experiment. The results from measurements during the experiment and after the experiment showed that the electrical conductivity increased from 0 µS/cm (for distilled water) to a maximum of 280 µS/cm (corresponding to a NaCl salinity of around 180 ppm). The pH changed from 7 to a minimum of 6.26. Hence the dissolution into the distilled water, even after multiple days of exposure in the core, was very small. Therefore a change in viscosity of the water can be regarded as negligible (e.g., ITTC, 2011).

5.5.3 Permeability prior to Deformation

Permeability measurements performed in the triaxial apparatus during steady state flow showed that the Buntsandstein samples have great differences between each other. Table 5.4 gives an overview of the permeability of all intact samples at 2.5 MPa and 30 MPa effective hydrostatic pressure. Appendix H.5 shows the evolution of the permeability with increasing/decreasing confining pressures for samples tested in the triaxial apparatus.

Table 5.4: Average permeability at different effective hydrostatic pressures for intact samples tested in the triaxial apparatus.

Sample block	Sample	Avg. permeability k [mD] at eff. hydrostatic pressure	
		2.5 MPa	30 MPa
SBS6-BD-50	BD-50-Y1	21 ± 3	2 ± 1.2
	BD-50-Z1	3 ± 0.3	0.03 ± 0.01
SBS6-BD-51	BD-51-Y1	144 ± 5.5	103 ± 6
	BD-51-Z1	25 ± 7.5	16 ± 1.2
SBS6-BD-52	BD- 52-X1	15 ± 0.1	10 ± 0.8
	BD-52-Z1	1 ± 0.04	0.8 ± 0.08
SRM6-MI-50	MI-50-Y1	61 ± 2.5	0.7 ± 2.8
	MI-50-Y2	64 ± 2.9	0.5 ± 0.3
	MI-50-Y4	0.7 ± 0.01	0.5 ± 0.07
	MI-50-Y5	1 ± 0.08	0.8 ± 0.8
	MI-50-Z2	47 ± 3.6	0.1 ± 0.03
SRG6-RU	RU-X1	643 ± 45	327 ± 8
Bentheim sandstone		1938 ± 348	-

In general, differences were observed for cores that were tested with the fluid flow direction perpendicular or parallel to bedding. An example for such differences are samples BD-50-Z1 and BD-50-Y1 from the unaltered Buntsandstein block SBS6-BD-50. The maximum permeability along the Z-direction was 1 ± 0.04 mD at 2.5 MPa effective hydrostatic pressure. When increasing the hydrostatic pressure up to 30 MPa, the permeability decreased slightly to around 0.8 mD. In comparison, the initial permeability in the Y-direction was higher (21 ± 3 mD) and decreased to about 2 mD at 30 MPa. The corresponding graph in Appendix H.5 shows a small permeability increase at 17 MPa. This was due to a change in the flow direction, where the permeability was slightly different. Such differences can be caused by, for example, trapped air bubbles, which have not been expelled during the extensive flushing regime prior to testing. To avoid such discrepancies, flow was kept in the same direction if possible. Nevertheless, also samples BD-52-Z1 and BD-51-Z1, BD-51-Y1 show

this behavior at 25, 40 and 25 MPa, respectively, due to a change in the flow direction. In general, however, changes in permeability were only minor.

Samples from the Buntsandstein block SBS6-BD-51 also display a clear difference of flow properties between cores in Y- and Z-direction. Whereas sample BD-51-Y1 has a high initial permeability of more than 140 mD, sample BD-51-Z1 only has about 25 mD at 2.5 MPa eff. hydrostatic pressure. As seen in Figure 5.8, the permeability decreased to 103 ± 6 mD at 30 MPa eff. hydrostatic pressure. In turn, the permeability of the sample in Z-direction decreased to around 16 mD. If the pressure is released from the specimens, the permeability stays more or less constant and even slightly decreases further (Figure 5.8 and Appendix H.5).

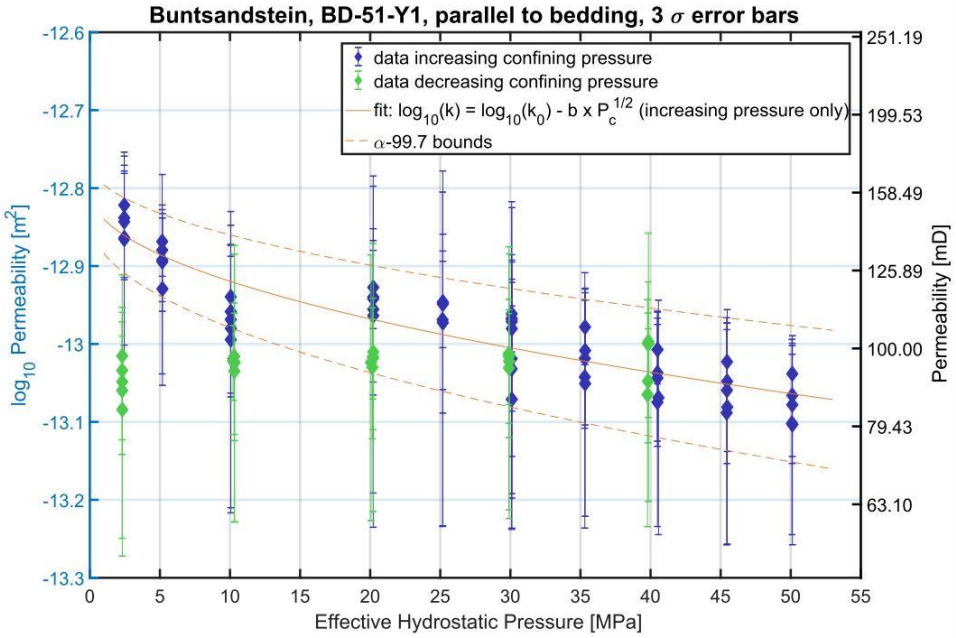

Figure 5.8: Permeability of sample BD-51-Y1 measured in the triaxial apparatus before fracturing the specimen.

Permeability values for the Buntsandstein samples from block SBS6-BD-52 are in the range of 7 to 15 mD at 2.5 MPa eff. hydrostatic pressure. The decrease at 30 MPa is around 30% in both samples. Specimen BD-52-X1 shows a small further decrease of approximately 1 mD when the confining pressure is increased to 40 MPa (Appendix H.5).

In regard, cores from the altered Buntsandstein SRM6-MI-50 have a very mixed permeability. Specimens MI-50-Y1 and MI-50-Y2 show a permeability of around 62 mD. The permeability decreases significantly by around 2 orders of magnitude when subjected to 30 MPa eff. hydrostatic pressure (Table 5.4). A similar behavior can be observed for sample MI-50-Z2. Two samples in Y-direction, MI-50-Y4 and MI-50-Y5, on the other hand, have a permeability of 1 mD and below (at 2.5 MPa eff. hydrostatic pressure), which do not change considerably at higher pressures. The second altered Buntsandstein block SRM6-MI-52 showed a permeability far below 0.1 mD, which was

determined on one sample in the triaxial machine and two more core samples in the Ruska gas permeameter. Both showed a permeability below 0.1 mD.

In comparison to the Buntsandstein samples, the Bentheim sandstone showed a permeability of 1938 ± 348 mD at 2.5 MPa eff. hydrostatic pressure. The tested Rüthener Grünsandstein has an initial permeability of 643 ± 348 mD, which decreased by 50% at 30 MPa. At decreasing confining pressures, the permeability then stayed constant at around 316 mD.

5.5.4 Shear Fractures

A number of rock samples was subjected to increasing differential stresses until the sample-failure. In result, shear fractures developed. Often a clear shear plane developed (e.g., MI-50-Y5 in Figure 5.9) as already observed in the uniaxial compression tests in Chapter 5.1. Images of various samples tested in the triaxial apparatus can be found in Figure 5.9 and Appendix H.1.1. There, the strong microstructural damage of samples MI-50-Y2 and BD-52-Z1 is depicted. In both samples, a major part of the matrix was ground up to a much smaller particle size (Appendix H.1.1).

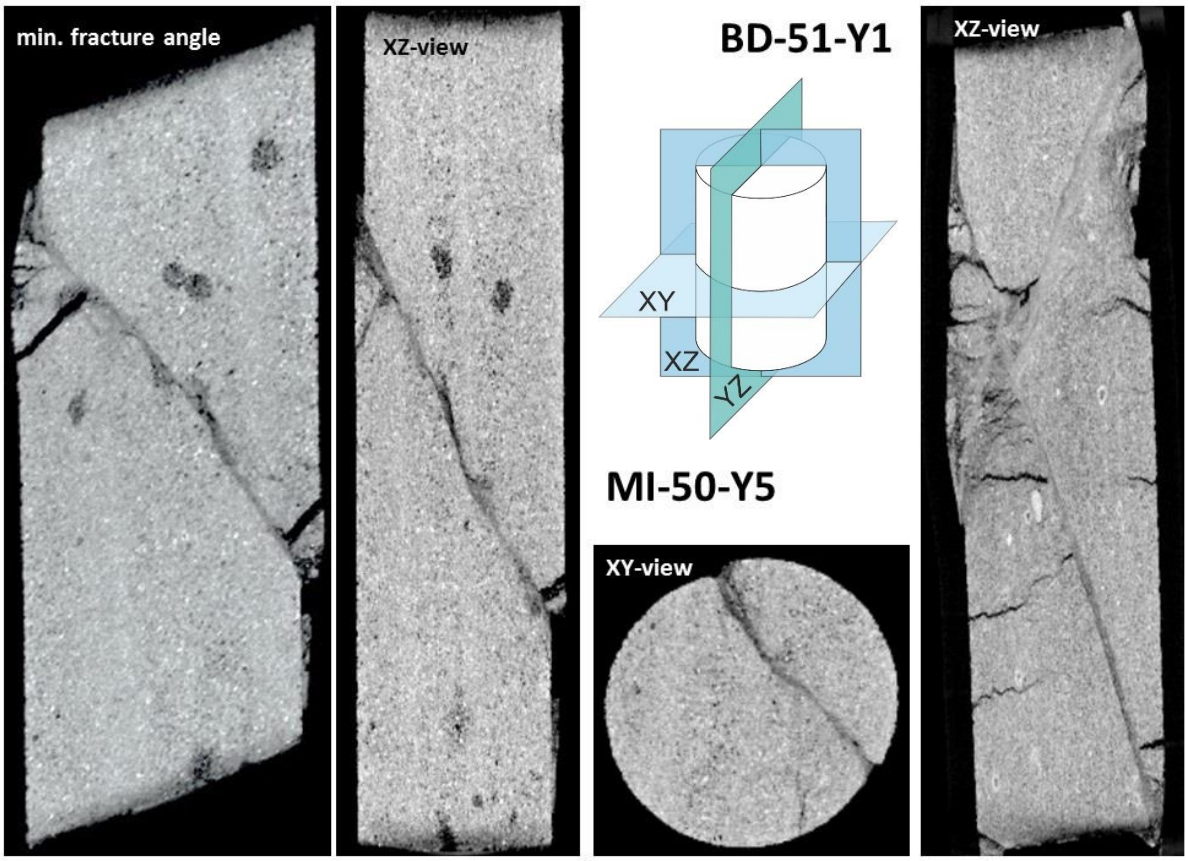

Figure 5.9: CT-scan images of the Buntsandstein samples MI-50-Y5 (left) and BD-51-Y1 (right) after shear failure in the triaxial apparatus. Samples are displayed in XY- and XZ-view. On the far left, sample MI-50-Y5 is displayed at an angle such the failure angle is minimal. The general sample height is about 75 mm, the diameter is 30 mm.

Overall, the peak compressive strength and the Young's modulus are much higher in the confined experiments. The Poisson's ratios in turn are much lower (Table 5.5). Figure 5.10 reveals that there is a clear difference between samples cored in different directions towards the bedding, as already seen in the UCS tests shown in Chapter 5.1. Overall, samples from the altered Buntsandstein block SRM6-MI-50 show less differences between the sample directions and can generally withstand higher stresses than the unaltered Buntsandstein samples. Figure 5.10 and Table 5.5 indicate the difference in ultimate peak strength depending on the sample direction. All samples in Fig. 5.10 were fractured at the same eff. hydrostatic pressure of 30 MPa.

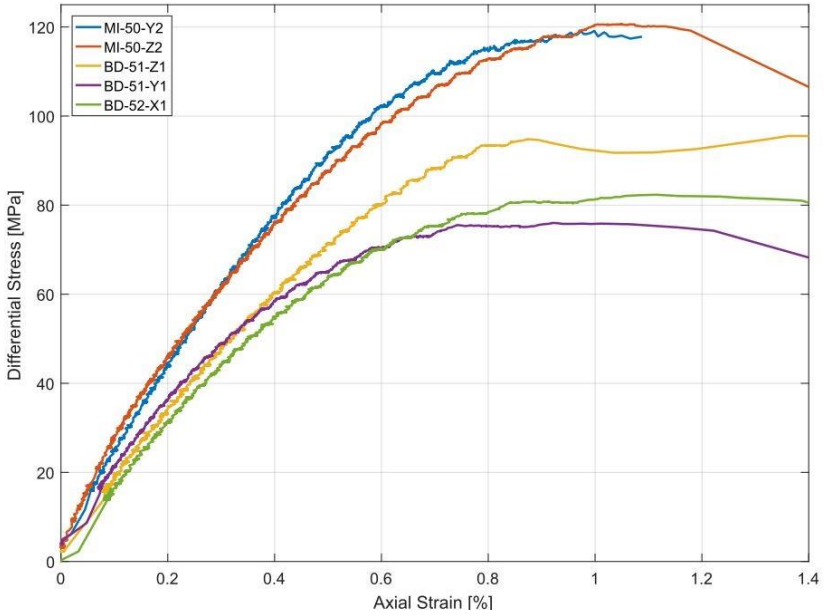

Figure 5.10: Stress-Strain curves for five Buntsandstein samples that were fractured at 30 MPa eff. hydrostatic pressure in the triaxial apparatus.

Furthermore, Appendix H.4 and Table 5.5 show the differences in peak compressive strength as well as Young's modulus and Poisson's ratio for sample cores drilled in the same direction towards bedding in the altered Buntsandstein block SRM6-MI-50. The data suggest that higher confining pressures result in higher peak compressive strengths of the samples as well as higher Young's moduli, whereas the Poisson's ratios become smaller. Samples cored in Z-direction have generally a higher peak compressive strength and a lower Poisson's ratio compared to samples from the same block cored in Y- or X-direction.

Table 5.5: List of the peak compressive strength and the elastic moduli for samples deformed at a certain confining pressure in the triaxial apparatus. σ_3 = confining pressure, σ_1 = peak compressive strength, E = Young's modulus, ν = Poisson's ratio.

Sample block	Sample	Core direction	σ_3 [MPa]	σ_1 [MPa]	E [GPa]	ν [-]
SBS6-BD-51	BD-51-Y1	Y	30	106.0	17.6	0.20
	BD-51-Z1	Z	30	125.5	15.7	0.17
SBS6-BD-52	BD-52-X1A	X	30	109.3	15.7	0.18
	BD-52-Z1	Z	40	137.2	15.9	0.23
SRM6-MI-50	MI-50-Y4	Y	5	71.4	15.3	0.37
	MI-50-Y5	Y	10	94.8	15.6	0.36
	MI-50-Y1	Y	15	111.5	19.9	0.31
	MI-50-Y2	Y	30	149.1	19.3	0.25
	MI-50-Z2	Z	30	150.6	25.9	0.16

With an increase in the differential stress, microcracks occur in the sample. At the yield point, the occurrence of micro-/macro-cracks can be associated with an increase in water flow into the sample. As an example, Figure 5.11 shows the increase of permeability with an increase in differential stress. The permeability has been calculated with the measured pore pressure difference and the flow rate, which is demonstrated in Appendix H.3 for sample MI-50-Y1. The flow started to increase at around 0.4% axial strain. At more or less yield strength of the sample the specimen became much more permeable. With a further increase in stress, the flow into the sample and the permeability increased significantly. When the sample failed, as seen for sample MI-50-Y1, the flow rate shot up and the measurement stopped. Appendix H.3 shows the associated permeability at different differential stress.

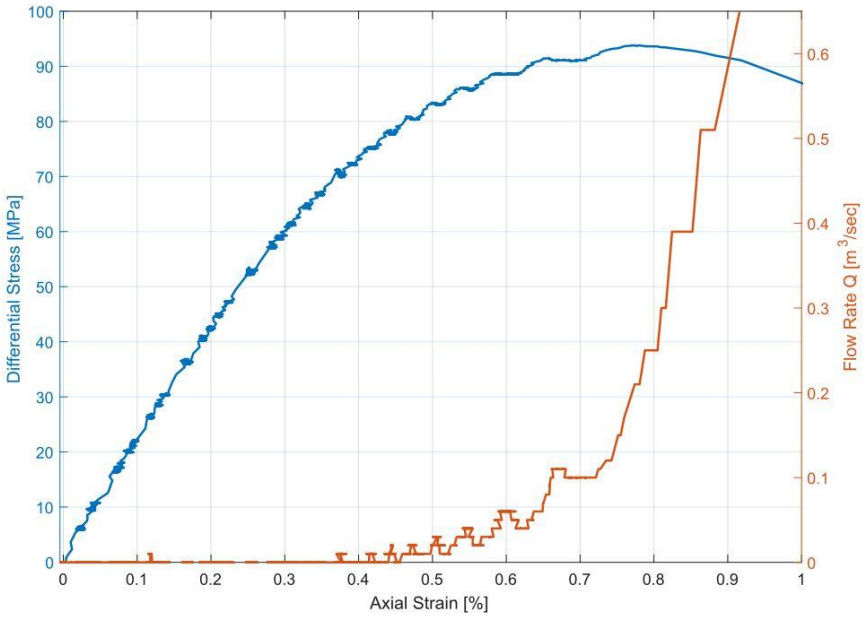

Figure 5.11: Development of the flow rate with increasing differential stress for sample MI-50-Y1.

After shear failure of each sample, the permeability was measured again at different steps of confining pressure for samples where the jacket remained sealing. The fractured samples from block SBS6-BD-51 show a large decrease in permeability (around a factor of 20). The permeability decreased even further at higher confining pressures. In case of sample BD-51-Y1, the last measured permeability at 2.5 MPa eff. hydrostatic pressure was 90 mD and reduced to 7 mD (Figure 5.8 and Figure 5.12). A similarly drastic reduction is seen in sample BD-52-Z1 (Appendix H.5). Sample MI-52-Y3B, which initially showed a permeability below detection limit, had a much higher permeability after shear deformation of the sample. However, the permeability after deformation was still below 1 mD. For rock specimens from the other altered Buntsandstein block SRM6-MI-50, shear fractures had no major effect on the permeability. In case of the samples MI-50-Y4 and MI-50-Y5, the permeability was still below 2 mD. Further sliding of the broken sample along the shear plane showed no significant change in permeability (Appendix H.5). The cataclasis and the post-experiment microstructure after the experiments can be observed in Chapter 4.3.

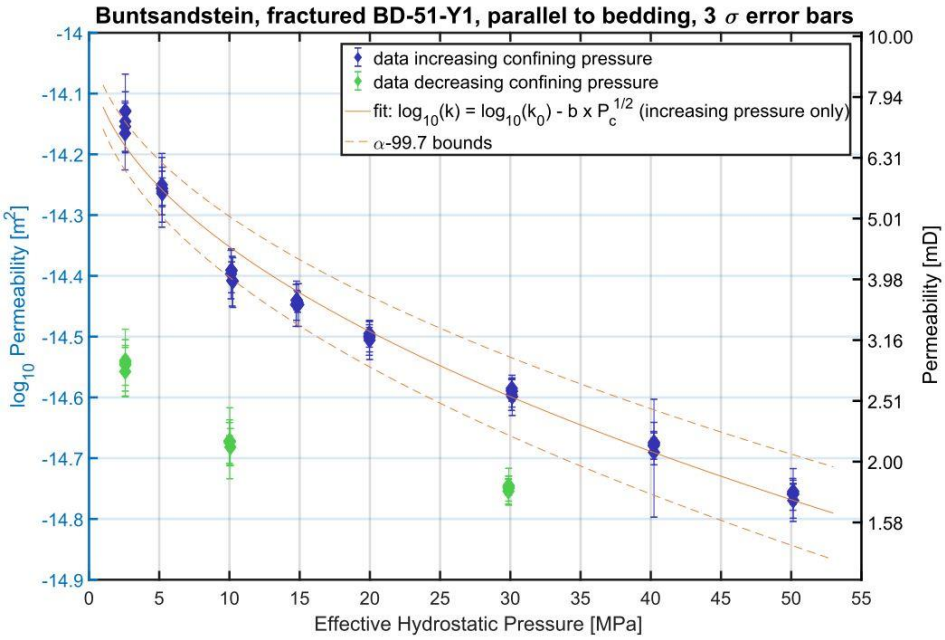

Figure 5.12: Permeability of sample BD-51-Y1 measured in the triaxial apparatus after fracturing the specimen.

5.5.5 Tensile Fractures

Tensile fractures were created for four samples of the low-permeability Buntsandstein block SRM6-MI-52 with the "Mode I frackers". All samples were deformed at 2.5 MPa effective hydrostatic pressure. Appendix H.1.2 displays CT-images of the four broken samples (MI-52-Y3A, MI-52-Y3B, MI-52-Z6 and MI-52-Z8). For MI-52-Y3A, the steel wedges of the Mode I frackers are visible at the top and bottom in the XZ-view. In samples cored in X- or Y-direction, the crests of the steel wedges were aligned parallel towards the bedding, resulting in a fracture opening more or less parallel to the

bedding (Appendix H.1.2). On the top, further cracks often distribute sideways. These cracks most likely occurred during a further increase in axial load, when the steel wedges pushed deeper into the sample. It is therefore assumed that these cracks occurred in the last stage of the experiment, when high axial stresses were imposed. Cracks distributed sideways rather represent shear fractures instead of opening fractures. This is more clearly visible in Figure 5.13, which shows the fracture planes from a rendered 3D volume from sample MI-52-Z8. The large vertical fracture that divides the sample is the created opening fracture, whereas the smaller, tilted fracture is the fracture caused by shearing of the top right part of the specimen. As indicated in the CT-scan images, the fracture opening varies along the fracture plane (see e.g., Figure 5.13).

The bedding in the sample is recognizable on the left image. The crests of the steel wedges are oriented perpendicular to the bedding.

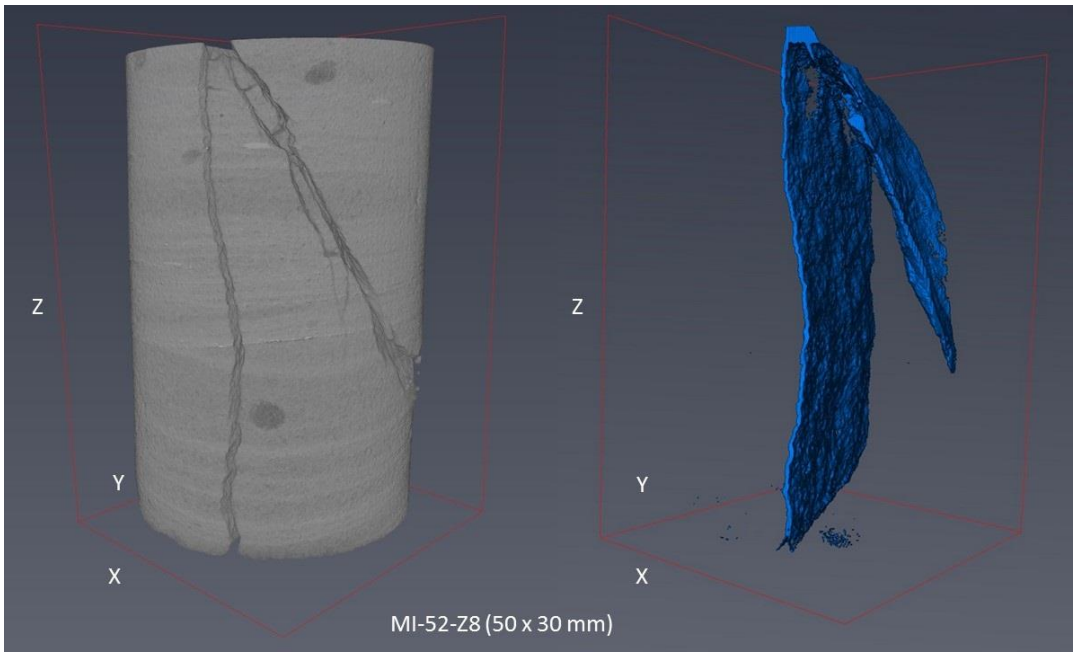

Figure 5.13: Rendered 3D volume (left) from sample MI-52-Z8 with a sample height of 50 mm and a diameter of 30 mm. On the right are the major fractures (blue) extracted from the 3D volume.

Figure 5.14 displays the calculated fracture aperture versus the associated permeability for samples MI-52-Y3A and MI-52-Z8. After deformation, sample MI-52-Z8 has an average permeability of 3.2 mD at 2.5 MPa eff. hydrostatic pressure, whereas hardly any flow through the sample could be observed beforehand. Permeability measurements of the intact sample MI-52-Y3B in the triaxial apparatus showed that this type of sandstone is almost impermeable.

In contrast, the permeability of sample MI-52-Y3A is high after creating an opening fracture (Figure 5.14). At an apparent aperture of 400 µm of a single fracture the permeability is as much as 450 mD. Widening the fracture by around 100 µm increased the permeability by a factor of 2 to 3. This

permeability increase with a widening of the fracture was also observed in sample MI-52-Z8, where the permeability more than doubled for a 50% increase in fracture aperture (Figure 5.14).

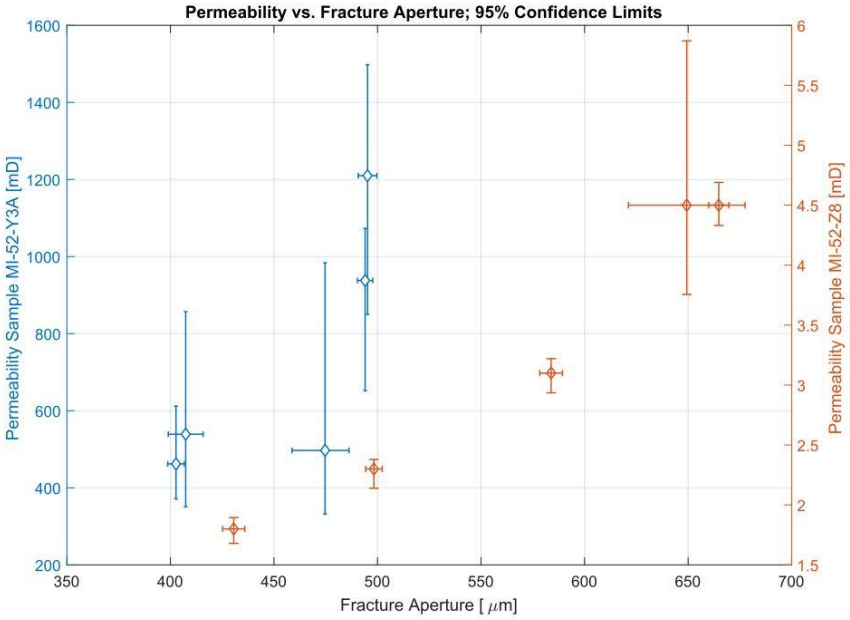

Figure 5.14: Fracture aperture versus associated permeability for sample MI-52-Y3A and MI-52-Z8. The fractures were caused by the Mode I frackers in the triaxial apparatus under 2.5 MPa confining pressure.

For samples MI-52-Y2B and MI-52-Z6, a permeability above 1000 mD was measured. Sample MI-52-Y2B has an average permeability of 2073 mD at an aperture of 2776 µm, whereas the permeability of sample MI-52-Z6 is 1112 mD at an apparent aperture of 1294 µm. The permeability decreased significantly with a 50% decrease in apparent apertures. Sample MI-52-Y2B has only around 38 mD at 1208 µm aperture and the permeability of MI-52-Z6 is about half with 510 mD at 655 µm (Appendix H.6 and H.7). The relative errors of the measurements in samples with a high permeability are rather large compared to measurements in less permeable specimens. This is due to the higher flow rates required to measure the permeability at larger apertures.

For each aperture-fracture relationship measured for all four samples, an exponential fit has been applied. The fits were averaged to one exponential fit to map the general trend. The trendline equations for each sample as well as the averaged exponential trendline equation are shown in Appendix H.8. The result of the averaged trendline shows that the permeability increases by a factor of roughly 2 with a widening of the apparent aperture by 100 µm up to apertures of 600 µm. Since the increase is exponential, this factor increases at higher apertures.

5.5.6 Dependence of Fracture Strength on Stress

To graphically represent the relationship between stress and fracturing of the formation/samples, Mohr's stress circles were constructed with the results from the unconfined compression tests and the triaxial experiments. As an input, the peak compressive stress σ_1 and the confining pressures (minimum principal stress σ_3) were used, as well as the angles of the shear plane towards σ_1, where rupture occurred. The angle between σ_3 and the failure plane is θ. The failure angle has been taken as 35° towards σ_1, which was more or less the angle observed in the tests on numerous samples. However, this angle varies for each sample and is therefore only an approximation. The fracture angle θ can also be obtained from the following equation:

$$\theta = 45 - 0.5 \cdot \varphi \qquad \textbf{(21)}$$

where φ is the angle of internal friction (see Figure 5.15). The tangent of φ is the coefficient of internal friction. As observed in Figure 5.15 and Appendix H.9, increasing the confining pressure subsequently increases the strength of the rock. The shear failure for each circle/sample is illustrated with a diamond-shaped point in the graphs. The angle of internal friction φ is 30.3° for SRM6-MI-50 (see Figure 5.15), 29.4° for SBS6-BD-51 and 26.5° for SBS6-BD-52. The cohesive strength, τ_0, for those samples is 14.1 MPa, 7.8 MPa and 9.5 MPa, respectively. Based on these results, the theoretical angle where shear fractures form is about 31° according to Equation 21, which is comparable to the observations made in the post failure core analysis.

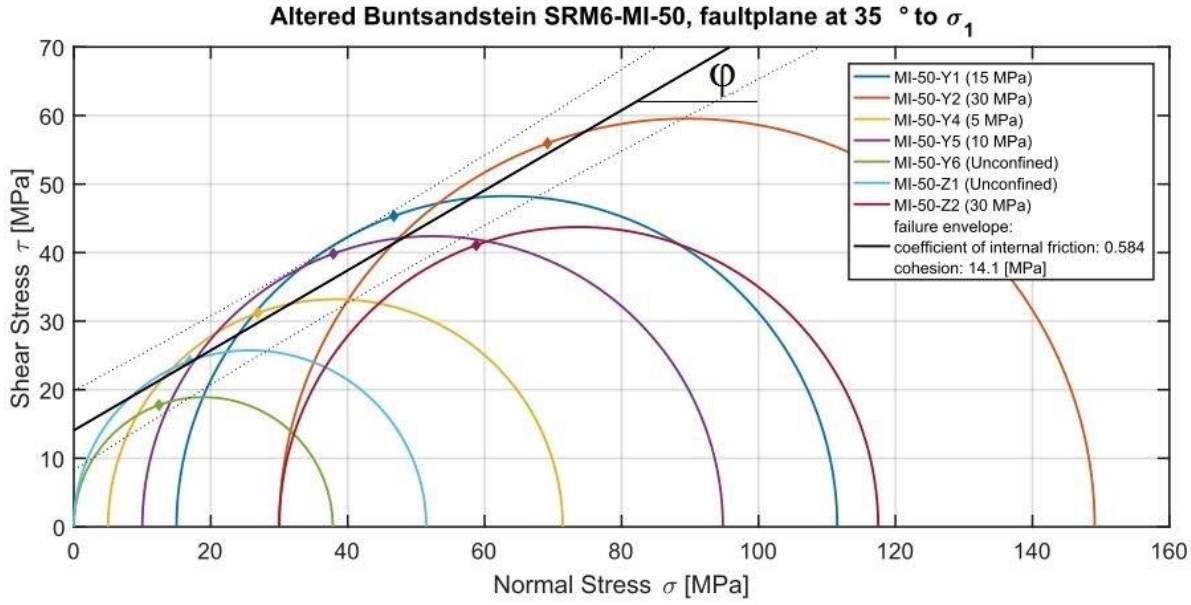

Figure 5.15: Mohr's stress envelope for the altered Buntsandstein block SRM6-MI-50 with 50% error bounds. Shear failures are illustrated as diamonds. Effective hydrostatic pressures at the moment of failure are listed in brackets in the legend for each experiment. The angle of internal friction (φ) is indicated. No rock anisotropy is assumed. The shown failure criteria only gives a rough estimate.

6. Discussion

6.1 Samples

6.1.1 Buntsandstein Comparison

In general, the porosity of the Buntsandstein samples varies between 10 and 20%. The dominant components are quartz and alkali-feldspar with minor amounts of phyllosilicates and clay. Due to the high quartz content, most samples can be classified as subarkose after Folk (1965).

Since the tested samples were taken from quarries in Germany, they can be substantially different from the Buntsandstein present in the West Netherlands Basin. No core samples from the Buntsandstein in the WNB have been available for testing. However, a comparison of the Buntsandstein samples tested in this thesis project can be made with rock specimens previously analyzed from wells in the WNB.

Cores from the Hardegsen Formation in well Gaag-2A (3080 - 3090 m MD) and from well Gaag-5 (3085 – 4095 m MD) were studied. Furthermore samples of the Upper Detfurth Sandstone Member from well Gaag-5 (4095 – 4104 m MD) are described.

Similar to the Buntsandstein samples tested in this study, the main components are predominantly monocrystalline quartz and alkali-feldspar. Furthermore, heavy minerals such as zircon and rutile are also present in the Buntsandstein samples from the WNB and feldspars partially show degradation and partial dissolution. Phyllosilicates and mudclasts occur in minor to trace amounts (www.nlog.nl, 2017). This is in line with the observations made for the rocks studied in this thesis.

The porosities found in well Gaag-2A are between 14 and 21%, the porosities in well Gaag-5 are 5 – 14% (www.nlog.nl, 2017). This wide range shows that the porosity can vary significantly, which was also observed in the Buntsandstein samples studied in this thesis, where the porosities were between 10 and 24%.

The dominant clay fraction found in the WNB was identified to be illite with a minor amount of chlorite by using XRD (www.nlog.nl, 2017b). The XRD analysis from the samples of this project likewise suggest illite as clay type. In the WNB, authigenic illite occurs bladed or as a fibrous rimming phase around the grains, which are the same structures as observed in the thin section analysis. The amount of illite found in both the Hardegsen Formation and the Upper Detfurth Sandstone Member are identical. The same accounts for the fractions of the quartz and feldspar, which have on average 84 and 5% wt., respectively, and are therefore similar to the samples of this project. Solely the high amount of the authigenic anhydrite at the top of the Hardegsen Formation stands out. However, none of the sample blocks available for testing was from this formation (see Chapter 4.1). Dolomite as

found in the wells Gaag-2A (mean: 4.2% of authigenic components) and Gaag-5 (mean: 4.8% of authigenic components) has not been identified in thin section analysis with a petrographical microscope or the analysis with the EPMA. However, XRD and XRF suggest the presence of dolomite of around 2.5% wt. (semi-quantitatively determined) in rock sample SRM6-MI-50 and 3.1% wt. in sample SBS6-BD-50. It should be mentioned that the quantification performed with the Software EVA Brucker Diffraction Suite has to be considered as semi-quantitative interpretation and due to the very limited amount of dolomite it indicated its occurrence only.

A study done by Purvis & Okkerman (1996) described the presence of three main types of pore-filling cements in core samples of the Main Buntsandstein, being dolomite, anhydrite and halite. In their studies the authors conclude that the cementation by anhydrite and halite had a negative effect on the permeability of the Buntsandstein. That caused an inversion of primary reservoir properties, leading to low porosities and a low permeability. In this thesis, neither anhydrite nor halite were found and dolomite is only present in a minor amount.

An important observation is the clay as pore fill of most tested Buntsandstein samples. Clays can form a cement in porous sandstones and clog up the pores, reducing the permeability drastically. If clays are transported, they can also fill fractures. That way, a change in pressure, pore-fluid chemistry or temperature can cause clay to have different effects on the overall reservoir quality (Syed et al., 2010). Illite, as the main clay type identified in the Buntsandstein samples is one of the main clay minerals. It does, compared to smectites, not exhibit high changes in volume after coming in contact with fluids. Taylor & Smith (1986) estimate the average free swelling of illite to be around 90% in reference to the initial volume. In comparison, Na-smectite can increase in volume by 1500%. Therefore it can be expected that the swelling of illite will have no major impact on the overall quality of a potential geothermal Buntsandstein reservoir. A relocation of illite into fractures, when geothermal fluids are circulating in the reservoir, might not be significant, as the only samples showing a higher illite content are very low permeable sandstones (blocks SRM6-MI, permeability below 0.01 mD). Therefore the clay content with a maximum of around 6% does not appear to clog the pores as seen in the thin sections and the EPMA analysis. Without a connection of the pores or only little sweep possible, clay minerals will essentially not be able to relocate, as they remain trapped in the pore space. However, if the pores are well connected, which can be the case in, for example, the damage zone of a fault, the clay can be swept out of the pores and accumulate elsewhere.

6.1.2 Weathering

One reason the sandstones do not exhibit a high amount of cementation could be due to the sampling procedures. Blocks might have been taken relatively close to the surface of the formation in the quarries. Therefore blocks from which the samples were drilled could have been affected by

weathering. Meteoric water entering the pore space could have dissolved a certain amount of minerals present in the pore space. The weathering might lead to changes in the mechanical properties of the rocks (Mosch, 2008). This might lead to an underestimation of the physical rock properties. In case of hydraulic stimulation of, for example, the Buntsandstein in the WNB, the predicted deformation pressure can be underestimated.

6.2 Uniaxial Compression Tests

The unconfined compressive strength (UCS) and elastic moduli are important parameters to determine in sedimentary rocks, as they are often used as an input for modeling or geomechanical characterizations. They can, for example, help to asses sanding potential, solve problems concerning wellbore instabilities, well drilling, reservoir depletion or stress alteration (Chang et al., 2006; Li & Fjær, 2012). Additionally, they are important input parameters for controlled hydraulic stimulation measures.

The test results of the unconfined compression test vary considerably between the samples from the Buntsandstein. As seen in the mechanical properties, unaltered Buntsandstein samples have on average a lower ultimate strength than altered Buntsandstein samples. Within the SBS6-BD blocks the average strength varies significantly between 55 and 27 MPa. Also the altered Buntsandstein blocks (SRM6-MI) are very different in terms of average porosity and mechanical parameters measured (Table 6.1). A relationship between porosity and ultimate strength (σ_{max}), however, cannot necessarily be made, as seen in Table 6.1. Here, for example, block SBS6-BD-54 has the lowest ultimate strength from the unaltered blocks, even though the porosity is lower than other blocks such as SBS6-BD-51.

Table 6.1: Average porosity and mechanical properties measured for various sample blocks with the helium pycnometer and the unconfined compression test. The standard deviation (SD) is given. The average values include tested samples that were drilled in different orientations towards the bedding (X-, Y-, Z-direction). # samples = number of samples tested in the unconfined compression test; ϕ = Porosity; E = Young's modulus; ν = Poisson's ratio; σ_{max} = max. uniaxial compressive strength.

Sample block	# samples	ϕ ± SD [%]	σ_{max} ± SD [MPa]	E ± SD [GPa]	ν ± SD [-]
SBS6-BD-50	5	13.9 ± 0.2	55.2 ± 5.0	11.2 ± 0.4	0.34 ± 0.02
SBS6-BD-51	2	23.5 ± 0.5	28.1 ± 5.7	6.8 ± 1.8	0.34 ± 0.01
SBS6-BD-52	2	19.1 ± 1.2	31.5 ± 4.5	7.9 ± 1.6	0.30 ± 0.02
SBS6-BD-53	2	20.8 ± 0.5	33.6 ± 10.9	7.8 ± 2.9	0.34 ± 0.02
SBS6-BD-54	2	19.6 ± 0.9	27.3 ± 1.6	8.3 ± 0.0	0.23 ± 0.07
SRM6-MI-50	4	19.1 ± 0.6	44.1 ± 7.2	8.1 ± 2.4	0.38 ± 0.08
SRM6-MI-52	2	9.9 ± 0.4	61.2 ± 5.2	10.1 ± 0.8	0.33 ± 0.01
SRG6-RU	2	25.4 ± 1.2	14.3 ± 0.8	4.9 ± 0.1	0.09 ± 0.00

This phenomenon has already been observed on various other rocks such as the Tablerock sandstone (Lee et al., 2016). Lee et al. (2016) shows that the investigated Tablerock sandstone has a relatively high uniaxial compressive strength of 39 MPa and a Poisson's ratio of 0.2, even though the porosity was measured to be 28%. The main reason for the high strength in case of the Tablerock is the strong cementation of the grains by microcrystalline quartz. This silica cement is a result of precipitation of dissolution from circulating hydrothermal water.

The fact that an increased quartz cementation of sand grains, leading to a decrease in porosity, results in a higher compressive strength was also observed in case of the Upper Buntsandstein (Mainsandstein; Mosch, 2008). In comparison, the Buntsandstein samples tested in this thesis show hardly any cementation. Solely block SBS6-BD-50 has areas which are cemented together by alkali-feldspar minerals and a minor amount of microcrystalline quartz. On the other hand, blocks SBS6-BD-50 and SRM6-MI-52 both have the highest ultimate strength and the highest Young's modulus within their rock group and show the lowest average porosity. A linear relationship between compressive strength and porosity was described in David (2006) for Lower and Upper Buntsandstein samples. Also English (2012) indicates an empirical relationship between porosity of clean sandstones and unconfined compressive strength. This observation is based on a porosity reduction of sandstones with an increase in overburden. In the West Netherlands Basin, the overburden can have a significant effect on the compaction of the Buntsandstein. In the samples tested in this study, the compaction can be observed in the change in length and diameter. Appendix H.11 shows a comparison of the lengths and diameters of the samples before ("initial") and after ("final") subjecting the samples to effective hydrostatic pressures up to 50 MPa. Here, the length decreased between 0.001 and 0.025% compared to the initial length, the diameter decreased between 0.001 and 0.035%.

Due to the compaction, lower porosities are expected at the depths of the Buntsandstein, depending on the location in the WNB. Therefore the elastic moduli might be influenced. Elastic properties are routinely determined at unconfined, ambient conditions and might need a correction for lower porosities. Generally the Young's modulus decreases with a decrease in porosity, whereas the Poisson's ratio increases (English, 2012). Moreover, porosity is a key parameter in the mechanical behavior of the rocks, as there is often a strong correlation between porosity and permeability (e.g., Vajdova et al., 2004). In most cases, an associated permeability change due to a mechanical compaction of a porous rock is important in terms of aquifer/reservoir production (Baud et al., 2012).

In this study, a correlation between the Young's modulus (E) and the uniaxial compressive strength (UCS) is indicated in Table 6.1. The correlation between those two parameters is a common observation in most cases (Reyer & Philipp, 2014). Figure 6.1 illustrates the relationship for the

samples tested in the uniaxial compression test. The regression functions for the unaltered and the altered Buntsandstein can be written as follows:

Blocks SBS6-BD: UCS [MPa] = 5.2284 E [GPa] - 7.9604 **(22)**

Blocks SRM6-MI: UCS [MPa] = 4.3501 E [GPa] + 12.516 **(23)**

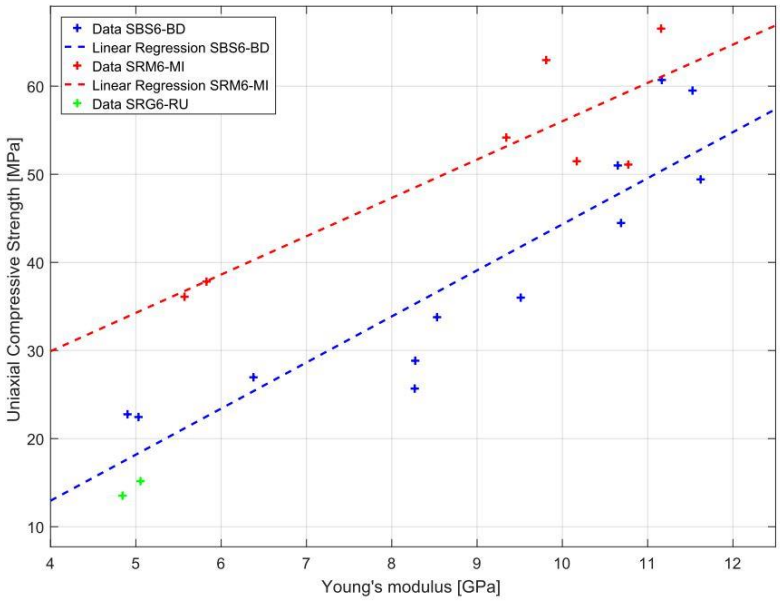

Figure 6.1: Uniaxial compressive strength versus Young's modulus for samples tested in the uniaxial compression test.

Further results of the uniaxial compressive strength (UCS) and the Young's modulus with other Buntsandstein samples are presented in studies of Reyer & Philipp (2014), David (2006), Weber & Lepper (2002) and Stück et al. (2012). Table 6.1 and

Table 6.2 present the differences between results from this work and those presented in the literature. Comparing the values shows that there is generally a wide range of properties for different Buntsandstein samples and no direct comparison can be made between most studies. Overall, samples tested by Reyer & Philipp (2014) had lower porosities and much higher Young's moduli. Results from tests with specimens of the Wesersandstein generally have a very wide range and are therefore hard to compare. Lower Buntsandstein samples from the studies of Stück et al. (2012) are comparable to the results of this study in terms of porosity range and Young's moduli results. In that study the sandstones are classified as sublitharenites of the Buntsandstein, for which a mean compressive strength of 69 MPa is mentioned. The Buntsandstein samples in this thesis are generally classified as subarkose (see Chapter 4.2) and are therefore not significantly different in terms of mineral composition. The average uniaxial compressive strength of all tested Buntsandstein samples is 43 MPa. Hence samples break under a lower load. Compressive strengths for the Miltenberg sandstone measured by Menschik (2015) are lower than values found in the study of this thesis for sandstones

of block SRM6-MI (Miltenberger sandstone). The Leistädter sandstone, from which sample blocks SBS6-BD are taken, has also been studied by Hugues et al. (2005). His results show a higher range of compressive strength values (

Table 6.2). The Rüthener Grünsandstein, which was used as a comparison, has a very low compressive strength of 14.3 ± 0.8 MPa and a very high porosity (25.4 ± 1.2%), indicating a correlation between those two factors. Therefore, a large variety of sandstones needs to be investigated, in case that the properties of the Buntsandstein found in the subsurface of the WNB has very different properties from the tested Buntsandstein samples in this study.

Table 6.2: Literature values for porosity, uniaxial compressive strength and Young's modulus of Buntsandstein samples.

Rock Type	ϕ [%]	σ_{max} ± SD [MPa]	E ± SD [GPa]	Reference
Grauer Wesersandstein (Middle Buntsandstein)	5.7 - 13.9	66.7 - 212.8	-	Weber & Lepper, 2002
Roter Wesersandstein (Middle Buntsandstein)	10.2 - 19.1	36.7 - 121.1	-	Weber & Lepper, 2002
Detfurth-Sandstone Gt1DU3	3.6	164 ± 20	37.0 ± 5.9	Reyer & Philipp, 2014
Volpriehausen-Sandstone Gt1VS2	2.8	187 ± 15	35.1 ± 2.8	Reyer & Philipp, 2014
Miltenberger sandstone	-	36	-	Menschik, 2015
Leistädter sandstone	-	66 - 75	-	Hugues et al., 2005
Lower Buntsandstein	13-20	42 - 80	-	Stück et al., 2012
Middle Buntsandstein	18	58	-	David, 2006

Regarding the uncertainties of the results from the uniaxial compression test, it was seen that certain samples show a significantly larger axial strain before reaching the elastic region (e.g., sample MI-50-Y3). A possible influence could be a misalignment of the testing apparatus with respect to the inserted sample. Additionally, the sample itself might not have been ground fully plan parallel. This can lead to an unequal load concentration on, for example, protruding grains at early stages of the experiment ("asperity deformation").

Moreover, the tangent for calculating the Young's modulus was consistently taken in the early stage of the elastic part, around 20 - 40% of the failure stress. This was necessary to avoid "asperity deformation" and alignment issues at low stress and to make sure the moduli were taken in the linear elastic region above the crack closure threshold and below the unstable crack growth threshold (Figure 6.2). Taking the same approach as Heap & Faulkner (2008), the linear elastic region was assumed to range up to about 40% of the peak stress. However, the work of Heap & Faulkner (2008) was done on granitic rocks (Westerly granite) and might not be appropriate for other rock types.

Nevertheless, the region selected for stress-strain curves for the sandstones tested in this thesis is appropriate, as it respects the elasticity of the samples. To characterize the stages of the overall failure process, a normalized stress-strain curve of sample BD-51-X1 with the approximate stages of crack development is presented according to Heap & Faulkner (2008) in Figure 6.2.

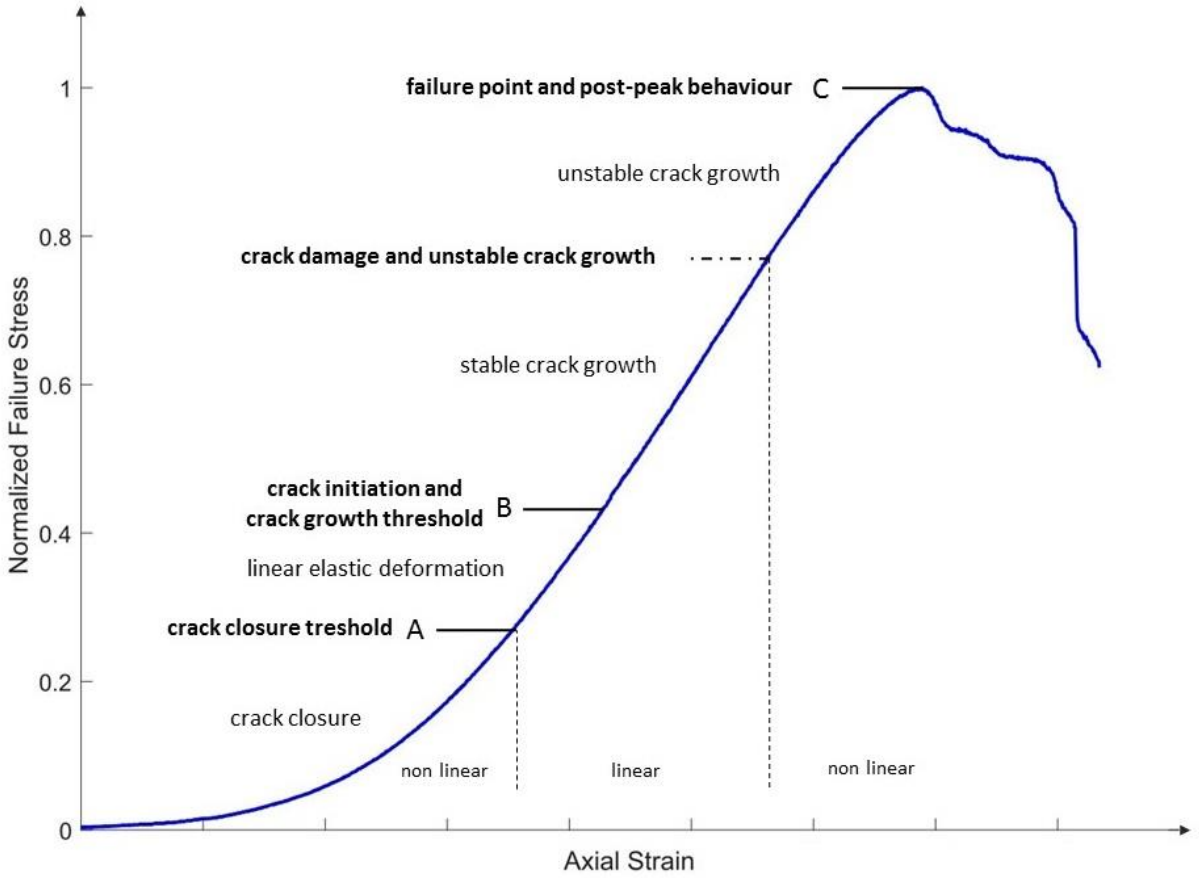

Figure 6.2: Normalized stress-strain curve of sample BD-51-X1 illustrating the approximate stages of crack development after Heap & Faulkner (2008). The stress was normalized to the ultimate compressive strength, the axial strain was normalized to the maximum value. The sample was tested under uniaxial compression.

The first stages shown in Figure 6.2 are related to the crack closure phase. Here, present microcracks in the sample are closed during axial loading. This leads to volume compaction and the measured volumetric strain is positive. At point A, the crack closure threshold is reached and linear elastic deformation follows (AB). In region AB, the elastic properties of the samples were obtained. After reaching point B, microcracks start to develop with a further load increase (Heap & Faulkner, 2008; Brantut et al., 2013). These microcracks occur as there is a stress concentration at the grain contacts, leading to Hertzian fractures, causing intergranular cracking (Baud et al., 2013). The crack growth is steadily increased and proceeds stably. At a certain point, microcracks link up when they propagate and become macro-cracks. At a further increase of the load, the crack growth becomes unstable. A noticeable volume increase can then generally be observed. Stage C marks the failure point, at which

the sample breaks (Heap & Faulkner, 2008; Brantut et al., 2013). These stages were observed in all tested samples during uniaxial loading. Due to the low stiffness of the tested Rüthener Grünsandstein, however, the explained stages are very different in terms of the fraction of the stress.
Overall, the results indicate a great variety of the Buntsandstein samples. The elastic deformation of the brittle sandstones is relatively different for the unaltered compared to the altered Buntsandstein specimens. A strong influence of the alteration process on the final uniaxial compressive strength can be expected. As the comparison with the literature values from the Buntsandstein and the results from the uniaxial compression test indicate, the variety between the Buntsandstein samples can be great. Buntsandstein layers in the WNB may be considerably weaker or stiffer (higher/lower Young's modulus), depending on the formation and the location. Therefore it is useful to analyze the mechanical rock properties of a large variety of samples from outcrop analogues. During drilling and before commencing hydraulic stimulation in the reservoir, the in-situ rock properties can be correlated with the laboratory results and the most reasonable scenario can be taken as a reference. During the drilling process, drill cores can be taken from the Buntsandstein in the WNB, which will ultimately help in the development of further wells in the local region.

6.3 Velocity Measurements

The determination of ultrasonic wave velocities is nowadays a common parameter to measure in reservoir rocks. However, information of seismic velocities from the Buntsandstein measured under similar conditions as in this thesis are scarce. Most velocity measurements are performed downhole, and tests on core samples are rather rare. Acoustic measurements in the borehole usually take a larger volume into account, and features such as fractures are included. This is the reason why velocities measured downhole are generally lower than in the laboratory and cannot be directly compared (Reyer & Philipp, 2014).

As a comparison for the lab results, recorded P-wave velocities for the Miltenberg sandstone presented by Menschik (2015) are between 500 – 1700 m/s lower than velocities found for this specific sandstone in this thesis (Table 6.3). However, no indication has been given on the orientation of the samples relative to the bedding. As the results for the velocity show in this thesis, there is a large difference between the P-Wave velocities measured perpendicular or parallel to the bedding (up to 25% difference). This effect is much smaller for S-wave velocities (max. 10% difference). Further studies by Reyer & Philipp (2014) on Buntsandstein samples show much higher velocities compared to velocities measured in this thesis. However, the porosities for the samples tested is significantly lower, which has subsequently a large effect on the velocity (Han et al., 1986).

Table 6.3: Literature values for porosity and P-wave (V_p) and S-wave velocities (V_s).

Rock type	ϕ [%]	V_p ± SD [m/s]	V_s ± SD [m/s]	Reference
Detfurth-Sandstone Gt1DU3	3.6	4906 ± 96	-	Reyer & Philipp, 2014
Volpriehausen-Sandstone Gt1VS2	2.8	4539 ± 54	-	Reyer & Philipp, 2014
Miltenberger sandstone	-	2498	-	Menschik, 2015
Berea sandstone	18.7	3346	2343*	Yew, 1978

*shear-wave measurement was done at 20.7 MPa confining pressure

Samples of Berea sandstone, which is comparable to Buntsandstein samples from block SBS6-BD-54 in terms of porosity, showed P-wave velocities in the same range (Yew & Jogi, 1978). The S-wave velocities, however, were around 13% higher than the ones measured in the BD-54 samples in studies (Yew & Jogi, 1978). Nevertheless, the S-wave velocity of the Berea sandstone was measured at 20.7 MPa confining pressure. This confining pressure most likely resulted in a compaction of the sample, which in turn led to higher velocities. Such an increase in velocity was also observed in this thesis for all samples tested in the unconfined compression tests as shown in Appendix E.5.3.

The large scatter of measured velocities can have multiple reasons. But the main one arises from the heterogeneity of all samples, which contributes most to the differences, as seen by measurements of cores drilled in different directions. Velocities also depend on porosity and mineral composition, as each mineral has a specific elastic wave velocity (Reyer & Philipp, 2014). Another influence causing differences in S-wave velocities can be trapped fluids. S-waves are not able to travel through fluids, as liquids do not have any shear strength. Hence small amounts of enclosed fluids can influence the S-wave measurements. To make sure the uncertainty of trapped liquids inside the rock core is as small as possible, samples were dried for at least multiple days.

The results from the velocity measurements can be used to give an approximate indication of micro-/macro- cracking, as the velocity changes with an increase in axial load/axial strain. The understanding of the exact occurrence of microcracking can be used to understand, for example, the processes occurring around faults (Heap & Faulkner, 2008) which are still an important geothermal drilling target, as they can show higher permeability than the surrounding formations (ENERCHANGE, 2013). The change in velocity can be tracked over the stress-strain curves, illustrated in Appendix E.5.3 and E.5.4. To correlate the velocities to certain stages of crack development, stages of crack development after Heap & Faulkner (2008) can be used (see Figure 6.2). Further along, the differences of static and dynamic moduli are useful for tracking rock

deformation processes, and increasing-amplitude cyclic loading allows to determine the microcracking contribution towards a static elastic response (Heap & Faulkner, 2008).

A comparison of the static elastic moduli from the uniaxial compression test with the dynamic elastic moduli from the ultrasonic measurements of wave velocities is presented in Table 6.4. The dynamic Poisson's ratios are comparable to the static values. Exceptions are seen for sample SRM6-MI-50, where the Poisson's ratio is much lower, with 0.26 compared to a dynamic ratio of 0.45. Moreover, the low static Poisson's ratio of 0.09 of sample block SRG6-RU is more in the range of the Buntsandstein sample for the dynamic Poisson's ratio, with values around 0.3.

The dynamic Young's modulus on the other hand is much higher than the static values derived from the stress-strain curves. On average, dynamic values are 65% higher (Table 6.4). For the Rüthener Grünsandstein block SRG6-RU, dynamic Young's moduli are even three times more than the static ones.

Table 6.4: Comparison between static and dynamic Young's moduli and Poisson's ratios.

Sample block	Sample	Core direction	Static		Dynamic	
			E [GPa]	*v* [-]	E [GPa]	*v* [-]
SBS6-BD-50	BD-50-Y2	Y	11.6	0.34	24.8	0.28
	BD-50-Z3	Z	11.2	0.34	21.5	0.33
SBS6-BD-52	BD-52-X1B	X	6.4	0.32	16.7	0.27
	BD-52-Z2	Z	9.5	0.29	17.0	0.28
SBS6-BD-53	BD-53-X2B	X	4.9	0.36	17.5	0.26
	BD-53-Z2B	Z	10.7	0.32	16.8	0.28
SBS6-BD-54	BD-54-X3A	X	8.3	0.30	21.5	0.24
	BD-54-Z2A	Z	8.3	0.17	27.9	0.23
SRM6-MI-50	MI-50-Y6	Y	5.8	0.45	20.6	0.21
	MI-50-Z1	Z	10.2	0.30	22.7	0.37
SRM6-MI-52	MI-52-Y4A	Y	9.8	0.33	25.0	0.23
	MI-52-Z7	Z	9.3	0.32	24.4	0.33
SRG6-RU-51	RU-X3	X	4.8	0.09	13.4	0.27
	RU-Z3	Z	5.1	0.09	13.5	0.21

As the comparison of the Young's moduli already might imply, a direct relation of the static and the dynamic moduli cannot be directly made. A large number of other studies report a poor relationship between the two moduli (Martínez-Martínez & Benavente, 2012; Tiab & Donaldson, 2015). In dry rocks it is not uncommon that the dynamic Young's modulus is much higher than the static modulus, and for example, a two times higher modulus is not uncommon (Chang et al., 2006; Philipp et al., 2007). Li & Fjær (2012) explain this difference by the varying deformation already present at the

grain interfaces of the rock. At increasing shear stress and during the formation of microcracks the difference is therefore supposed to increase due to newly formed cracks (Appendix I).

Uncertainties in the dynamic measurements might be due to trapped pore fluids in the specimens. However, even rocks that have generally been dried for very long periods (1 month and longer) in a heating chamber show much higher dynamic moduli. Another factor that can affect the relationship between dynamic and static moduli is the frequency dependency of the velocity. In this study, 1 MHz transducers were used. But studies reveal that frequencies in the range from 10^1-10^6 Hz only show a minor effect on the measured velocity (Ciccotti & Mulargia, 2004; Chang et al., 2006). The Poisson's ratio on the other hand is generally not affected by the frequency (Ciccotti & Mulargia, 2004). Table 6.4 shows that most dynamic Poisson's ratios measured are in the same range of the static values with some exceptions. A sensitivity analysis of the dynamic elastic moduli for differences in the first arrivals of P- and S-waves has been done. The analysis is based on a 10% change in P- and S-wave arrivals, resulting in an average velocity change of 363 m/s and 195 m/s, respectively. The result yields an average change of the Young's modulus by 1.8 ± 0.7 GPa, the Poisson's ratio changes by 0.14 ± 0.05. Hence the total change in the Young's modulus is around 7% compared to the average initial modulus. The Poisson's ratio, on the other hand, changes by 45%. Therefore an exact picking of the first arrivals is important for an accurate determination of Poisson's ratios. Since the dynamic Poisson's ratios in this thesis vary, on average, only around 5% from the static values, the accuracy of the first arrivals can be regarded as acceptable.

Even though the static and the dynamic moduli might not be directly comparable, empirical relations are useful to characterize the material responses. Deviations of the two moduli can be important indicators for fractures, voids and decay processes (Martínez-Martínez & Benavente, 2012). This is especially useful when characterizing fractured reservoirs or, for example, the effect of fracturing on the reservoirs. To better compare the two methods (static and dynamic), the dynamic modulus can be corrected by certain proposed coefficients, such as an attenuation correction factor (Martínez-Martínez & Benavente, 2012).

Since core plugs (from a geothermal reservoir) are not always available, certain velocity correlations might be useful when dealing with geomechanical problems. These correlations can be applied when dealing with similar types of rocks (Chang et al., 2006), namely the Buntsandstein in the WNB.

Freyburg (1972) developed a relationship between uniaxial compressive strength and P-wave velocity. He based his experiments on samples from the Lower and Middle Buntsandstein of the Thüringen area. The relationship is expressed as follows:

$$\mathbf{UCS = 0.035\ V_p - 31.5} \qquad \mathbf{(24)}$$

where UCS is the uniaxial compressive strength in MPa and V_p is the P-wave velocity in m/s.

Using Equation 24 with the P-wave velocities of the Buntsandstein measured in this thesis shows that the calculated compressive strength would be highly overestimated (85 – 140% overestimation; Appendix H.10) using the relationship of Freyburg (1972). An empirical relationship has been made for the unaltered Buntsandstein block SBS6-BD-50, SBS6-BD-51 and SBS6-BD-52, as these were the only blocks which showed a linear trend. For V_p, a linear fit shows a good match with the results. The shear-wave relationship on the other hand fits less good, as the data are very scattered. Both linear relationships for V_p and V_s can be expressed as:

$$\mathbf{UCS = 0.0341\ V_p - 68.451} \quad \mathbf{(25)}$$

$$\mathbf{UCS = 0.1396\ V_s - 211.49} \quad \mathbf{(26)}$$

During uniaxial testing, the velocity was calculated with increasing axial load. The data points can be fitted exponentially to set the evolution of the velocities into relation with the UCS. Figure 6.3 shows the P-wave velocity compared to the UCS. A figure showing the UCS versus the S-wave velocities is found in Appendix E.5.5, the trendline equations can be found in Appendix E.5.6.

Since the static moduli are much lower than the dynamic moduli, using the static moduli for a characterization of the elastic response of the target rock is recommended. This is mainly due to the fact that velocities of propagating fractures are rather slow in comparison to the seismic wave velocities, and therefore the dynamic elastic moduli might not be as accurate (Philipp et al., 2007). A direct characterization of the rock properties and the propagation of fracture upon hydraulic stimulation with velocity measurements also needs to take into account the presence of naturally existing fractures, voids and other heterogeneities. These have not been considered in the cores taken in the laboratory, and might lower the in-situ elastic moduli considerably. Primarily discontinuities in the formation itself change the rock mechanical properties of the target formation. For the Buntsandstein, a study by Philipp et al. (2007) reports interbedded shale layers (cm-scale) in the Middle Buntsandstein in an outcrop in Bad Karlshafen, Germany. The study shows that fracturing is essentially inhibited at the layer contacts (stress barriers). This would indicate that interbedded shale layers could be a potential fluid flow barrier and significantly influence the overall quality of a Buntsandstein reservoir. Since layering in rock formations is generally common, these can be expected for the Buntsandstein in the West Netherlands Basin and have to be taken into account when considering hydraulic stimulation. Moreover, if fractures were already present, precipitation in the fractures may have formed mineral veins that can influence the rock strength. They can, for example, act as a strong cement. On a larger scale, measured mechanical rock properties from the laboratory might therefore not be valid anymore.

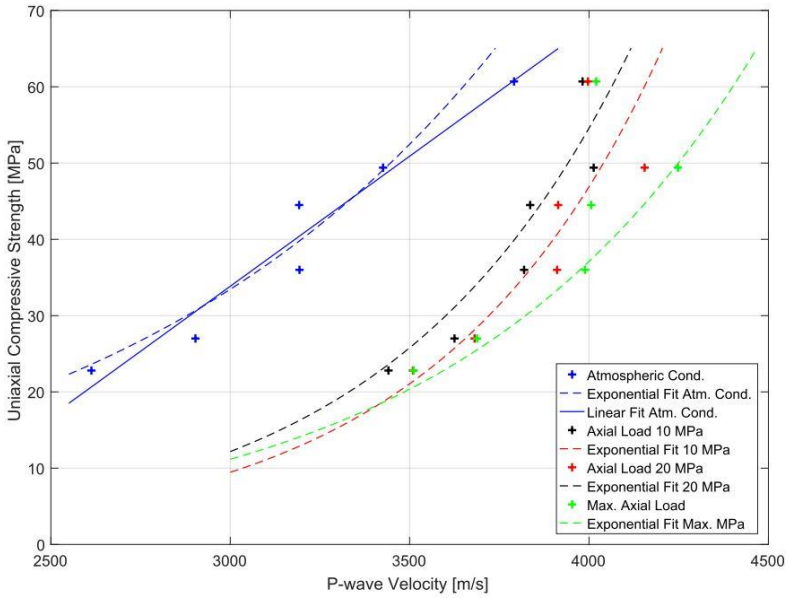

Figure 6.3: Correlation of the UCS with the P-wave velocity for Buntsandstein samples from block SBS6-BD-50, SBS6-BD-51 and SBS6-BD-52. Trendline equations can be found in Appendix E.5.6.

6.4 Cyclic Loading Test

To further investigate the microcracking in Buntsandstein samples, cyclic loading tests on Buntsandstein samples were conducted to study their response to a cyclic opening and closing of cracks. This essentially leads to cyclic fatigue microcracking (Heap & Faulkner, 2008). Increased cycles led to a degradation of the specimen over time. This is noticeable in the exponential increase of the Poisson's ratio of the samples. The increase can be related to crack damage that accumulates in the rock specimen (Heap & Faulkner, 2008). The degradation of the samples resulted in a much lower uniaxial compressive strength in case of sample MI-52-Y2C and BD-53-Z1A. Overall, the samples underwent less than 10 cycles. But it is commonly known that the amount of loading cycles significantly affects the shear strength (Xiao et al., 2011; Singh & Suresh Naidu, 2000). The Young's modulus increased with increasing cycles, which was also observed in Singh & Suresh Naidu (2000) and Ray et al., (1999). This can be related to the further compaction of the sandstones and the decrease in pore volume. For other rock types, such as granite, the Young's modulus may decrease with an increase in loading cycles due to the immediate propagation of pre-existing microcracks (Heap & Faulkner, 2008).

Observations from the cyclic loading test and the acoustic measurements during uniaxial compression testing reveal similarities in the change of elastic moduli. As seen in the cyclic loading tests, the elastic moduli increase with higher stresses. Also the dynamic elastic moduli increase at higher stresses. Both the dynamic Young's modulus and the Poisson's ratio can on average be around 35% higher than at zero axial load. Li & Fjær (2012) explain the increase of the dynamic moduli with the

effects of crack closure at low stresses. A decrease in the dynamic elastic moduli with the occurrence of newly forming micro-/macro-cracks is seen in the sample. Figure 6.4 illustrates the evolution of the dynamic Young's modulus with increasing stress for sample BD-53-X2B. For this sample the Young's modulus starts increasing, as existing cracks are closing. At around 40% axial stress the dynamic Young's modulus decreased slightly and stayed then constant up until roughly 80% axial stress. This stage aligns with the threshold for crack damage and unstable crack growth proposed by Heap & Faulkner (2008). After unstable crack growth is continuing (see Figure 6.2), the Young's modulus decreases rapidly when the sample approaches failure (Figure 6.4).

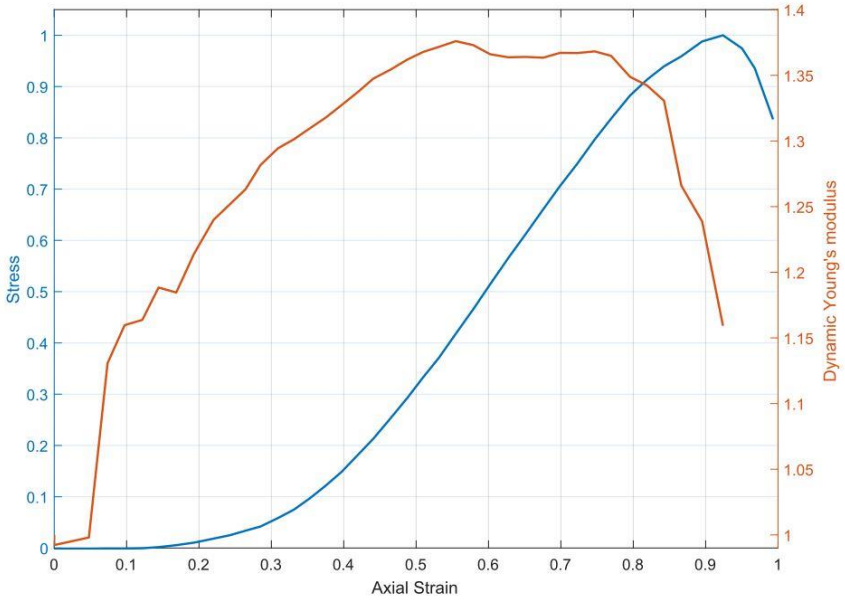

Figure 6.4: Dynamic Young's modulus and stress plotted against axial strain for sample BD-53-X2B. The stress was normalized to the ultimate compressive strength, the axial strain was normalized to the maximum value. The Young's modulus was normalized to the modulus at zero axial stress.

This change in elastic moduli shows the discrepancy between the dynamic and the static Young's moduli that increased with the increase in stress. Measuring ultrasonic velocities during cyclic loading gives more insight into the characterization of crack damage. Under triaxial stress conditions, Browning et al. (2017) concluded that further damage in dry sandstone samples only occurs if the maximum differential stress of the previous cycle is exceeded. Hence each cycle maximum sets a new threshold value for the amount of crack damage. For each cycle in their study, solely the minimum principle stress was decreased. For the Mohr's circle, this will ultimately result in a dynamic damage envelope, where the envelope approaches the failure envelope further after each additional cycle. This implies that crack damage can occur through unloading of the sample (reduction of minimum principle stress; Browning et al., 2017). Therefore, Buntsandstein samples tested may have a different amount of crack damage compared to in-situ Buntsandstein rocks in the WNB due to the probable difference in the tectonic history of the rocks. Moreover, crack damage in

fault zones can be significantly increased during unloading (Browning et al., 2017), which might enhance the local permeability. Fault zones in the Buntsandstein in the WNB should therefore be considered as a potential target for drilling geothermal wells.

Knowledge of the mechanical response of the Buntsandstein can be relevant to predict the strength of a rock that has undergone geological processes, which is important for drilling operations or blasting of rocks (Ray et al., 1999; Singh & Suresh Naidu, 2000). In case of the Buntsandstein in the WNB, this can be a primary compaction of the sediments due to the overburden in the basin. Secondly, tectonic uplift and further subsidence represent different loading cycles (unloading and loading). Due to these processes, samples might already be influenced by compaction and microcracking processes to a certain extent. Since the quarry where the samples were taken is more than 300 km away from the central WNB and is exhumed, the tested samples have most likely a very different tectonic history compared to the Buntsandstein in the WNB. This might be a possible reason why the tested samples can fail at quite different compressive strengths, even if the properties are similar. Therefore it is useful to take a large variety of samples and from quarries at different locations. Overall the results from the cyclic loading tests already give a good indication on the rock strength after compaction and decompaction of the rock. However, microcracking reduces the rock's ability to withstand higher axial stresses. This marks a difference with the Buntsandstein present in the subsurface of the WNB, where microcracking is suppressed by the confining pressure. Moreover the formation is under hydrostatic stress. To further investigate, cycling loading tests can be done in the triaxial apparatus to mimic the stress alteration under conditions close to in-situ. Moreover, CT-scans after each cycle can give a detailed insight into the development of new cracks and the linkage of microcracks can be studied.

6.5 Indirect Tensile Strength Test

In total, the indirect tensile strength (or "splitting" tensile strength; T_0) results showed a good correlation amongst each other and specific trends for certain orientations of the bedding towards the applied load. Samples of the Rüthener Grünsandstein (block SRG6-RU) have a tensile strength in the same range as the unaltered Buntsandstein samples (blocks SBS6-BD). Even though the porosity is generally higher, this does not seem to be represented in the tensile strength. In contrast, the altered Buntsandstein specimens (block SRM6-MI-52) tested have a significantly higher T_0 and the orientation of the sample played an important role. Differences between the orientations are also shown for Buntsandstein samples tested by (Reyer & Philipp, 2014). For the two presented Buntsandstein samples in Table 6.5 it is, on the other hand, seen that the standard deviation is quite

large. The difference between samples with an axial load parallel to bedding and perpendicular to bedding is rather small.

The tensile strength of the unaltered Buntsandstein samples is very comparable to results from Roxborough & Phillips (1975), who found a T_0 of 2.64 MPa.

Literature values presented for the Ruhrsandstein in Table 6.5 are 5 to 6 times higher than the tensile strength measured for block SRG6-RU (Molenda et al., 2013). This again shows the strong differences that sandstones can generally have. The Berea sandstone, which should have porosities in the range of 19% (see Table 6.3), has a more than 40% higher indirect tensile strength than tested samples from the unaltered Buntsandstein with similar porosities (Table 6.5; ASTM, 2001). Tested Bebertal sandstones, which have porosities in the range of the altered Buntsandstein (Table 6.1), show results in a similar range. Sample from block SRM6-MI-52 have an average T_0 of 4.6 MPa (regardless of the bedding orientation towards the load), whereas the Bebertal sandstone has a tensile splitting strength of 4.1 ± 1.2 MPa (Molenda et al., 2013).

Table 6.5: Literature values for porosity and indirect tensile strength (T_0).

Rock Type	ϕ [%]	T_0 ± SD [MPa]			Reference
		Without Orientation	Par. to Bedding	Perp. to Bedding	
Detfurth-Sandstone Gt1DU3	3.6	n.a.	9.3 ± 2.7	10.2 ± 0.7	Reyer & Philipp, 2014
Volpriehausen-Sandstone Gt1VS2	2.8	n.a.	7.0 ± 1.7	8.3 ± 1.2	Reyer & Philipp, 2014
Buntsandstein	-	2.6	-	-	Roxborough & Phillips, 1975
Ruhrsandstein	4.4	13.2 ± 2.1	-	-	Molenda et al., 2013
Berea sandstone	-	3.9	-	-	ASTM, 2001
Bebertal sandstone	8.3	4.1 ± 1.2	-	-	Molenda et al., 2013

Often, the brittleness index is used to estimate the fracture toughness for the Mode I failure criterion (K_{IC}), as it is easier to obtain in the laboratory (Kahraman & Altindagm, 2004). However, the rock tensile strength determination with the Brazilian test provides a convenient method to set up correlations between the rock tensile strength and the fracture toughness (Guo et al., 1993). Results of K_{IC} obtained in this thesis were approximated with a correlation from Guo et al. (1993) and generally yield lower values compared to the sandstone tested in their study, which found an average K_{IC} of 0.67 MN/m$^{1.5}$. But the properties of the given sandstone are not clear, as Guo et al. (1993) do not give further details on the rock properties. In comparison with the Berea sandstone the K_{IC} values

found are very similar to the ones obtained for the unaltered Buntsandstein with similar porosities. Their K_{IC} is around 0.23 ± 0.02 MN/m$^{1.5}$, whereas the Berea sandstone has a K_{IC} of 0.28 MN/m$^{1.5}$ (Atkinson & Meredith, 1987). The K_{IC} found by Atkinson & Meredith (1987) for the Ruhrsandstein illustrates the great variety that can be found in sedimentary rocks. In their studies they mention a fracture toughness of 1.02 – 1.39 MN/m$^{1.5}$, which is very high compared to the Buntsandstein samples.

Overall, this method for obtaining the fracture toughness can be regarded as useful and fast. The obtained fracture toughness can be used for applications concerning rock propagation and will be a good approximation for models. However, since this method is solely based on the correlation and study of Guo et al. (1993), the compatibility for a wider range of rock types still has to be proven and should be further investigated. For proving the consistency of the results, the crack initiation and the propagation of the crack with increasing load can be recorded with, for example, a high-speed camera. Knowing the crack length allows to make a correlation between the stress intensity factor and the crack length, which in turn yields more consistent results for calculating the Mode I fracture toughness. Since the fracture toughness of sandstones is also dependent on the temperature and the water saturation of the rock (Jung et al., 2001), further studies can be done on the behavior of the Buntsandstein under different conditions. This is useful, since the in-situ conditions are not similar to the experimental conditions of the indirect tensile strength test, which can give significantly different results. For the hydraulic stimulation of a potential Buntsandstein reservoir in the WNB, the knowledge about the fracture toughness is very important, as an overestimation of the tensile strength of the rock can lead to excessive pressures applied to the formation. As a result, uncontrolled fractures may cause damage to the reservoir formations or the reservoir seal, which may decrease the overall reservoir quality.

6.6 Triaxial Experiments

6.6.1 Mechanical Changes

Triaxial tests indicated that the confining pressure has a significant effect on the compressive strength and the elastic moduli of siliciclastic sedimentary rocks. As an example, the peak compressive strength of samples from block SBS6-BD-51 increased by a factor 4 – 5 at 30 MPa confinement in comparison to the unconfined uniaxial experiments. The Young's modulus increased by a factor of 2 – 3 and the Poisson's ratio decreased by around 1/3. Similar observations in terms of changes in compressive strength and elastic moduli were made by various other studies (e.g., Reyer & Philipp, 2014; Dong et al., 2010; Vajdova et al., 2004).

The peak compressive strength seems to correlate linearly with the confining pressure in case of sample block SRM6-MI-50, which is visible in the Mohr failure envelops presented in Chapter 5.5.6. Experiments done at a constant loading rate deliver a good first-order approximation of the peak compressive stress.

After reaching the peak compressive strength during triaxial compression tests, induced Mode II fractures allowed the calculation of the cohesion and the coefficient of internal friction. Typical for coarse grained sediments, the cohesive strength is rather low, whereas the friction angle is relatively high.

In comparison to the Berea sandstone, the Buntsandstein samples show a similar friction angle of around 30°. The cohesive strength, on the other hand, is more than 2 times lower for the Buntsandstein samples, as indicated in Table 6.6. The less porous Pottsville sandstone, for comparison, has a cohesive strength of around 15 MPa, which is similar to the altered Buntsandstein SRM6-MI-50).

Table 6.6: Results and literature values for porosity (ϕ), cohesive strength (τ_0) and friction angle (φ) for various rocks. SD = standard deviation,

Rock Type	ϕ ± SD [%]	τ_0 [MPa]	φ [°]	Confining pressure range [MPa]	Reference
Buntsandstein (block SBS6-BD-51)	23.5 ± 0.5	7.8	29.4	0 - 33	this study
Buntsandstein (block SBS6-BD-52)	19.1 ± 1.2	9.5	26.5	0 - 43	this study
Buntsandstein (block SRM6-MI-50)	19.1 ± 0.6	14.1	30.3	0 - 33	this study
Berea sandstone	18.2	27.2	27.8	0 - 200	Goodman, 1989
Pottsville sandstone	14.0	14.9	45.2	0 - 203	Goodman, 1989

Additional to τ_0 and φ, shear and normal stresses acting on a plane in the subsurface can be found for certain depths. As indicated in the Mohr circles for the Buntsandstein in Chapter 5.5.6, it becomes clear that extensional Mode I fractures can generally only occur when the principal stress σ_3 is negative (tensional). Tensional stresses in the earth's crust, however, do not exist in the subsurface at greater depth and can only occur in rare occasions (Zoback, 2007; Primarini, 2015). If there are negative differential stresses present, shear failure is the primary failure mode. To induce shear failures downhole, the induced stress needs to overcome the shear strength of the rock. To compute the theoretical shear failure, the given Mohr circles for the Buntsandstein can be used. Here, the shear stress (τ) is defined as the sum of the cohesion (c) and the product of normal stress (σ_n) and the coefficient of internal friction (tan(φ)), expressed as (Jaeger et al., 2007):

$$\tau = c + \sigma_n \tan(\varphi) \quad \textbf{(27)}$$

Thereby, the failure of a rock is controlled by the principal stresses. Including an applied pore fluid pressure, which is applied to displace the fracture planes, they can be expressed as the effective stresses, σ_i' (Jaeger et al., 2007):

$$\sigma_i' = \sigma_i - P_p \quad \textbf{(28)}$$

with i = [1, 2, 3] and the pore pressure P_p.

To extrapolate to borehole conditions, the mechanical laboratory provides a useful relationship. Together with the hydrostatic pressures present in the Buntsandstein in the WNB (see Chapter 2.8) the stresses necessary to create shear fractures can be estimated. This is not only useful when shear fracturing in the target reservoir is planned, but is also important with respect to fault planes already present in the WNB. Drilling into faults to make use of potential enhanced permeability zones needs to be studied in detail, since a collapse of the wellbore is to prevent.

In case of creating opening fractures as the preferred fracture type, hydraulic stimulation needs to be performed in the reservoir to reach economical flow rates for geothermal exploitation. To open new fractures at depth, the downhole pressure needs to exceed the breakdown pressure as well as the minimum horizontal stress, which is often referred to as the loss threshold. Knowing the tensile strength T_0 of the rock, the breakdown pressure, causing tensile failure in a saturated rock, can be expressed by the following equation (Jaeger et al., 2007):

$$P_B = 3\sigma_3 - \sigma_1 + T_0 + P_p \quad \textbf{(29)}$$

Where P_B is the breakdown pressure, σ_1 is the maximum far-field stress and σ_3 is the minimum far-field stress. The pore-fluid pressure P_p effectively reduces the stress equally in all directions. Since opening fractures are likely to close after the initiation of fractures, the pressure has to be increased again to reopen the fracture. The reopening pressure is defined as (Jaeger et al., 2007):

$$P_r = 3\sigma_3 - \sigma_1 - P_p \quad \textbf{(30)}$$

whereby the tensile strength is equal to zero, as it does not have to be overcome. Hence a relationship between breakdown pressure and reopening pressure can be set to compute the tensile strength of the intact rock with

$$T_0 = P_B - P_r \quad \textbf{(31).}$$

Therefore, minifrac tests, as described in Chapter 2.8 are important to get a measure of the in-situ tensile strength of the target rock formation. The results can then be correlated to the laboratory results to prove the relevance of the experiments and to optimize hydraulic stimulation results.

Despite the advantages of the Mohr's method, a downside is the negligence of the effect of the mean principal stress σ_2. This results in an unknown and yields an inconsistency with respect to the triaxial experiments. In a study on dry sandstones by Browning et al. (2017), the intermediate principal stress σ_2 was found to have an important role, as a reduction of σ_2 can potentially suppress the crack damage in a rock to a certain extent.

6.6.2 Porosity

The application of radial and axial pressure (loading phase) showed only a very small reduction in the porosity for all tested samples. A study from Dong et al. (2010) shows a decrease in porosity of around 1.5% after applying 50 MPa eff. hydrostatic pressure for sandstones with initial porosities of 17 to 18%. Since the porosity reduction calculated from the in- and out-flowing water when decreasing/increasing the confining pressure gives changes of less than 0.2%, this method is assumed to underestimate the change in porosity in comparison the results from Dong et al. (2010). However, the results clearly show the trends and indicate that there are processes such as compaction of the pore volume going on, which in turn reduce the permeability. Also the increase in porosity in the unloading phase clearly shows that the stress on the sample reduces and that a certain amount of permanent compaction is present. The compaction can be linked to a relative movement of the grains, as thin section analyses of samples after the experiments show (see Chapter 4.2).

6.6.3 Permeability prior to Deformation

Permeability measurements prior to the deformation of tested sandstones indicate that the decrease in pore volume causes changes in permeability. A significant decrease in permeability was observed in samples that have a high initial pore fluid flow (e.g., sample BD-51-Y1). For unaltered Buntsandstein samples this decrease was even more drastically (e.g., sample MI-50-Y1). This permeability reduction under hydrostatic loading was also observed in other studies on different porous sandstones (Vajdova et al., 2004; Baud et al., 2012; Benson et al., 2005). All these studies showed that the rock

permeability is primarily reduced due to closure of microcracks and a rearrangement and fragmentation of the grains with an increase in eff. hydrostatic pressure (David et al., 1994).

A dependency of the permeability in relation to the bedding orientation is observed for all sample blocks. In general, permeability is higher with the bedding orientated parallel to the flow direction, which is in line with observations from Dong et al. (2010). For the unaltered Buntsandstein the permeability was 6 – 15 times higher when the flow occured parallel to bedding compared a flow perpendicular to bedding. This impact can primarily be related to the microstructure of the samples, as described in Chapter 4.3. Small internal layers of the rock cores act as partial flow barriers, decreasing the flow perpendicular towards the bedding (Chapters 4.2 and 5.5).

In total, permeability tests were done on 15 Buntsandstein samples. Out of these, 4 had an initial permeability above 30 mD, which is taken as a threshold for guaranteeing sufficient flow rates for a geothermal project in the Buntsandstein of the WNB.

Table 6.7 illustrates the permeability of all samples, including the Rüthener Grünsandstein (RU-X1) and the Bentheim sandstone, for two confining pressures. In comparison to the very permeable Rüthener Grünsandstein (643 ± 45 mD) and Bentheim sandstone (1938 ± 348 mD), the highest permeability in a Buntsandstein sample was found in BD-51-Y1 (144 mD), which still had good permeability with a confinement of 30 MP (103 mD). All other Buntsandstein samples had less than 16 mD at higher eff. hydrostatic pressures.

Table 6.7: Average permeability at 2.5 MPa and 30 MPa effective hydrostatic pressure of various samples tested in the triaxial apparatus. All permeability values listed are for intact samples.

Sample block	Sample	Avg. permeability k [mD] at eff. hydrostatic pressure	
		2.5 MPa	30 MPa
SBS6-BD-50	BD-50-Y1	21 ± 3	2 ± 1.2
	BD-50-Z1	3 ± 0.3	0.03 ± 0.01
SBS6-BD-51	BD-51-Y1	144 ± 5.5	103 ± 6
	BD-51-Z1	25 ± 7.5	16 ± 1.2
SBS6-BD-52	BD- 52-X1	15 ± 0.1	10 ± 0.8
	BD-52-Z1	1 ± 0.04	0.8 ± 0.08
SRM6-MI-50	MI-50-Y1	61 ± 2.5	0.7 ± 2.8
	MI-50-Y2	64 ± 2.9	0.5 ± 0.3
	MI-50-Y4	0.7 ± 0.01	0.5 ± 0.1
	MI-50-Y5	1 ± 0.1	0.8 ± 0.8
	MI-50-Z2	47 ± 3.6	0.1 ± 0.03
SRG6-RU	RU-X1	643 ± 45	327 ± 8
Bentheim sandstone		1938 ± 348	-

6.6.4 Permeability after Deformation

Hydraulic stimulation was simulated for 9 Buntsandstein samples by mechanically inducing either a shear- or an opening fracture in the triaxial apparatus. Results showed that shear deformation of the porous sandstones from block SBS6-BD-50 leads to a significant decrease of the permeability by a factor of 15 to 20. Shear fractures in altered Buntsandstein samples of block SRM6-MI-50 with a low initial permeability increase the permeability only slightly (Table 6.8).

Table 6.8: Average permeability at 2.5 MPa effective hydrostatic pressure of various Buntsandstein samples before and after deformation in the triaxial apparatus. BDL = below detection limit.

Sample block	Sample	Avg. permeability k [mD] at 2.5 MPa eff. hydrostatic pressure	
		Prior to deformation	Post deformation
SBS6-BD-51	BD-51-Z1	25 ± 7.5	1.7 ± 0.1
	BD-51-Y1	144 ± 5.5	7.3 ± 0.7
SRM6-MI-50	MI-50-Y4	0.7 ± 0.01	1.9 ± 0.1
	MI-50-Y5	1 ± 0.1	1.4 ± 0.7
SRM6-MI-52	MI-52-Y3B	BDL	0.7 ± 0.1

Likewise, the Coconino sandstone (porosity ~23%) has a reduced permeability after shear deformation (Teufel, 1987). This stands in contrast to observations by Al Enezi et al. (2007) on the porous Berea sandstone. These contrasting observations show that shear fracturing of porous sandstones does not necessarily imply a permeability reduction and is highly dependent on the rock type.

In general, the decrease of the permeability due to shear fracturing of the Buntsandstein specimens can be related to the microstructural changes. At shear failure, the pores collapse and grains get ground up due to the high amount of friction. The created debris essentially fills the fracture and builds up a fluid barrier (see Chapter 4 and David et al., 1994).

Apart from shear fracturing the Buntsandstein, opening fractures were created in four samples for the unaltered sandstone. Creating opening fractures (Mode I) generally increased the permeability by several orders of magnitude. Sample MI-52-Z8, on the other hand, did not experience a large permeability increase (max 4.5 mD at around 650 µm apparent aperture). This could possibly be related to the creation of a secondary shear fracture by the “Mode I frackers”, where the increase of the axial load resulted in a closing of the original Mode I fracture. Overall, the occurrence of a fluid pathway due to opening fractures can significantly improve the permeability if Mode I fractures stay open. In general, the permeability is highly dependent on the opening width of the fracture, which

can be seen in Appendix H.7. The measured permeability is highly inconsistent with the calculated apparent fracture aperture. As an example, the permeability for an aperture of 500 µm varies between approximately 2 and 920 mD. To increase the consistency of the results, the increase in the aperture by applying axial load to the sample has to be done in smaller steps. It is then recommended to calculate the permeability based on a reference permeability at the first step. Therefore, the relative change in permeability with a relative increase in diameter can be studied. However, it is rather difficult to relate the aperture to the diameter measured when failure of the sample occurred, as the impact of the axial load can still have a great effect on the extension of the sample. Additionally, the calculated permeability is related to a flow through the entire sample, which is very subjective. Considering the size of a potential Buntsandstein reservoir with a thickness of, for example, 30 m and a lateral extension over hundreds of meters, the amount of fractures and/or the aperture of a fracture should be much greater to achieve economical flow rates.

Ultimately, the fluid flow is affected by the fracture geometry, which is not considered in the experiments. At high flow rates, which are generally used for geothermal wells, asperities of the fracture surface increase the tortuosity, which causes friction loss, essentially resulting in a lower permeability. For a 4 km deep geothermal well in the WNB the economic impact on the project due to lower flow rates needs to be considered.

6.6.5 Reservoir Implications

Considering the high amount of energy needed for heating greenhouses or for electricity production, a sufficient flow rate for the production and the injection of water into the reservoir is one of the key parameters. Assuming similar rock properties of the Buntsandstein present in the WNB as the samples studied in this thesis, the permeability found is in more than 90% of the cases below the threshold of 30 mD at 30 MPa effective hydrostatic pressure. With the hydrostatic pressure of the Buntsandstein in the WNB being generally above 30 MPa, this would imply that most Buntsandstein reservoirs would need stimulation in order to gain a higher permeability. However, this strongly depends on the local in-situ formation properties found in the subsurface. The in-situ permeability can be significantly higher than for the Buntsandstein samples tested in the laboratory. Rock specimens that were used in the experiments generally did not have any visible macroscopic fractures, voids or joints, which are usually present in formations, such as the in-situ Buntsandstein. Therefore, laboratory data, such as the compressive strength, tend to be overestimated in comparison to the in-situ properties. Hence, it is often useful to consider the lower bound of the measured data as an orientation (Chang et al., 2006).

Shear deformation of the samples showed that the permeability decreases due to cataclasis of the grains. At a larger scale, this cataclasis could cause a potential fluid barrier in the reservoir, as seen

in the core experiments. Similar to the laboratory, this fluid barrier can alter the overall reservoir quality, having a negative effect on the permeability. The amount of decrease in permeability thereby depends on the lateral extension of the shear fractures as well as the resulting damage zone. In contrast to the laboratory experiments, the permeability might be enhanced in the damage zone on a larger scale. This can be observed in fault zones, which often have a preferential flow path parallel to the fault zone in the damage zone, whereas the fault core often builds a barrier for fluids (Philipp et al., 2007). Similarly, on the small scale of the laboratory experiments, the rock specimen might be permeable in the damage zone. However, due to the orientation of the induced shear fracture, which is angular to the flow direction, the fluids might be completely blocked by the sealing core of the shear zone, even though the surrounding rock has an enhanced permeability. Since in a larger reservoir induced shear fractures are most likely not vertically cross-cutting the entire reservoir formation, fluid flow can be increased in the proximity of the fracture and can bypass the sealing sections at a certain point.

The creation of tensile fractures and the control of the permeability by the fracture aperture has been proven in the experiments and is commonly known for Mode I fractures in subsurface reservoirs (e.g., Philipp et al., 2007). Nevertheless, for a geothermal doublet an interconnected network of fractures needs to exist to allow flow from the injection-well to the production-well. The existence of such a connected network can be referred to as the percolation threshold (see Appendix J; Stauffer & Aharony, 2003; Philipp et al., 2007). The permeability of the cores with tensile fractures is solely based on a single fracture, whereas in-situ formations commonly contain natural fractures at the meso- and macro-scale. Created tensile fractures will therefore most likely propagate in a certain direction, leading to the connection of already pre-existing fractures. The direction and the amount of propagation thereby strongly depends on the local stress field. With the horizontal stress σ_1 in the WNB being roughly in the direction NS-SW, hydraulic fractures tend to propagate along this trend (Veldkamp & Boxem, 2015). Therefore the well placement has to be considered carefully, since different fracture orientations can lead to different thermal breakthrough times.

Upon commencing hydraulic stimulation, a variety of uncertainties has to be taken into account. Observations in Soultz-Sous-Forêts by Evans et al. (2005) have shown that tensile fractures are the primary cause of failure close to the wellbore when creating tensile fractures. But further away from the borehole, pre-existing fractures tend to fail in shear. In case of crystalline rocks at Soultz-Sous-Forêts it was observed that shear failure and the resulting cataclastic shear structures greatly enhance the permeability, whereas it is believed that the tensile fractures only have a minor effect on the overall permeability. Also a study by Ito & Hayashi (2003) on crystalline reservoirs using hot dry

rock (HDR) technology shows that mostly shear fractures, induced by increasing the fluid pressure, are responsible for a permeability increase. Although, this might be very different in case of other rock types as indicated in this study.

Results from laboratory studies combined with outcrop analogues can predict the frequency of fractures and approximate the effect of those on the overall permeability. Knowing the physical parameters of the rock allows to estimate how existing fractures might propagate and how newly created fractures with hydraulic stimulation will create a fracture network. To make further predictions, the available data can be combined and used in numerical simulations, increasing the likelihood of success.

7. Numerical Model

7.1 General

As the effective recovery is influenced by fractures (Brantut et al., 2013), the key impacts need to be further analyzed by introducing modeled scenarios in case of the Buntsandstein in the West Netherlands Basin in the context of a fully coupled thermo-hydro-mechanical (THM) analysis. The model allows to gain an insight on the effects of fractures and a resulting change in flow properties in the subsurface on a field scale. This ultimately affects the production life of a geothermal injector-producer pair.

The model simulates a Buntsandstein reservoir using laboratory data obtained for this thesis. In general, the essential features for a good geothermal reservoir quality are a high flow rate (high permeability), a high temperature of the reservoir fluid and a long lifetime.

The model primarily allows to estimate the initial rock properties, such as permeability, on a larger scale. Thereby outflow of hot water (e.g., 140°C) from the production well and inflow of colder water (e.g., 80°C) is assumed. Known reservoir parameters are set to be similar to the Buntsandstein reservoir of the West Netherlands Basin, if known.

7.1.1 Heat Capacity of the Model

For a 4 km deep Buntsandstein reservoir an initial reservoir temperature of 140°C is set in the model. The temperature difference between the reservoir output and the input, $\Delta\vartheta$, is kept at 60°C. Assuming a flow rate of 50 L/s, the thermal heat capacity, $\dot{Q}$ [kW], of a potential geothermal project can be calculated with the following equation:

$$\dot{Q} = \dot{m} \cdot c_w \cdot \Delta\vartheta \qquad \textbf{(32)}$$

with the mass flow of water, $\dot{m}$ [kg/s], the effective heat capacity of water, c_w [kJ/(kg·K)], and the temperature difference, $\Delta\vartheta$ [K]. With water as reservoir medium, the total heat capacity for the reservoir model would therefore be approximately:

$$\dot{Q} = 50\,\frac{kg}{s} \cdot 4.187\,\frac{kJ}{kg \cdot K} \cdot 60\ K = 12561\ kW_{th} \approx 12.6\ MW_{th}$$

Hence 12.6 MW geothermal energy would be available for generating electricity or to use for district heating.

7.1.2 Model Setup

In the fully coupled THM model the maximum and minimum principal stresses in the artificial reservoir are applied along the x- and y-axes. In general, the pseudo 3D-reservoir is a rectangular

block with 1 m thickness. No flow conditions have been set at the boundaries of the reservoir. The model used in the simulation extends 1000 m in X-direction and 400 m in the Y-direction. Overall, the reservoir represents an equivalent porous medium with a uniform porosity. Since fractures can be up to several hundreds of meters long after hydraulic stimulation (King, 2009), the distance between the production and the injection well was set to 600 m. This represents a created fracture network after inducing fractures of a length of 400 m extending from each of the two wells. The injection was set constant at 80°C water temperature. The initial reservoir temperature was set to 140°C. Temperature has been set as boundary condition. In general, flow rates of 50 L/s and more need to be achieved to economically produce from such depths and to increase the thermal heat capacity. Based on the pressure profile, the flow rate has been adapted, since a high flow rate eventually leads to very high drawdown and build-up pressures. The applied pressure at the injection well was kept below 10 MPa pressure difference compared to the initial reservoir pressure. According to Chapter 2.8, the hydrostatic reservoir pressure at 4 km depth is around 43 MPa, which was set as the initial reservoir pressure in the model. Often, the injection pressure is limited by governmental legislation, as in the Netherlands, and the bottomhole pressure (BHP) in the two wells has to be kept within a certain frame. The pressure at the production well was therefore kept above 30 MPa. The general input parameters of the model are listed in Table 7.1.

Table 7.1: General input parameters for the THM model.

Parameter	Value	Unit
Length	1000	m
Width	400	m
Grid blocks (initial model)	562	-
Initial reservoir temperature	140	°C
Injection temperature of water	80	°C
Initial reservoir pressure	43	MPa
Bulk modulus rock	12.87	GPa
Bulk modulus fluid	2	GPa
Viscosity water	$0.34 \cdot 10^{-3}$	Pa·s
Thermal conductivity of rock	2.58	W/(m·K)
Thermal conductivity of fluid	0.58	W/(m·K)
Specific heat capacity rock	1089	J/(K·kg)
Specific heat capacity fluid	4200	J/(K·kg)
Density fluid	1000	Kg/m²
Density rock	2300	kg/m²
Porosity	0.19	-
Sigma X (Compression)	85	MPa
Sigma Y (Compression)	43	MPa
Poisson ratio	0.19	-
Young's modulus	19.3	GPa
Casing diameter	8½	”
Initial permeability (model I)	30	mD
Initial permeability (model II)	7	mD
Initial permeability (model III)	93	mD

The permeability is set according to the values found in the laboratory measurements in case of two Buntsandstein samples. The values were extrapolated to hydrostatic pressures of 43 MPa. In total, three models were done with a permeability of 7 mD (permeability of samples BD-52-X1; Model I), 30 mD (model II) and 93 mD (permeability of samples BD-51-Y1; model III). In all cases, a 10% lower permeability was chosen in the Y-direction to implement a permeability anisotropy, which is generally common for a natural sandstone reservoir. The Young's modulus was set to 19.3 GPa, the Poisson's ratio was chosen to be 0.19.

To model the injectivity in relation to the injection and the production, the permeability was set in correlation with the stress. After each time step, the permeability was updated as a function of the stress in the reservoir. The number of times steps was kept at 3 per year of injection and production, effectively updating the permeability every 4 months. The maximum duration of the circulation was 30 years. The minimum permeability was kept at 5% of the initial permeability.

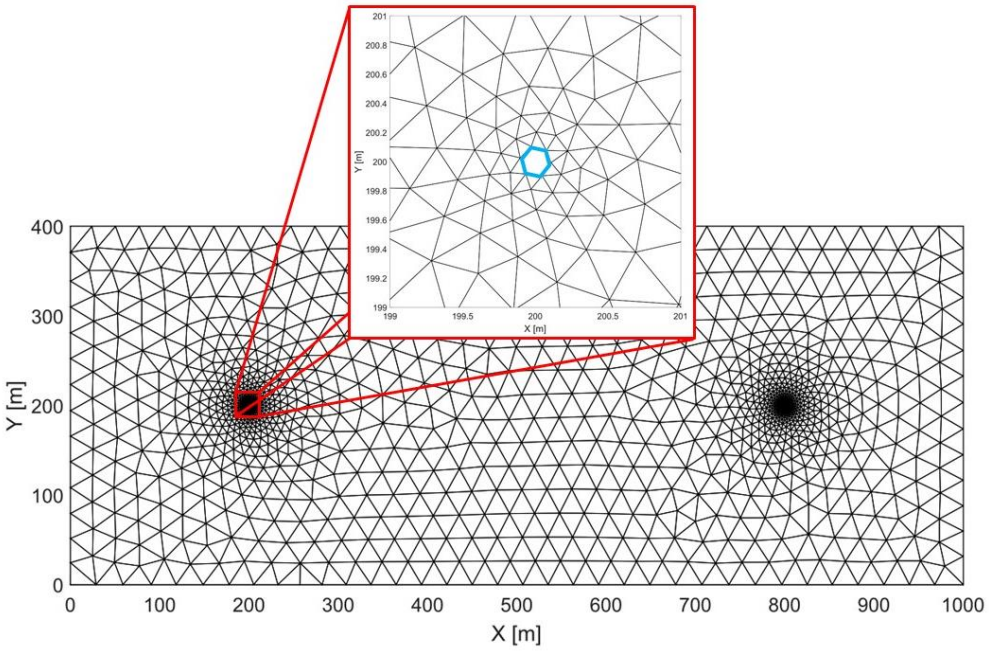

Figure 7.1: Generated mesh for the simulation including two cavities with a diameter of 8½" representing the boreholes. The nodes for the set injection/production are represented as the edges of the blue hexagon in the detail-window of the left cavity.

In geothermal wells with depths of around 4000 m a 7" perforated liner is generally set in an open hole section with a diameter of 8½" (Dumas et al., 2013). Therefore a diameter of 8½", represented as a circle, was set to model the borehole (Figure 7.1). To measure the effect of negative skin due to, for example, acidizing, hydraulic stimulation or radial jet drilling, the wellbore diameter was changed to represent the effective wellbore radius, so as to improve the computational efficiency. As a result

of this assumption, stress effects are not considered in the context of wellbore stability. The effective wellbore radius, r_{eff} [m], can be calculated as follows:

$$r_{eff} = r_w \cdot e^{-S} \quad \textbf{(33)}$$

with the wellbore radius r_w [m] and the skin S [-]. Thereby, a negative skin factor represents an enhancement of the flow capacity. For sandstone formations such as the Buntsandstein, Veldkamp & Boxem (2015) expect a maximum negative skin of -2 for acidizing, whereas hydraulic stimulation of the reservoir of 25 to 100 m in practice often causes a skin of -4 to -5.

As seen a field example for a Buntsandstein reservoir in the Netherlands, the two wells in the geothermal project in Vierpolders have a skin of 0.2 and 3.5. In the wells (around 2200 m TVD), the skin was effectively reduced by a factor of 10 by acidizing the formation (personal comunication with A. Sandén, Veegeo Energy). Hydraulic fracturing could further decrease the skin. Together with the permeability and additional reservoir parameters, the Darcy equation of radial inflow can be calculated, which can be describend as follows (Bell & Cuthill, 2008):

$$Q = \frac{2\pi kh \cdot (p_e - p_w)}{\mu \cdot [\ln\left(\frac{r_e}{r_w}\right) + S} \quad \textbf{(34)}$$

with the flowrate Q [m³/s], the permeability k [m²], the reservoir height h [m], the pressure at the reservoir boundary p_e [Pa], the pressure at the wellbore p_w [Pa], the fluid viscosity μ [Pa·s], the radius of the reservoir boundary r_e [m] and the radius of the wellbore r_w [m].

In case of the geothermal project in Vierpolders, with a reservoir permeability between 120 and 170 mD (personal communication with Axel Sandén), the approximate inflow potential is between 0.7 and 1.7 L/s per meter of perforated well section. This gives a good approximation on the amount of flow necessary to achieve sufficient flow rates.

7.2 Results

7.2.1 Model I

In model I, the thermal front moved gradually towards the production well. Figure 7.2 shows the temperature distribution of model I with 7 mD initial permeability after 30 years of injection. In the model, the injection of cold water cools down the reservoir rock around the wellbore. From the production well, water with 140°C is extracted. After 30 years, the thermal front moved around 200 m forward. Due to the low permeability, the flow rate was set to 0.02 L/s in order to remain low build-up and drawdown pressures. After 30 years of injection, the BHP of the injection well is around 50 MPa, in the production well the pressure is around 33 MPa. As Figure 7.2 and Appendix K.1 illustrate, the initial reservoir temperature at the production well can be maintained for a very long period of time. Hence at this flow rate over a distance of 600 m, there can be a continuous production at high temperatures. In Appendix K.1, the temperature distribution after 10, 20 and 30 years of injection and production is shown.

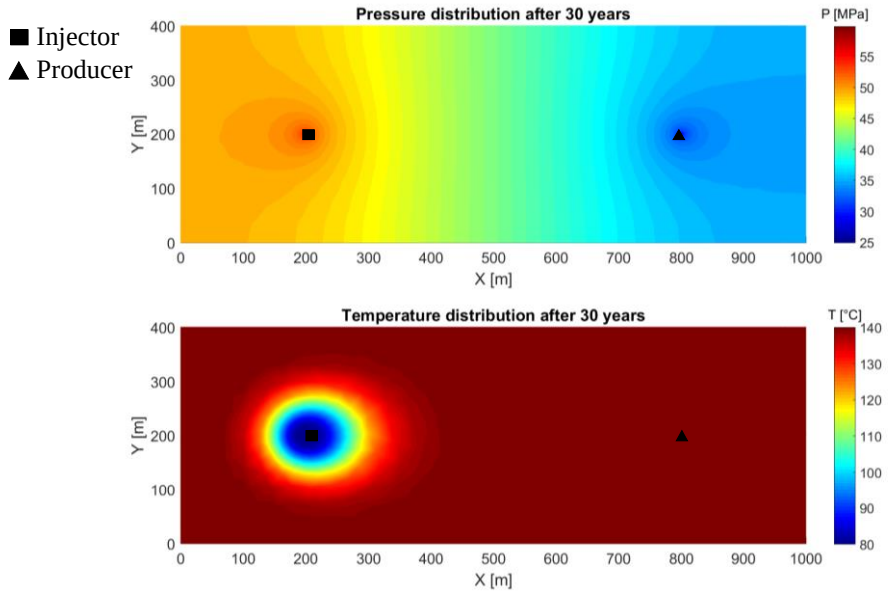

Figure 7.2: Pressure and temperature distribution after 30 years of injection and production for model II. The initial permeability is 30 mD and the flow rate 0.02 L/s. The initial reservoir temperature is 140°C, the injection temperature is 80°C. Further model parameters are shown in Appendix A.1.

7.2.2 Model II

A gradual drop in the temperature is seen with an increase in time. Figure 7.3 illustrates the temperature decrease at different time steps. The initial permeability was set to 30 mD, the flow rate was 0.1 L/s. As indicated in the figure, the thermal breakthrough took place close to around 20 years of injection.

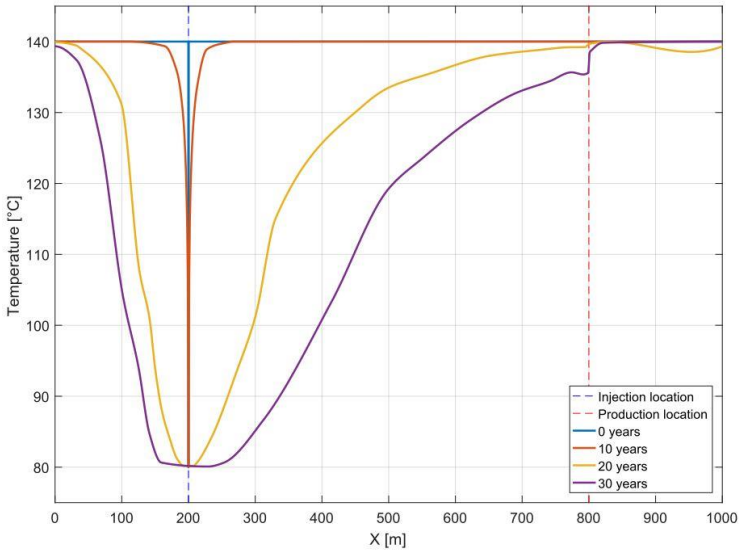

Figure 7.3: Temperature distribution at different time steps of model II. The initial permeability is 30 mD, the flow rate was set to 0.1 L/s. Further model parameters are shown in Appendix A.1.

After starting the injection and production of water in the reservoir, the injection pressure decreases over the years, as the permeability declines. After 20 years, the injection pressure is about 1.3 times the initial pressure (Figure 7.4 and Appendix K.2).

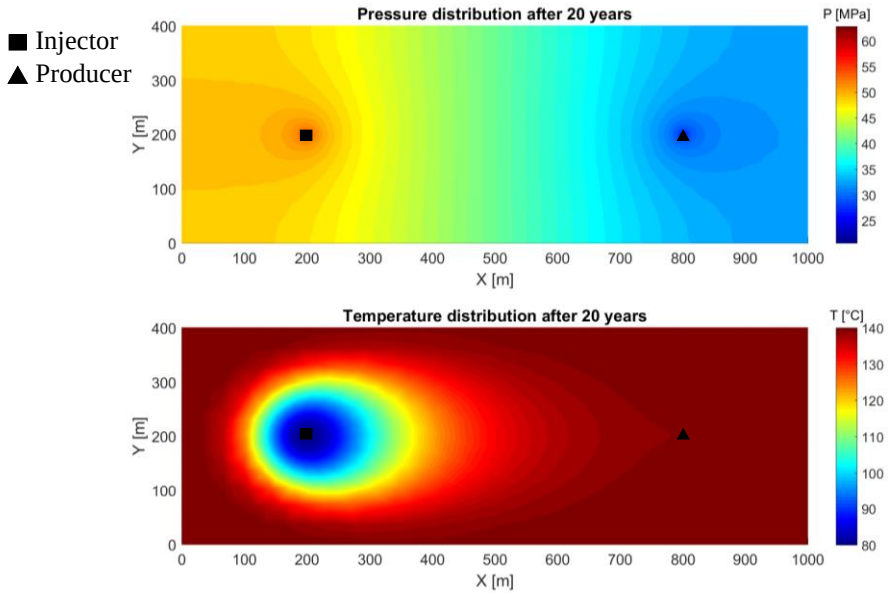

Figure 7.4: Pressure and temperature distribution after 20 years for model II, with an initial permeability of 30 mD and a flow rate of 0.1 L/s. The initial reservoir temperature is 140°C, the injection temperature is 80°C. Further model parameters are shown in Appendix A.1.

7.2.3 Model III

With an initial reservoir permeability of 93 mD, the flow rate could be more or less doubled in comparison to model I. At a flow rate of 0.2 L/s, the thermal breakthrough occurs approximately after

15 years of injection. A comparison of two different flow rates (0.2 and 0.4 L/s) on the reservoir temperature shows that after 20 years, the reservoir has significantly cooled down at 0.4 L/s (Figure 7.5). The temperature at the production well is less than 120°C after 20 years. At a lower flow rate, the production temperature can be kept more constant in this time period. Appendix K.3 shows the pressure distribution for model III after 20 years with a flow rate of 0.2 L/s.

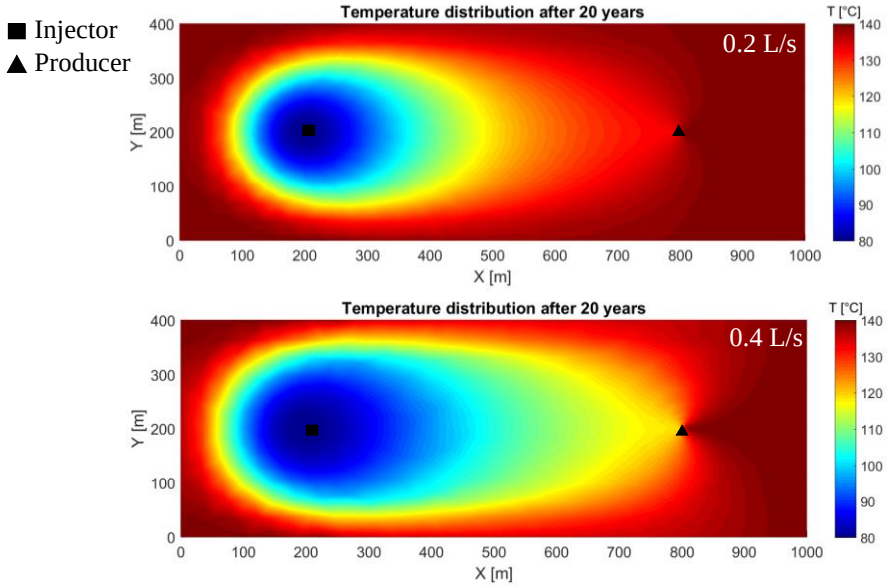

Figure 7.5: Temperature distribution after 20 years of production and injection for a reservoir with 93 mD initial permeability. Cold water of 80°C is injected at a rate of 0.2 L/s (top) and at 0.4 L/s (bottom). The initial reservoir temperature is 140°C. Further reservoir parameters are shown in Appendix A.1.

7.2.4 Sensitivity Analysis

To verify the model parameters and to understand the sensitivity with the data provided in the laboratory, various parameters in the model were changed by ± 20%. As a base case, model II with a permeability of 30 mD was chosen. The model was adapted, so the permeability stays constant. The results of the sensitivity analysis show that a change in porosity and the bulk modulus lead to the largest changes of all varied parameters. With a decrease in porosity, the initial pressure difference between the injector well and the producer well higher. However, the changes are still very small. Figure 7.6 shows the pressure difference between the injection and the production well, normalized to the base case. As the figure indicates, the porosity deviates only by around 0.05% in comparison to the base case after 5 years of injection. An increase in the elastic moduli causes an increase in the pressure difference. Since the bulk modulus is a function of the Young's modulus and the Poisson's ratio, an increase in the bulk modulus causes an increase in the pressure difference.

For the temperature, the strongest deviation to the base model is seen when changing the porosity. After 25 years of injection and production the temperate difference between the wells is about 0.2% higher than in the base case for a 20% higher porosity (23% total porosity instead of the initial 19%

porosity in the reservoir; Appendix K.5 and K.6). Other parameters seem to have no (or no significant) effect on the temperature distribution in the reservoir for this model. Appendix K.4 shows the pressure difference for changing parameters.

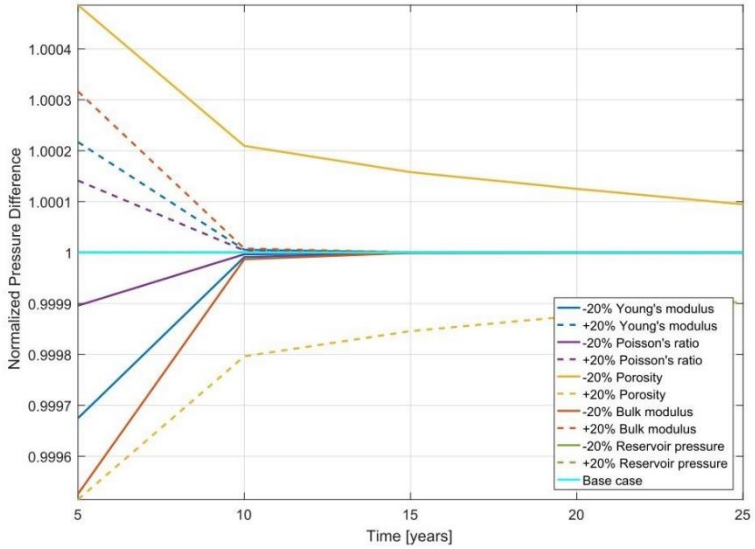

Figure 7.6: Normalized pressure difference between the injection and the production well over 25 years. The influence of a change in different model parameters in regard to the base case can be observed.

7.2.5 Skin

Using Equation 33, the effective wellbore radius, r_{eff}, was calculated for multiple negative skin factors. As an example, the effective wellbore radius is around 6 m, assuming a skin of -4 for a borehole diameter of 8½".

Figure 7.7 illustrates the change in pressure difference, ΔP, with an increase in r_{eff}. The figure shows that the pressure difference decreases with an increasing negative skin.

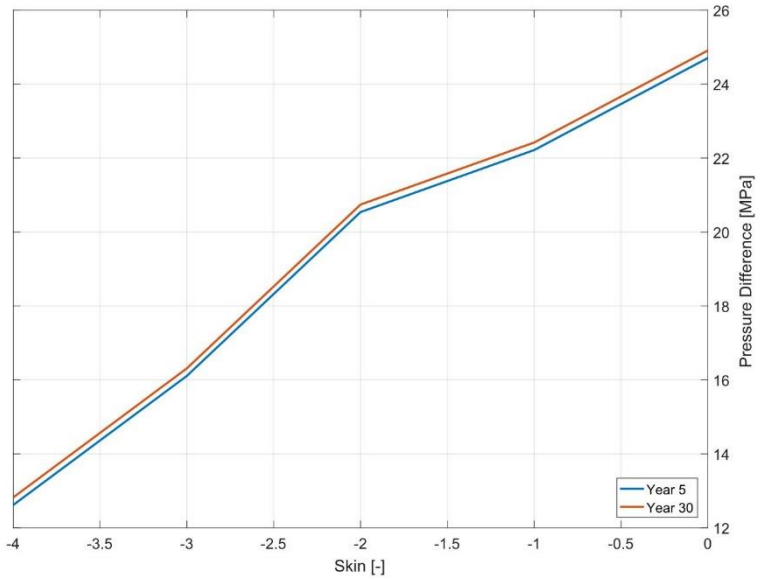

Figure 7.7: Effect of different negative skin factors on the pressure difference between the injection and the production well.

7.3 Discussion

In general, the models give a good understanding on the processes affecting the injection and the production in a reservoir with a geothermal doublet. The long term fluid circulation in the reservoir and the modeling of the thermal breakthrough time provide an approximation of the overall lifetime of a geothermal well in the Buntsandstein. This allows to build a basis for calculations of the economic viability of a potential project in the Buntsandstein. As shown, with a circulation rate of 0.2 L/s and a relatively high permeability of 93 mD, the calculated production temperature remains constant over almost 20 years. Hence the thermal power of 12.6 MW_{th} in the Buntsandstein would remain constant in this time period. If reservoir conditions allow, even higher flow rates can be applied, resulting in a higher thermal energy capacity. However, as the model shows, the thermal breakthrough will be earlier at higher flow rates.

In comparison to the inflow potential of the geothermal project in Vierpolders, the flow rates used in the models are by around one order of magnitude lower. Therefore it has to be researched if the total flow rate that can be achieved in a geothermal project is sufficient to economically produce from a depth of 4 km. The total flow rate depends on multiple factors such as the permeability, the reservoir height and the skin (see Equation 34).

Overall, the biggest sensitivity in the model comes from the flow rate and the permeability. Due to the higher stress applied at higher flow rate, the pressure in the reservoir increases in the injection and production wells. Thus the pressure increases less at lower flow rates.

Tischner et al. (2010) simulated the lifetime of a geothermal doublet for a reservoir in the Middle Buntsandstein at 4 km depth. There, a single well concept with a weekly cycle scheme is used in a hydraulically fractured reservoir. In their model, 60°C cold water was circulated at a rate of 4 L/s over 25 years. The results of the model showed that the reservoir temperature stayed almost constant. Although the injection rate is much lower than in a geothermal doublet, this shows that for a single well concept the reservoir rock is assumed to only cool down relatively close to the wellbore. This is essentially a similar case as proposed by the model. At low flow rates, the thermal breakthrough might not be achieved during the lifetime of the wells.

Important to note is that in the model, matrix flow cannot be combined with fracture flow at the same time. Therefore, this model is solely assuming fluid flow through the matrix. However, in a hydraulically fractured Buntsandstein reservoir in the WNB with a very low initial permeability, a pure fracture flow is a more likely scenario. But for the accurate modeling of flow through a fractured reservoir, a good understanding of the fracture geometry and distribution in the reservoir is required (Souley et al., 2015).

Moreover, the fracture aperture can increase or decrease, depending on the properties of the injected water. An injection of cold water can cause stress changes due to the cooling of the reservoir rock, which in turn can lead to a change in the permeability around the wellbore. A THM model by Cao et al. (2015) for heat extraction in an EGS system shows that heat extraction leads to a contraction of the volume, which in turn leads to tensile stress in the reservoir. Moreover, the long term circulation of fluids can trigger chemical effects that influence, for example, the wellbore injectivity (Rühaak et al., 2015).

In the models presented in this thesis a fracture network over 800 m is shown. This distance might be possible, but since no hydraulic stimulation of the Buntsandstein in the West Netherlands Basin has been done so far, the possibility of such fracture lengths has to be proven. A shorter distance between the injection and the production well may lead to a significantly earlier thermal breakthrough, resulting in a smaller thermal energy after a specific time.

The reservoir was assumed to be homogenous, only having a small permeability anisotropy. However, reservoirs naturally show internal layering, voids or inclusions. In case of the Buntsandstein, an interbedding of shale layers influences the overall stiffness of the rock and changes the propagation of hydrofractures (Philipp et al., 2007). This can have either negative or positive effects on the reservoir. Therefore, outcrop studies should be used to refine the model based on the observations made to get a more detailed facies model. The outcome of a number of simulations (on a field scale) can be compared to a real case scenario of a geothermal doublet in a reservoir with a high amount of fracture fluid flow (e.g., Soultz-sous-Forêts). Modeling the heterogeneity of a reservoir can significantly affect the overall results. Running a variety of different models with different heterogeneities can reveal uncertainties and allows to predict the flow behavior. This is important to decrease the economic risks.

8. Conclusions

The West Netherlands Basin has a high potential of producing geothermal energy from the Triassic Buntsandstein at 4 km depth due to the relatively high temperature of around 140°C that has been found in the well correlation done in this thesis. Moreover, the correlation proves the approximately expected hydrostatic pressures at these depths in the WNB, which have shown to be important in terms of mechanical behavior of the rocks.

So far, the Buntsandstein has not been used for geothermal exploitation in the WNB at depths greater than 3 km and the mechanical characteristics of the formation in the WNB are still not well researched. In the scope of this thesis, a characterization of the physical properties of samples from analogue Buntsandstein quarries has been done. The results indicate strong similarities between the tested samples and studies on cores from the subsurface in the WNB in terms of mineralogy. However, the mechanical characterization of the tested specimen yields very different results between the cores, even from samples drilled in the same block. Especially altered and unaltered samples show a clear distinction in terms of yield strength, uniaxial compressive strength and elastic moduli due to their difference in properties, such as porosity, mineralogy and degree of cementation. Additionally, the P- and S-wave velocities were measured for a variety of cores. A correlation between the orientation of the cores with respect to the bedding and the velocity could be made, where cores drilled perpendicular to the bedding (Z-direction) show 20 ± 9% higher P-wave velocities than in X- and Y-direction. The S-wave velocity, on the other hand, was roughly equal. These results point out the large mechanical anisotropy of the Buntsandstein even on a small scale. Additionally, acoustic velocities measured in unconfined compression tests showed to give a good indication on the changes in microcrack density. The yield strength expressed in the velocity evolution can generally be matched with observations from the stress-strain curve.

In cyclic loading experiments it was demonstrated that applying cyclic stress changes the static elastic moduli of the Buntsandstein significantly. Where the maximum stress was increased in each cycle, the Young's modulus increased by a factor of 1.7 ± 0.2 in all cases. The Poisson's ratio increases by a factor of 3.4 ± 0.8. The changes in the Young's modulus can be related to a further compaction of the sandstones and existing cracks, resulting in a decrease in pore volume, while the Poisson's ratio increased due to the development of microcracks parallel to the direction of the stress.

To economically produce from a 4 km deep reservoir, high flow rates are necessary, which can only be achieved in reservoirs with a sufficient permeability. In this study it was shown that the majority of the rock samples from the Buntsandstein tested in the triaxial apparatus has a low initial permeability of 15 mD and considerably lower at an effective hydrostatic pressure of 30 MPa. The

decrease ranged from factors of 1.5 to more than 100, depending on the rock type. At even higher effective pressures the permeability decreased further due to compaction of the rocks.
Generally, cores drilled both perpendicular and parallel to bedding exhibit a permeability anisotropy. Parallel to bedding, cores were between 6 and 47 times more permeable than perpendicular to bedding. A relationship between permeability and depth was made, allowing extrapolation to higher pressures.
The low permeability indicates that a stimulation of the Buntsandstein in the subsurface is necessary, if reservoir parameters turn out to be similar. The different effects of creating shear fractures or tensile fractures on the permeability was effectively shown in this thesis. Due to the strong cataclasis in the shear zone after shear deformation, the permeability reduced by a factor of 17 ± 3 in porous sandstones, from 85 ± 60 mD to 5 ± 3 mD. Altered Buntsandstein samples with a low initial permeability of 1 ± 0.2 mD showed only a slight increase to 2 ± 0.3 mD. In contrast, tensile fractures greatly enhanced the permeability, depending on the fracture aperture. On average, the permeability increased by a factor of approximately 1.9 for each increase in the fracture aperture of 100 µm, indicating an exponential increase. These results show, that hydraulic stimulation of the Buntsandstein will only lead to higher permeabilities if tensile fractures are created. However, this statement only holds true if reservoir parameters turn out as measured in the laboratory experiments. Generally, a Mode I hydraulic stimulation often leads to an additional creation of shear fractures in the reservoir, resulting in a combination of fracture types. This can have either positive or negative effects on the permeability.

Upon the hydraulic stimulation of a reservoir and a resulting fracture network of tensile (and shear) fractures, the achieved higher permeability was proven to have a significant effect on the thermal cooling. With production and injection into a fractured reservoir with 30 mD initial permeability, a constant production of 140°C hot water over a period of 20 years was estimated to be possible in a numerical thermo-hydro-mechanical model. This holds valid for a flow rate of 0.1 L/s per meter of perforated well section. Overall, the models show that the permeability needs to be sufficiently high to achieve high flow rates necessary for producing from a geothermal reservoir. In case of a low permeable Buntsandstein reservoir, a stimulation of the reservoir needs to be applied in some way to enhance the permeability.

9. Recommendations

- Since it was shown in the thesis that the mechanical properties of the samples can vary greatly, it is recommended to test further types of Buntsandstein samples gathered from multiple outcrops. This allows more flexibility in predicting certain rock specific parameters. Moreover, not only the most homogeneous samples should be taken, as natural rock formations are generally heterogeneous.

- Since the fracture distribution of the Buntsandstein in the subsurface of the West Netherlands Basin is unknown, it would be beneficial to study analogue outcrops in more detail, as done, for example, by Philipp et al. (2007). As mentioned in the thesis, shear dilation treatments are less expensive to apply in a reservoir than Mode I hydraulic stimulation, if natural fractures are present. In order to choose the right application scenario, information about the naturally present fractures and their distribution needs to be collected. Additionally, sedimentary layering (e.g., interbedded shale layers) in the formation and their influence on the propagation of fractures should be studied further.

- Since acoustic measurements can give a good insight into microcracking processes, it is recommended to also apply acoustic measurements during triaxial testing. So far, tests have only been done during unconfined compression tests. Conducting acoustic measurements at confining pressures would give results more comparable to in-situ conditions. Furthermore, mounting sonic transducers around the sample might help to better understand the location of crack occurrence in the rock specimen.

- So far, tensile fractures have only been created in four tested samples. To give a better quantification of the increase in the apparent aperture, further tests need to be done. It is recommended to apply smaller steps when opening up the fracture aperture. Thereby the opening of the fracture can be set in a better relationship to an antecedent measurement.

- For a significant increase in geothermal energy in the Netherlands many challenges have to be overcome. Drilling down to depths of 4 km (and deeper) is associated with very high initial costs. Therefore projects need a backup plan in case the permeability in the Buntsandstein in the WNB is not sufficient. If the target reservoir shows a moderate permeability, radial jet drilling can be applied. This technique is rather inexpensive and a much smaller amount of

water is necessary for the process compared to hydraulic stimulation. However, this technique has not been tested in siliclastic geothermal reservoirs yet. Further research should be done to study the effect on the overall reservoir properties after radial jet drilling and how fluid flow can be enhanced with multiple laterals. In a numerical model and/or on field tests, the effect of hydraulic stimulation after radial jet drilling can be investigated. Due to the jetted laterals, fractures might propagate in the direction of the laterals. This could provide an effective and cost efficient technique to apply in a reservoir.

- The first geothermal doublet planned in the Buntsandstein in the WNB at a depth of about 4 km is the Trias Westland project. The anticipated drilling start of the first well is in fall 2017. This is a good opportunity to get hold of the reservoir potential of this formation at such great depths in the Netherlands. The project allows to do research on the mechanical parameters, and, for example, cores and cuttings can be further studied and set into relation with the findings of this thesis. This will help to predict reservoir parameters for following projects.

References

Van Adrichem Boogaert, H.A. & Kouwe, W.F.P. (1997) Stratigraphic nomenclature of the Netherlands, revision and update by RGD and NOGEPA. *Mededelingen Rijks Geologische Dienst (Haarlem) 50*.

Angus, D.A., Fisher, Q.J. & Verdon, J.P. (2012) Exploring trends in microcrack properties of sedimentary rocks: An audit of dry and water saturated sandstone core velocity–stress measurements.

Aquilina, L., Genter, A., Elsass, P. & Pribnow, D. (2000) Evolution of Fluid Circulation in the Rhine Graben: Constraints from the Chemistry of Present Fluids. *Hydrogeology of Crystalline Rocks*, 34, pp.177–203. Available from: <http://dx.doi.org/10.1007/978-94-017-1816-5_8>.

ASTM (2001) Standard Test Method for Splitting Tensile Strength of Intact Rock Core Specimens. , p.3.

Atkinson, B.K. & Meredith, P.G. (1987) Experimental Fracture Mechanics Data for Rocks and Minerals. In: *Fracture Mechanics of Rock*. pp.477–525.

Van Balen, R.T., Van Bergen, F., De Leeuw, C., Pagnier, H., Simmelink, H., Van Wees, J.D. & Verweij, J.M. (2000) Modelling the hydrocarbon generation and migration in the West Netherlands Basin, the Netherlands. *Geologie en Mijnbouw / Netherlands Journal of Geosciences 79 (1): 29-44*.

Baud, P., Meredith, P. & Townend, E. (2012) Permeability evolution during triaxial compaction of an anisotropic porous sandstone. *Journal of Geophysical Research: Solid Earth*, 117 (5).

Baud, P., Wong, T.F., Vajdova, V., Meredith, P. & Brantut, N. (2013) Time-dependent deformation in rocks. Available from: <https://www.waddenacademie.nl/fileadmin/inhoud/pdf/03-Thema_s/Geowetenschap/Bodemdaling/07-Baud-2-SC-meeting-public.pdf>.

Bell, M. & Cuthill, D. (2008) Next-generation perforating system enhances testing, treatment of fracture stimulated wells. In: *Completing the Well*.

Benson, P.M., Meredith, P.G., Platzman, E.S. & White, R.E. (2005) Pore fabric shape anisotropy in porous sandstones and its relation to elastic wave velocity and permeability anisotropy under hydrostatic pressure.

Berlin.de faq-untergrund.pdf [Internet]. Available from: <http://www.stadtentwicklung.berlin.de/umwelt/wasser/hydrogeo/de/broschuere/faq-untergrund.pdf> [Accessed 6 June 2017].

Brantut, N., Heap, M.J., Meredith, P.G. & Baud, P. (2013) Time-dependent cracking and brittle creep in crustal rocks. *Journal of Structural Geology 52(1):17-43 · July 2013*.

Browning, J., Meredith, P.G., Stuart, C.E., Healy, D., Harland, S. & Mitchell, T.M. (2017) Acoustic characterization of crack damage evolution in sandstone deformed under conventional and true triaxial loading. *Journal of Geophysical Research: Solid Earth*, p.18.

Byrne, M. & Patey, I. (2004) Core Sample Preparation - An Insight Into New Procedures.

Cao, W., Huang, W. & Jiang, F. (2015) A Thermal-Hydraulic-Mechanical Fully Coupled Model for Heat Extraction in Enhanced Geothermal Systems. In: *Proceedings World Geothermal Congress 2015*. p.7.

Chang, C., Zoback, M. & Khaksar, A. (2006) Empirical relations between rock strength and physical properties in sedimentary rocks. *Journal of Petroleum Science and Engineering*, 51, pp.223–237.

Ciccotti, M. & Mulargia, F. (2004) Differences between static and dynamic elastic moduli of a typical seismogenic rock. *Geophs. J. Int.*, 157, pp.474–477.

Council, N.R. (2013) *Induced seismicity potential in energy technologies*.

Dachroth, W.R. (2013) Der Buntsandstein der Lothringen-Pfalz-Senke. *Deutsche Stratigraphische Kommission (Hrsg.; Koordination und Redaktion: J. Lepper & H.-G. Röhling für die Subkommission Perm-Trias): Stratigraphie von Deutsch- land XI. Buntsandstein. – Schriftenreihe der Deutschen Gesellschaft für Geowissenschaften*, 69, pp.487–513.

Daumas, L. (2017) The Netherlands: Adaptation and Renewables [Internet].

David, C. (2006) Buntsandsteine - Bausandsteine, Marburger Bausandstein unter der Lupe. *Marburger Geowissenschaften, Band 3*, p.4.

David, C., Wong, T.F., Zhu, W. & Zhang, J. (1994) Laboratory measurement of compaction-induced permeability change in porous rocks: implication for the generation and maintainance of pore pressure excess in the crust. *Pure and Applied Geophysics*, 143, pp.425–456.

Delfiner, P. (2007) Three Statistical Pitfalls of Phi-K Transforms. *Reservoir Evaluation & Engineering*, pp.609–617.

Deming, D. (1989) Application of Bottom-Hole Temperature Corrections in Geothermal Studies. *Geothermics*, 18 (5/6), pp.775–786.

Dong, J.J., Hsu, J.Y., Shimamoto, T., Hung, J.H., Yeh, E.C., Wu, Y.H. & Sone, H. (2010) Stress-dependence of the permeability and porosity of sandstone and shale from TCDP Hole-A. *International Journal of Rock Mechanics & Mining Sciences 2*, 47, pp.1141–1157.

Donselaar, M. (2015) Reservoir Geology and Geothermal Potential of the Delft Sandstone Member in the West Netherlands Basin. In: *World Geothermal Congress 2015*. p.9.

Dumas, P., Antics, M. & Ungemach, P. (2013) *Report on Geothermal Drilling*.

ENERCHANGE (2013) Wohin bohren im Malm des bayerischen Molassebeckens? [Internet].

Available from: <http://www.tiefegeothermie.de/top-themen/wohin-bohren-im-malm-des-bayerischen-molassebeckens>.

Al Enezi, S., Grader, A. & Halleck, O. (2007) Effects of Shear-Fracture Displacement and Orientation on Fracture Topology and Absolute Permeability. *International Symposium of the Society of Core Analysts held in Calgary, Canada, 10-12 September, 2007*.

English, J.M. (2012) Thermomechanical origin of regional fracture systems. *AAPG Bulletin*, 96 (9), pp.1597–1625.

Evans, K.F., Genter, A. & Sausse, J. (2005) Permeability creation and damage due to massive fluid injections into granite at 3.5 km at Soultz: 1. Borehole observations. *Journal of Geophysical Research*, 110 (B04203), p.19.

Folk, R.L. (1965) *Petrology of Sedimentary Rocks*. Hemphill.

Fossen, H. (2010) *Structural Geology*.

Freyburg, E. (1972) Der Untere und mittlere Buntsandstein SW-Thüringen in seinen gesteinstechnicschen Eigenschaften. *Ber. Dtsch. Ges. Geol. Wiss. Nummer*, 17, pp.911–919.

Frick, S., Kaltschmitt, M. & Schröder, G. (2010) Life cycle assessment of geothermal binary power plants using enhanced low-temperature reservoirs. *Energy*, 35 (5), pp.2281–2294.

Geluk, M.C. (2007) Triassic. *Geology of the Netherlands, chapter Triassic, Royal Netherlands Academy of Arts and Sciences*.

Goodman, R.E. (1989) *Introduction to Rock Mechanics*. Vol. 2. New York, Wiley.

Goutorbe, B., Lucazeau, F. & Bonneville, A. (2007) Comparison of several BHT correction methods: a case study on an Australian data set. *Geophysical Journal International*, 170 (2), pp.913–922.

Green Well Westland (2016) No Title [Internet]. Available from: <www.green-well-westland.nl/> [Accessed 3 November 2016].

Guo, H., Aziz, N.I. & Schmidt, L.C. (1993) Rock fracture-toughness determination by the Brazilian test. *Engineering Geology, 33 (1993) 177-188*.

Han, D., Nur, A. & Morgan, D. (1986) Effects of porosity and clay content on wave velocities in sandstones. *Geophysics*, 51 (11), pp.2093–2107.

Heap, M.J. & Faulkner, D.R. (2008) Quantifying the evolution of static elastic properties as crystalline rock approaches failure. *International Journal of Rock Mechanics & Mining Sciences*, 45, pp.564–573.

Hossain, M.M., Rahman, M.K. & Rahman, S.S. (2002) A Shear Dilation Stimulation Model for Production Enhancement From Naturally Fractured Reservoirs. *SPE Journal June 2002*, pp.183–195.

Hugues, T., Steiger, L. & Weber, J. (2005) *Dressed Stone: Types of Stone, Details, Examples*.

Van Hulten, F.F.N. (2009) Brief history of petroleum exploration in the Netherlands. *Energie Beheer Nederland B.V., Netherlands*.

Van Hulten, F.F.N. (2006) Reservoir quality distribution as tool for better exploration prospect evaluation and estimation of the resource base in the Netherlands. *Van Hulten, FFN & Lutgert, JE (comp.). Tight gas fields in the Netherlands, workshop EBN-TNO*, 19 (September).

Ito, T. & Hayashi, K. (2003) Role of Stress-controlled Flow Pathways in HDR Geothermal Reservoirs. *Pure and Applied Geophysics*, 160, pp.1103–1124.

ITTC (2011) *ITTC – Recommended Procedures: Fresh Water and Seawater Properties*.

Jaeger, J.C., Cook, N.G.W. & Zimmerman, R.W. (2007) *Fundamentals of Rock Mechanics*. Fourth Edi. Blackwell.

Jager, J., Doyle, M.A., Grantham, P.J. & Mabillard, J.E. (1996) Hydrocarbon Habitat of the West Netherlands Basin. In: H. E. Rondeel, D. A. J. Batjes, & W. H. Nieuwenhuijs eds. *Geology of gas and oil under the Netherlands*. pp.191–209.

Jianhong, Y., Wu, F.Q. & Sun, J.Z. (2009) Estimation of the tensile elastic modulus using Brazilian disc by applying diametrically opposed concentrated loads. *International Journal of Rock Mechanics & Mining Sciences 46 (2009) 568–576*.

Juhasz, I. (1986) Conversion of routine air-permeability data into stressed brine-permeability data. *Transactions of the SPWLA 10th European Formation Evaluation Symposium, Society of Professional Well Log Analysts*, pp.1–15.

Jung, Y.B., Lee, H.K., Synn, J.H. & Park, C. (2001) Determination of mode I fracture toughness of rocks at low temperature. *Rock Mechanics in the National Interest*, p.8.

Kahraman, S. & Altindagm, R. (2004) A brittleness index to estimate fracture toughness. *International Journal of Rock Mechanics & Mining Sciences*, 41, pp.343–348.

Kakar, S. (2013) Fracking vs Acidizing [Internet]. Available from: <http://info.emilcott.com/ehswire-blog/bid/315991/Fracking-vs-Acidizing>.

Kamel, A.H. (2014) RJD revitalizes mature Kansas oilfield. *Oil and Gas Journal 112(10):60, October 2014*.

King, G.E. (2009) Fracturing Basics [Internet]. Available from: <http://gekengineering.com/Downloads/Free_Downloads/Fracturing.pdf> [Accessed 8 July 2017].

Kirsch, C. Geschichte [Internet]. Available from: <http://r.roderfeld.de/kirsch/> [Accessed 19 July 2017].

Kohar, J.P. & Gogoi, S. (2014) Radial Drilling Technique For Improving Recovery From Existing Oil Fields. *International Journal of Scientific & Technology Research Volume 3, Issue 11, Nov.*

2014.

Lee, H., Moon, T. & Haimson, B.C. (2016) Borehole Breakouts Induced in Arkosic Sandstones and a Discrete Element Analysis. *Rock Mech Rock Eng*, 49, pp.1369–1388.

Li, L. & Fjær, E. (2012) Modeling of stress-dependent static and dynamic moduli of weak sandstones. *Journal of Geophysical Research*, 117 (B05206).

Lipsey, L., Pluymaekers, M., Goldberg, T., Van Oversteeg, K., Ghazaryan, L., Cloetingh, S. & Van Wees, J.D. (2016) Numerical modelling of thermal convection in the Luttelgeest carbonate platform, the Netherlands. *Geothermics*, 64, pp.135–151.

Martínez-Martínez, J. & Benavente, D. (2012) Comparison of the static and dynamic elastic modulus in carbonate rocks. *Bull Eng Geol Environ*, 71, pp.263–268.

Matev, P.S. (2011) Comprehensive reservoir quality assessment of Buntsandstein sandstone reservoirs in the West Netherlands Basin for geothermal applications in Zuid Holland province area.

Menschik, F. (2015) Analysis of Performance and Wear of Electrical Rock Hammer Drills.

Molenda, M., Stöckhert, F., Brenne, S. & Alber, M. (2013) Comparison of Hydraulic and Conventional Tensile Strength Tests. In: *Effective and Sustainable Hydraulic Fracturing*.

Mosch, S. (2008) Optimierung der Exploration, Gewinnung und Materialcharakterisierung von Naturwerksteinen.

De Mulder, E., Geluk, M.C., Ritsema, I., Westerhoff, W.E. & Wong, T.E. (2003) *De ondergrond van Nederland, Geologie van Nederland, deel 7*. Peeters, Herent, Belgie.

Nieto, J.A., Yale, D.P. & Evans, R.J. (1994) Improved Methods for Correcting Core Porosity to Reservoir Conditions. *The Log Analyst*, pp.21–30.

Paterson, M.S. & Wong, T. (2005) *Experimental Rock Deformation - The Brittle Field*.

Pavicic, T. (2015) So funktioniert ein Geothermie-Kraftwerk [Internet].

Pellet, F.L. & Keshavarz, M. (2010) Mechanical behaviour of a crystalline hard rock subjected to ultra high temperature and consequences for underground opening stability. *Rock Mechanics in Civil and Environmental Engineering by Zhao, Labiouse, Dudt & Mathier (2010)*.

Peters, S.A. (2015) Production Performance of Radial Jet Drilled Laterals in Tight Gas Reservoirs in the Netherlands - A Simulation Approach and Economic Analysis. *MSc thesis Delft University of Technology*.

Philipp, S.L., Gudmundsson, A. & Oelrich, A.R.I. (2007) How structural geology can contribute to make geothermal projects successful. In: *Proceedings European Geothermal Congress*. p.10.

Primarini, M. (2015) Fracture Mode Analysis, Geomechanics, Petrophysics, and Fracture Characterization: An Experimental Investigation on Whitby Shales and Various Other Rock

Types. *MSc thesis Delft University of Technology*.

Purvis, K. & Okkerman, J.A. (1996) Inversion of reservoir quality by early diagenesis: an example from the Triassic Buntsandstein, offshore the Netherlands. *Rondeel et al. (eds). Geology of gas and oil under the Netherlands, 179-189, 1996*.

Racero-Baena, A. & Drake, S.J. (1996) Structural Style and Reservoir Development in the West Netherlands Oil Province. In: *Rondeel et al. (eds). Geology of gas and oil under the Netherlands, 179-189, 1996*. pp.211–227.

Ray, S.K., Sarkar, M. & Singh, T.N. (1999) Effect of cyclic loading and strain rate on the mechanical behaviour of sandstone. *International Journal of Rock Mechanics and Mining Sciences*, 36, pp.543–549.

Reyer, D. & Philipp, S.L. (2014) Empirical relations of rock properties of outcrop and core samples from the Northwest German Basin for geothermal drilling. *Geothermal Energy Science*, (2), pp.21–37.

Roxborough, F.F. & Phillips, H.. (1975) Rock excavation by disc cutter. *Int. J. Rock .Mech. Min. Sci. Geomech. Abstr.*, 12, pp.361–366.

Rühaak, W., Pei, L., Bartels, J., Heldman, C.D., Homuth, S. & Sass, I. (2015) No Title. In: *Proceedings World Geothermal Congress 2015*. p.11.

Sanjuan, B., Millot, R., Dezayes, C. & Brach, M. (2010) Main characteristics of the deep geothermal brine (5 km) at Soultz-sous-Foreˆts (France) determined using geochemical and tracer test data. *C. R. Geoscience 342 (2010) 546–559*.

Shafiq, M.U. & Mahmud, H.B. (2017) Sandstone matrix acidizing knowledge and future development. *Journal of Petroleum Exploration and Production Technology*, p.12.

Singh, T.N. & Suresh Naidu, A. (2000) Effect of cyclic loading and strain rate on the mechanical behaviour of sandstone. *Indian Journal of Engineering & Materials Sciences*, 8, pp.8–12.

Singhal, B.B.S. & Gubpta, R.P. (2010) *Applied Hydrogeology of Fractured Rocks*.

Souley, M., Lopez, P., Boulon, M. & Thoraval, A. (2015) Experimental Hydromechanical Characterization and Numerical Modelling of a Fractured and Porous Sandstone. *Rock Mech Rock Eng*, 48, pp.1143–1161.

Stauffer, D. & Aharony, A. (2003) *Introduction to Percolation Theory*. 2nd Revise. Taylor & Francis.

STMWIVT (2012) *Bayrischer Geothermieatlas*.

Stück, H.L., Ruedrich, J. & Siegesmund, S. (2012) STATISTICAL ANALYSES OF PETROGRAPHICAL & PETROPYHSICAL PROPERTIES OF SANDSTONES: AN APPROACH FOR PREDICTING CONSTRUCTION SUITABILITY. *12th International Congress on the Deterioration and Conservation of Stone Columbia University, New York*,

2012. Available from: <http://iscs.icomos.org/pdf-files/NewYorkConf/stucetal.pdf>.

Syed, A.A., Clark, W.J., Moore, W.R. & Dribus, J.R. (2010) Diagenesis and Reservoir Quality. *Oilfield Review Summer 2010*, 22 (2).

Taylor, R.K. & Smith, T.J. (1986) The Engineering Geology of Clay Minerals: Swelling, Shrinking and Mudrock Breakdown. *Clay Minerals*, 21, pp.235–260.

Tester, J.W., Anderson, B.J., Batchelor, A.S., Blackwell, D.D., DiPippo, R., Drake, E. & Petty, S. (2006) *The Future of Geothermal Energy: Impact of enhanced geothermal systems (EGS) on the United States in the 21st century*.

Teufel, L. (1987) Permeability changes during shear deformation offractured rock. *28th US Symposium on Rock Mechanics / Tucson/29 June- 1 July 1987*.

Tiab, D. & Donaldson, E.C. (2015) Petrophysics - Theory and Practice of Measuring Reservoir Rock and Fluid Transport Properties. , Fourth Edi, p.894.

Tischner, T., Evers, H., Hauswirth, H., Jatho, R., Kosinowski, M. & Sulzbacher, H. (2010) New Concepts for Extracting Geothermal Energy from one Well: The GeneSys-Project. In: *Proceedings World Geothermal Congress 2010*. p.5.

Tomac, I. (2014) Micro-Mechanical Aspects of Hydraulic Fracture Propagation and Proppant Flow and Transport for Stimulation of Enhanced Geothermal Systems.

Vajdova, V., Baud, P. & T., W. (2004) Permeability evolution during localized deformation in Bentheim sandstone. *Journal of Geophysical Research, Vol. 109, B10406*.

Vaughan, A. (2017) Almost 90% of new power in Europe from renewable sources in 2016 [Internet].

Veldkamp, J.G. & Boxem, T.A.P. (2015) *Sector Outlook: Geothermal power increase in the Netherlands by enhancing the capacity*.

Weber, J. & Lepper, J. (2002) Depositional environment and diagenesis as controlling factors for petro-physical properties and weathering resistance of siliciclastic dimension stones: integrative case study on the 'Wesersandstein' (northern Germany, Middle Buntsandstein). In: *SIEGESMUND, S., WEISS, T. & VOLLBRECHT, A. 2002. Natural Stone, Weathering Phenomena, Conservation Strategies and Case Studies. Geological Society, London, Special Publications, 205*. pp.103–114.

www.coretest.com/ (2016) SFG-426 Single Face Grinder [Internet]. Available from: <http://www.coretest.com/product_detail.php?p_id=19> [Accessed 1 May 2017].

www.geothermie.nl (2017) 'Installaties in Nederland' [Internet]. Available from: <www.geothermie.nl> [Accessed 4 July 2017].

www.nlog.nl (2017) No Title [Internet]. Available from: <http://nlog.nl/keuzelijst-boringen> [Accessed 3 July 2017].

Xiao, J.Q., Feng, X.T., Ding, D.X. & Jiang, F. (2011) Investigation and modeling on fatigue damage evolution of rock as a function of logarithmic cycle. *Int. J. Numer. Anal. Meth.. Geomech.*, 35, pp.1127–1140.

Yew, C.H. & Jogi, P.N. (1978) The Determination of Biot's Parameters for Sandstones. *Experimental Mechanics*, pp.167–172.

Zanotto, E.D. (2005) Pressure dependence of viscosity. *The Journal of Chemical Physics 122(7):074511, March 2005*.

Zoback, M.D. (2007) *Reservoir Geomechanics*. Cambridge.

Table of Figures

List of Tables

Appendices

Appendix A Introduction

A.1 Binary Cycle System

Schematic diagram presenting the basic concept of a geothermal binary cycle system (Frick et al., 2010). A heat exchanger can be used to extract additional heat from the water before reinjection. This energy can be used, for example, for district heating.

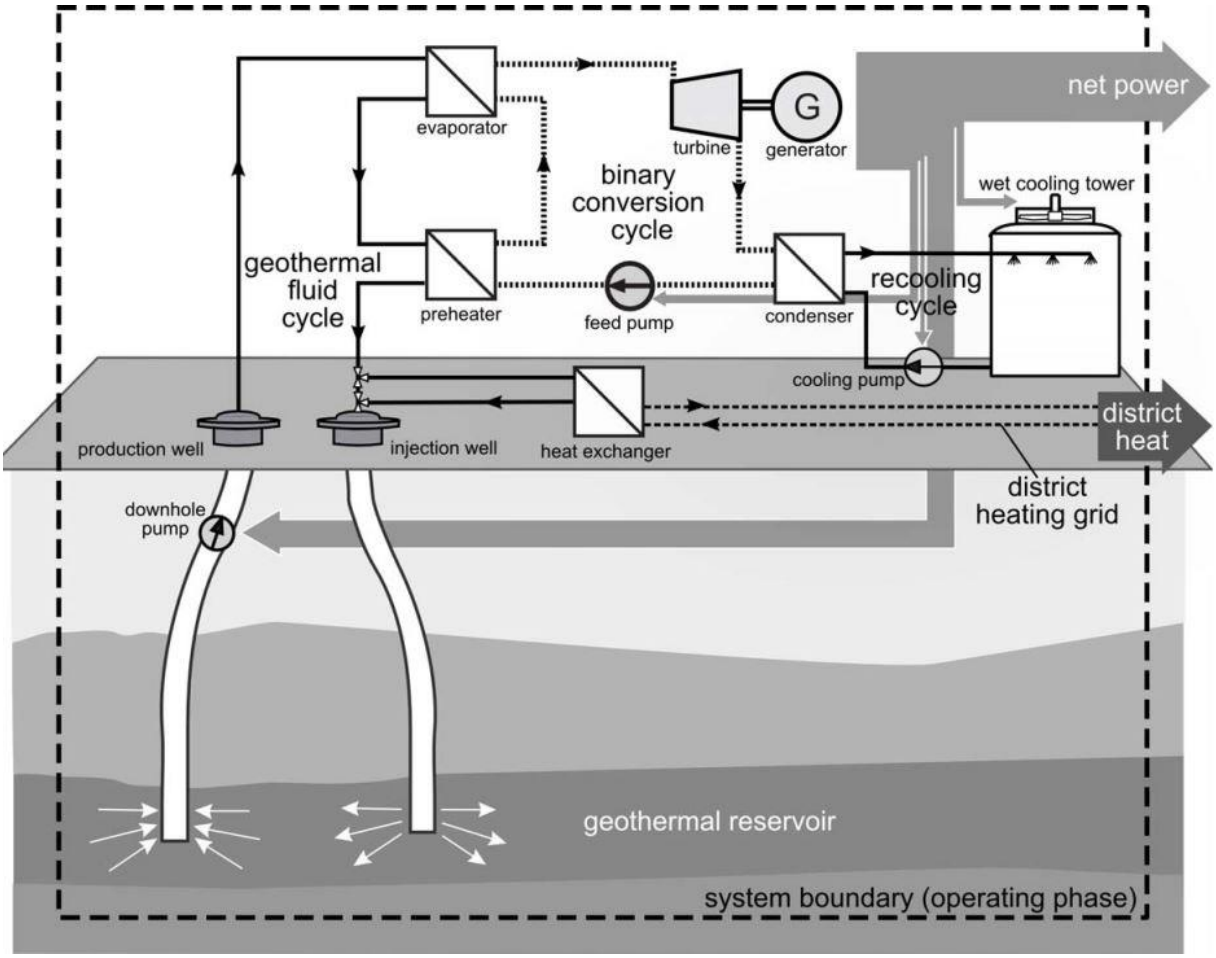

A.2 Fracture Types

Stress conditions for 3 types of fractures: Extension fractures, shear fractures and hybrid extension-shear fractures (after Singhal & Gubpta, 2010).

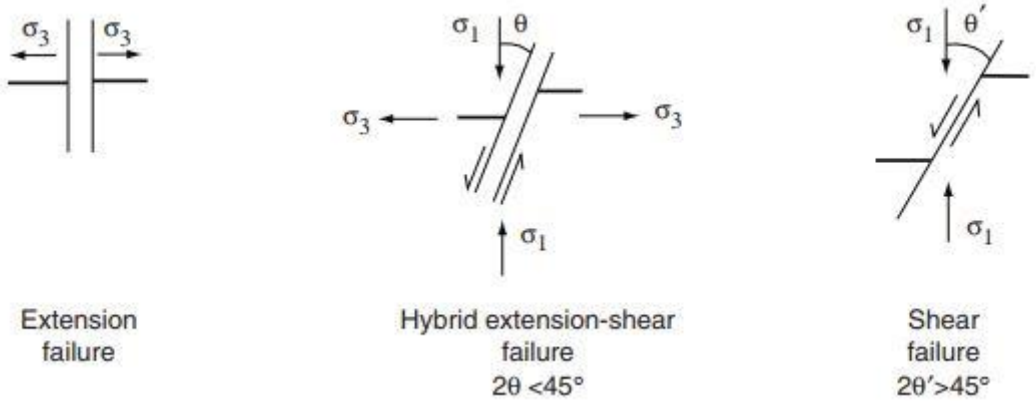

Appendix B Regional Geology

B.1 Triassic Depth Map

Triassic depth map of the Netherlands onshore (after De Mulder et al., 2003).

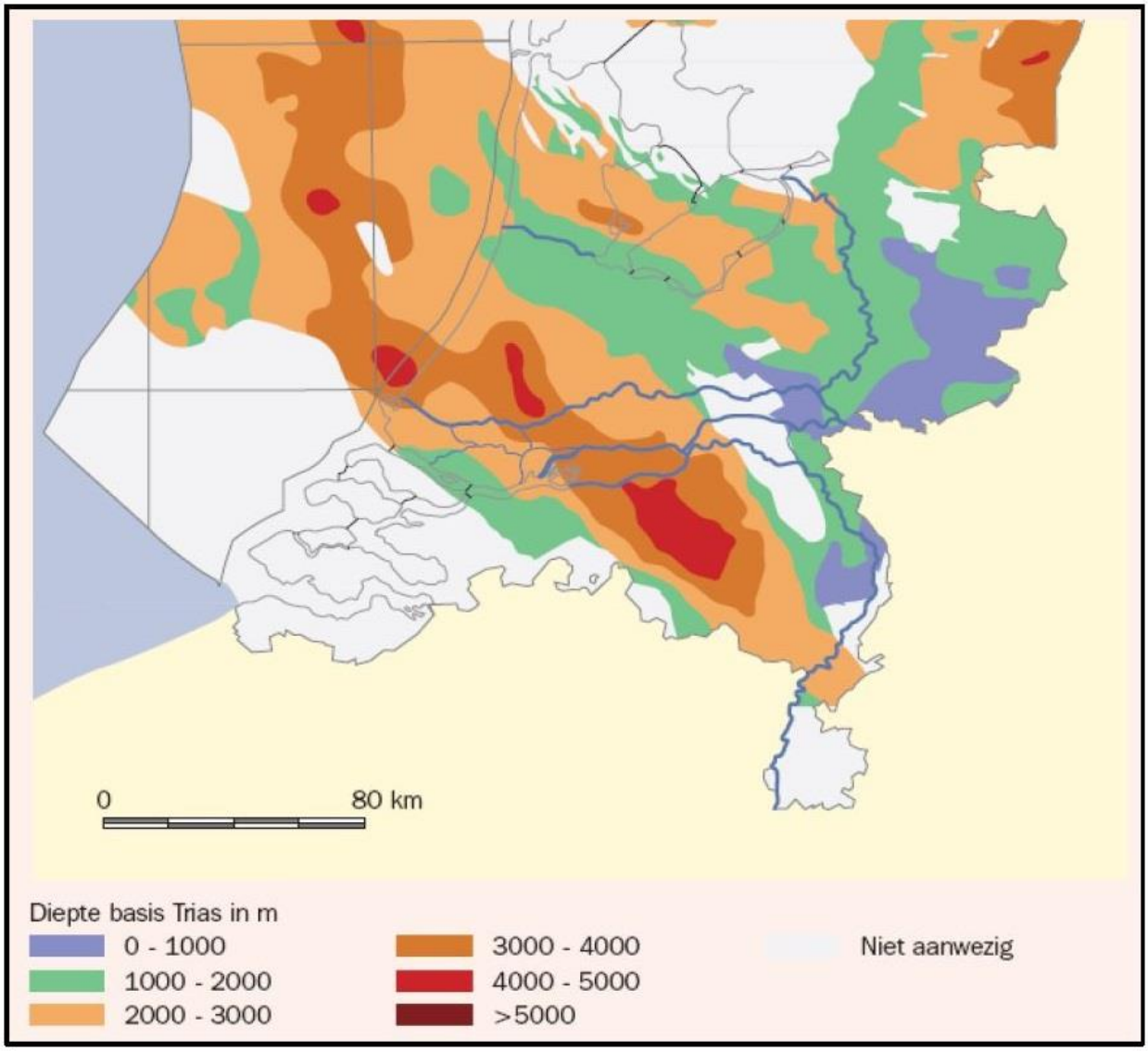

B.2 Thickness Distribution

Thickness distribution of each formation calculated from the well intersections with the formation that were evaluated in the cross section in Figure 1.23. The main reservoir sections of the Main Buntsandstein are indicated in yellow. Non reservoir sections are shown in grey.

Formation	Thickness [m]		
	Average	Maximum	Minimum
Solling Claystone Member	19	58	3
Basal Solling Sandstone Member	4	9	1
Hardegsen Sandstone	40	52	11
Detfurth Claystone	17	29	8
Detfurth Sandstone	10	20	4
Volpriehausen Clay-Siltstone	30	73	3
Volpriehausen Sandstone	39	67	7
Rogenstein	72	129	8
Main Claystone	105	154	35

B.3 Wells in the Buntsandstein

List of wells used for the reservoir characterization of the Buntsandstein in the WNB. Wells used for the permeability characterization are marked in bold, pressure data has been taken from wells marked in italic, and temperature data was used from wells indicated in light grey.

ARV-01	***GAG-03***	*LSM-01*	OAS-01	**RZB-01**	URS-01	**WWN-01-S2**
BRAK-01	**GAG-05**	***MKP-14***	***OBLZ-01***	*SGZ-01-S1*	***VAL-01***	***WWN-03***
BRT-02-S1	*GAG-06-S1*	*MOL-02-S2*	***OTL-01***	*SPG-01-S2*	WAA-01	**WWS-01-S1**
BRTZ-01	*HEK-01*	*MON-02*	*PKP-01*	SPK-01	*WAS-23-S2*	**WWS-02**
BRTZ-02-S3	*HST-02-S1*	*MON-03*	***PRW-01***	**SPKO-01-S1**	WED-02	
BRTZ-03	HSW-01-S1	MRK-01	PRW-02	***SPKW-01***	***WED-03***	
BSKP-01	*HVB-01*	**MSG-01**	PRW-04	SPL-01	*WGD-01*	
BTL-01	HVS-01	**MSG-02**	PRW-05	SPL-01-S1	WLK-01	
CAP-01	IJS-64-S2	MSV-01	***RDK-01***	STM-01-S1	WRV-01	
GAG-02-S1	***LIR-45***	***NWK-02***	***RTD-01***	**STW-01**	WWK-01	

permeability	temperature	*pressure*

B.4 West Netherlands Basin Cross-Section

Well correlation through the West Netherlands Basin from well RZB-01 (A) to URS-01 (I). The exact location of the wells used in the well correlation is shown in the overview map below. The overview map was created in Google Earth Pro.

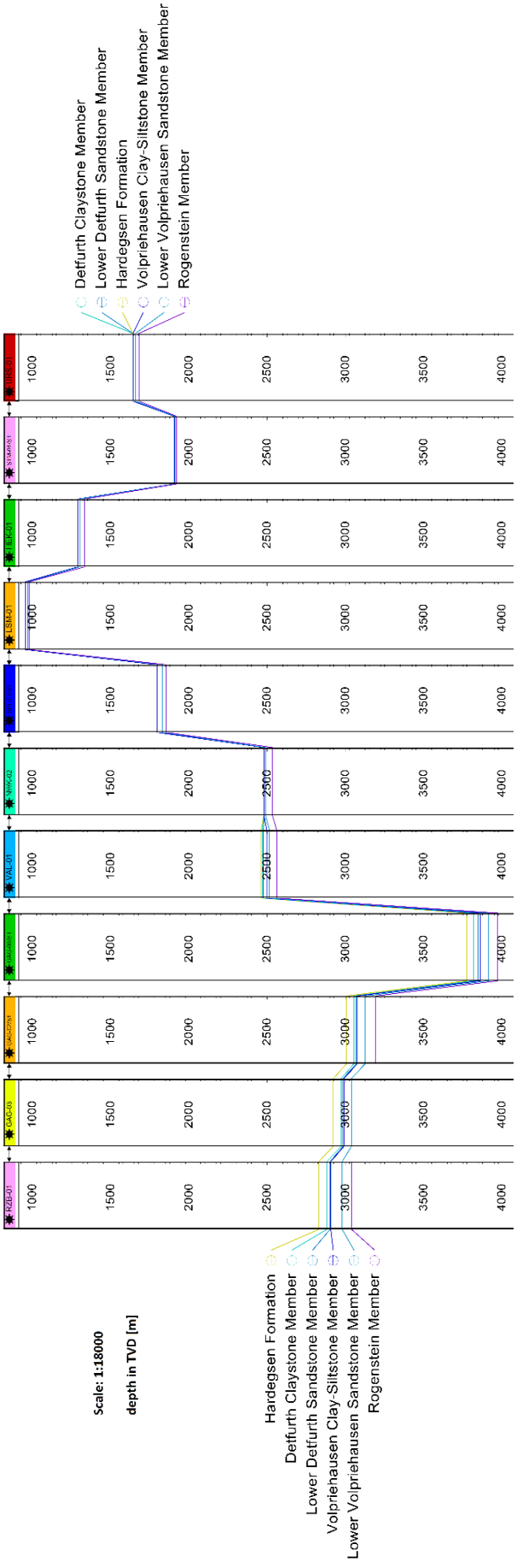
Detfurth Claystone Member
Lower Detfurth Sandstone Member
Hardegsen Formation
Volpriehausen Clay-Siltstone Member
Lower Volpriehausen Sandstone Member
Rogenstein Member
URS-01
STM-01-S1
HEK-01
LSM-01
SPL-01
NWK-02
VAL-01
GAG-03
RZB-01
1000
1500
2000
2500
3000
3500
4000
Scale: 1:18000
depth in TVD [m]
Hardegsen Formation
Detfurth Claystone Member
Lower Detfurth Sandstone Member
Volpriehausen Clay-Siltstone Member
Lower Volpriehausen Sandstone Member
Rogenstein Member

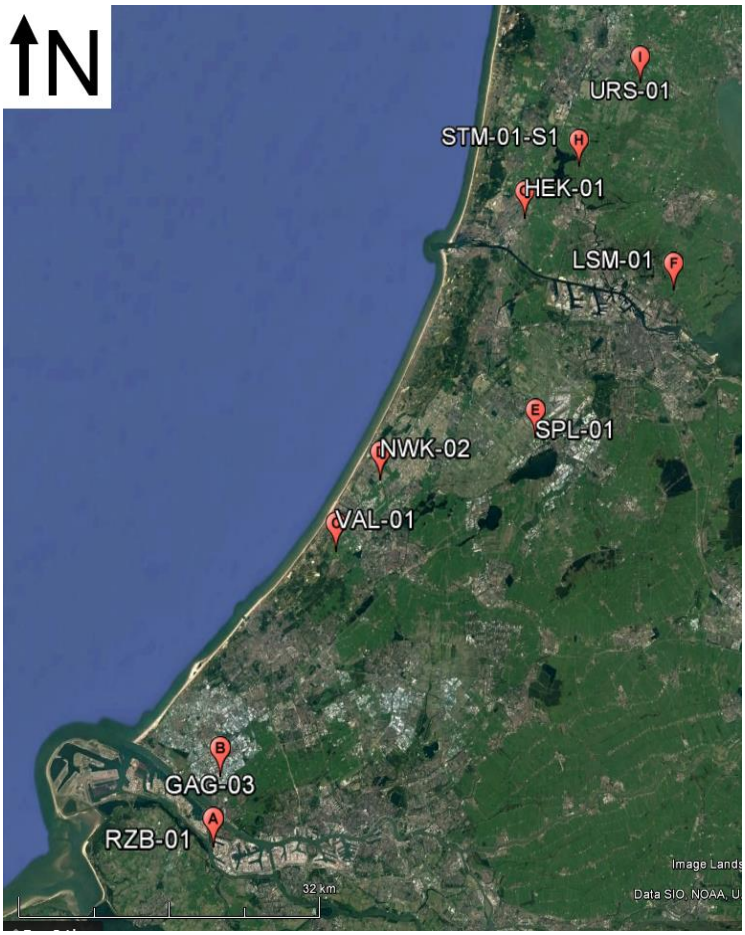
N
URS-01
STM-01-S1
HEK-01
LSM-01
SPL-01
NWK-02
VAL-01
GAG-03
RZB-01
32 km
Image Lands
Data SIO, NOAA, U

B.5 Wells in the West Netherlands Basin

Overview map of the Netherlands showing the locations of all wells listed in Appendix B.3. Source: Google Earth Pro.

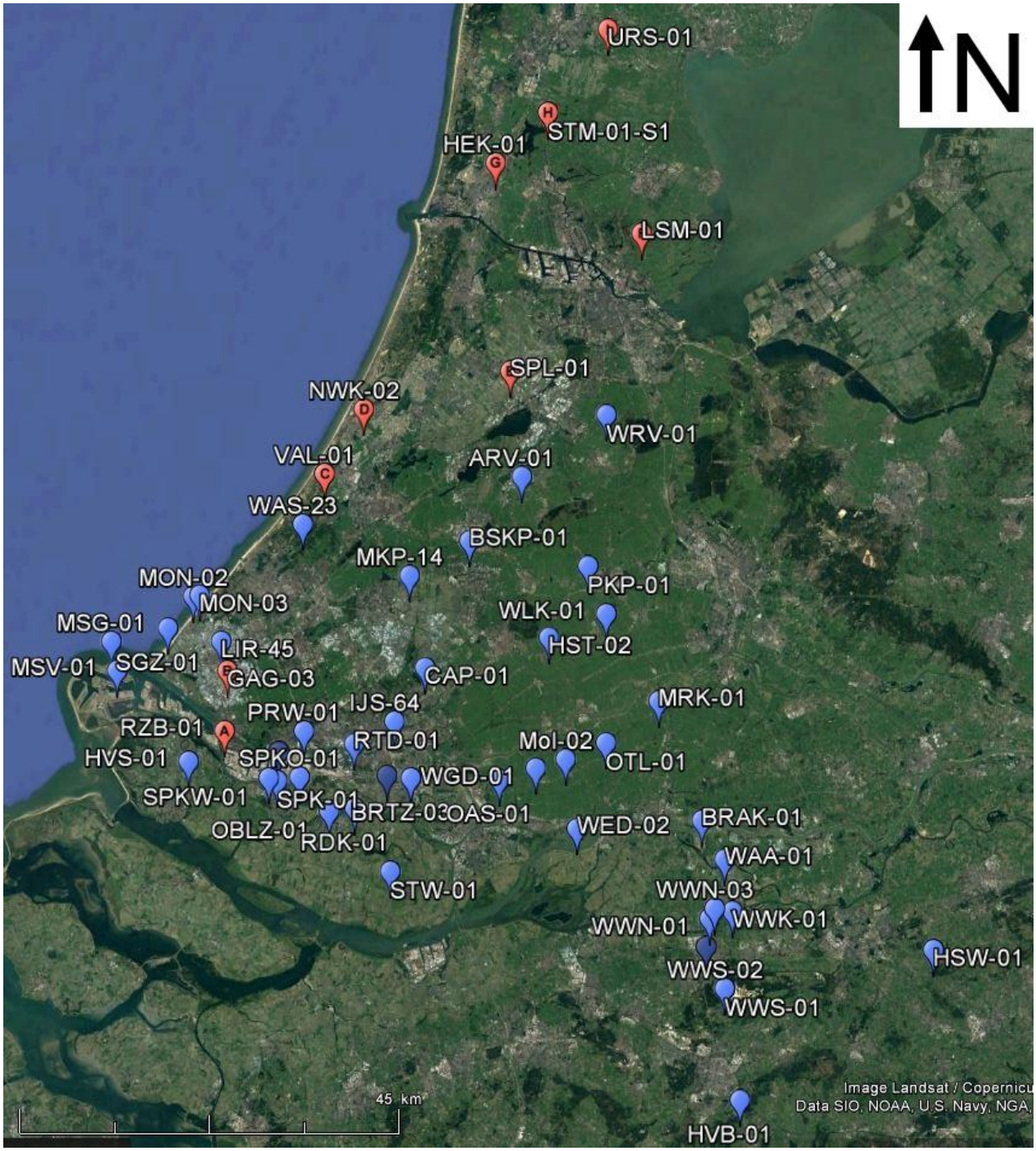

B.6 Geothermal Projects in the Netherlands

Table listing the developed geothermal projects in the WNB with the according production temperature and depth. Source: https://geothermie.nl/index.php/nl/geothermie-aardwarmte/installaties-in-nederland; last accessed: 3.07.2017.

Geothermal project	Depth [m]	Production temperature of water [°C]
Van den Bosch 1 & 2	1600	60
Van den Bosch 3 & 4	1800	70
Vierpolders	2200	82
De Lier 1 & 2	2600	85
Nature's Heat	2500	85
Green Well Westland	2900	85
Duijvestijn	2300	70
Aardwarmte Vogelaer	2500	85
Ammerlaan TGI	2100	70
Floricultura Heemskerk	2700	100

B.7 Temperature Correction

Graph of corrected temperature versus depth in the West Netherlands Basin.

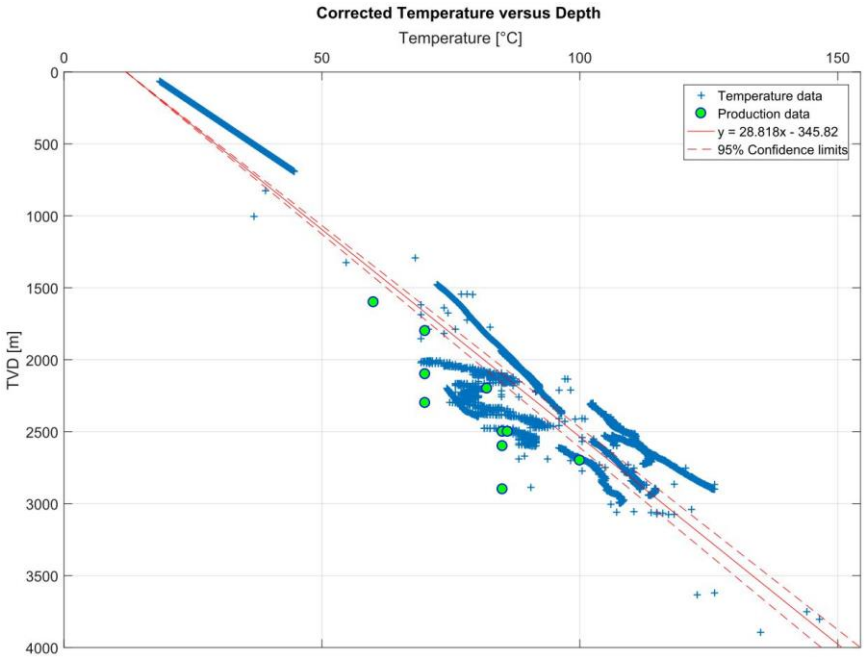

Appendix C Methodology

C.1 Quarry Locations

Buntsandstein unaltered (blocks coded as SBS6-BD): Bad Dürkheim, GPS: 49.477361, 8.156390, Quarry owner: Otto Göbel GmbH

Buntsandstein altered (Roter Mainsandstein; blocks coded as SRM6-MI): Miltenberg, GPS: 49.713244, 9.254810, Quarry owner: Peter Wassum GmbH

Bentheim sandstone: Nordhorn, GPS: 52.30234, 7.105134, Quarry owner: Natursteinwerk Monser GmbH

Rüthener Grünsandstein (blocks coded as SRG6-RU): Rüthen, Quarry owner: Rüthener Grünsandstein-Werk Kirsch GmbH

C.2 General Sample Properties

Sample Properties. Values in brackets are rough estimations. ϕ = porosity, n.d. = not detected.

Sample block	Sample	Core direction	Length [mm]	Diameter [mm]	Mass [g]	ϕ [%]
SBS6-BD-50	BD-50-Y1	Y	76.2	29.70	n.d.	(14)
	BD-50-Y2	Y	75.70	29.78	n.d.	n.d
	BD-50-Y4	Y	75.20	29.71	n.d.	n.d
	BD-50-Z1	Z	75.65	29.75	n.d.	(14)
	BD-50-Z2	Z	73.43	29.79	n.d.	n.d
	BD-50-Z3	Z	75.35	29.79	n.d.	n.d
SBS6-BD-51	BD-51-X1	X	70.51	29.81	102.05	23.24
	BD-51-Y1	Y	70.86	29.81	103.19	24.21
	BD-51-Z1	Z	70.45	29.82	102.36	22.80
	BD-51-Z2	Z	70.48	29.83	102.34	23.62
SBS6-BD-52	BD-52-X1A	X	75.01	29.66	112.01	18.64
	BD-52-X1B	X	74.63	29.67	110.87	18.64
	BD-52-Z1	Z	74.51	29.69	109.90	20.14
	BD-52-Z2	Z	74.50	29.68	109.84	22.20
SBS6-BD-53	BD-53-X2A	X	74.86	29.67	111.53	20.82
	BD-53-X2B	X	74.5	29.67	110.73	20.82
	BD-53-Z1A	Z	75.05	29.68	110.89	20.47
	BD-53-Z2B	Z	74.37	29.68	109.45	20.11
SBS6-BD-54	BD-54-X3A	X	75.07	29.68	111.10	19.49
	BD-54-Z2A	Z	74.78	29.70	113.24	19.14
SRM6-MI-50	MI-50-Y1	Y	76.10	29.77	n.d.	(14)
	MI-50-Y2	Y	75.42	29.79	116.79	(14)
	MI-50-Y3	Y	75.45	29.75	n.d.	n.d
	MI-50-Y4	Y	75.73	29.75	115.99	18.51
	MI-50-Y5	Y	75.10	29.80	115.30	(14)
	MI-50-Y6	Y	75.48	29.79	n.d.	n.d
	MI-50-Z1	Z	75.71	29.78	n.d.	n.d
	MI-50-Z2	Z	72.02	29.80	113.84	(14)
	MI-50-Z3	Z	75.45	29.73	n.d.	n.d
SRM6-MI-52	MI-52-X1	X	70.02	29.72	116.91	9.73
	MI-52-Y3A	Y	48.97	29.74	81.95	9.30
	MI-52-Y2C	Y	74.90	29.65	121.38	9.98
	MI-52-Y3B	Y	73.63	29.71	123.91	9.73
	MI-52-Y4A	Y	70.92	29.71	115.68	9.98
	MI-52-Z6	Z	49.10	29.70	81.45	9.98
	MI-52-Z7	Z	75.13	29.68	125.76	9.98
	MI-52-Z8	Z	48.86	29.70	79.84	10.91
SRG6-RU	RU-X1	X	75.37	29.67	108.74	22.72
	RU-X3	X	74.65	29.69	107.13	24.87
	RU-Z3	Z	75.12	29.68	108.13	27.47
Bentheimer Sandstone		n.d.	75.27	29.69	n.d.	(20)

C.3 Triaxial Experiment Set-up Procedure

- Applying vacuum to the jacketed sample to suck all air out of the system
- Flushing the core with CO2 (around 20 minutes)
- Flushing the pipe from pump A with water
- Connecting the pipe from pump A to the core and flushing water through the core
- Connecting the pipe of pump B to the core and flush it with water
- Flushing the pipes from the pore pressure difference measurement tool
- Start applying a confining pressure (e.g., 50 bars)
- Applying a pore pressure of 25 bars
- Flushing the core with 3 times the pore volume of the core sample

C.4 Triaxial Steel Pistons

Upper steel piston with a uniform carving to distribute the water evenly trough specimens, once the rock sample is mounted on and flushed with water.

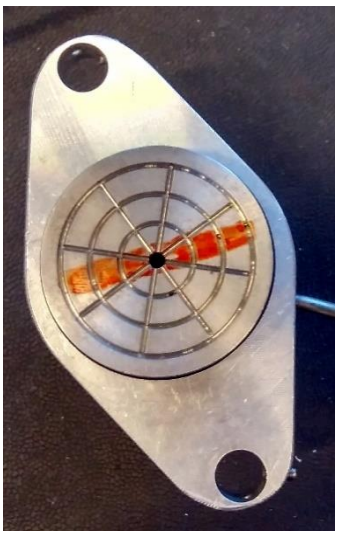

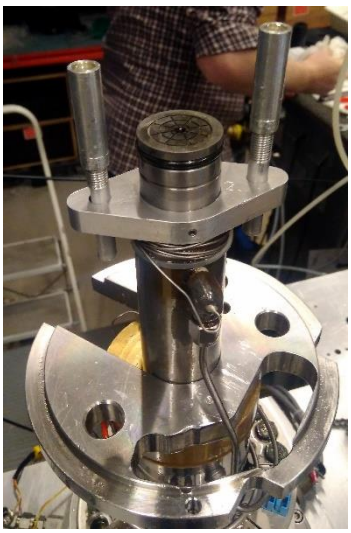

C.5 XRF Sample Analysis Results

SRM6-M1-52	
Compound	Conc. [wt%]
SiO2	82.166
Al2O3	10.653
K2O	3.899
Fe2O3	1.480
MgO	0.632
TiO2	0.219
Na2O	0.217
CaO	0.151
P2O5	0.147
NiO	0.111
BaO	0.099
SO3	0.089
Cl	0.025
ZrO2	0.021
Cr2O3	0.019
ZnO	0.018
PbO	0.015
SrO	0.012
MnO	0.011
Rb2O	0.011
CuO	0.004

SRM6-M1-50	
Compound	Conc. [wt%]
SiO2	84.805
Al2O3	9.756
K2O	3.435
Fe2O3	0.799
MgO	0.458
Na2O	0.245
P2O5	0.099
NiO	0.096
TiO2	0.082
CaO	0.066
BaO	0.059
Cr2O3	0.024
Cl	0.023
SO3	0.017
SrO	0.010
Rb2O	0.010
ZrO2	0.009
CuO	0.004
PbO	0.003
ZnO	0.002

SBS6-BD-50	
Compound	Conc. [wt%]
SiO2	86.175
Al2O3	8.532
K2O	2.563
Fe2O3	1.202
MgO	0.399
TiO2	0.353
BaO	0.224
Na2O	0.152
SO3	0.122
NiO	0.109
P2O5	0.045
CaO	0.042
Cr2O3	0.022
ZrO2	0.022
Cl	0.014
Rb2O	0.008
SrO	0.007
CuO	0.003
PbO	0.002
ZnO	0.002

SBS6-BD-51	
Compound	Conc. [wt%]
SiO2	89.506
Al2O3	6.499
K2O	2.337
Fe2O3	0.879
MgO	0.216
Na2O	0.154
NiO	0.120
TiO2	0.088
BaO	0.040
P2O5	0.035
CaO	0.032
Cr2O3	0.026
Cl	0.018
SO3	0.013
ZrO2	0.008
Rb2O	0.007
MnO	0.006
SrO	0.005
CuO	0.003
PbO	0.003
ZnO	0.002

SBS6-BD-52	
Compound	Conc. [wt%]
SiO2	87.847
Al2O3	7.760
K2O	2.616
Fe2O3	0.851
MgO	0.300
Na2O	0.159
TiO2	0.145
NiO	0.111
BaO	0.048
CaO	0.041
P2O5	0.039
Cl	0.020
Cr2O3	0.016
SO3	0.011
ZrO2	0.010
Rb2O	0.008
MnO	0.008
SrO	0.007
PbO	0.003

SBS6-BD-52	
Compound	Conc. [wt%]
SiO2	87.785
Al2O3	7.654
K2O	2.512
Fe2O3	0.975
MgO	0.311
TiO2	0.186
Na2O	0.160
NiO	0.146
CaO	0.045
P2O5	0.042
BaO	0.041
Cr2O3	0.035
SO3	0.027
CeO2	0.024
Cl	0.014
ZrO2	0.012
Rb2O	0.008
MnO	0.007
SrO	0.006
PbO	0.004
CuO	0.004
ZnO	0.003

C.6 Stress Intensity Factor Estimation

Estimate of the stress intensity factor (SIF) for a dimensionless radius of 0.15 used for the rock specimens of the Buntsandstein. A qualitative estimate of the dimensionless SIF gave a value of 0.08. The red lines indicate the taken values. The graph was extracted from Guo et al., (1993).

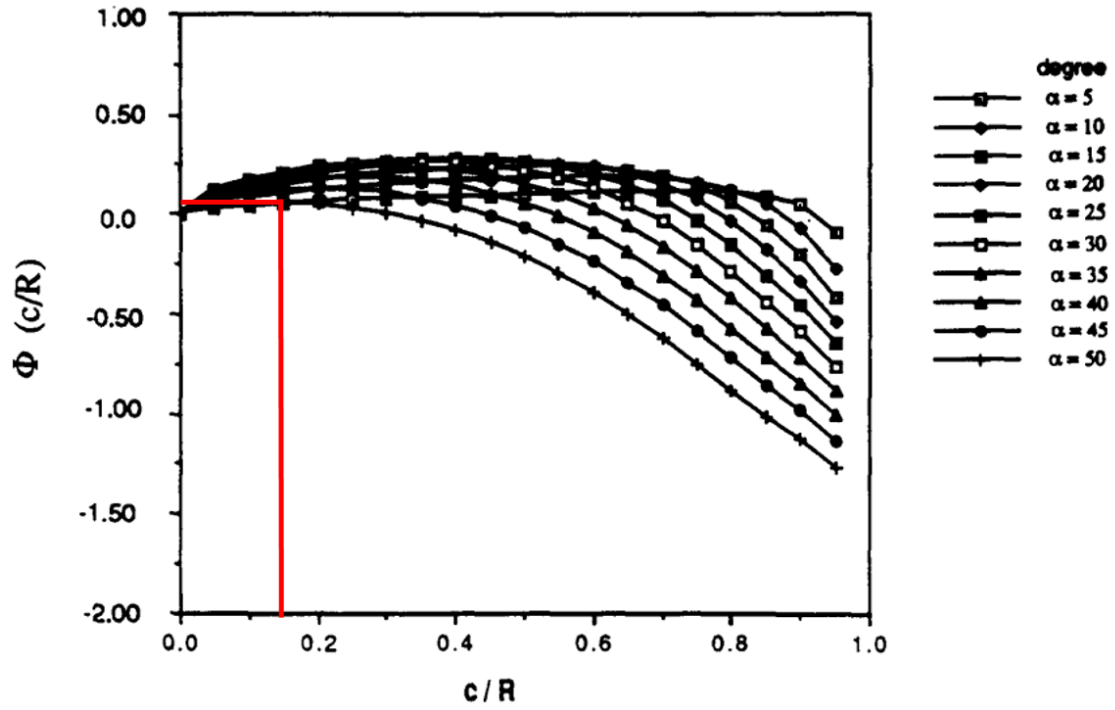

Appendix D Rock Characterization

D.1 Microstructural Analysis

Images of thin sections with the petrographic microscope and secondary-electron (SE) images collected with the EPMA.

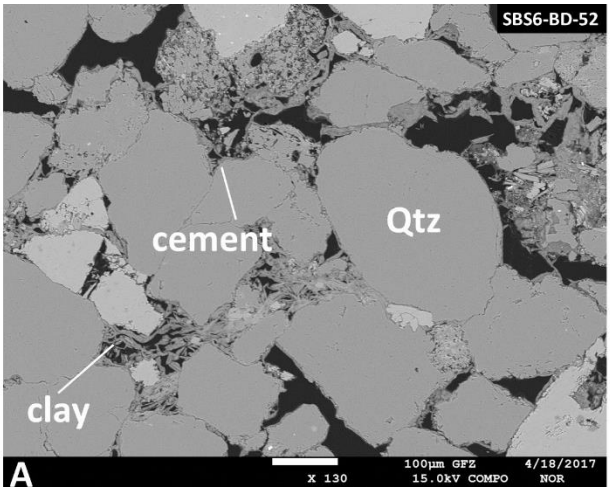

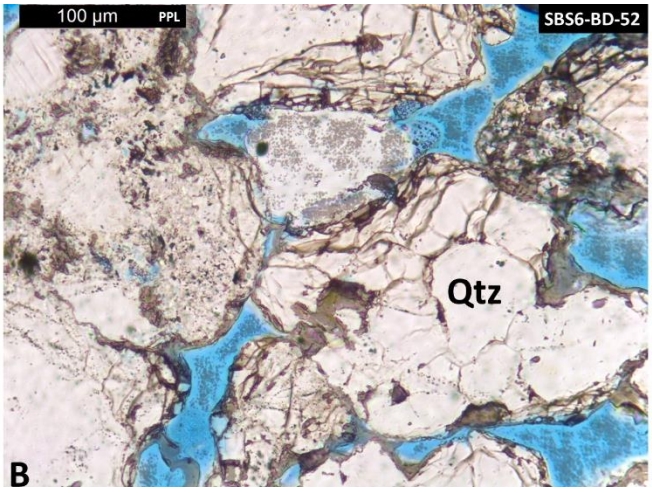

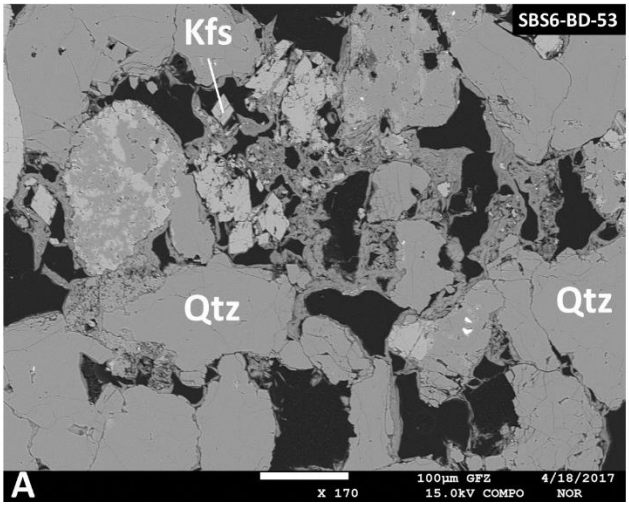
SBS6-BD-53
Kfs
Qtz
Qtz
A
x 170
100µm GFZ
15.0kV COMPO
4/18/2017
NOR

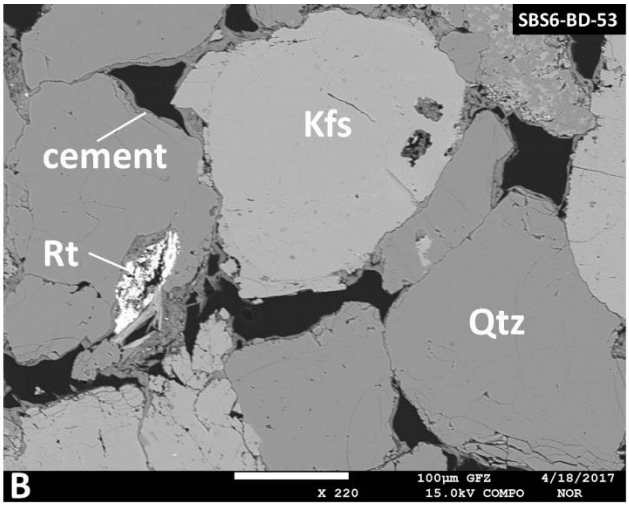
SBS6-BD-53
cement
Kfs
Rt
Qtz
B
x 220
100µm GFZ
15.0kV COMPO
4/18/2017
NOR

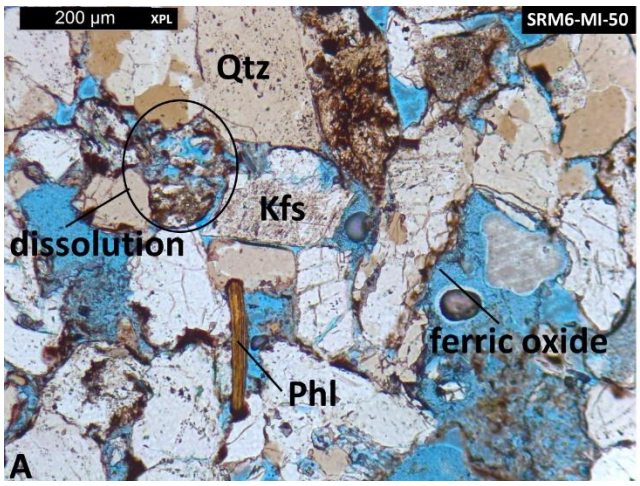
200 µm
XPL
SRM6-MI-50
Qtz
Kfs
dissolution
ferric oxide
Phl
A

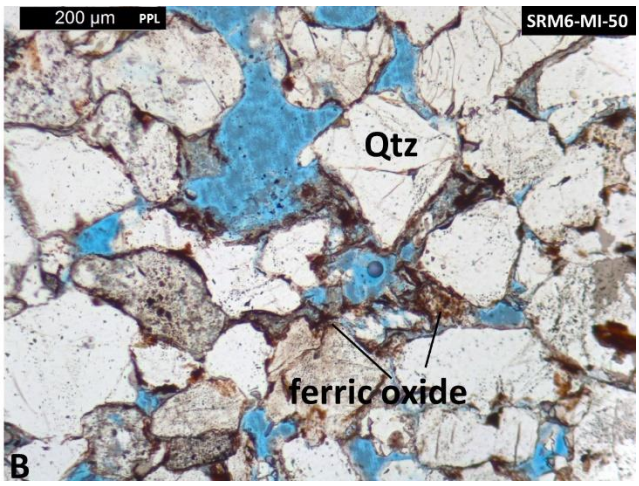
200 µm
PPL
SRM6-MI-50
Qtz
ferric oxide
B

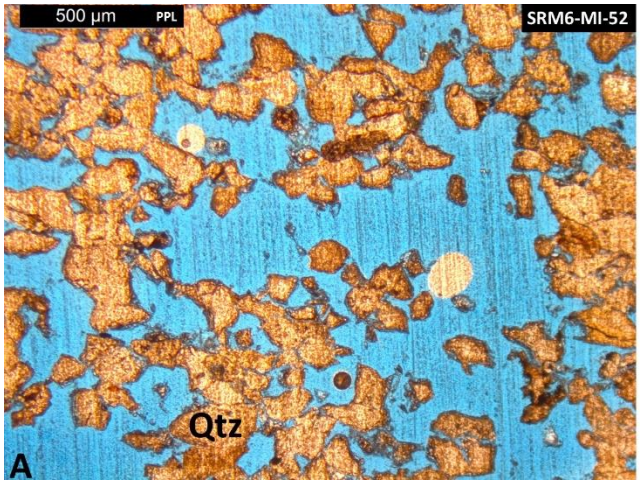
500 µm
PPL
SRM6-MI-52
Qtz
A

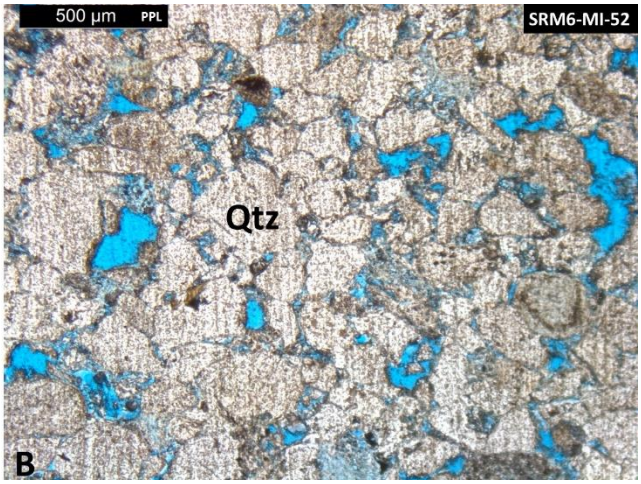
500 µm
PPL
SRM6-MI-52
Qtz
B

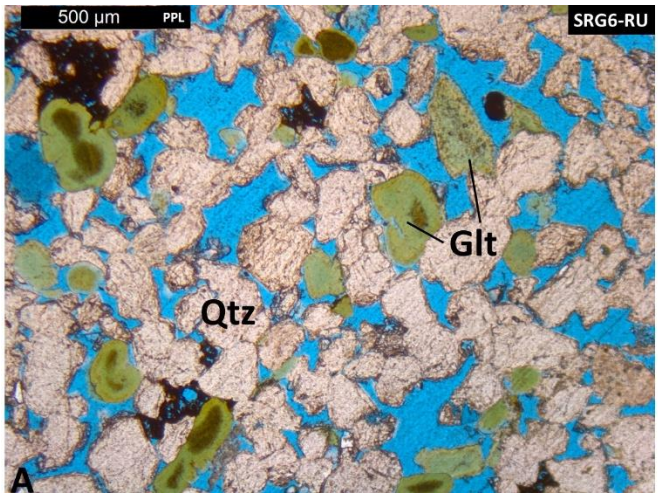

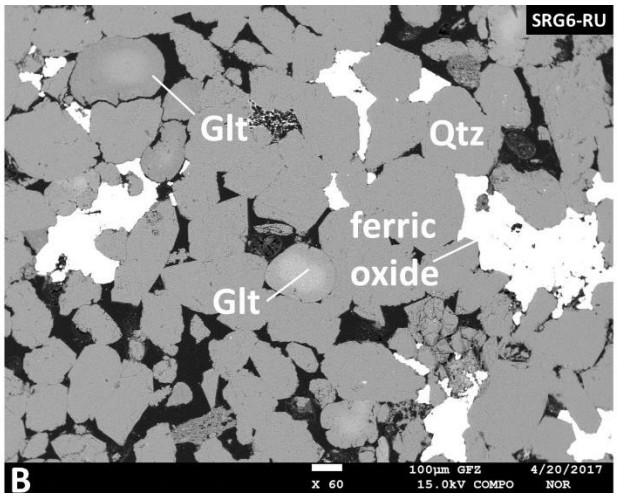

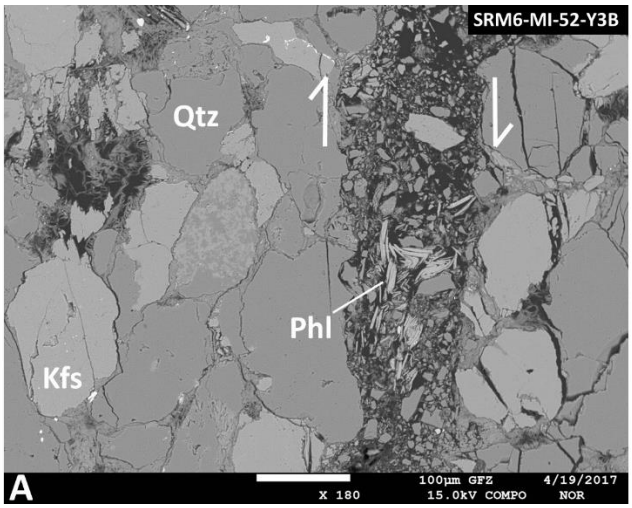

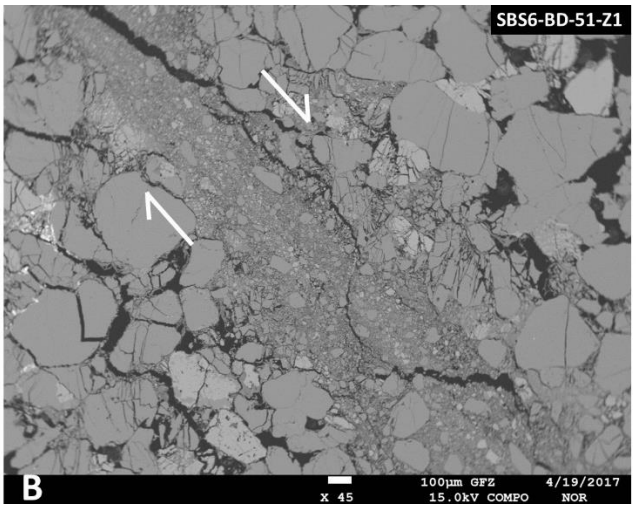

D.2 Sandstone Classification

Classification of the sample sandstones after Folk (1965):

Q = quartzose grains; F = feldspars; R = rock fragments.

Due to the similarity of the sandstones in terms of composition, values were clustered. Most samples can be classified as subarkose.

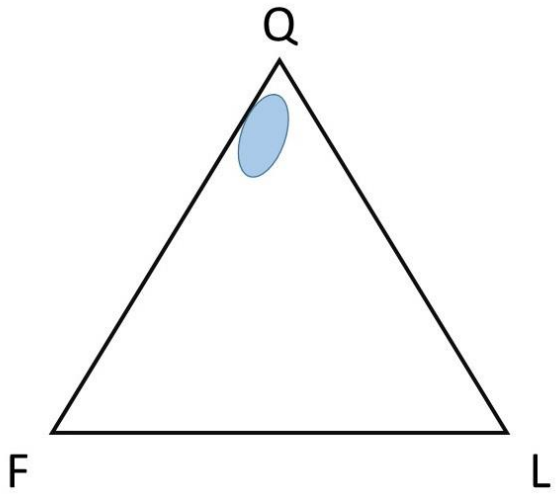

Appendix E Unconfined Compression Test

E.1 Stress-Strain Comparison

Axial strain, radial strain and volumetric strain as a function of axial stress for unaltered Buntsandstein samples BD-50-Y4 and BD-50-Z2 from unconfined compression tests.

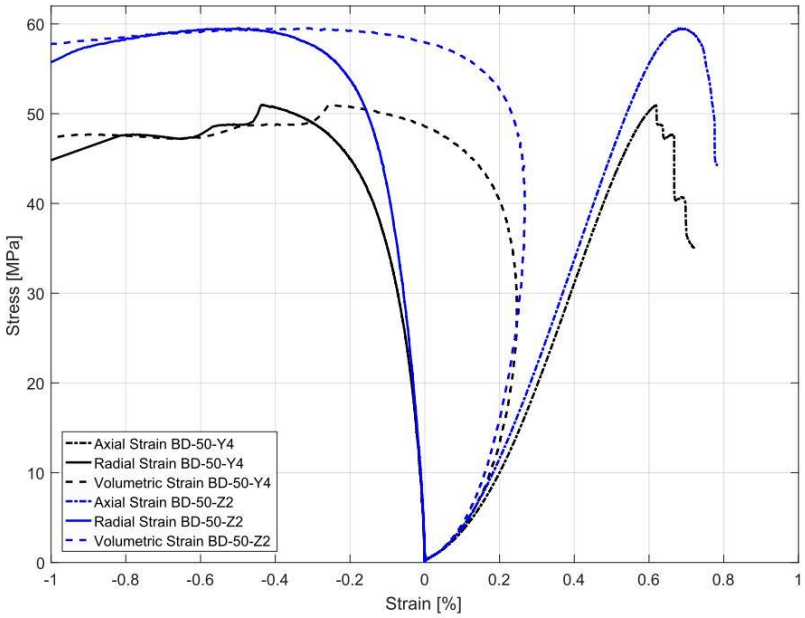

E.2 UCS Results

E.2.1

Stress-strain curves of the UCS tests with unaltered Buntsandstein cores from block SBS6-BD-50, SBS6-BD-51, SBS6-BD-52, SBS6-BD-53 and SBS6-BD-54 in Y- and X-direction.

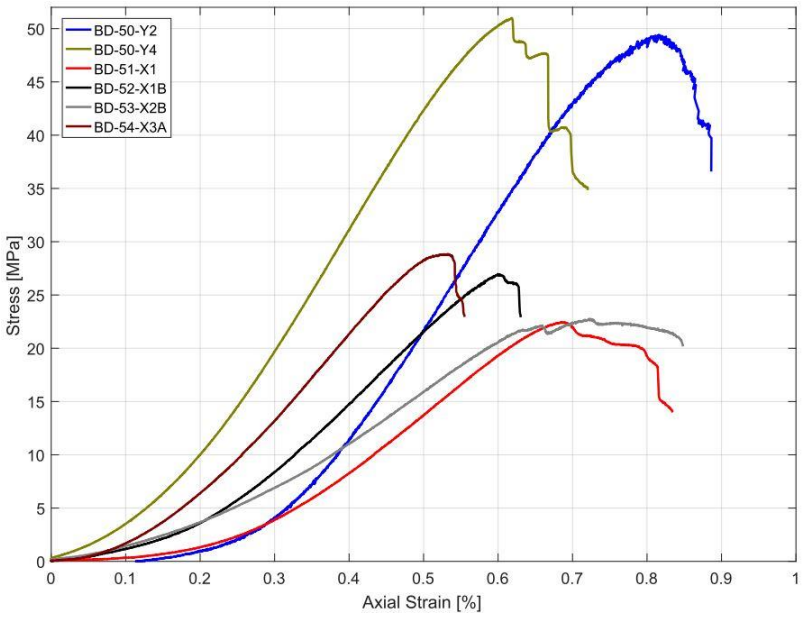

E.2.2

Stress-strain curves of the UCS tests with altered Buntsandstein cores from blocks SRM6-MI-50 and SRM6-MI-50 and from the Rüthener Grünsandstein block SRG6-RU. Cores were drilled in Y- and X-direction.

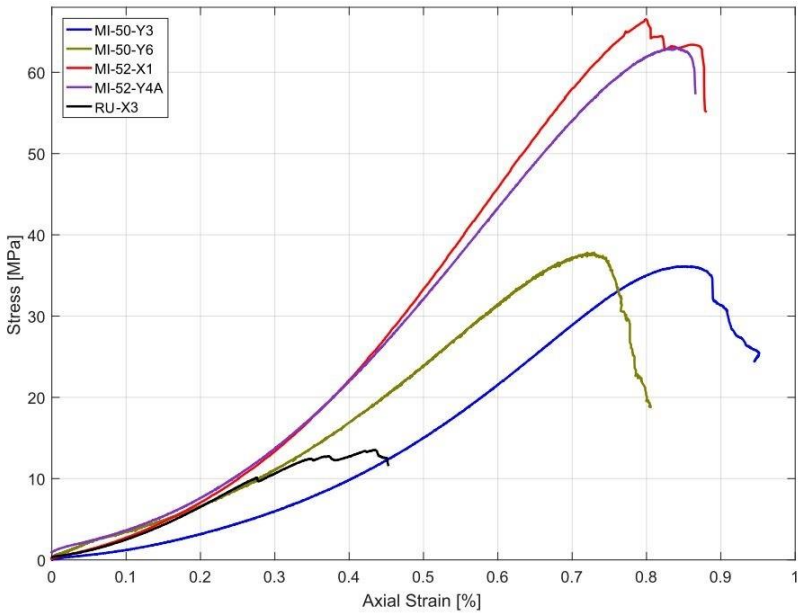

E.2.3

Stress-strain curves of the UCS tests with unaltered Buntsandstein cores from block SBS6-BD-50, SBS6-BD-51, SBS6-BD-52, SBS6-BD-53 and SBS6-BD-54 in Z-direction.

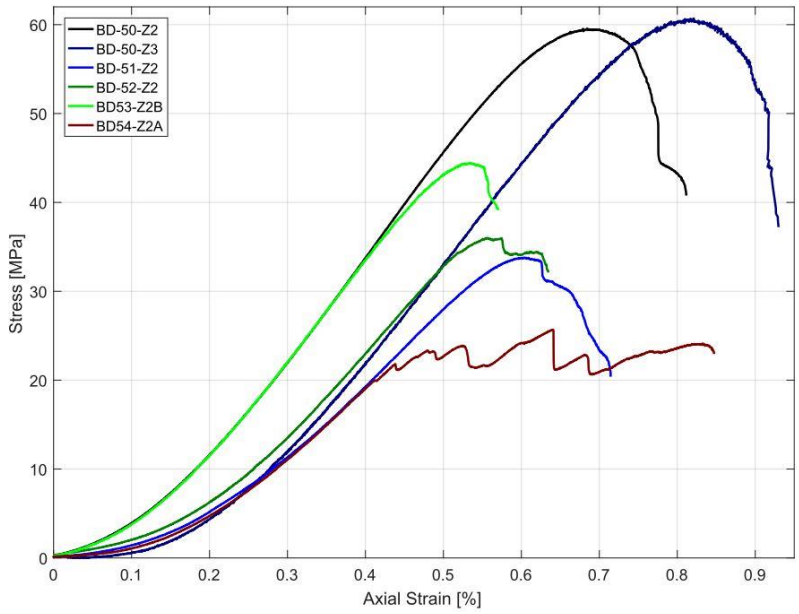

E.2.4

Stress-strain curves of the UCS tests with altered Buntsandstein cores from blocks SRM6-MI-50 and SRM6-MI-50 and from the Rüthener Grünsandstein block SRG6-RU. Cores were drilled Z-direction.

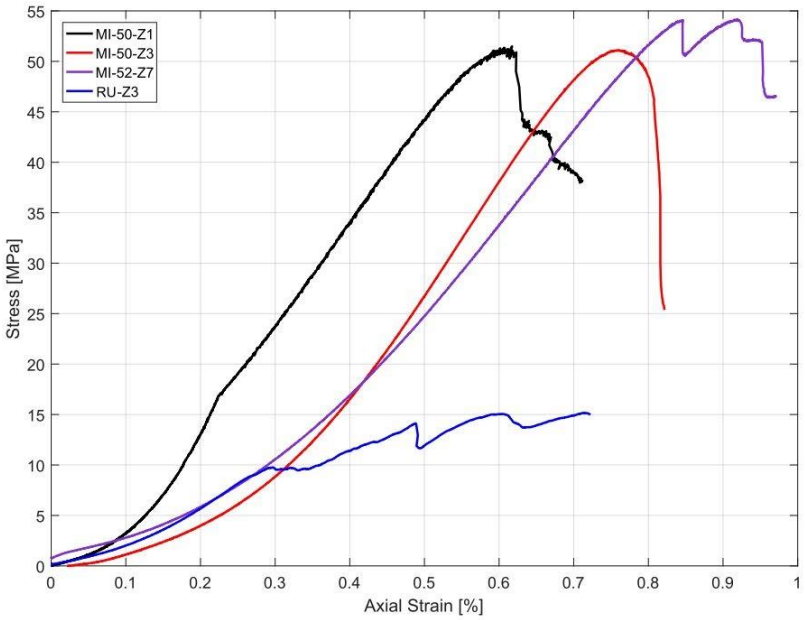

E.3 Specimens after the Uniaxial Compression Test

MI-50-Y3

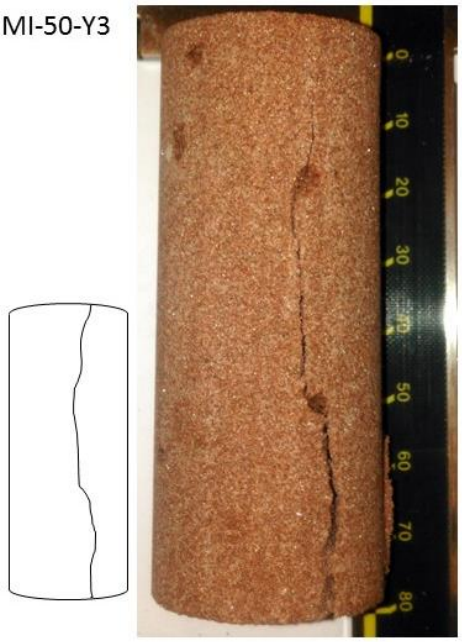

MI-50-Z3

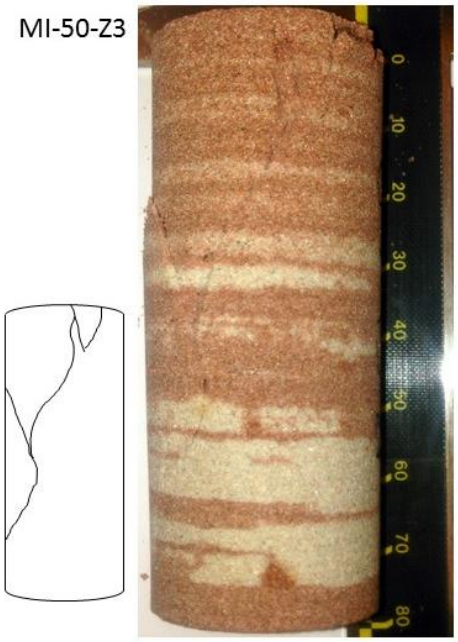

MI-50-Y6

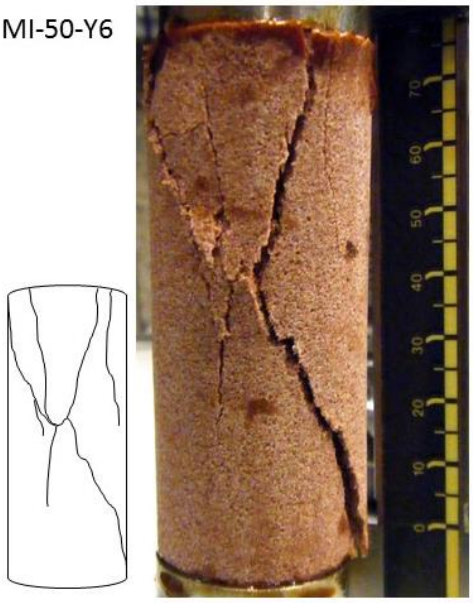

MI-50-Z1

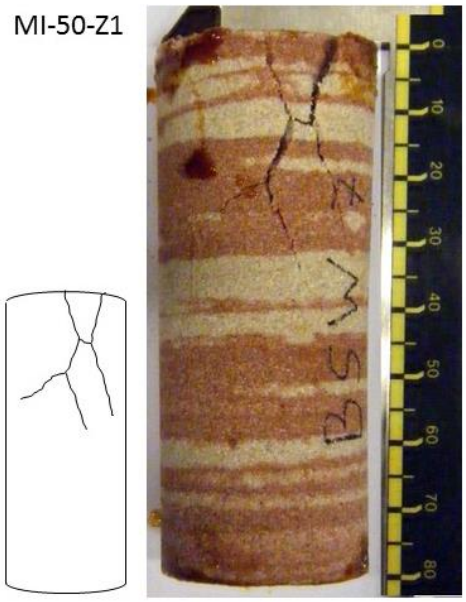

E.4 Acoustic Measurements

P- and S-wave velocities measured during the UCS tests at different levels of stress.

Sample block	Sample	Core direction	Velocities [m/s]					
			10 MPa V_p	20 MPa V_p	30 MPa V_p	10 MPa V_s	20 MPa V_s	30 MPa V_s
SBS6-BD-50	BD-50-Y2	Y	4013	4155	4209	2191	2235	2247
	BD-50-Z3	Z	3982	3997	4013	2195	2311	2370
SBS6-BD-52	BD-52-X1B	X	3625	3681	-	1857	1864	-
	BD-52-Z2	Z	3819	3911	3989	1874	1910	1926
SBS6-BD-53	BD-53-X2B	X	3441	3509	-	1903	1909	-
	BD-53-Z2B	Z	3836	3914	3990	1947	1990	1999
SBS6-BD-54	BD-54-X3A	X	4052	4051	-	2147	2155	-
	BD-54-Z2A	Z	3947	4102	-	2136	2225	-
SRM6-MI-50	MI-50-Y6	Y	3684	3903	4000	2085	2161	2191
	MI-50-Z1	Z	4258	4261	4246	2006	2015	2048
SRM6-MI-52	MI-52-Y4A	Y	3636	3869	3981	2051	2084	2132
	MI-52-Z7	Z	3918	3953	3987	2012	2061	2080
SRG6-RU	RU-X3	X	-	-	-	-	-	-
	RU-Z3	Z	4172	-	-	1833	-	-

E.5 Velocities

E.5.1

P-wave (full line) and S-wave (dotted line) velocities of samples cored in X- and Y-direction measured during UCS tests.

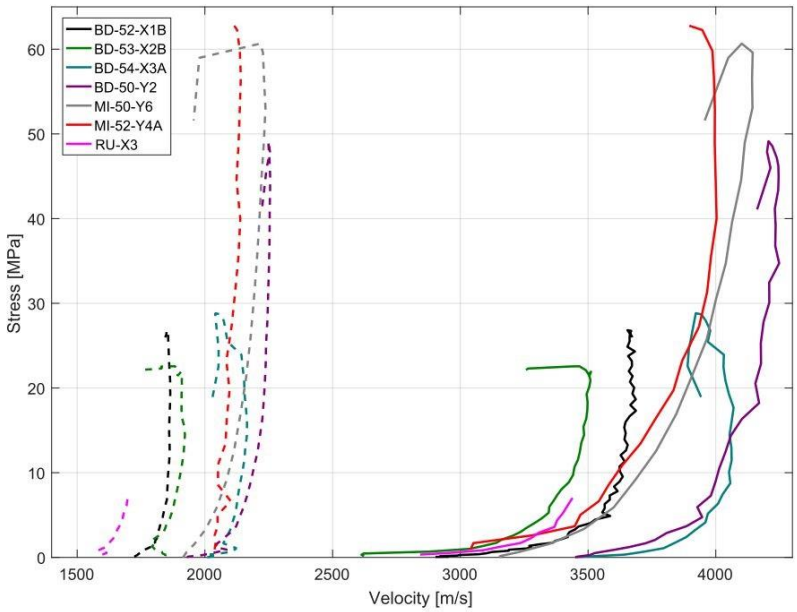

E.5.2

P-wave (full line) and S-wave (dotted line) velocities of samples cored in Z-direction measured during UCS tests.

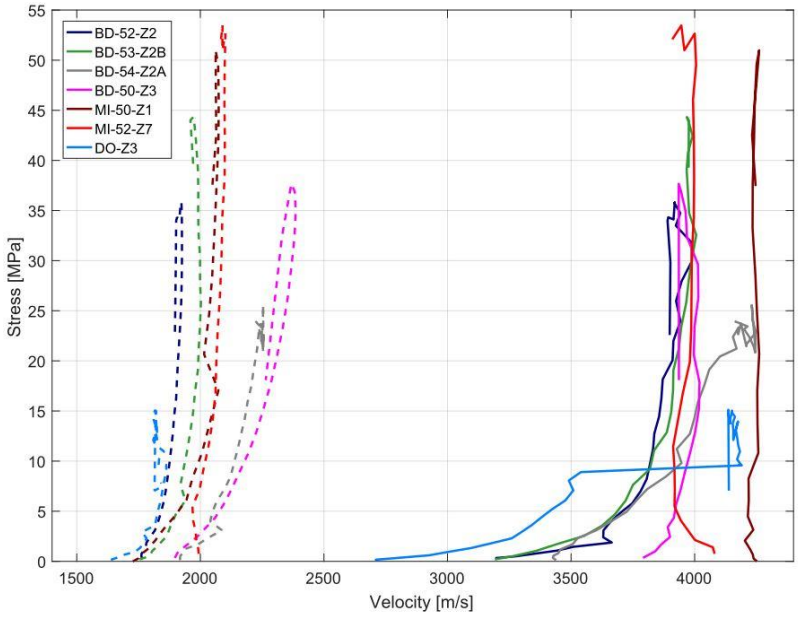

E.5.3

P-wave velocity and stress plotted against axial strain for sample BD-53-X2B. The stress was normalized to the ultimate compressive strength, the axial strain was normalized to the maximum value. The P-wave velocity was normalized to the velocity at zero axial stress.

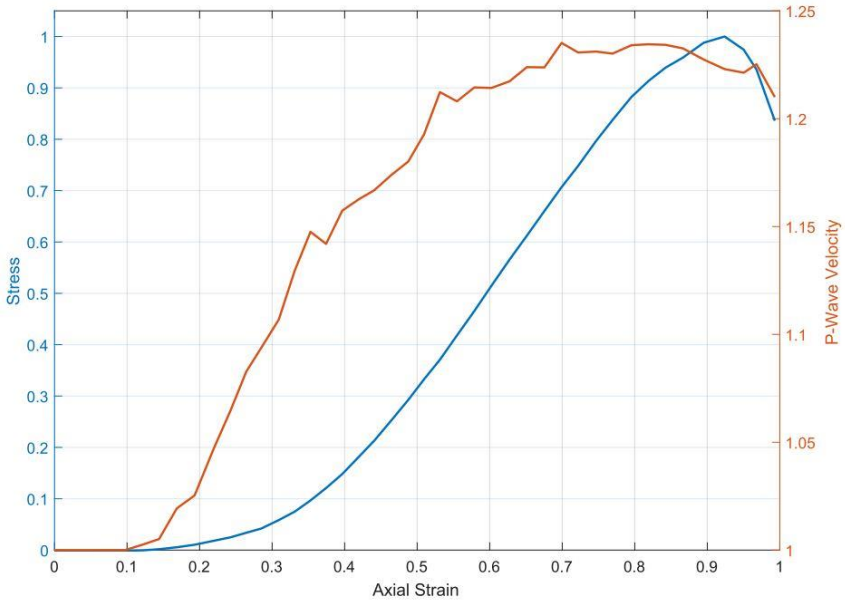

E.5.4

S-wave velocity and stress plotted against axial strain for sample BD-53-X2B. The stress was normalized to the ultimate compressive strength, the axial strain was normalized to the maximum value. The S-wave velocity was normalized to the velocity at zero axial stress.

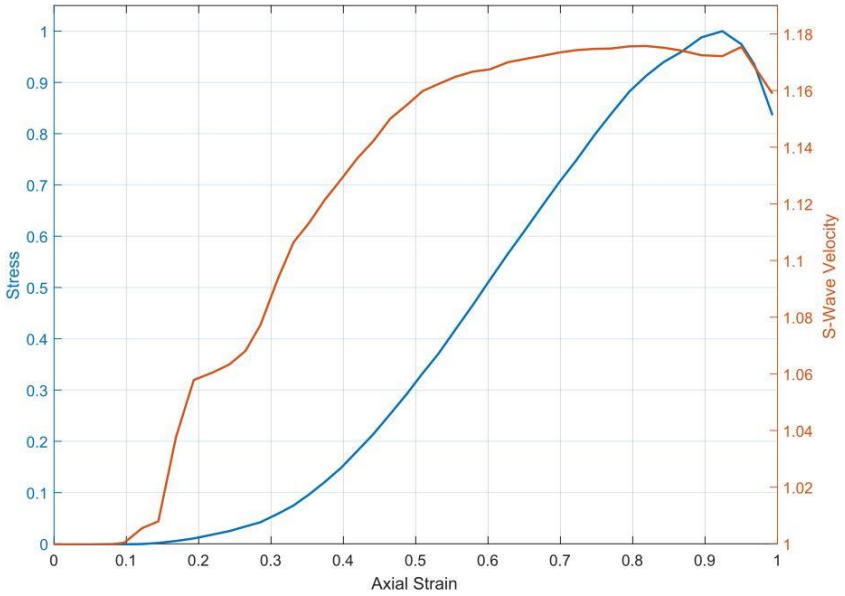

E.5.5 Uniaxial Compressive Strength versus S-Wave Velocity

Correlation of the UCS with the S-wave velocity for Buntsandstein samples from block SBS6-BD-50, SBS6-BD-51 and SBS6-BD-52. Trendline equations can be found in Appendix E.5.6.

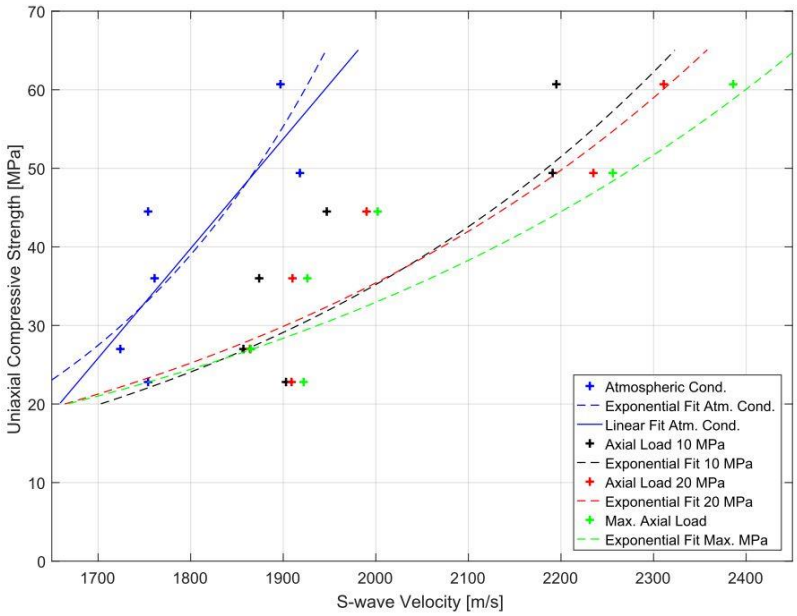

E.5.6 Trendline Equations

Trendline equations for fits shown in Figure 6.3 and Appendix E.5.5. The unit of the UCS is in MPa, the velocity is expressed in m/s.

	Linear	Exponential			
	Atmospheric cond.	Atmospheric cond.	10 MPa	20 MPa	Max. axial load
V_p	UCS = 0.0341 V_p - 68.451	UCS= $2.2483e^{0.0009\ Vp}$	UCS = $0.0779e^{0.0016\ Vp}$	UCS = $0.1353e^{0.0015\ Vp}$	UCS = $0.3053e^{0.0012\ Vp}$
V_s	UCS = 0.1396 V_s - 211.49	UCS = $0.0716e^{0.0035\ Vs}$	UCS = $0.7876e^{0.0019\ Vs}$	UCS = $1.182e^{0.0017\ Vs}$	UCS = $1.6408e^{0.0015\ Vs}$

Appendix F Cyclic Loading Experiments

F.1 Cycle Loads

Overview of the maximum applied load for each cycle in the cyclic loading experiments for samples MI-52-Y2C, BD-53-X2A and BD-53-Z1A.

Cycle number	Max. applied load [MPa]		
	MI-52-Y2C	BD-53-X2A	BD-53-Z1A
1	12.5	6.9	8.9
2	18.9	9.0	13.4
3	24.9	11.4	17.8
4	31.0	13.7	22.3
5	37.1	16.0	26.6
6	43.1	18.2	31.1
7	49.2	20.6	33.7
8	49.4	22.8	-
9	-	25.0	-
10	-	27.2	-

F.2 Stress-Strain Curves

Stress-strain curves for the cyclic loading experiments of samples BD-53-X2A and BD-53-Z1A. In comparison, stress-strain curves of samples BD-53-X2B and BD-53-Z2B (tested under constant strain rate conditions) are plotted in the graphs (black dotted lines). Negative strain values correspond to the radial strain, positive values belong to the axial strain.

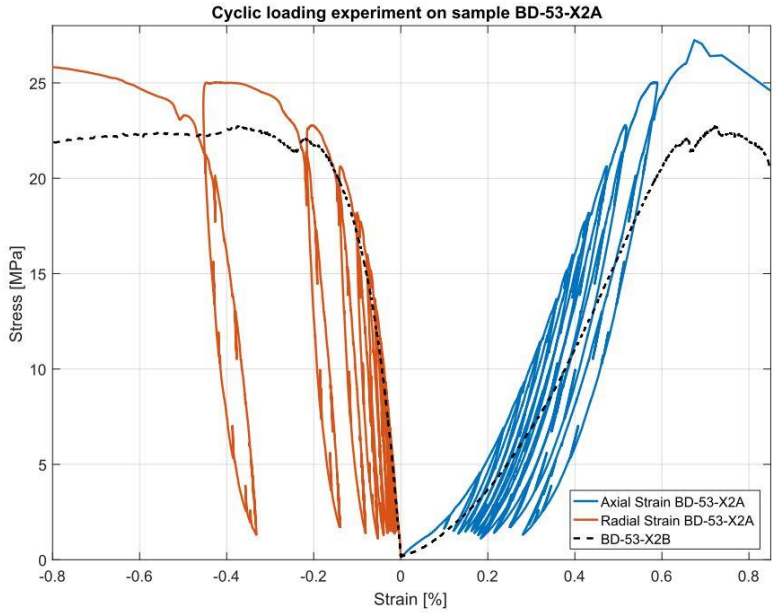

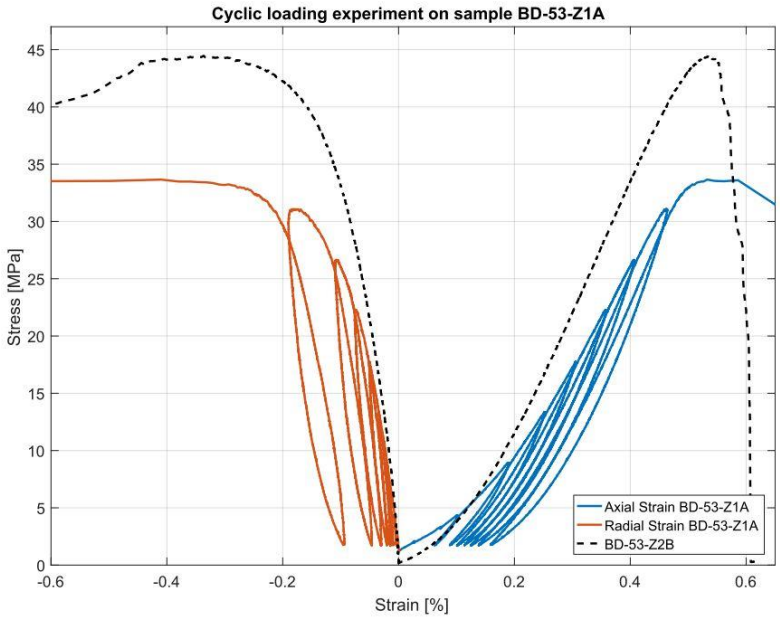

F.3 Static Moduli Evolution

Evolution of the Young's modulus and the Poisson's ratio for samples BD-53-X2A and BD-53-Z1A during cyclic loading tests. Relative errors for each measurement are indicated as bars.

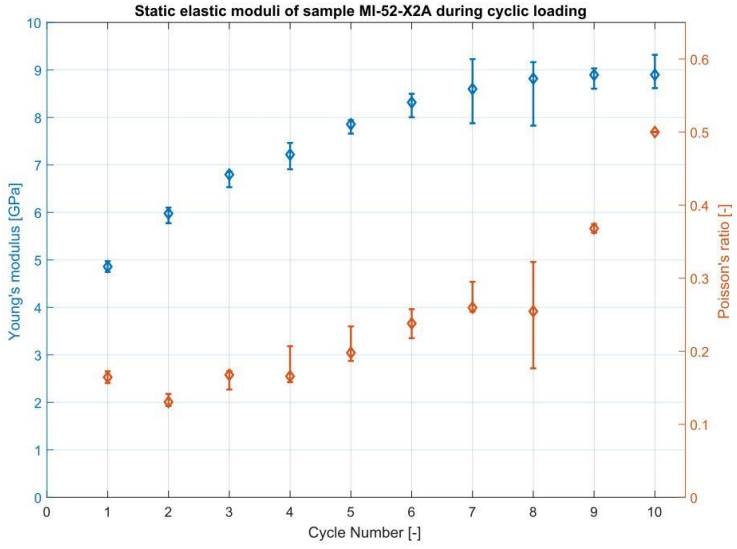

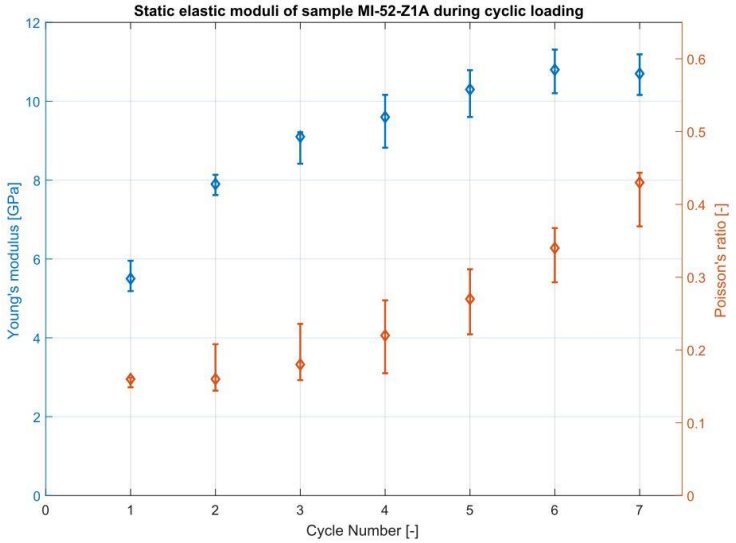

Appendix G Brazilian Disc Test Results

Test results from the Brazilian test made on sample blocks SBS6-BD52, SBS6-BD53, SRM6-MI-52 and SRG6-RU.

Sample	Core direction	Orientation of applied load towards bedding	Splitting tensile strength σ_t [MPa]	Max. applied load F_{max} [kN]	Local min. load P_{min} [kN]	Max. compressive strength [MPa]	Fracture toughness K_{IC} [MN/m$^{1.5}$]
BD52-Z1-1	Z	n.a.	3.47	2.73	1.72	3.91	0.28
BD52-Z1-2		n.a.	2.52	1.95	1.14	2.81	0.19
BD52-Z1-3		n.a.	2.20	1.55	1.48	2.28	0.26
BD52-Z3-1		n.a.	2.73	2.02	1.45	2.91	0.25
BD52-Z3-2		n.a.	2.43	1.65	1.60	3.48	0.30
BD52-X1A-1	X	n.a.	2.45	1.70	1.18	2.44	0.21
BD52-X1A-2		n.a.	2.73	1.96	1.49	2.83	0.26
BD52-X2A-1		n.a.	2.71	1.77	1.46	2.54	0.28
BD52-X2A-2		n.a.	2.00	1.55	1.27	2.41	0.21
BD53-X1A-1	X	n.a.	2.05	1.58	1.07	2.28	0.17
BD53-X1A-2		n.a.	1.92	1.42	1.16	2.06	0.20
BD53-Z1B	Z	n.a.	3.03	2.20	1.42	3.17	0.25
BD53-Z2A		n.a.	2.44	1.73	1.26	2.49	0.22
SRM6-MI-52-Y1A	Y	perpendicular	5.66	4.32	2.76	6.24	0.46
SRM6-MI-52-Y1B		perpendicular	5.69	4.03	2.57	5.82	0.46
SRM6-MI-52-Y1C		along	3.37	2.13	1.48	3.08	0.30
SRM6-MI-52-Y3A		along	3.21	2.06	1.31	2.97	0.26
SRM6-MI-52-Y3B		perpendicular	6.21	4.21	2.44	6.08	0.48
SRM6-MI-52-Y4		along	2.14	1.39	1.00	2.00	0.19
SRM6-MI-52-Y6A		along	2.43	1.71	1.63	3.52	0.29
SRM6-MI-52-Y6B		along	2.47	1.64	1.04	2.36	0.20
SRM6-MI-52-Y6C		perpendicular	7.03	4.99	2.79	7.19	0.50
SRM6-MI-52-Y6D		perpendicular	6.23	4.30	2.05	6.20	0.37
SRM6-MI-52-Y6E		angular	5.51	3.51	2.22	5.06	0.44
SRM6-MI-52-Y6F		angular	3.92	2.41	1.49	3.48	0.31
SRM6-MI-52-Y6G		angular	4.78	3.31	2.18	4.95	0.40
SRM6-MI-52-Y6H		angular	4.81	3.23	1.95	4.65	0.37
SRM6-MI-52-Y6I		along	3.68	2.85	2.06	4.22	0.34
SRM6-MI-52-Y6J		along	2.33	1.75	1.30	4.42	0.22
SRM6-MI-52-Y6K		perpendicular	6.02	4.21	2.39	6.05	0.43
SRG6-RU-Z1	Z	n.a.	2.30	1.64	1.19	2.37	0.21
SRG6-RU-Z2		n.a.	2.48	1.78	1.36	2.56	0.24
SRG6-RU-Z3		n.a.	2.29	1.67	1.29	2.41	0.22
SRG6-RU-X2	X	n.a.	2.58	2.05	1.55	2.94	0.25
SRG6-RU-X3-1		n.a.	2.70	1.88	1.09	2.68	0.20
SRG6-RU-X3-2		n.a.	2.66	1.87	1.27	2.71	0.23

Appendix H Triaxial Apparatus Results

H.1 CT-Scans

H.1.1 Shear Deformation

CT-scan images of the Buntsandstein samples MI-50-Y1, MI-50-Y2 and BD-52-Z1 after shear failure in the triaxial apparatus. Samples are displayed in XY- and XZ-view. The general sample height is about 75 mm, the diameter is 30 mm.

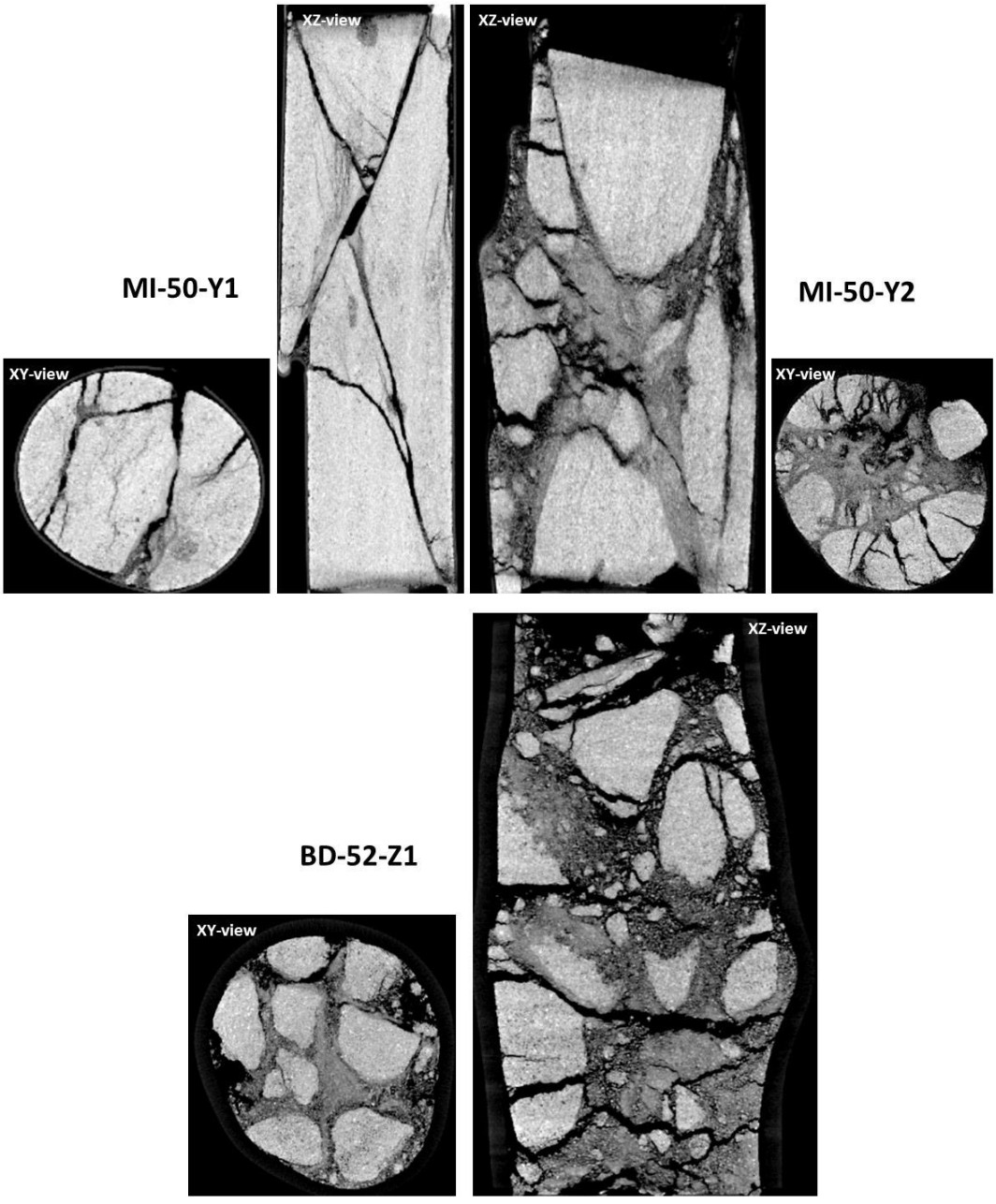

H.1.2 Tensile Fracturing

CT-scan images of the Buntsandstein samples MI-52-Y3A, MI-52-Y3B, MI-52-Z6 and MI-52-Z8 after failure in the triaxial apparatus with the “Mode I frackers”. The “Mode I frackers” were placed parallel to the bedding. Samples are displayed in XY- and XZ-view. The sample height is 50 mm, the diameter is 30 mm.

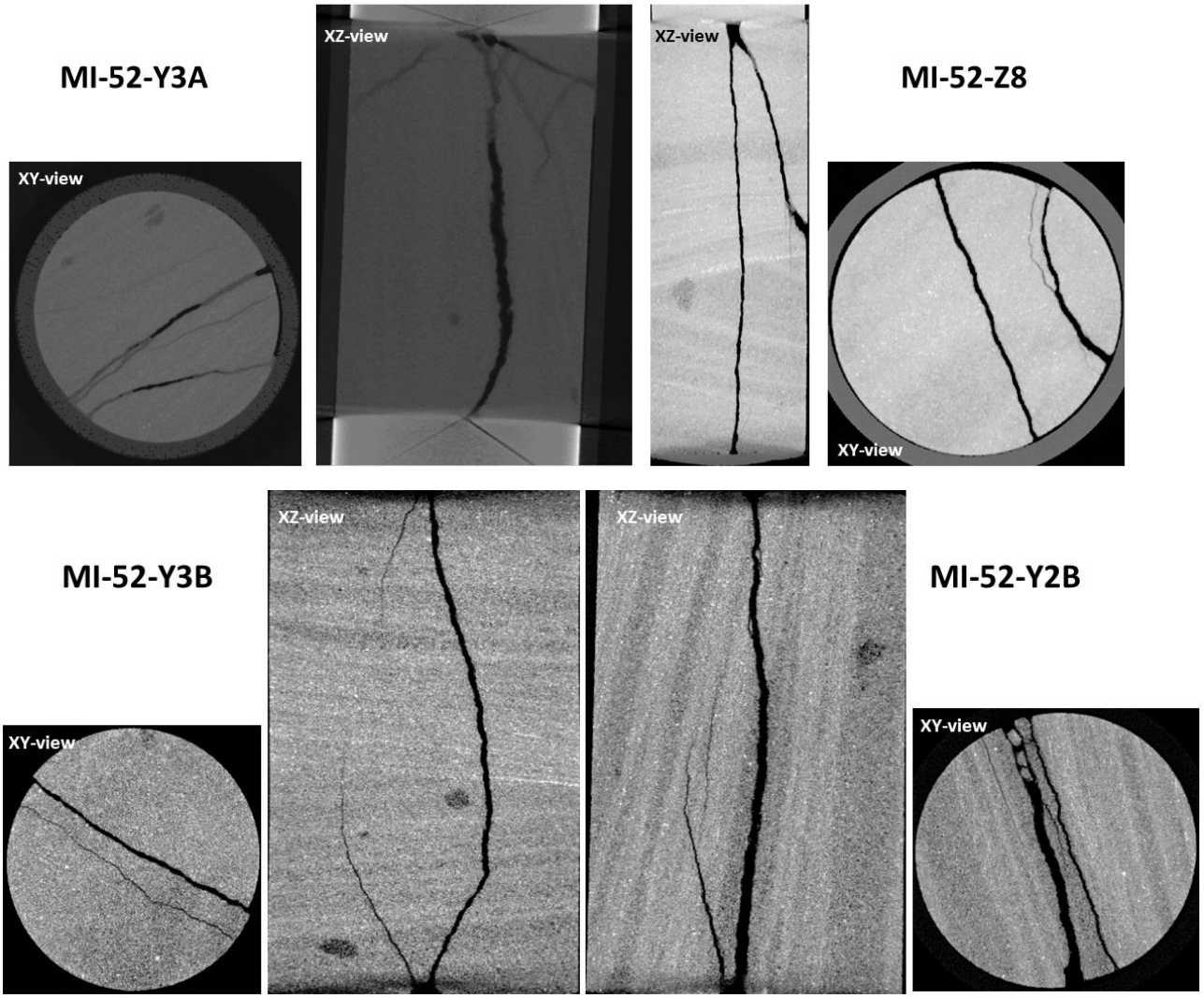

H.2 Porosity Evolution

Porosity decrease and increases related to changes in effective hydrostatic pressures for several core samples. Relative errors are within the marker points.

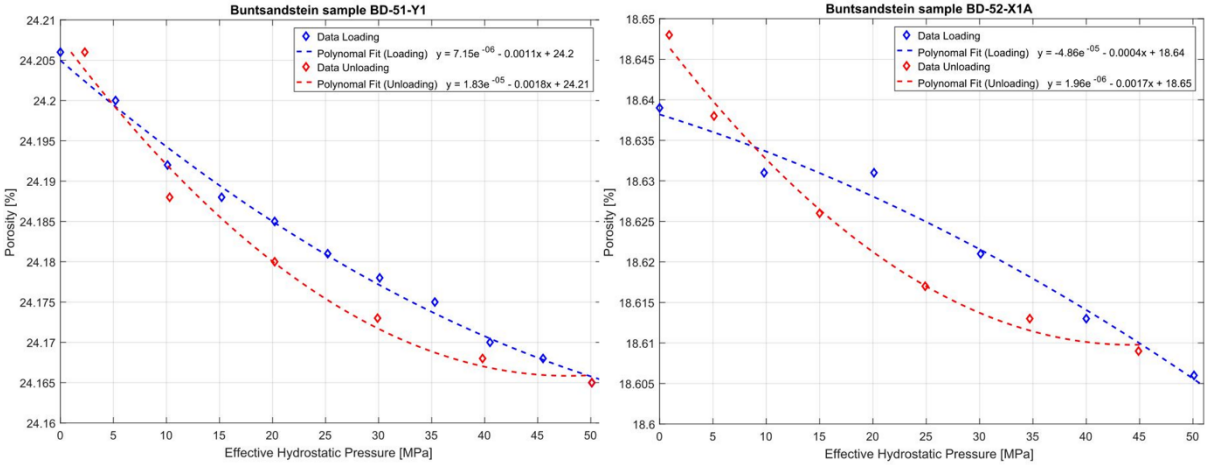

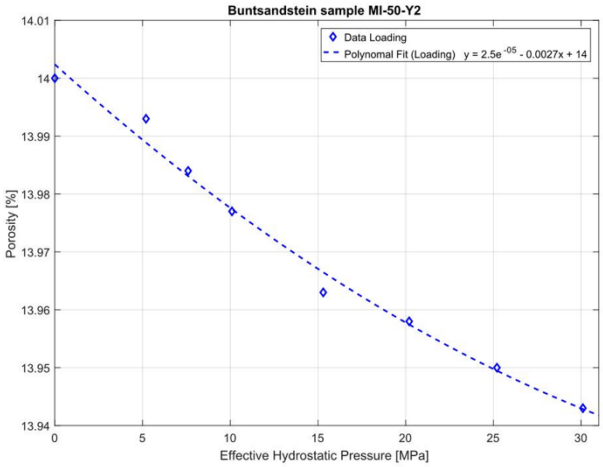

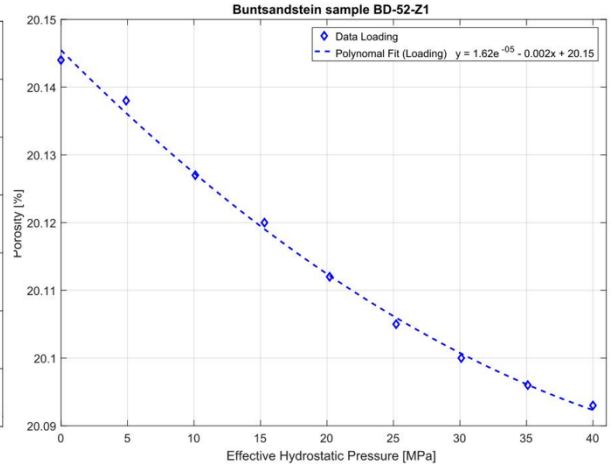

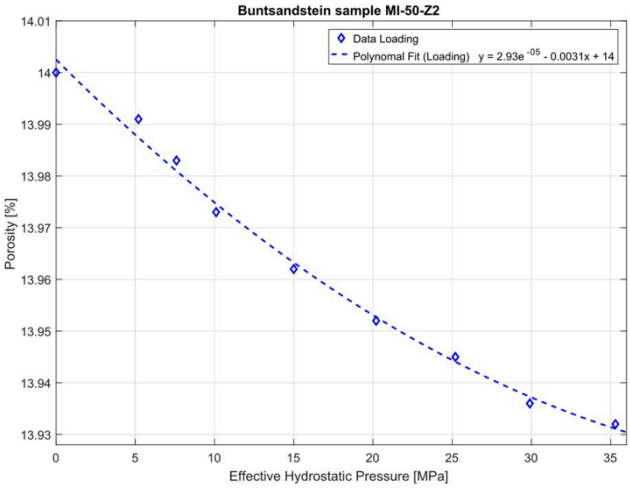

H.3 Permeability Evolution

Permeability development with increasing differential stress for sample MI-50-Y1.

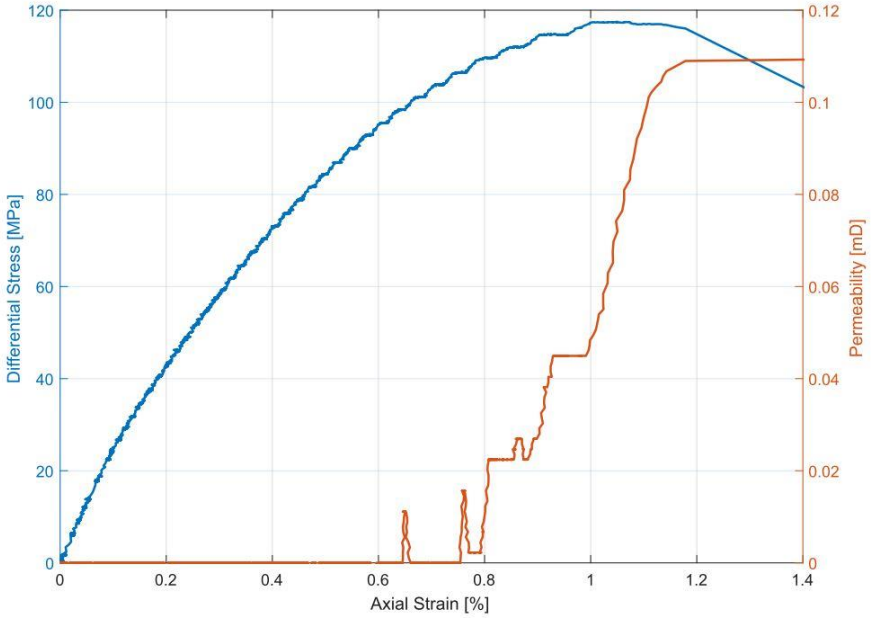

H.4 Triaxial Deformation

Stress-Strain curves for four Buntsandstein samples that were fractured at different confining pressures, ranging from 5 MPa to 40 MPa, in the triaxial apparatus.

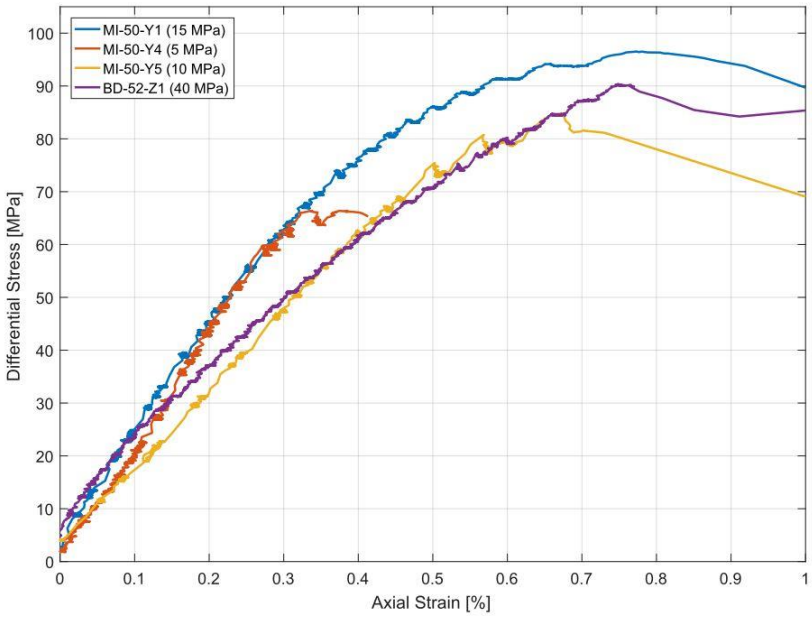

H.5 Permeability Measurements

Permeability measurements for samples tested in the triaxial apparatus. Several samples were fractured (shear fracture or opening fracture).

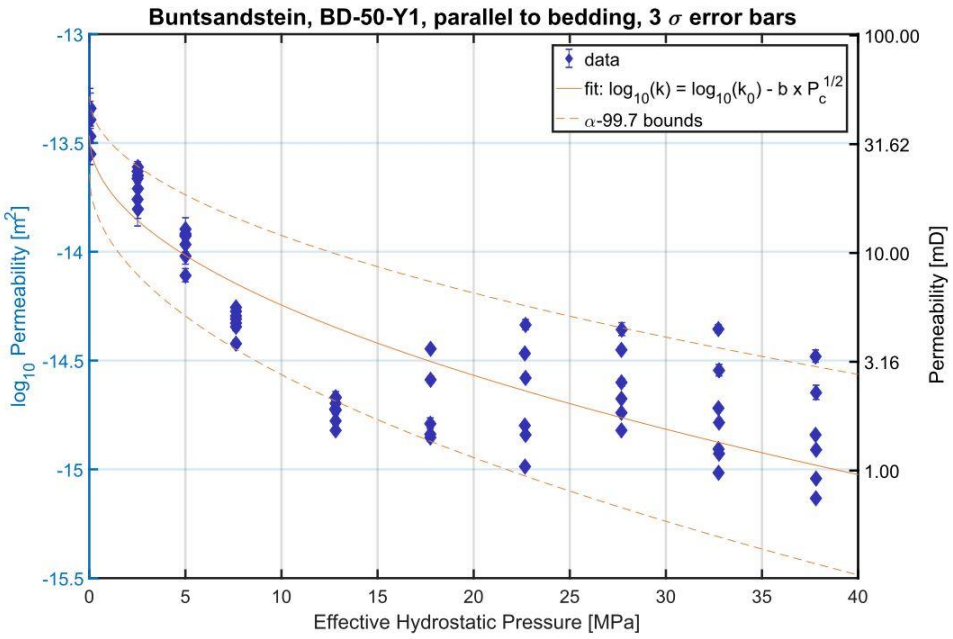
Buntsandstein, BD-50-Y1, parallel to bedding, 3 σ error bars
data
fit: log10(k) = log10(k0) - b x Pc^1/2
α-99.7 bounds
log10 Permeability [m2]
Permeability [mD]
Effective Hydrostatic Pressure [MPa]

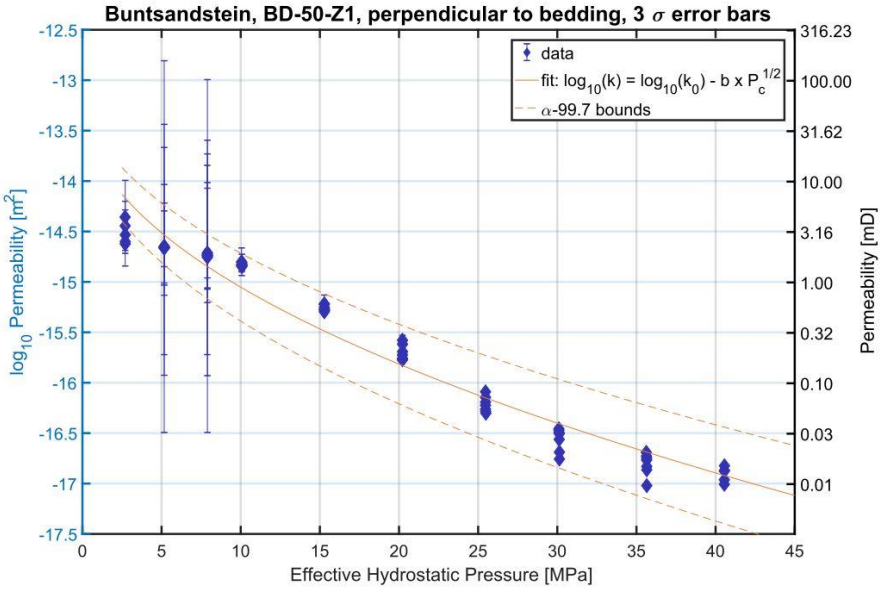
Buntsandstein, BD-50-Z1, perpendicular to bedding, 3 σ error bars
data
fit: log10(k) = log10(k0) - b x Pc^1/2
α-99.7 bounds
log10 Permeability [m2]
Permeability [mD]
Effective Hydrostatic Pressure [MPa]

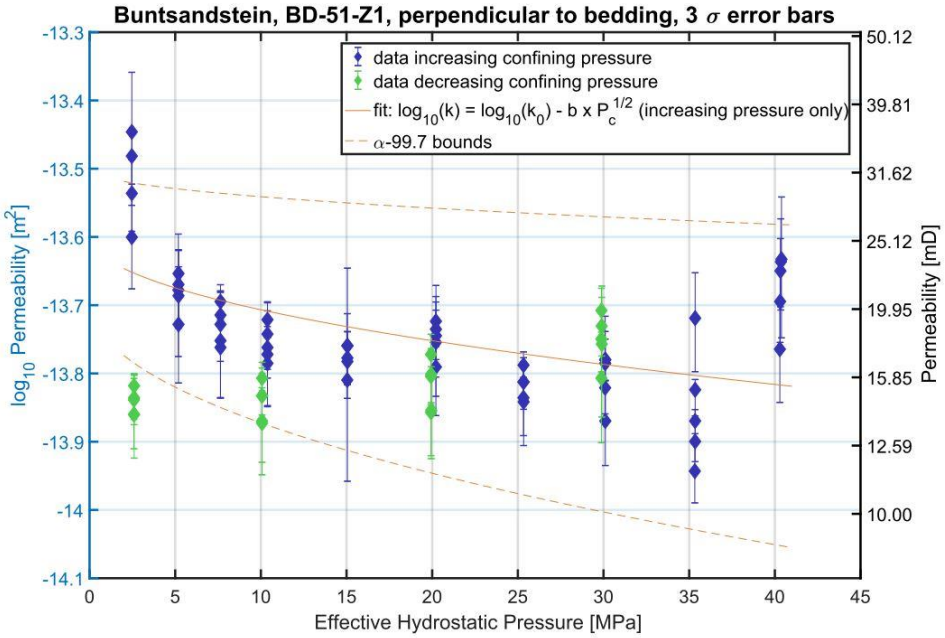
Buntsandstein, BD-51-Z1, perpendicular to bedding, 3 σ error bars
data increasing confining pressure
data decreasing confining pressure
fit: log10(k) = log10(k0) - b x Pc^1/2 (increasing pressure only)
α-99.7 bounds
log10 Permeability [m2]
Permeability [mD]
Effective Hydrostatic Pressure [MPa]

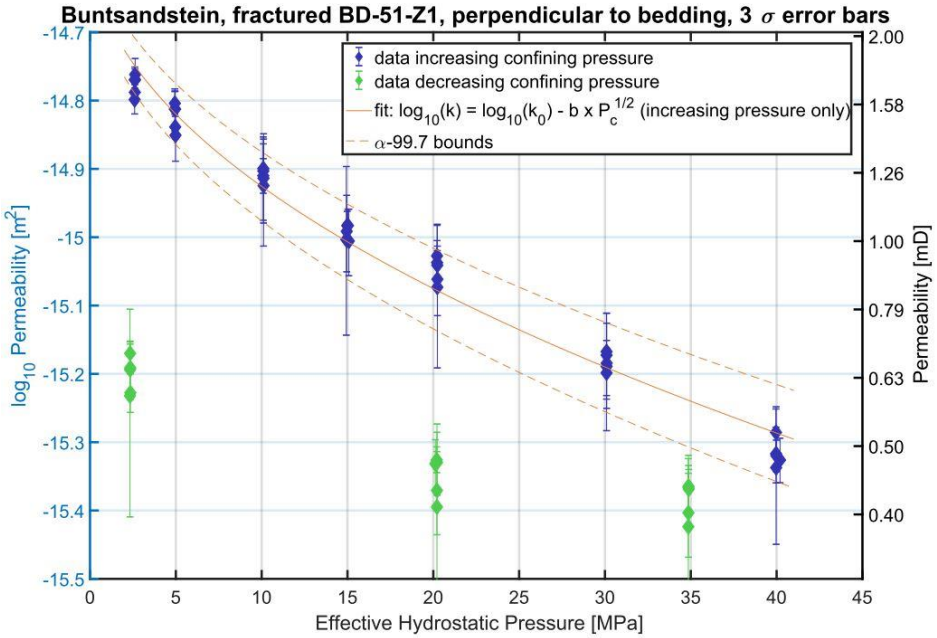
Buntsandstein, fractured BD-51-Z1, perpendicular to bedding, 3 σ error bars
data increasing confining pressure
data decreasing confining pressure
fit: log10(k) = log10(k0) - b x Pc^1/2 (increasing pressure only)
α-99.7 bounds
log10 Permeability [m2]
Permeability [mD]
Effective Hydrostatic Pressure [MPa]

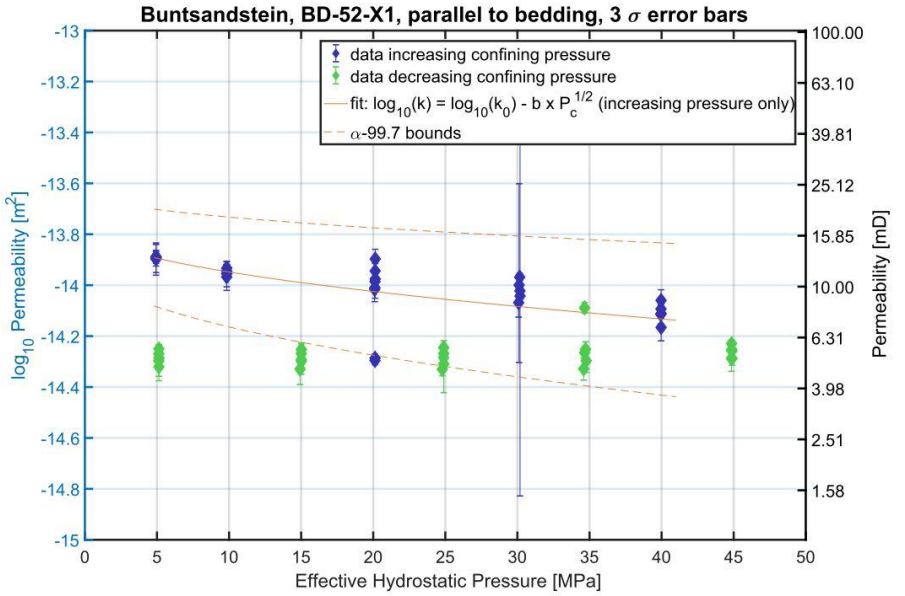
Buntsandstein, BD-52-X1, parallel to bedding, 3 σ error bars
data increasing confining pressure
data decreasing confining pressure
fit: log10(k) = log10(k0) - b x Pc^1/2 (increasing pressure only)
α-99.7 bounds
log10 Permeability [m2]
Permeability [mD]
Effective Hydrostatic Pressure [MPa]

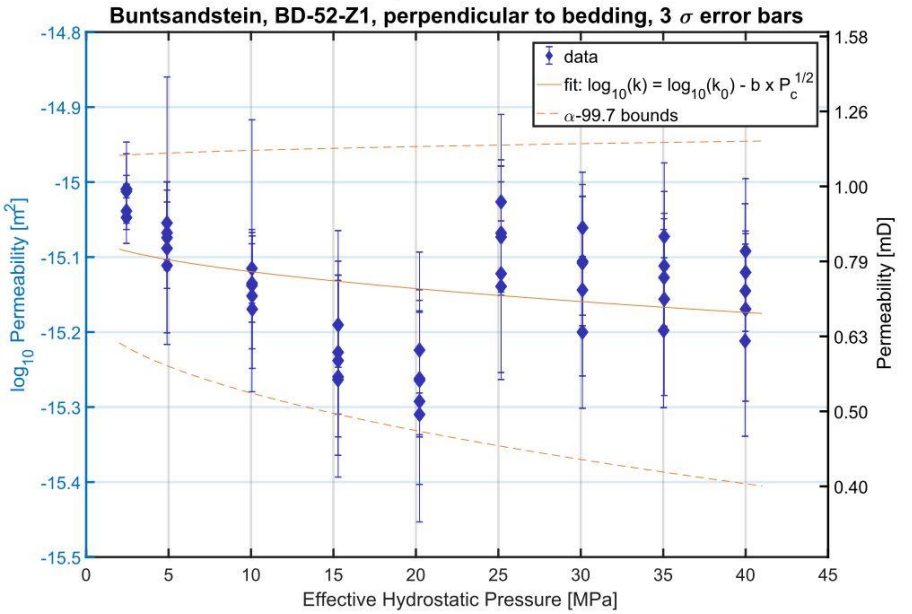
Buntsandstein, BD-52-Z1, perpendicular to bedding, 3 σ error bars
data
fit: log10(k) = log10(k0) - b x Pc^1/2
α-99.7 bounds
log10 Permeability [m2]
Permeability [mD]
Effective Hydrostatic Pressure [MPa]

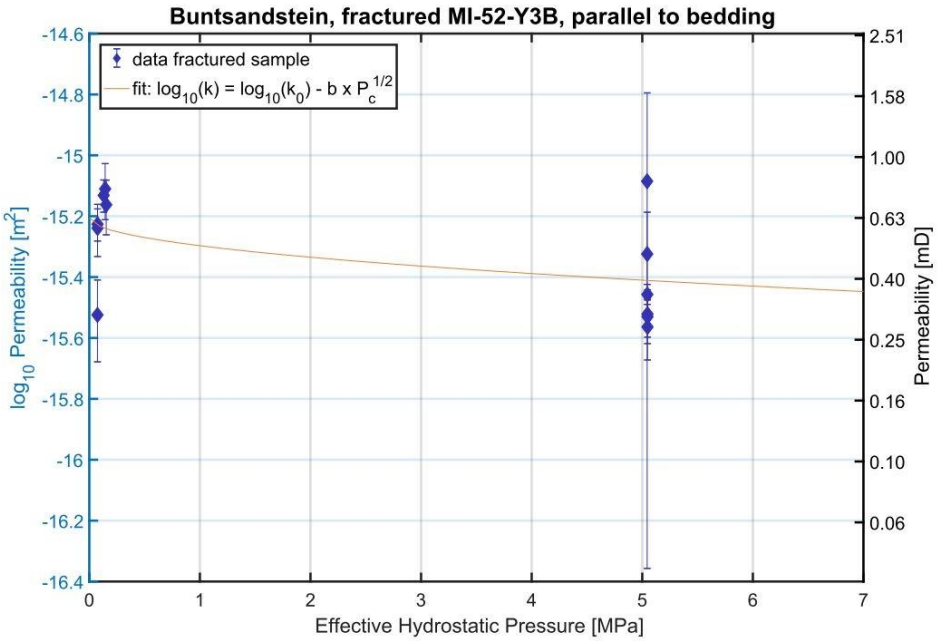
Buntsandstein, fractured MI-52-Y3B, parallel to bedding
data fractured sample
fit: log10(k) = log10(k0) - b x Pc^1/2
log10 Permeability [m2]
Permeability [mD]
Effective Hydrostatic Pressure [MPa]

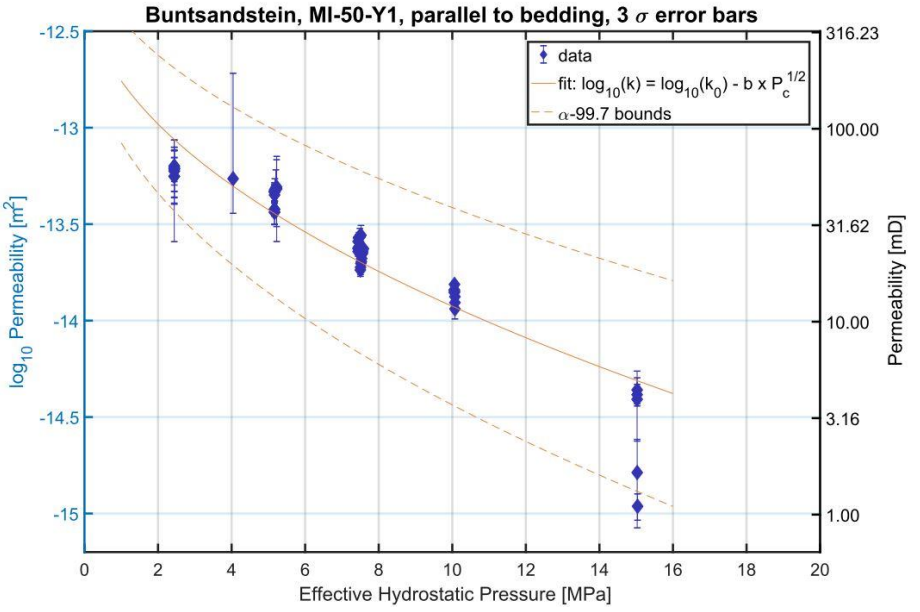
Buntsandstein, MI-50-Y1, parallel to bedding, 3 σ error bars
data
fit: log10(k) = log10(k0) - b x Pc^1/2
α-99.7 bounds
log10 Permeability [m2]
Permeability [mD]
Effective Hydrostatic Pressure [MPa]

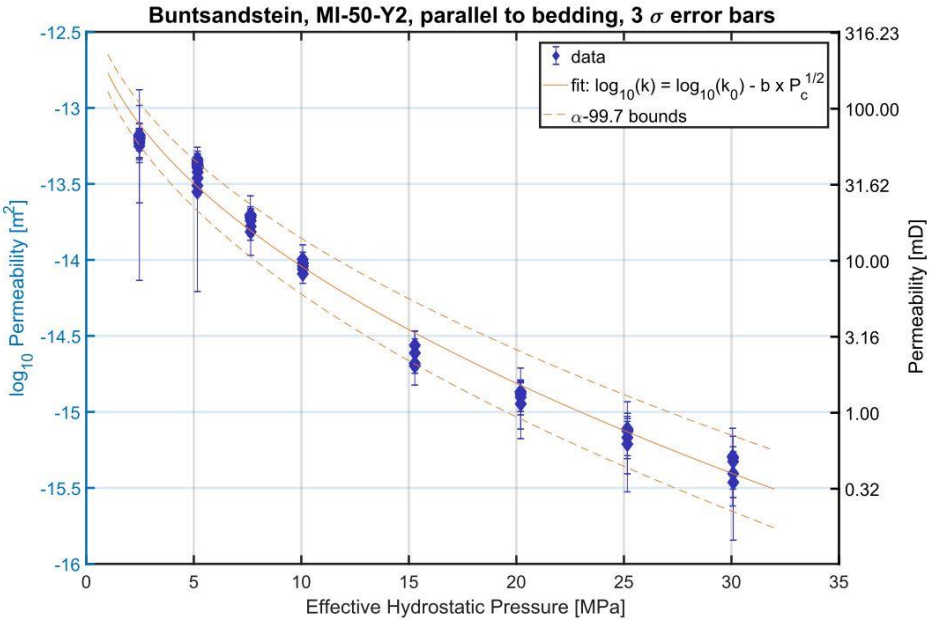
Buntsandstein, MI-50-Y2, parallel to bedding, 3 σ error bars
data
fit: log10(k) = log10(k0) - b x Pc^1/2
α-99.7 bounds
log10 Permeability [m2]
Permeability [mD]
Effective Hydrostatic Pressure [MPa]

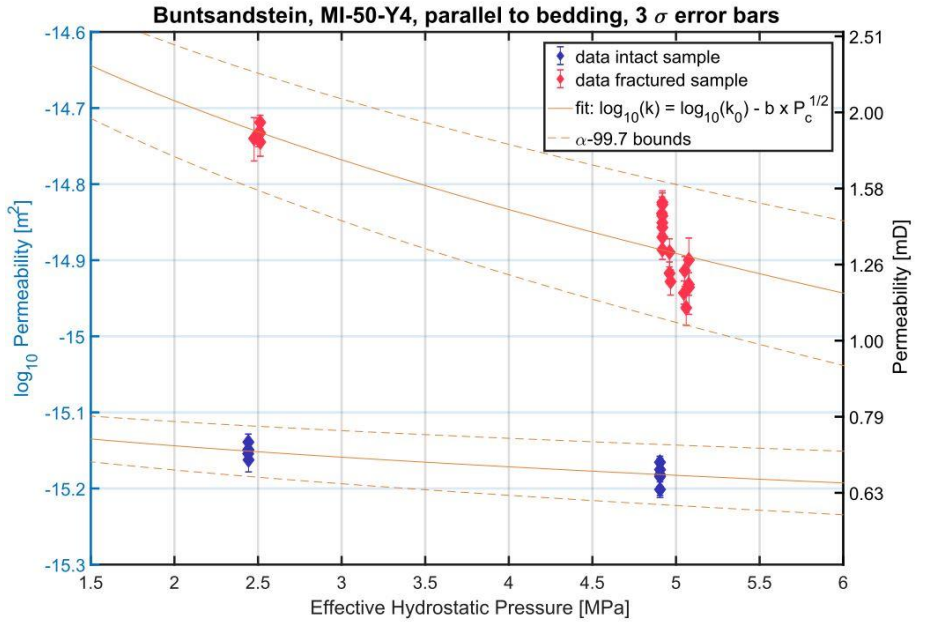
Buntsandstein, MI-50-Y4, parallel to bedding, 3 σ error bars
data intact sample
data fractured sample
fit: log10(k) = log10(k0) - b x Pc^1/2
α-99.7 bounds
log10 Permeability [m2]
Permeability [mD]
Effective Hydrostatic Pressure [MPa]

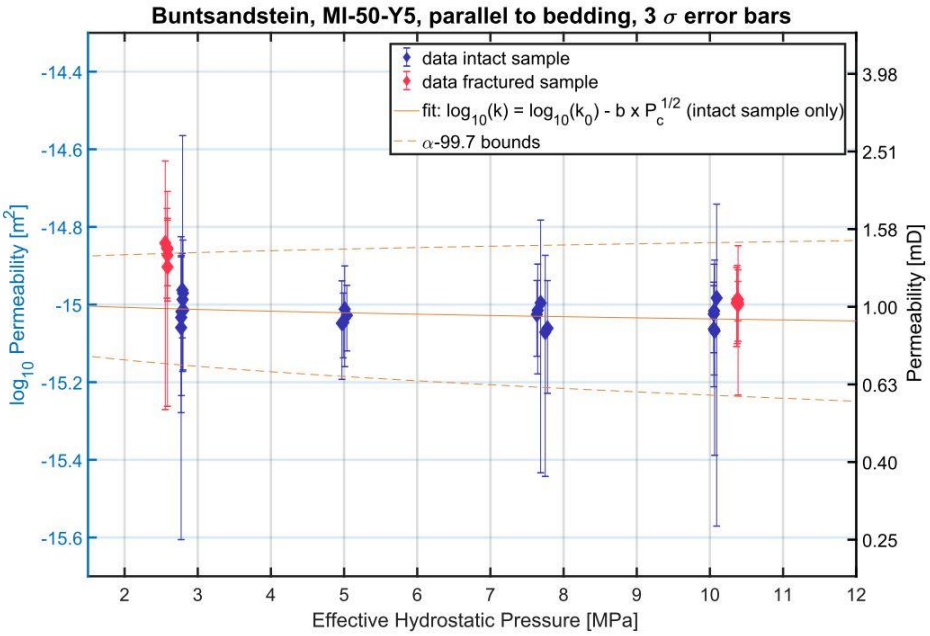
Buntsandstein, MI-50-Y5, parallel to bedding, 3 σ error bars
data intact sample
data fractured sample
fit: log10(k) = log10(k0) - b x Pc^1/2 (intact sample only)
α-99.7 bounds
log10 Permeability [m2]
Permeability [mD]
Effective Hydrostatic Pressure [MPa]

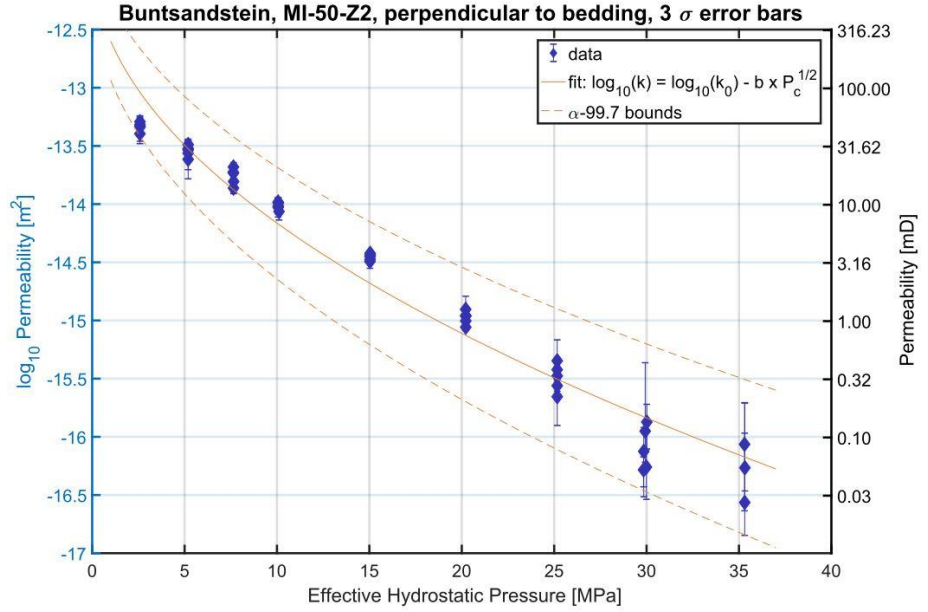
Buntsandstein, MI-50-Z2, perpendicular to bedding, 3 σ error bars
data
fit: log10(k) = log10(k0) - b x Pc^1/2
α-99.7 bounds
log10 Permeability [m2]
Permeability [mD]
Effective Hydrostatic Pressure [MPa]

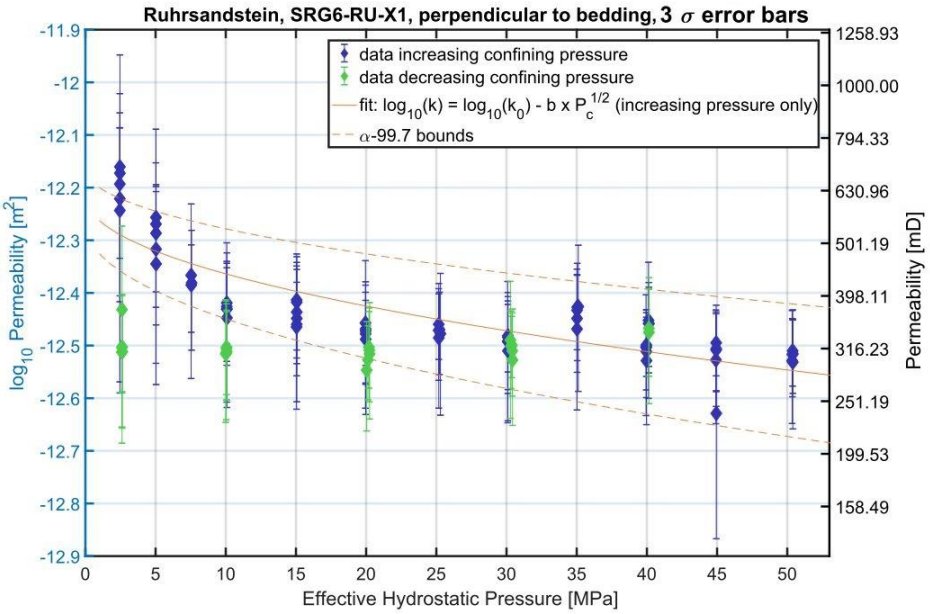

H.6 Fracture Aperture versus Permeability

Fracture aperture versus associated permeability for sample MI-52-Y2B and MI-52-Z6. The fractures were caused by the Mode I frackers in the triaxial apparatus under 2.5 MPa confining pressure.

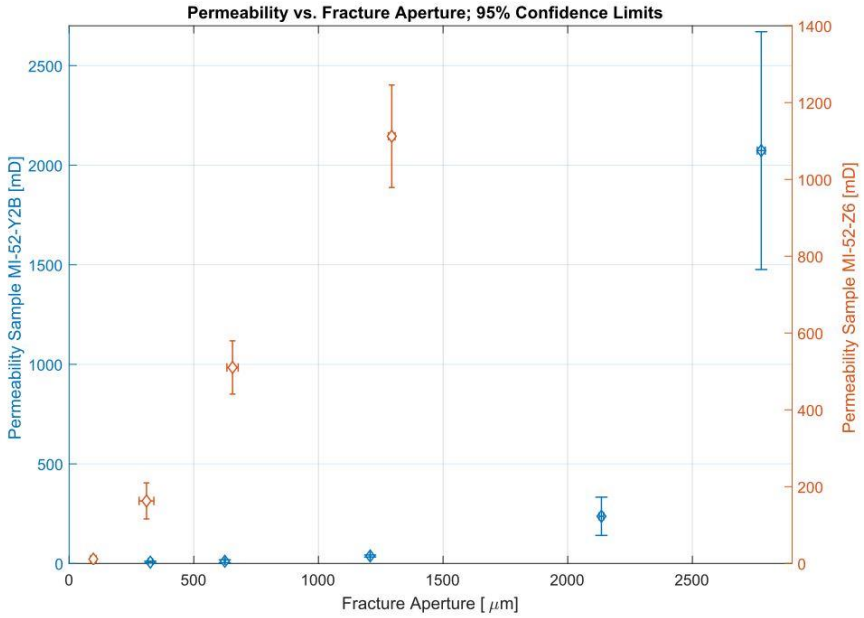

H.7 Apparent Apertures

Table showing the average permeability of four altered Buntsandstein samples from block SRM6-MI-52 at different apparent fracture apertures.

Sample	Effective hydrostatic pressure [MPa]	Avg. permeability [mD]	Avg. apparent aperture [µm]
MI-52-Y3A	4.0	539	407
		462	403
		497	475
		1210	495
		938	494
MI-52-Y2B	2.0	7	326
		11	625
		38	1208
		237	2135
		2073	2776
MI-52-Z8	4.0	1.8	431
		2.3	498
		3.1	584
		4.5	665
		4.5	649
MI-52-Z6	2.0	11	97
	4.5	163	310
	9.5	510	655
	9.5	1112	1294

H.8 Combined Trendline for Aperture-Permeability Relationship

Table showing the trendline equations for a polynomial fit of the aperture-permeability plots from Figure 5.14 and Appendix H.6. The listed trendlines were averaged, resulting in the data and the fit shown in the figure below.

Sample	Trendline equation
MI-52-Y3A	$y = 26.426e^{0.0071x}$
MI-52-Y2B	$y = 2.668e^{0.0023x}$
MI-52-Z8	$y = 0.293e^{0.0041x}$
MI-52-Z6	$y = 25.282e^{0.0033x}$
Average	$y = 11.897e^{0.0062x}$

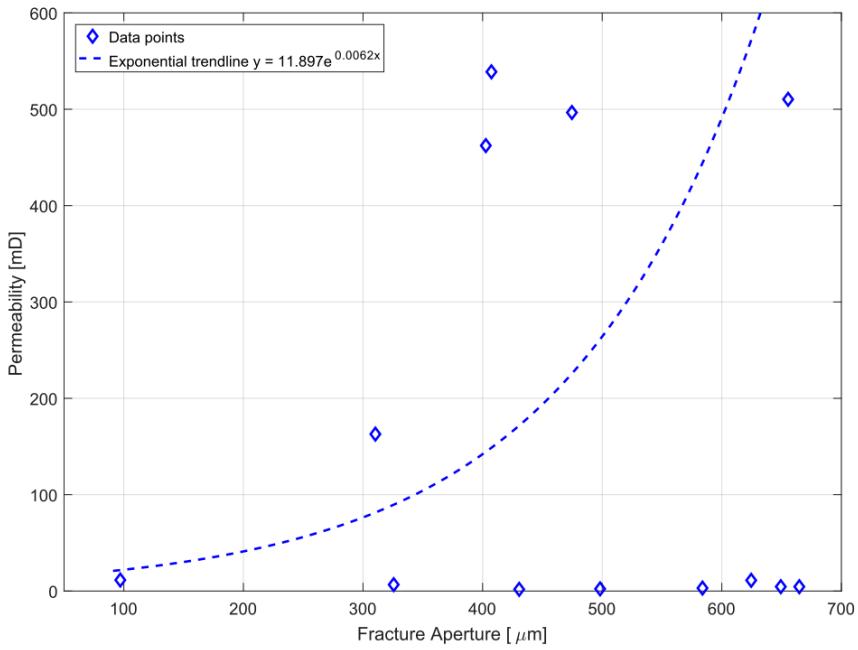

H.9 Mohr Circles

Mohr's stress envelope for the altered Buntsandstein blocks SBS6-BD-51 and SBS6-BD-52 with 50% error bounds. Shear failures are illustrated as diamonds. Effective hydrostatic pressures at the moment of failure are listed in brackets in the legend for each experiment. No rock anisotropy is assumed. The shown failure criteria only gives a rough estimate.

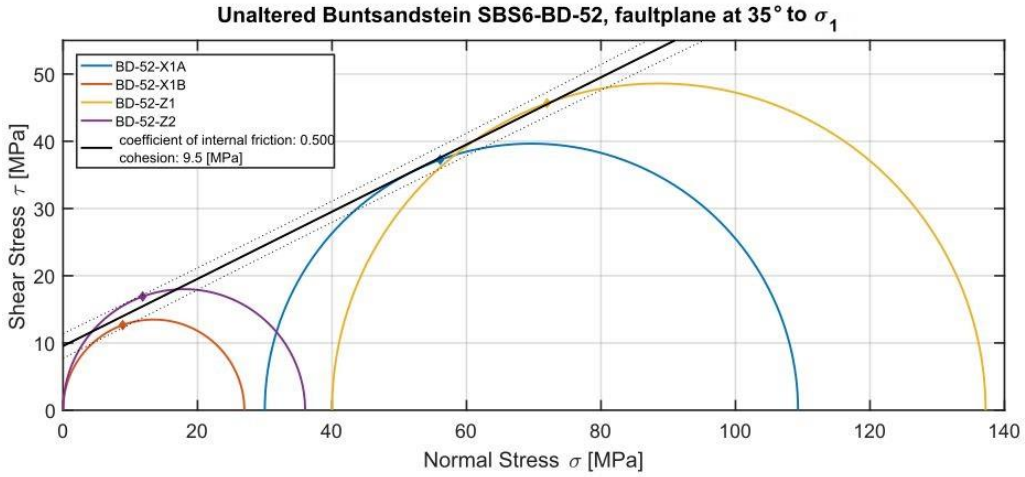

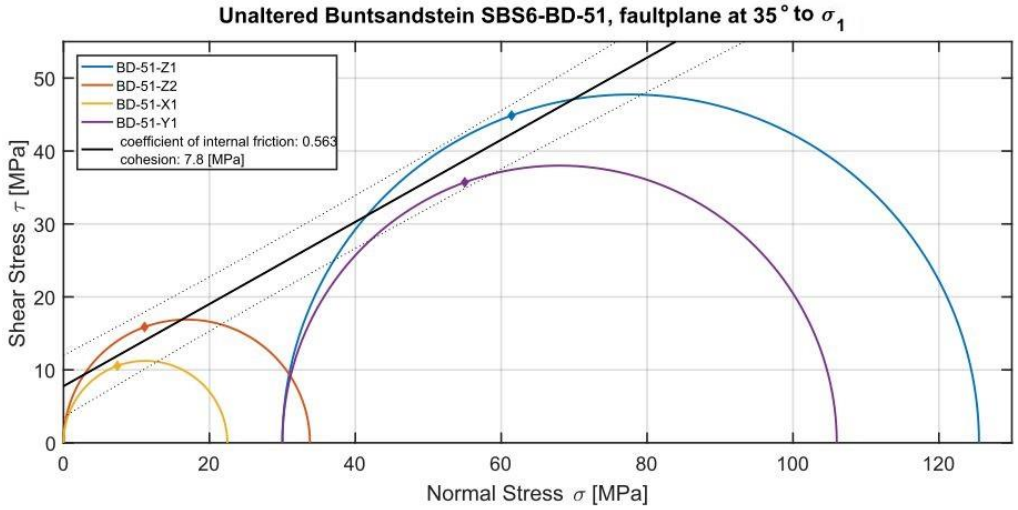

H.10 Freyburg Relationship

Relationship between the measured compressive strength σ_{max} and the compressive strength calculated with the empirical UCS-V_p relationship of Freyburg (1972).

Sample block	Sample	σ_{max} [MPa]	σ_{max} after Freyburg (1972) [MPa]
SBS6-BD-50	BD-50-Y2	49.4	88.4
	BD-50-Z3	60.7	101.2
SBS6-BD-52	BD-52-X1B	27.0	70.1
	BD-52-Z2	36.0	80.3
SBS6-BD-53	BD-53-X2B	22.8	59.9
	BD-53-Z2B	44.5	80.2
SBS6-BD-54	BD-54-X3A	28.8	89.5
	BD-54-Z2A	25.7	88.4
SRM6-MI-50	MI-50-Y6	37.8	78.9
	MI-50-Z1	51.5	115.6
SRM6-MI-52	MI-52-Y4A	63.0	74.9
	MI-52-Z7	54.2	105.3

H.11 Diameter and Length Changes during Triaxial Compression

Approximate initial length and diameter for various samples tested in the triaxial apparatus. After subjecting the samples to increased effective hydrostatic pressure, the (final) length and the (final) diameter were measured again after the experiment.

Sample	Max. eff. hydrostatic pressure [MPa]	Length [mm]		Diameter [mm]	
		Initial	Final	Initial	Final
BD-50-Y1	38	76.20	75.87	29.70	29.25
BD-50-Z1	25	74.46	73.56	29.71	29.45
BD-52-X1	50	75.01	74.95	29.66	28.63
BD-52-Z1	40	74.46	72.63	29.71	28.94
BD-51-Z1	40	70.45	70.38	29.82	29.78
BD-51-Y1	50	70.86	70.67	29.81	29.58
RU-X1	50	75.37	75.34	29.67	28.23

Appendix I Crack Closure

Crack closure in the sample at lower stresses during a uniaxial compression test (left). Increasing the axial stress leads to the formation of new cracks parallel to the direction of stress (right). This may lead to the changes in the velocity and ultimately influences the dynamic elastic moduli (Li & Fjær, 2012).

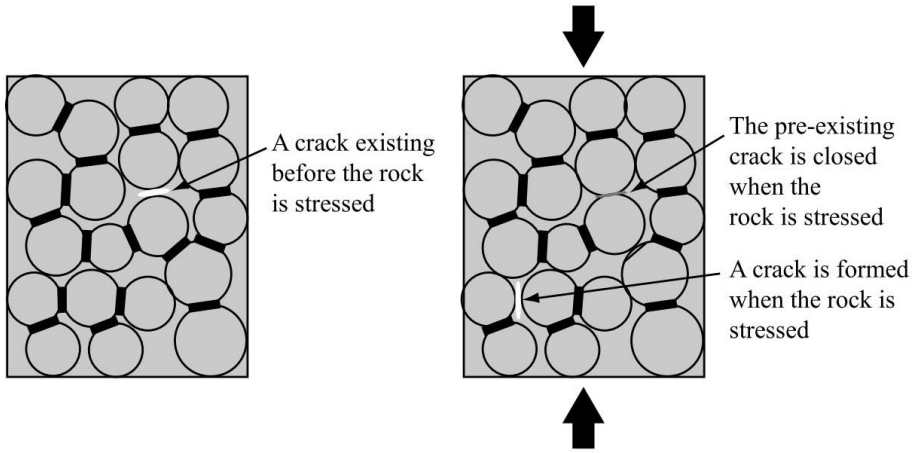

Appendix J Percolation Threshold

Schematic illustration of a fracture cluster. If the fractures are not interconnected, there is no flow possible between A and B. Connected fractures, on the other hand, allow a flow from A to B. The point marking the boundary where flow is possible and the permeability increases significantly is called the percolation threshold (Philipp et al., 2007).

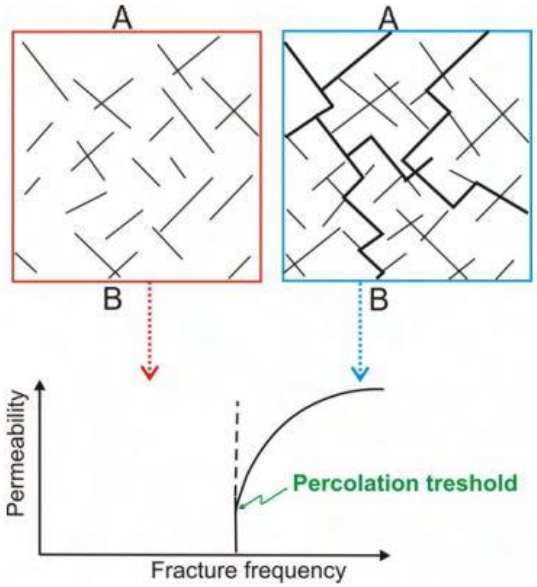

Appendix K Numerical Simulation

K.1 Temperature Evolution of Model I

Temperature evolution over time (10 years, 20 years, 30 years) for a reservoir with 7 mD initial permeability. Cold water of 80°C is injected at a rate of 0.02 L/s. The initial reservoir temperature is 140°C. Further reservoir parameters are shown in Appendix A.1.

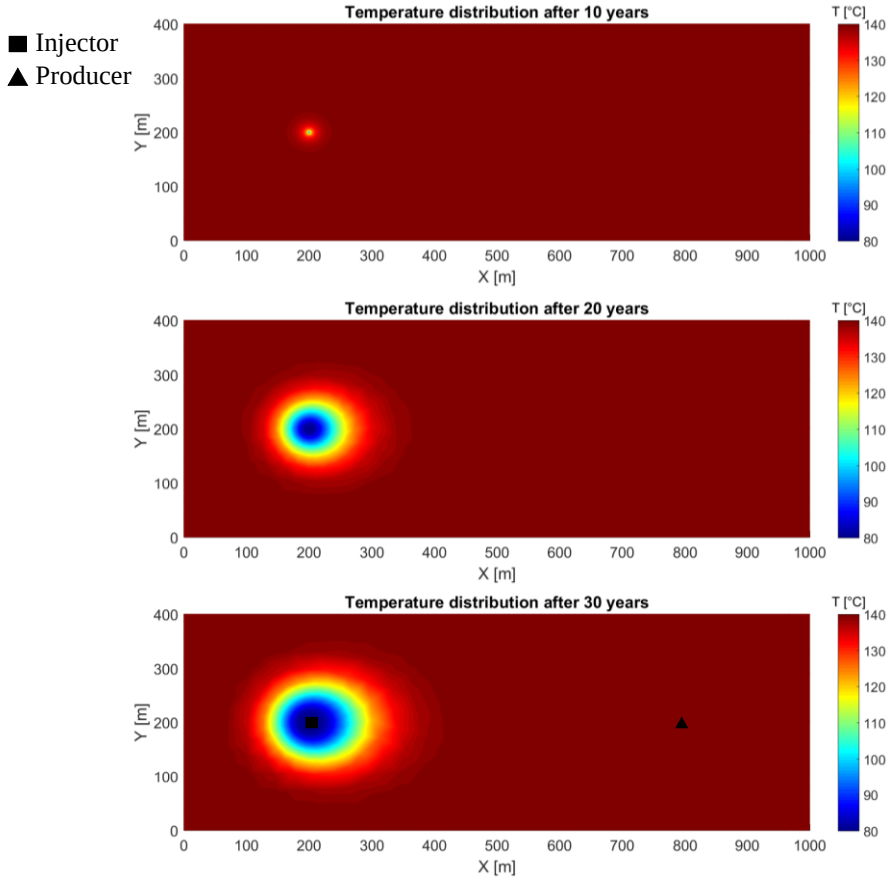

K.2 Pressure Evolution of Model II

Temperature evolution over time (10 years, 20 years, 30 years) for a reservoir with 30 mD initial permeability. Cold water of 80°C is injected at a rate of 0.1 L/s. The initial reservoir pressure is 43 MPa. Further reservoir parameters are shown in Appendix A.1.

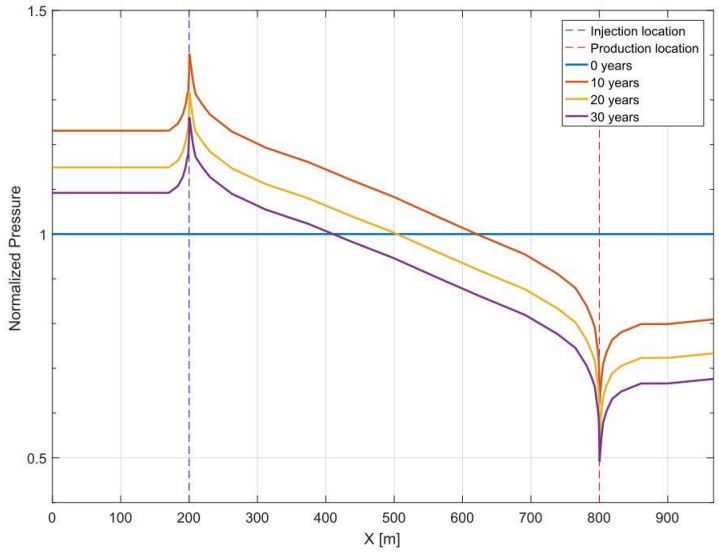

K.3 Pressure distribution of Model III

Pressure distribution after 20 years of production and injection for a reservoir with 93 mD initial permeability. Cold water of 80°C is injected at a rate of 0.2 L/s. The initial reservoir pressure is 43 MPa. Further reservoir parameters are shown in Appendix A.1.

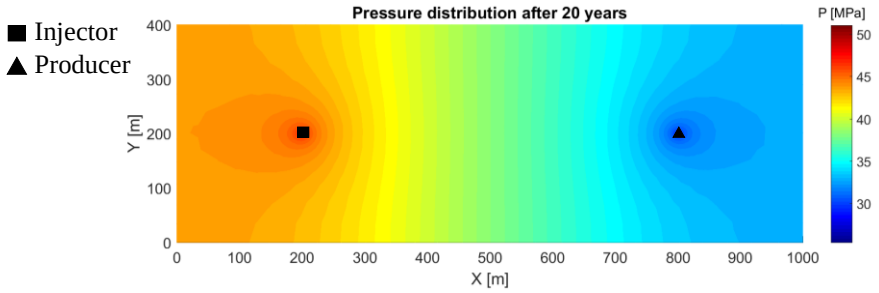

K.4 Sensitivity Analysis and Effects on the Pressure Difference

Sensitivity of certain parameters on the pressure difference between the production and the injection well in a modeled reservoir with 30 mD initial permeability. Further reservoir parameters are shown in Appendix A.1.

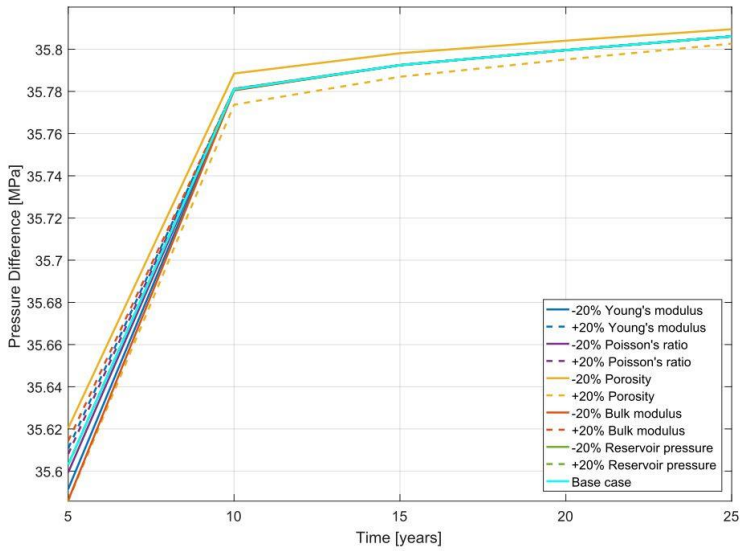

K.5 Sensitivity Analysis and Effects on Production Temperature

Sensitivity of certain parameters on the temperature at the production well in a modeled reservoir with 30 mD initial permeability. Further reservoir parameters are shown in Appendix A.1.

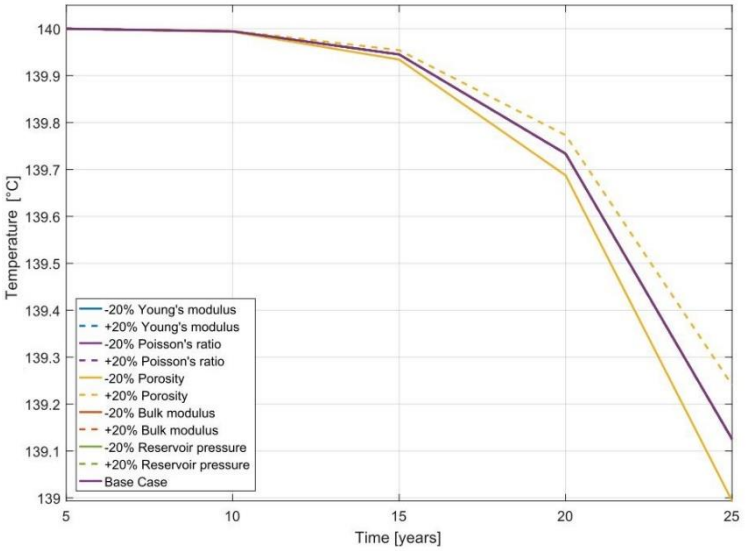

K.6 Sensitivity Analysis and Effects on the Temperature Difference

Sensitivity of certain parameters on the temperature difference of the injection and the production well in a modeled reservoir with 30 mD initial permeability. The data has been normalized to the base case. Further reservoir parameters are shown in Appendix A.1.